Investigating Approaches to Continuous Crystallisation Using Process Analytical Technology: Establishment of a Steady-State Cooling Crystallisation Process

by

Ikechukwu Ifeanyi Onyemelukwe

A Doctoral Thesis

Submitted in partial fulfilment of the requirements for the award of the degree of Doctor of Philosophy in Chemical Engineering of Loughborough University

January 2019

Abstract

In this work, two approaches to continuous crystallisation are investigated. The first approach is the mesoscale continuous oscillatory flow crystalliser which possesses a smooth periodic constriction design (herein known as the SPC mesoscale crystalliser) and is a tubular device operating at turbulent flow conditions. The second of these approaches is the popular mixed suspension mixed product removal (MSMPR) crystalliser based on stirred tank technology. The investigation of both approaches is aided by integrated process analytical technology (PAT), newly developed characterisation methods, and offline solid-state analytical tools. The SPC mesoscale crystalliser is a type of continuous oscillatory baffled crystalliser (COBC), which unlike the plug flow crystalliser (PFC), decouples mixing from net flow by combining oscillatory flow with steady flow. This enables significantly longer residence times to be achieved in practical lengths of the crystalliser for crystallisation purposes. In the past few years, COBCs have gained increasing attention as promising platforms for developing robust continuous crystallisation processes and transforming already existing commercial batch processes in industry. This small-diameter SPC mesoscale crystalliser, however, has had very little application to crystallisation despite possessing superior capabilities for efficient mixing and solids suspension, and small volume requirements for process development. The MSMPR crystalliser is an idealised crystalliser model that assumes steady-state operation of a well-mixed suspension with no product classification, and uniform supersaturation throughout, leading to constant nucleation and growth rates.

The investigation of both approaches in this work involves the characterisation of the mixing and heat transfer performance, and the development of processes for the continuous cooling crystallisation of glycine (GLY) from water in both platforms. A characterisation of the mixing performance of the SPC mesoscale crystalliser is performed using a newly developed RTD measurement technique. The technique known as non-invasive dual backlit imaging involves the use of two high-definition (HD) cameras and light sources to simultaneously and precisely capture the concentration of a tracer in the crystalliser as a function of grayscale intensity. The new technique is benchmarked against the more traditional invasive conductivity measurements to determine the reliability of both techniques. Using the dual backlit imaging technique, the liquid and solid phase axial dispersion performance the SPC mesoscale crystalliser is determined, and the optimum conditions for solid-liquid plug flow are identified for crystallisation. A series of heat transfer experiments are performed to

characterise the heat transfer performance of the SPC mesoscale crystalliser and its suitability for tight control of temperature and local supersaturation. Based on these experiments, an empirical correlation is developed to predict the tube-side Nusselt number and enable spatial temperature profile predictions in the SPC mesoscale crystalliser for cooling crystallisation. A seeded continuous cooling crystallisation process is then carried out based on metastable zone width (MSZW) measurements in a batch version of the SPC mesoscale crystalliser.

A rapid intermittent vacuum transfer technique is applied to the single- and two-stage configurations of the MSMPR crystalliser to successfully mitigate transfer line blockage issues and obtain uninterrupted steady-state operation. The RTD performance of the MSMPR crystalliser is characterised and benchmarked against the SPC mesoscale crystalliser, confirming the contrasting RTD profiles offered by each platform. Solid suspension performance and determination of critical residence time for heat transfer is also carried out for the MSMPR platform to aid crystallisation process development. Subsequently, using a complete recycle operation, the unseeded cooling crystallisation of GLY from water is investigated systematically to understand the effect of mean residence time, MSMPR operating temperature, and number of MSMPR stages on the GLY product mean size, crystal size distribution (CSD), and yield.

The systematic study of GLY-water seeded continuous cooling crystallisation in the SPC mesoscale crystalliser identified an operating strategy for obtaining desired product attributes. Specifically, seeding with small-sized seeds, running at longer mean residence times (by extending the crystalliser length), operating at near plug flow conditions, and implementing a spatial cubic temperature profile will lead to larger product mean sizes, with narrower CSDs, and higher yields. In the MSMPR crystalliser, experimental investigations showcased the higher degree of operational capability offered by cascade operation, whereby a two-stage MSMPR configuration enabled operation at much lower MSMPR temperature than possible in the single-stage MSMPR and provided higher yield. Results particularly highlighted the importance of controlling supersaturation distribution in the MSMPR system by manipulating operating variables such as mean residence time and MSMPR stage temperatures to achieve desired product quality.

Overall, the investigations carried out in this body of work demonstrate the potential of the SPC mesoscale crystalliser for application to continuous crystallisation process development of small-volume active pharmaceutical ingredients (APIs). Both platforms are therefore equally feasible for crystallisation process development and manufacturing.

Dedication

To my wonderful parents Geoffrey and Ifeoma for their continued guidance, prayers, and support.

Declaration

I declare that the work as presented in this thesis is my own except as acknowledged in the text and has not been submitted either in whole or in part, for a degree at this or any other institution.

_____

Acknowledgements

I would like to thank my heavenly Father for His blessings upon my life, and for granting me the strength and courage to embark on and complete this academic milestone. Secondly, I would like to thank my mum, dad, and siblings for all their support during this process. To my close friends William Onojeharho and David Odetade, thank you guys for being the best lads and listening to my numerous rants.

I am indebted to my supervisors Professor Chris Rielly and Professor Zoltan Nagy for their unwavering support and guidance throughout my PhD. To Professor Chris Rielly especially, I am most grateful for giving me the opportunity to do a PhD with the Loughborough Crystallisation Group. He was supportive in many ways despite his very busy schedule as Dean of the School of Aeronautical, Automotive, Chemical and Materials Engineering (AACME), and his invaluable insights greatly improved my critical assessments. I have learned so much from him as a scientist.

Next, I would like to thank Dr. Ian Houson, Dr. Amy Robertson, and Dr. Helen Wheatcroft for giving me the opportunity to do an industrial placement with AstraZeneca, Macclesfield during my PhD. I am also thankful to Dr. Nuno Reis for his encouragement, and insights which were helpful in my PhD. My appreciation goes to the Doctoral Training Centre of the EPSRC Centre for Continuous Manufacturing and Crystallisation (CMAC) for the extensive training years and opportunities provided throughout my PhD which aided my research. I appreciate the numerous CMAC colleagues and members of my 2012 cohort who helped in one way or another. Financial support from EPSRC grant no. EP/I033459/1 and CMAC grant no. EP/K503289/1 is also acknowledged.

My PhD would not have completed without the help and support of the technical staff at Loughborough University. I greatly appreciate Tony Eyre for his technical drawings and numerous discussions, Mark Barron and Steve Bowler of the workshop for fabricating many of the components, also Jim Muddimer, Paul Izzard, Graham Moody, Pradip Karia, and Sean Creedon. The technical personnel at Soham Scientific, Sealco, and Indatech are also appreciated for consultations, products, and fabrications of specially designed components during my PhD. I would also like to thank Dr. Qinglin Su and Ravi Parekh for their help and friendship during my PhD.

Lastly, I wish the best of luck to my colleagues Dimitris Fysikopoulos, Emmanuel Kimuli, Elena Simone, and Akos Borsos along with all my friends in the Chemical Engineering department and in Loughborough University.

Table of Contents

List of Figures

List of Tables

List of Abbreviations

API	active pharmaceutical ingredient
ATR	attenuated total reflectance
CCD	charge coupled device
cGMP	current good manufacturing practice
CLD	chord length distribution
CM	continuous manufacturing
CMAC	Continuous Manufacturing and Crystallisation
COBC	continuous oscillatory baffled crystalliser
COBR	Continuous oscillatory baffled reactor
COBRA	Centre for Oscillatory Baffled Reactor Applications
CPP	critical process parameters
CQA	critical quality attributes
CRD	Cambridge Reactor Design
CryPRINS	Crystallisation Process Informatics System
CSD	crystal size distribution
CSTC	continuous stirred tank crystalliser
CSTR	continuous stirred tank reactor
CWMC	continuous wet milling-crystallisation
DAQ	data acquisition module
DFT	discrete Fourier transform
DI	deionised
DN	diameter nominal
DR	dispax reactor
DSC	differential scanning calorimetry
DTA	differential thermal analysis
EPSRC	Engineering and Physical Sciences Research Council
FBRM	focused beam reflectance measurement
FDA	Food and Drug Administration
FFT	fast Fourier transformation
FTIR	Fourier transform infra-red
GCP	good calibration practice
GLY	glycine

GMP	good manufacturing practice
GSK	GlaxoSmithKline Ltd.
ICH	International Council for Harmonisation of Technical Requirements for Pharmaceuticals for Human Use
IDS	intelligent decision support
I.D.	internal diameter
IR	infra-red
LED	light emitting diode
LMTD	log mean temperature difference
MIT	Massachusetts Institute of Technology
MLR	multiple linear regression
MSMPR	mixed suspension mixed product removal
MSZW	metastable zone width
NCE	new chemical entities
NIR	near infra-red
OBC	oscillatory baffled crystalliser
OBR	oscillatory baffled reactor
ODE	ordinary differential equation
OFR	oscillatory flow reactor
PAT	process analytical technology
PBE	population balance equation
PCA	principal component analysis
PCR	principal component regression
PFC	plug flow crystalliser
PFR	plug flow reactor
PIV	particle image velocimetry
PLS	partial least squares
PLSR	partial least squares regression
PT&D	Pharmaceutical Technology and Development
PTFE	polytetrafluoroethylene
PVC	polyvinyl chloride
PVI	process video imaging
PVM	particle vision microscope
PXRD	powder x-ray diffraction

QbD	quality-by-design
R&D	research and development
RCI	retreat curve impeller
RGB	red, green, blue
RMSEP	root mean square error of prediction
ROI	region of interest or return on investment
RSS	residual sum of squares
RTD	residence time distribution
SAV	surface area to volume ratio
SEPC	sharp-edged periodic constrictions
SNV	standard normal variate
SPC	smooth periodic constrictions
SSE	sum of squared errors
STC	stirred tank crystalliser
STR	stirred tank reactor
SWMCL	square-weighted mean chord length
TGA	thermo-gravimetric analysis
UV	ultra-violet
WIP	work-in-progress

Nomenclature

A	outside heat transfer area of the inner tube or heat transfer area
A_c	area of a 4 mm-long constriction outer surface
A_{CS}	cross-sectional area of tube
A_0	orifice area
A_{plain}	total heat transfer area of plain meso-tube
A_{SPC}	total heat transfer area of SPC meso-tube
A_s	area of a 9 mm-long outer straight surface of the inner tube
B_c	birth term
C	solute or solution concentration
$\boldsymbol{C}$	concentration matrix
C^*	dimensionless concentration for tracer
$C^*(\theta)$	model response
$C_0^*(\theta)$	inlet response
$C_1^*(\theta)$	output response
C_D	drag coefficient
C_d	discharge coefficient
C_l	concentration of solute in the liquid phase at the crystal surface
C_1	steady-state concentration of the outlet stream
C_2	integration constant
C_f	feed stream concentration
C_i	initial concentration of species
C_p	specific heat capacity of the solution at incoming feed temperature
C_s	seed stream concentration
C_{sat}	equilibrium solubility or concentration
C_{ss}^i	steady-state concentration in the ith crystalliser
ΔC	absolute supersaturation
D	tube internal diameter
D_{mean}	tube mean internal diameter
D_c	death term
D_{ax}	axial dispersion coefficient
D_{ax}/uL	axial dispersion number

D_{1im}	tube mean inside diameter
D_{1o}	outer tube diameter of the inner tube
D_i	impeller diameter
$\boldsymbol{E_x}$	error matrix for $\widetilde{\boldsymbol{X}}$
G	linear growth rate
Gr	Graetz number
I	intensity
I_0	incident light intensity
L	length of crystalliser or test section
L_{SPC}	length of SPC meso-tube
L_1	active tube length
L_{1tot}	total active tube length of all temperature-controlled segments
L_c	characteristic size of crystal
L_i	chord length in the ith size bin
L_p	product mean size
L_s	initial seed mean size
$M(\theta)$	system transfer function
N	number of equal-sized tanks-in-series
N_{Re}	impeller Reynolds number
N_i	rotational speed of the impeller
N_{js}	just-suspended speed
Nu_a	Nusselt number in the annulus
Nu_t	tube-side Nusselt number
P	power
$\boldsymbol{P}$	loading matrix for $\widetilde{\boldsymbol{X}}$
Pr	Prandtl number
P_0	impeller power number
Q	volumetric flow rate
Q_1	heat transfer rate relating to the process fluid
Q_k	volumetric flow rate of influent and effluent streams
R^2	coefficient of determination or R squared
$R_{conv,c}$	resistance to convective heat transfer from the wall to cooling fluid
Re_n	net flow Reynolds number

Re_o	oscillatory Reynolds number
R_w	wall resistance
S	supersaturation ratio
St	Strouhal number
S_c	seed surface area
S_{ij}	sensitivity coefficient
$S_{ij}\big\vert_{t=t_k}$	sensitivity of the ith output to the jth parameter at a sampling time t_k
$\boldsymbol{T}$	latent or score matrix
$\boldsymbol{T_1}$	latent or score matrix for $\widetilde{\boldsymbol{X}}$
$\boldsymbol{T_2}$	latent or score matrix for $\tilde{\boldsymbol{c}}$
T_{1in}	entry temperature of process fluid
T_{1out}	exit temperature of process fluid
T_{2in}	entry temperature of cooling fluid
T_{2out}	exit temperature of the cooling fluid
T_{cr}	desired operating temperature of the MSMPR
T_f	incoming feed temperature
T_j	MSMPR jacket temperature
T_{lim}	temperature at which cloudiness is detected
T_{sat}	saturation temperature
T_w	annulus temperature
ΔT_{max}	metastable zone width
U	overall heat transfer coefficient between the circulating fluid and feed solution
U_{21}	overall heat transfer coefficient between the cooling and process fluids
V	volume of solution in crystalliser
V_{L1}	measured volume in the active tube length
V_{SPC}	measured volume in an SPC meso-tube
V_{cr}	crystalliser operating volume
V_s	volume of liquid or solution
W_s	seed mass
X	mass ratio of solid to liquid
$\boldsymbol{X}$	matrix of multiple variables
$\widetilde{\boldsymbol{X}}$	normalised data matrix

$\boldsymbol{X_{meas}}$	matrix of measured vectors
$\boldsymbol{\widetilde{X}_{meas}}$	normalised measurement matrix
X_i	mass fraction of water in each flow stream
$\boldsymbol{X_j}$	matrix of the selected parameters vectors at the jth stage
$\boldsymbol{Z}$	sensitivity matrix
abs	absorbance of species
$\boldsymbol{b}$	vector containing all regression coefficients
c	particle or dye concentration
$\boldsymbol{c}$	concentration vector
$\boldsymbol{\tilde{c}}$	PLSR model response (concentration)
$\boldsymbol{c_{pred}}$	predicted concentration vector
d_0	constriction diameter
d_p	mean diameter of particles
$d_{4,3}$	volume mean diameter
d_{10}	diameter below which 10% of the population lies
d_{50}	diameter below which 50% of the population lies
d_{90}	diameter below which 90% of the population lies
$\boldsymbol{e_c}$	error vector for $\boldsymbol{\tilde{c}}$
f	oscillation frequency
f_0	mass flow rate of water in the feed stream
f_1	mass flow rate of water in the outlet stream
f_s	mass flow rate of water in the seed stream
g	acceleration due to gravity
$\boldsymbol{g}$	eigenvector
h	ratio of the distance between baffles/constrictions to tube internal diameter
h_a	heat transfer coefficient in the annulus
h_i	process heat transfer coefficient
h_o	jacket heat transfer coefficient
h_t	tube-side heat transfer coefficient
h_w	wall heat transfer coefficient
k	number of streams in and out of the crystalliser, or upper size bin, or total number of temperature-controlled segments
k_1	thermal conductivity of the process fluid

k_d	mass transfer coefficient
k_g	thermal conductivity for the inner tube wall material
k_v	volumetric shape factor
l	baffle/constriction spacing
l_p	optical path length
$\dot{m}_i$	total mass flow rate in each flow stream
$\dot{m}_1$	mass flow rate of the process fluid
n	population density function of crystals
n_i	number of counts corresponding to the ith bin
n_0	population of nuclei
n_{L1}	total number of constrictions and straight surfaces in the active length
n_c	number of constrictions
n_p	number of parameters
p_j	vector of the jth parameter
$\bar{\boldsymbol{p}}$	nominal vector of parameters
$\bar{p}_j$	nominal value of jth parameter
$\boldsymbol{q}$	loading matrix for $\tilde{c}$
$\boldsymbol{r}_i$	orthogonal projection of $\boldsymbol{s}_i$
s	impeller geometrical constant
$\boldsymbol{s}_i$	sensitivity vector corresponding to the parameter p_i
t	time
$\boldsymbol{t_1}$	score for matrix $\boldsymbol{T_1}$
$\boldsymbol{t_{1meas}}$	scores for $\widetilde{\boldsymbol{X}}_{\boldsymbol{meas}}$
$\boldsymbol{t_2}$	score for matrix $\boldsymbol{T_2}$
t_k	sampling time
u	superficial or mean axial velocity
$u(t)_{max}$	peak oscillatory velocity
u_m	mean velocity
u_p	steady-state settling velocity of particles
$\boldsymbol{w}$	eigenvector
x	axial position
$\bar{\boldsymbol{x}}$	normalised sample vector

x_0	centre-to-peak amplitude
$\hat{y}_i$	vector of the numerically calculated aspect ratio at kth point in time.
$\bar{y}_i\|_{t=t_k}$	correlation prediction of the ith output evaluated at a sampling time
z	position along the axial length
z^*	dimensionless length

Greek Letters

α	open cross-sectional area
ρ	fluid or liquid density
ρ_c	mass or molar density of crystal
ρ_p	particle density
ρ_s	glycine solution density
ε	power density or specific power input
ϵ	molar absorptivity coefficient or light-scattering cross-section of a particle
η	surface shape factor
θ	dimensionless time
$\wp$	the set of estimable parameters
μ	bulk fluid viscosity
τ	mean residence time
$\tau_{critical}$	critical mean residence time
τ_L	mean residence time in test section
φ	velocity ratio
ν	bulk fluid viscosity
λ	cut-off value
ω	angular frequency of oscillation or frequency space
π	pi

Chapter 1 Introduction and motivation

1.1 The challenges of the pharmaceutical industry

The pharmaceutical industry is a highly innovative, research-intensive, and conservative industry. For the last 50 years the socio-economic relevance of this industry has grown owing to its numerous drug developments that alleviate and cure a wide range of medical ailments, providing better lives for millions of people (Shah, 2004; Poechlauer et al., 2012). Batch manufacturing has dominated the pharmaceutical industry right from the mid-1900s; and stirred tank technologies in the form of stirred tank crystallisers (STCs) have for long been a well-understood simple, trusted, and proven technology for isolating and purifying high value active pharmaceutical ingredients (APIs) (Shah, 2004). The relevance of batch manufacturing in today's pharmaceutical industry is emphasised by the large number (about 80%) of manufactured pharmaceutical drugs that involve at least one crystallisation step (Bakar et al., 2009). Pharma's chronic dependence on batch manufacturing has earned the industry a reputation of backwardness, considering that other major industries such as petrochemical, bulk chemical, dairy and food have established and used continuous manufacturing (CM) for a long time now (Alvarez et al., 2011). This lack of innovation is a consequence of large-sized pharmaceutical companies (collectively known as 'big pharma') relying on a 'blockbuster' business model, where priority is placed on developing large-volume new chemical entities (NCEs) which would yield high returns of approximately US$1 billion/year (Booth, 1999). As at the year 2000, the total cost of developing and introducing an NCE into a market amounted to US$500 million. With drug patents having a span of 20 years, NCEs that survive the development phase usually have a payback period of only 8 – 12 years before patent expiration (Grabowski, 1997; Bauer and Fischer, 2000). The blockbuster business model was therefore justified by the short time companies had to maximise revenue from their patented drugs before losing market share to generic companies (Shah, 2004; Plumb, 2005). Consequently, little or no investment went into developing innovative manufacturing technologies.

The pharmaceutical industry is going through a period of great change in the face of significant challenges as it strives to reinvent itself for a sustainable and competitive future. Global competition continuously increases and the only way for large research and development-based companies to stay ahead of generic competitors is through reduction of process development times and investment costs for implementing new technologies, while also considering the rising cost of resources (Plumb, 2005; Buchholz, 2010). Key issues

including sustainability of process development, production, and application of medicines have become the focus of public attention. Fewer blockbuster drugs are being discovered, R&D productivity (numbers of NCEs per unit amount of investment) is declining, and more medicines are being aimed at niche markets (Badman and Trout, 2015).

When compared with other major process industries, the pharmaceutical industry has operational performance levels well below process industry norms of 3.4 defects per million units, otherwise known as 6σ (six sigma). In terms of right-first-time quality (i.e. number of defects) and process repeatability, most pharmaceutical firms operate at levels between 3 and 4σ, costing the global industry some $20 billion annually (Srai et al., 2015). The blockbuster model has resulted in large, centralised batch manufacturing facilities. Product supply chains for distributing medicines to patients, are typically 1 – 2 years in length, with a huge associated cost of inventory. This means an existing infrastructure that is lacking the flexibility to meet changes to markets, products, and scale; and an entire industry that is unprepared for dealing with an unexpected global epidemic. Current industry trends suggest that smaller, more niche volume products will become the norm with fewer blockbusters (Srai et al., 2015). Hence, future production and supply chain models that can deliver significantly greater product variety and volume flexibility are needed.

1.2 Potential for continuous manufacturing to transform the pharma industry

Over the last decade, there have been significant investments in continuous manufacturing (CM) development by big pharma companies (e.g. GlaxoSmithKline, Novartis, Pfizer, Lilly, Abbott), measuring well over a billion dollars in aggregate (Badman and Trout, 2015; Page et al., 2015). The ambition to adopt CM in the pharmaceutical industry is driven by a strong desire to reduce the cost of drug quality (i.e. number of failed batches); reduce operating, inventory, and capital costs; enhance process safety; and significantly accelerate development times across the medicines' supply chain (Baxendale et al., 2015; Page et al., 2015).

The vision of CM is one where all relevant chemical and pharmaceutical process steps are fully integrated, based on a systems approach, having model-based control, and utilising flow (Nepveux et al., 2015; Badman and Trout, 2015). There have so far been collaborative efforts between industry and academia to speed up the adoption of CM, most notably the Novartis-MIT Centre for Continuous Manufacturing, Centre for Oscillatory Baffled Reactor

Advancement (COBRA), and the UK-based consortium EPSRC Centre for Continuous Manufacturing and Crystallisation (CMAC). In just four years, there has been a substantial increase in the output of academic publications on the subject (Rougeot et al., 2015; McGlone et al., 2015; Zhang et al., 2017; Wang et al., 2017; Chavan et al., 2018; McWilliams et al., 2018; Wang et al., 2018). There are also dedicated forums bringing together the manufacturing community to promote discussions on the development and deployment of CM, particularly the CMAC-MIT International Symposium on Continuous Manufacturing of Pharmaceuticals held every two years. The current regulatory environment including the US Food and Drug Administration (FDA) and the European Medicines Agency (EMA) supports abandoning of some traditional manufacturing practices in favour of cleaner, more flexible, and more efficient continuous manufacturing (Poechlauer et al., 2012; Siemens, 2013; Allison et al., 2015). Clearly, a paradigm shift towards CM is progressing; however, achieving the vision of CM will require significant momentum.

An ideal pharmaceutical crystallisation process produces a pure product with desired attributes, at high yield while minimizing energy input, process equipment footprint, and complexity (Wong et al., 2012). CM is essentially a form of process intensification with the potential to make better, more uniform/consistent products, whilst simplifying production, saving energy, resources and cost (Plumb, 2005; McKenzie et al., 2006; Schaber et al., 2011; Wong et al., 2012). The key to changing the paradigm from batch to continuous manufacturing is to adopt a systems approach by viewing the entire pharmaceutical processing system as a value stream through a pipeline, from chemical raw materials (inputs) to downstream finished dosage forms (for delivery of intended pharmacological effect in the patient), rather than considering each process step as a stand-alone unit operation. Batch crystallisation, however, remains the most critical and challenging process step to convert pharmaceutical manufacturing into a continuous process. It is for this reason that continuous crystallisation has received rapidly growing attention from both industry and academia (Chavan et al., 2015; McGlone et al., 2015; Zhang et al., 2017; Gao et al., 2017; Brown et al., 2018; McWilliams et al., 2018; Wang et al., 2018), and is the focus of this research work. With a ‘wide-pipe’ vision shown in Figure 1.1, pharma can have:

- An integrated systems approach requiring process understanding and real-time control;
- End-to-end process integration;
- Continuous flow of material;
- 24 hour/day operations.

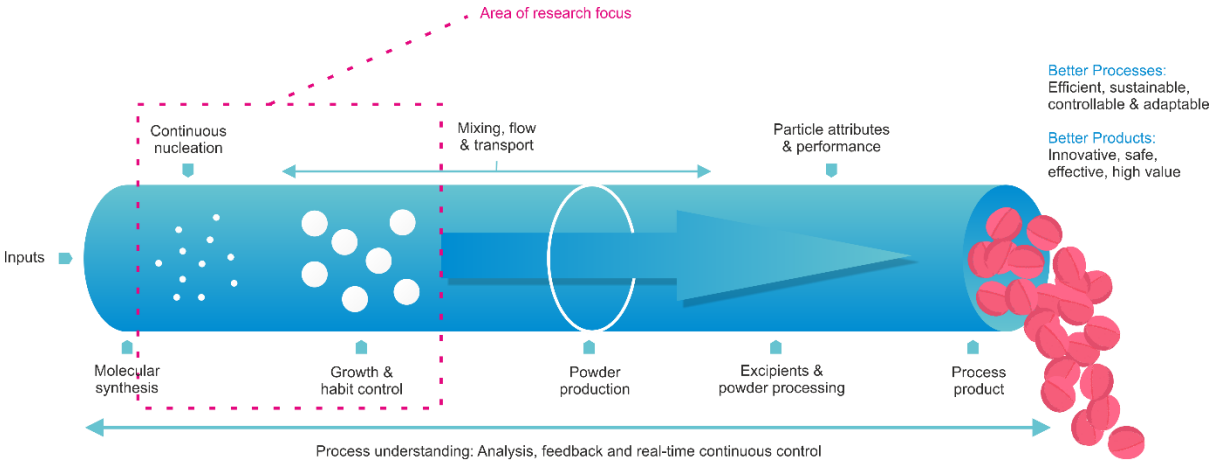

Figure 1.1 A 'wide-pipe' vision for continuous pharmaceutical manufacturing showing the area of research focus.

With CM, it is envisioned that processes will be run 24/7 for 50+ weeks a year, with 1 or 2 weeks for annual maintenance (Badman and Trout, 2015). End-to-end supply chains will provide greater product and volume flexibility for serving relatively smaller niche markets. Inventory will be significantly reduced by moving away from a long-term forecasting approach to a 'demand-driven' replenishment model (Srai et al., 2015). Drug product quality will improve at lower overhead costs through robust and reproducible processes (Byrn et al., 2015). Other potential benefits of implementing CM in the pharmaceutical industry are outlined in Table 1.1.

The quality-by-design (QbD) initiative introduced by the FDA (Guidance for Industry, 2004) has propelled advancements in process analytical technology (PAT) which have enabled real-time monitoring and control, and improved understanding of crystallisation process dynamics (Hishamuddin et al., 2011; Calabrese and Pissavini, 2011; Saleemi et al., 2012). The role of PAT in the ambitious strides to establish continuous crystallisation as a new standard in the pharmaceutical industry cannot be over-emphasised. PAT has been successfully applied to batch crystallisation processes at small and large scale to improve efficiency and manage batch-to-batch product variability (Plumb, 2005; Calabrese and Pissavini, 2011; Hishamuddin et al., 2011). These successes are a motivation to use available PAT tools and techniques in this research to investigate continuous crystallisation processes that will be developed.

Table 1.1 Potential benefits of continuous manufacturing to the pharmaceutical industry

Capital investment	Smaller plant footprint with lower CAPEX; reduced drug development cost by up to 10%	Poechlauer et al., 2012; Harrington, 2013; Srai et al., 2015
Operating costs	Less operational overheads; less labour and raw material costs; increased asset utilisation	Calabrese and Pissavini, 2011; Harrington, 2013; Srai et al., 2015; Badman and Trout, 2015
Inventory	Up to 50% reduction in inventory possible with primes from >200 days to <70 days; less WIP, material handling and transport	Harrington, 2013; Srai et al., 2015
Quality	Highly consistent product; lower cost of quality, achieve $>5\sigma$	Harrington, 2013; Srai et al., 2015; Badman and Trout, 2015
Strategic	Greater product and volume flexibility; more tailored to specific market needs	Shah, 2004; Srai et al., 2015; Nepveux et al., 2015; Konstantinov and Cooney, 2015
Scale-up	Rapid and seamless scale-up development; reduced scale-up cost	Plumb, 2005; Poechlauer et al., 2012; Srai et al., 2015; Page et al., 2015; Nepveux et al., 2015
Supply chain	More responsive 'demand-driven' end-to-end supply chain; reduction in cycle time by half	Srai et al., 2015
Process intensification & sustainability	Minimizes space, waste, energy consumption (cut by as much as 95%); lower solvent and material use through controlled recycling and higher yield	Plumb, 2005; Calabrese and Pissavini, 2011; Poechlauer et al., 2012; Nepveux et al., 2015; Allison et al., 2015
Multipurpose	Allows multi-product production through parallel standardized units	Calabrese and Pissavini, 2011; Konstantinov and Cooney, 2015
Plant safety	Less risk in handling of smaller material amount at any time during the process, and process intensification	Calabrese and Pissavini, 2011; Poechlauer et al., 2012; Allison et al., 2015
Throughput	Production targets met through increased throughput and not volume amounts	Calabrese and Pissavini, 2011; Poechlauer et al., 2012; Nepveux et al., 2015

A perceived barrier for pharma moving towards CM is the established batch asset base accumulated during the 80s and 90s. Replacing these existing batch systems with continuous technologies must be justified by good return on investment (ROI). In terms of ROI, cost and speed to market are usually not as important as safety, robustness, and reproducibility for new products. CM adoption is also restrained by the fact that the pharmaceutical industry is more risk averse to adopting new manufacturing technologies. This means that CM must be proven as technologically and financially superior and tied to a product before widespread adoption will take place (Reay et al., 2008; Baxendale et al., 2015; Page et al., 2015; Byrn et al., 2015).

Accelerating the widespread adoption of CM will require in-depth understanding of CM technologies through intensive research, such as that which is presented in this thesis. Compelling evidence of technical benefits must be demonstrated through robust continuous processes to affect a mindset and cultural change required to turn CM from an interesting science and technology project into an established method of generating high quality medicines.

1.3 Approaches to continuous crystallisation

Industrial pharmaceutical crystallisations are performed in batch mode often using cooling or anti-solvent crystallisation (Alvarez et al., 2011; Zhang et al., 2012). While these batch crystallisation processes and their methodologies are reasonably well understood, the major issue of batch-to-batch process variability causes inconsistent product quality which is often problematic for downstream operations. Thus, it is pertinent that drug substance critical quality attributes (CQAs) such as crystal size distribution (CSD), polymorphic form, morphology, and purity be reproducible to prevent further processing steps such as milling or even re-crystallisation which are common in the pharmaceutical industry today (Zhang et al., 2012). The underlying principle of continuous crystallisation is steady-state operation, in which process variables in a system do not vary with time. With steady-state operation, it is possible to obtain a consistent process output, which can greatly aid downstream processing. Continuous crystallisation of small molecule APIs is currently an area of strong interest in pharmaceutical manufacturing due its potential for delivering consistent particle attributes (Lawton et al., 2009; Kwon et al., 2014; McWilliams et al., 2018), reducing manufacturing costs through process intensification (Schaber et al., 2011; Wang et al., 2018), and shortening process development times (Zhao et al., 2017; Agnew et al., 2017). The most common types of steady-state continuous crystallisers are the conventional plug flow crystalliser (PFC) (Eder et al., 2010; 2011), continuous oscillatory baffled crystalliser (COBC) (Lawton et al., 2009; McGlone et al., 2015), and the mixed suspension mixed product removal (MSMPR) crystalliser (Randolph and Larson, 1971). The selection of a suitable continuous crystalliser is usually guided by system-dependent factors such as crystallisation kinetics and fouling/agglomeration propensity (Brown et al., 2018), but also the ability of the crystalliser to consistently control a desired critical quality attribute (CQA) while satisfying yield constraints. Additional factors

such as solid-liquid density difference, viscosity, and solids loading are important, since they can affect crystallisation process performance (McGlone et al., 2015).

The material residence time distribution (RTD) is an important parameter that describes the time histories of crystals, and as such, the supersaturation histories of all crystals within a continuous crystalliser. Therefore, RTD can affect the CSD, an important critical quality attribute which determines filterability, drying times, and final drug product performance. The control of the full CSD is not possible in practice; however, some of its attributes such as mean size, span, coefficient of variation, and fines fraction can be controlled (Porru and Özkan, 2018). A typically large and narrowly distributed crystal product is usually desired from a crystallisation process to aid downstream processability (Yang and Nagy, 2014). The conventional PFC aims to provide a uniform environment for consistent particles by providing a narrow RTD. This ensures all crystals experience similar histories of supersaturation and hence similar crystal nucleation, growth, and agglomeration rates. The high flow rates required to achieve this, however, means that impractical tube lengths required for sufficient residence times limit application of the PFC to continuous crystallisation. The COBC overcomes the challenges of the conventional PFC by decoupling mixing from net flow through oscillatory flow. Therefore, longer mean residence times necessary for crystal growth and yield are possible in greatly reduced length to diameter ratios without settling issues. In addition, a range of RTDs is possible by finely controlling the net flow, frequency and amplitude of oscillations (Ni et al., 2003; Reis et al., 2004). The MSMPR at the opposite end of the mixing spectrum offers an RTD for both solution and crystals that is much broader than usually obtained in tubular crystallisers. Crystallisation studies in the conventional PFC and conventional scale COBCs (>10 mm internal diameter) have shown that these crystallisers can give narrow CSDs (Lawton et al., 2009; Eder et al., 2010; Ferguson et al., 2013; Briggs et al., 2015; Siddique et al., 2015) owing largely to their near-plug flow RTDs, but also tighter control of spatial supersaturation achievable in these platforms. A broad RTD from the backmixed MSMPR therefore suggests that broader steady-state CSDs are to be expected in MSMPR crystallisation.

This work contributes to an increased understanding of CM technologies by focusing on two steady-state crystallisers that offer a promising route to developing robust continuous crystallisation processes, namely the COBC, and the MSMPR crystalliser. Specifically, the development and investigation of a continuous crystallisation process in a small-scale COBC and two configurations of the MSMPR crystalliser will be carried out. Much attention will be on the small-scale COBC known as the mesoscale continuous oscillatory flow crystalliser with smooth periodic constrictions (known as the SPC mesoscale crystalliser) which has an internal

diameter (I.D.) of 5 mm. This small-diameter tubular device is a highly attractive design for potential application to continuous crystallisation due to its ability to efficiently suspend high particle concentrations (Reis et al., 2005; Ejim et al., 2017) and achieve near plug flow at very low net flows (Zheng and Mackley, 2008) than possible in conventional and pilot scale COBCs. Also, the small volume of this design can be especially beneficial for crystallisation process development, since the amount of raw material needed would be significantly lower than in conventional and pilot scale COBCs. Usually, in the early phases of drug substance development, only limited amounts of API are available, and it is often very high value material. The SPC mesoscale crystalliser platform could therefore potentially enable much faster process development from early phase through to late phase, with only a few kilograms of API. Despite the attractive features of this device, its application to continuous crystallisation has been very limited, mainly due to concerns about encrustation and blockage during crystallisation. Precipitation and protein crystallisations in closely similar mesoscale COBCs (3 – 4.4 mm I.D) have been reported by Castro et al. (2013; 2016; 2018); however, there is still limited understanding on the suitability of the SPC mesoscale crystalliser for continuous crystallisation, and its capability for consistent control of product CQAs.

Previous works by Ferguson et al. (2013) and Hou et al. (2014) have shown that increasing mean residence time in a single-stage MSMPR can improve steady-state CSDs. However, attaining longer mean residence times in an MSMPR usually requires operation at much lower flow rates, which can be a challenge to implement in pump operation due to non-representative withdrawal, and crystal settling during transfer. Su et al. (2017) addressed this issue using a pump-operated periodic flow MSMPR crystallizer. The technique involved a series of rapid addition and withdrawal cycles and a tuneable holding period between, which allowed the manipulation of material RTD in the MSMPR crystallizer. High flow rates were applied during additions and withdrawals to prevent sedimentation in transfer lines and enable a more representative slurry withdrawal. Interestingly, the periodic flow operation was able to extend mean residence time without overly broadening the material RTD, and larger mean sizes were obtained for the glycine product compared to the continuous flow operation. Periodic flow operation, however, can be described as a hybrid of batch and continuous crystallization, as the MSMPR crystallizer responds to periodic but controlled disturbances and achieves a "state of controlled operation" rather than the conventional "steady-state" operation described by Randolph and Larson (1971). This work investigates the continuous flow crystallization of a model compound in the MSMPR crystallizer with a primary objective of achieving uninterrupted steady-state operation. By implementing of a rapid intermittent transfer method

(Ferguson et al., 2013), transfer line blockage issues encountered during pump operation can be overcome to permit longer mean residence times and uncompromised continuous operation. Attempts to control product CSD using multistage MSMPR crystallisers have been reported in literature (Randolph et al., 1968; Tavare et al., 1986), and these studies have suggested that the single-stage MSMPR crystalliser is inefficient, because it produces a product with a broader CSD than the multistage MSMPR crystalliser. Also, in terms of process operability, the single-stage MSMPR crystalliser has limited temperature controllability because of its small heat transfer area (Zhang et al., 2012). With the inclusion of multiple stages in cascade configuration, RTD can be significantly improved, and the MSMPR system can operate closer to batch equilibrium conditions. For this reason, a single- and two-stage MSMPR crystalliser is studied in this work.

1.4 Research aim and objectives

The overall aim of this research is to investigate the cooling crystallisation of a model compound in two approaches to continuous crystallisation as a radical new approach to the purification of APIs, which will demonstrate the potential to transform industrial practice.

The research objectives that support the overall aim of this thesis are as follows:

- Develop accurate and reliable online characterisation techniques to gain understanding and control of equipment and platforms for the design of continuous crystallisation processes.
- Demonstrate the application of PAT tools for characterisation of steady-state operation in two approaches to continuous crystallisation via particle and/or solution phase monitoring.
- Rigorously assess the suitability of the SPC mesoscale crystalliser for continuous cooling crystallisation, and gain understanding of its process performance characteristics in terms of yield and product CQAs i.e. mean size, CSD, and polymorphic form.
- Develop laboratory scale continuous cooling crystallisation processes for a suitable polymorphic model system in the SPC mesoscale crystalliser and MSMPR crystalliser, representing two different approaches to continuous crystallisation.

- Implement the intermittent slurry withdrawal technique in the single- and two-stage MSMPR crystalliser to achieve uninterrupted steady-state operation and enable a systematic study of the inter-relationship of critical process parameters (CPPs) and CQAs.
- Collect reliable experimental data, aided by well-designed experimental methods, accurate measurement and analysis, and repeatable experiments, that could be used for parameter estimation of crystallisation kinetics and would serve as validation of mathematical models to aid better understanding and optimisation of continuous crystallisation processes.

1.5 Research methodology

The primary platform investigated in this work is the SPC mesoscale crystalliser. The SPC mesoscale crystalliser is a tubular mixer capable of achieving excellent heat transfer and near plug flow at low flow rates (ml min^{-1}). Conventional scale COBCs usually possess a 'sharp-edged periodic constriction' (SEPC) design, which makes them prone to 'dead corners' and less efficient at suspending solids as found by Ejim et al. (2018). The unique SPC geometry of the SPC mesoscale crystalliser (detailed description provided in section 3.3 of Chapter 3) favours uniform particle suspension (Reis et al., 2005), thus presenting a high potential for application to solids handling processes such as crystallisation (Wang et al., 2017). The presence of smooth constrictions in the SPC design reduces high shear regions and the likelihood of crystal attrition during crystallisation, which can be beneficial for particle shape and size distribution. The SPC mesoscale crystalliser is used for the development of a seeded continuous cooling crystallisation process in this work. Specifically, the effect of mean residence time, temperature profile, oscillatory conditions, seed size and loading, and polymorphic form on product mean size, CSD, and yield are investigated.

To address the backmixed nature of the MSMPR, different configurations have been employed with the chief aim of obtaining better CSD quality alongside process yield (Griffin et al., 2010; Yang et al., 2015; Acevedo et al., 2017; Gao et al., 2018). The MSMPR crystalliser presented in this work is a multi-stage configuration which affords more flexibility for decoupled operation to better control crystallisation mechanisms. A key design aspect of this platform is the use of rapid intermittent withdrawal for slurry transfer between stages. The intermittent transfer used in this work involves using a high vacuum to generate very high

velocities for withdrawal of up to ~10% of the slurry volume every one tenth of a residence time. Rapid intermittent withdrawal is considered a form of continuous operation since changes in steady-state conditions are negligible when slurry slug size withdrawn is less than 10% of the crystallizer volume (Garside et al., 2002; Hou et al., 2014). Transferring product in this way ensures that no disturbance is caused to the MSMPR system during operation while achieving representative withdrawal at constant-velocity (isokinetic) and avoiding crystal breakage during transfer. Attention is paid to ensuring representative withdrawal by characterising the solids suspension performance of the MSMPR for the model compound. Usually, an MSMPR crystalliser is operated with continuous feed supply and product withdrawal to and from the crystalliser using peristaltic pumps. By convention, to maintain a constant volume and sufficient residence time for crystals to grow in the MSMPR crystalliser, it is necessary to reduce the stream flow rates which often leads to classified withdrawal and tube settling due to low velocities. The intermittent method of transfer therefore allows for increased mean residence times, while solving transfer line settling frequently experienced in existing MSMPR operation. The method could also be better suited for dealing with encrustation related issues, where larger diameter tubes are not easily blocked by broken-off crusts of material. In all experiments, start-up from equilibrium batch suspension is utilised, with the MSMPR system operated in product recycle mode to minimise material consumption and waste generation. The impact of process parameters including MSMPR temperature, mean residence time, and number of MSMPR stages on the steady-state product CSD, mean crystal size, and yield is studied.

Experimental RTD and heat transfer characterisation methods are applied to understand the capabilities of both platforms for providing a reliable crystallisation environment. For seeded cooling crystallisation studies, a wet milling technique is used to minimise variability in seed material and improve process consistency. PAT tools and a multivariate calibration method are exploited to gain real-time process understanding in this work. The information gained from investigations can be utilised for future optimisation of continuous crystallisation processes in both platforms using a combination of mathematical modelling and experimental approaches.

1.6 Research strategy

The strategy for achieving the objectives mentioned above will include:

- **Characterisation of the SPC mesoscale crystalliser:** RTD and axial dispersion of the liquid and solid phase; heat transfer characteristics. These are reported in Chapter 4 and Chapter 5 respectively.
- **Crystallisation in the SPC mesoscale crystalliser:** Overcoming current challenges with continuous operation; getting to steady-state operation; maintaining and controlling the product CSD and yield; understanding the best operating strategies. These are reported in Chapter 6.
- **Characterisation of the MSMPR crystalliser:** RTD of the liquid phase; critical mean residence time for heat transfer; solids suspension performance. These are presented in the early part of Chapter 7.
- **Crystallisation in the MSMPR crystalliser:** Solving the problem of transfer line blockage; getting to steady-state operation; understanding the best operating strategies. These are reported in the later part of Chapter 7.

1.7 Research contribution

The significant contributions of this research are as follows:

- A new empirical tube-side Nusselt number correlation is developed from heat transfer measurements in the SPC mesoscale crystalliser. The correlation can be used in the prediction of overall heat transfer coefficients for different oscillatory and steady flow conditions and incorporated into heat balance equations alongside physical and material properties, to accurately predict spatial temperature profiles in the SPC mesoscale crystalliser for seeded continuous cooling crystallisation.
- Application of an estimability analysis reveals for the first time the dominant factors controlling the heat transfer rate characteristics of SPC mesoscale crystalliser which are smooth constrictions and net flow velocity, rather than oscillatory flow as established in the SEPC COBCs.
- A novel non-invasive dual backlit imaging technique is developed for RTD measurements of the liquid and solid phase which is proven to be more reliable and accurate than traditional invasive conductivity measurements commonly used in the

characterisation of platforms. This method may be used to characterise axial dispersion in other mesoscale COBCs.

- Solid phase RTD measurements are conducted using polystyrene particles to reveal for the first time the flow behaviour of solids in the SPC mesoscale crystalliser. The technique may be applied to reliably determine the dispersion experienced by crystals of a model compound during crystallisation process development and for use in process models.
- The application of a reliable monitoring framework is demonstrated, including the integration of FBRM and Raman to characterise steady-state operation in the SPC mesoscale crystalliser and the MSMPR crystalliser.
- A systematic study is carried out to assess the suitability of the SPC mesoscale crystalliser for seeded and unseeded continuous cooling crystallisation processes and understand its capability for controlling product CQAs. A seeded continuous cooling crystallisation process is developed in the SPC mesoscale crystalliser for the first time as an alternative approach to unseeded continuous cooling crystallisation.
- The characterisation of liquid RTD performance of a single- and two-stage MSMPR crystalliser is performed to draw a comparison with the RTD profiles and axial dispersion performance of the SPC mesoscale crystalliser as applies to continuous crystallisation and controlling product CSD.
- A rapid intermittent withdrawal method is applied to multiple configurations of the MSMPR crystalliser to solve transfer line blockage issues frequently encountered in literature; this enabled uninterrupted steady-state operation for systematic crystallisation studies in a single- and two-stage MSMPR crystalliser.

1.8 Thesis structure

This thesis comprises eight chapters organised as follows:

- **Chapter 1: Introduction and motivation.** This chapter introduces the economic motivations driving the current paradigm shift of the pharmaceutical industry towards continuous manufacturing and highlights the broader relevance of the research presented in this thesis. It also presents the current gaps in the advancement of continuous crystallisation, which this thesis addresses.

- **Chapter 2: Literature review.** This chapter introduces the fundamental concepts of crystallisation and examines the inherent problems with mixing and scale-up of batch crystallisation processes. A detailed review of the current state of continuous crystallisation technology is provided, with a focus on the operating principles, configuration types, and challenges of the main platforms available. The application of PAT for continuous process characterisation in these platforms is also discussed.
- **Chapter 3: Experimental materials and methods.** In this chapter, a detailed description of the SPC design, batch SPC mesoscale crystalliser, SPC mesoscale crystalliser platform, and the model system (chemical and solvent) chosen for investigation is provided. A multivariate calibration model development for real-time solute concentration measurement using Raman spectroscopy is described, and specially modified components for PAT integration with the platform are also highlighted. Experimental and offline characterisation methods employed in all investigations are described in detail.
- **Chapter 4: Liquid and solid phase axial dispersion performance of the SPC mesoscale crystalliser.** In this chapter, the liquid and solid phase axial dispersion performance of the SPC mesoscale crystalliser is reported. Homogeneous and heterogeneous tracer experiments are performed using a newly developed non-invasive dual backlit imaging technique and compared to identify the optimum oscillatory condition for achieving solid-liquid plug flow in the SPC mesoscale crystalliser for continuous crystallisation.
- **Chapter 5: Heat transfer characteristics of the SPC mesoscale crystalliser.** In this chapter, the heat transfer behaviour of the SPC design at low flow rates is reported. An estimability analysis is applied to better understand the relationship between steady flow, oscillatory flow, and heat transfer performance of the SPC meso-tube. An empirical Nusselt number correlation is developed and combined with a steady-state heat transfer model to predict spatial temperature profiles for continuous cooling crystallisation in the SPC mesoscale crystalliser.
- **Chapter 6: Seeded continuous cooling crystallisation in the SPC mesoscale crystalliser.** This chapter reports the development of a continuous cooling crystallisation process for the model system in the SPC mesoscale crystalliser. Prior measurement of the MSZW in a batch SPC mesoscale crystalliser is performed, and based on the results, the suitability of the SPC mesoscale crystalliser for unseeded continuous cooling crystallisation is assessed using different temperature profiles. A

systematic study of a seeded cooling crystallisation is subsequently performed in the SPC mesoscale crystalliser to determine the effect of key process variables including mean residence time, oscillatory conditions, spatial temperature profile, and seed size and loading on product mean crystal size, size distribution, and yield. In-line Raman spectroscopy and offline characterisation techniques are employed to determine steady-state operation and analyse product particle attributes.

- **Chapter 7: Continuous cooling crystallisation in a mixed suspension mixed product (MSMPR) crystalliser.** This chapter reports the work performed in the R&D laboratory of PT&D, AstraZeneca UK during a 3-month industrial secondment. The systematic study of the model system is extended to the MSMPR system. An interchangeable single- and two-stage configuration of the MSMPR crystalliser is operated using an intermittent vacuum transfer technique for slurry withdrawal. A characterisation of the liquid phase RTD, critical mean residence time for heat transfer, and just-suspended speed for solids suspension using a combination of experimental and modelling tools is reported. Unseeded and seeded continuous cooling crystallisation are carried out in the single- and two-stage MSMPR crystalliser using an FBRM for real-time steady-state monitoring. The effect of MSMPR operating temperature, mean residence time, and number of MSMPR stages on the product mean crystal size, size distribution, and yield is subsequently reported.
- **Chapter 8: Conclusions and future work.** This final chapter concludes the work, and recommendations for future work are discussed.

Chapter 2 Literature review

In the last decade, continuous manufacturing has gained significant momentum, and a growing number of pharmaceutical companies, academic institutions, and technology providers have become highly involved in the development of continuous processes for pharmaceutical manufacturing. The need for robust, efficient, and sustainable processes that can produce high quality drug substances at lower cost has spurred the research of various continuous platforms for crystallisation. To successfully develop robust and scalable continuous crystallisation processes, a proper understanding of the underlying scientific and engineering principles governing these processes is required. This chapter discusses the fundamental principles of crystallisation, highlights the major problems associated with batch crystallisation processes, and reviews the current state of knowledge on continuous crystallisation technologies. An examination of the two main continuous crystallisation platforms considered in this research is presented. Finally, this chapter will look at the PAT tools applied in this research for monitoring crystallisation in these continuous platforms, as well as the benefits and limitations of using each tool.

2.1 Solubility, supersaturation, and metastable zone width

Crystallisation is a phase change in which a purified crystalline product is obtained from an impure solution (Schwartz and Myerson, 2002). Before performing any crystallisation process, the solubility curve of a substance in a given solvent or solvent system must be determined. Solubility is thus defined as the maximum amount of solute that can be dissolved in a solvent at a given temperature at thermodynamic equilibrium. The solution formed at this maximum is said to be saturated. The solubility of a solute is a function of temperature and varies with solvent systems; as such, the temperature-dependency of solubility determines the crystallisation method employed. That said, APIs usually require cooling crystallisation and/or anti-solvent crystallisation due to their high thermal sensitivity (Gao et al., 2017). In the search for an appropriate solvent system for a solute, the equilibrium solubility is most accurately measured using isothermal methods (Schwartz and Myerson, 2001). For such methods, an excess of solute is added to a known mass of solvent and agitated at desired temperatures for $>$24 hours. A clear sample is taken and analysed using HPLC, UV absorption, ATR-FTIR or gravimetric technique (Jozwiakowski et al., 1996; Srinivasan, 2008; Lindenberg et al., 2009).

Long holding times ensure that a thermal equilibrium has been reached, since dissolution rates are slower near saturation (Saleemi, 2011).

Crystallisation, a rate process, is driven by supersaturation, which is expressed as a concentration difference called the absolute supersaturation, ΔC, in Equation (2.1) (Mullin and Sohnel, 1977; Smith, 2005):

$$\Delta C = C - C_{sat} \tag{2.1}$$

where C is the solution concentration, and C_{sat} is the equilibrium solubility at a given temperature. Supersaturation is also expressed as the supersaturation ratio, S, which is a ratio of concentrations:

$$S = C/C_{sat} \tag{2.2}$$

Supersaturation is most commonly generated in a solution by cooling, solvent evaporation, anti-solvent addition, or chemical reaction (Jones and Mullin, 1987; McCabe et al., 2005; Smith, 2005). The maximum amount of supersaturation generated before spontaneous homogeneous nucleation corresponds to the metastable limit or boundary (see Figure 2.1).

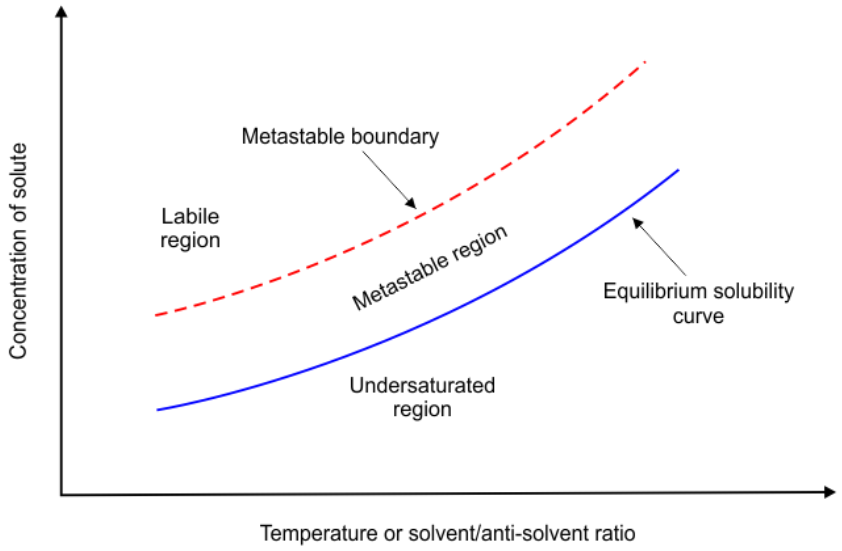

Figure 2.1 Solubility and the metastable zone (adapted from Tung and Paul, 2009).

The metastable zone, bounded by the equilibrium solubility curve and metastable boundary or limit, provides a region of supersaturation driving force where crystal growth takes place without spontaneous homogeneous nucleation. The region below the solubility curve is undersaturated, where crystals cannot exist in equilibrium with solution, while the region above the metastable boundary is the labile region where spontaneous nucleation dominates. The stability and induction time to nucleation of a supersaturated solution generally decreases with increasing supersaturation (Schwartz and Myerson, 2001). The MSZW is key data for designing and developing all crystallisation operations and varies for different solute-solvent systems. Therefore, a vital first step in the design, and ultimately control of a crystallisation process is the accurate determination of the MSZW. A system with a broad MSZW means that a large supersaturation is required for nucleation to occur, and that the system nucleates slowly. This is desired for a seeded crystallisation as it increases the design space across which seeds can be added. On the other hand, a very narrow MSZW (<2 °C) presents practical challenges for seeding (Brown et al., 2018). The MSZW is a kinetically limited quantity that varies with mixing scales and is highly dependent on process parameters such as the saturation temperature, rate of supersaturation generation (i.e. cooling rate, evaporation rate, or anti-solvent addition rate), agitation/mixing intensity, solution history, and fluid dynamics (Nývlt, 1968; Nývlt et al., 1985; Barrett and Glennon, 2002; Schwartz and Myerson, 2002; Sangwal, 2009a; Liang, 2002; Fujiwara et al., 2002; Liang et al., 2004). Other factors such as presence of seeds of desired substance, undissolved extraneous solid particles, impurities, and structurally related substances can affect the MSZW (Kwang-Joo Kim and Mersmann, 2001; Ni and Liao, 2010; Saleemi et al., 2013). A fast rate of supersaturation generation has been found to increase the MSZW in STCs (Fujiwara et al., 2002) and some OBCs (Ni and Liao, 2008; 2010). Higher agitation/oscillation intensity reduces the MSZW (Ni and Liao, 2010; Siddique et al., 2015), while a solution that is left undisturbed would take much longer to nucleate. MSZW is commonly determined using a polythermal method (Nyvlt, 1968; Nyvlt et al., 1985; Sangwal, 2009b). In this method, a solution of known concentration is heated above its saturation temperature, and then cooled at a constant rate (i.e. a linear cooling) until the occurrence of crystals is detected visually or instrumentally. Usually primary nuclei must grow to a certain size to be detectable, and the solution remains clear until the detectable size is reached at the metastable limit, indicating the width of the metastable zone. The metastable limit may be detected by visual observation (Fujiwara et al., 2002), turbidity measurements (Ni et al., 2004; Sun et al., 2018; Castro et al., 2018), or *in situ* measurements including attenuated total reflectance (ATR)-UV/Vis (Saleemi et al., 2013), Fourier transform infra-red (FTIR)

(Fujiwara et al., 2002), and focused beam reflectance measurement (FBRM) (Barrett et al., 2002; O'Grady et al., 2007; Siddique et al., 2015) to detect concentration and nucleation. Visual observation has been demonstrated by Fujiwara et al. (2002) to be an adequate method of detecting the metastable limit, although the authors have shown that FBRM is more sensitive in detecting the onset of nucleation. In this work, visual observation is used to detect the metastable limit in a batch SPC mesoscale crystalliser (see full description in section 3.4 of Chapter 3) for lack of a suitably-sized FBRM probe for the system. However, an FBRM probe is utilised for MSZW measurements in a 500 ml STC.

The scale-dependent nature of the MSZW means that it changes when a crystalliser's mixing/process conditions vary, particularly during scale-up from laboratory to industrial operation (Lawton et al., 2009; Ni and Liao, 2010). Non-uniform mixing is a norm in industrial crystallisers; good mixing is only achieved around the impeller zones, and poorer mixing is experienced elsewhere in the vessel. Such mixing variations in crystallisers create concentration and temperature gradients that have a detrimental effect on local supersaturation and MSZW. Furthermore, the surface area to volume ratio (SAV), which represents the amount of surface area per unit volume of fluid inside the crystalliser, is much lower for industrial crystallisers leading to slower heat transfer rates. Control of crystallisation is a common objective which involves, but is not limited to, operating crystallisation processes within the metastable zone to avoid nucleation, or to generate controlled nucleation/dissolution events (Aamir et al., 2010). Operation in the labile region is generally unwanted as it causes uncontrolled nucleation which produces too many fines, lots of agglomerates, and consumes supersaturation meant for crystal growth. Since crystallisation is often the first step when the pure solid product is separated from the liquid solution, it represents a crucial process to tailor the solid properties, such as CSD, morphology, polymorphic form, and purity (Nagy et al., 2013). Failure to do so could be detrimental to downstream processing and final drug product properties.

2.2 Nucleation

Nucleation is essentially the start of phase transformation, in which nuclei of the new phase are formed from a supersaturated solution phase (Gibbs, 1961). It is a highly non-linear process with respect to the chemical driving force between the phases (ter Horst et al., 2011). There are two categories of nucleation, namely primary and secondary nucleation. Primary

nucleation, which is prevalent in unseeded crystallisation, occurs when nuclei form in the absence of product crystals in the solution, and could be homogeneous or heterogeneous (Chianese et al., 1993; Smith, 2005). If a solution contains neither solid foreign particles nor crystals of its own type, then nuclei can be formed by homogeneous nucleation. Homogeneous nucleation is difficult to observe in practice due to the presence of dissolved impurities, and physical features such as crystalliser walls, baffles, and stirrers (Schwartz and Myerson, 2002). If foreign particles are present in the solution with no solute crystals, the nucleation is said to be facilitated and the nuclei form by heterogeneous nucleation (Mersmann, 2001). Secondary nucleation results from the presence of solute crystals in the supersaturated solution, usually in the form of added seed crystals. Nucleation could therefore result from fluid shear, contact (crystal-crystal, crystal-impeller, crystal-vessel), initial or needle breeding (dust on dry seeds or breakage of dendritic growth on parent crystals), and attrition. Figure 2.2 illustrates the general classification of nucleation. The classical nucleation theory (Volmer, 1939; Mersmann, 2001) is still the state-of-the-art theory to describe nucleation processes.

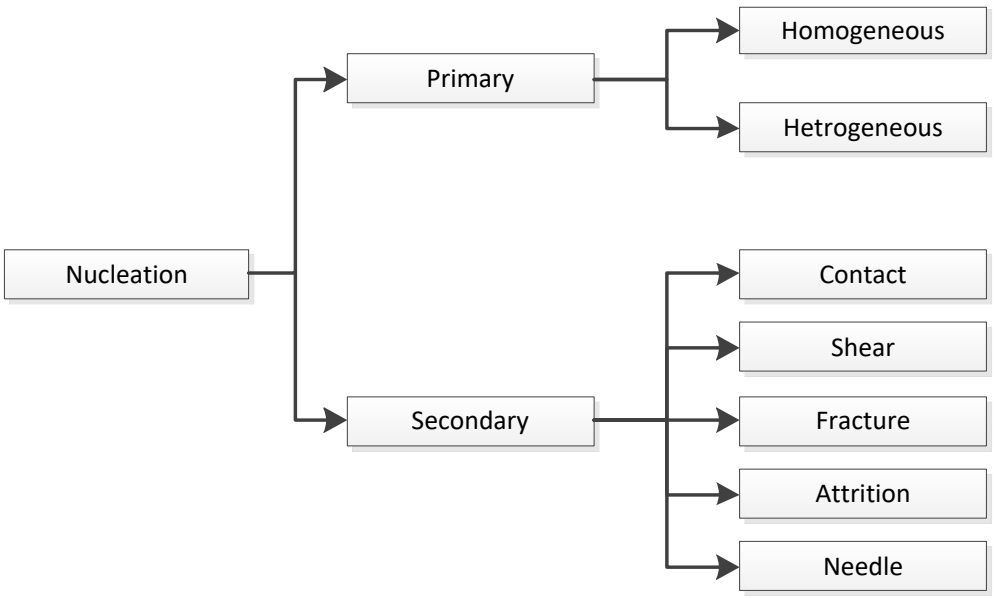

Figure 2.2 Classification of nucleation (adapted from Mersmann, 2001).

2.3 Crystal size distribution

The control of crystal size distribution (CSD) is of prime importance in crystallisation processes, particularly as the product CSD is the result of the direct relationship between nucleation and crystal growth/agglomeration rates, and slurry residence time distributions

(Mydlarz and Jones, 1994). In general terms, nucleation determines the number of nuclei formed, and growth/agglomeration controls the final size that nuclei grow to. However, the interactions between these mechanisms is complex and governed by supersaturation. For most drug substances, the CSD is a CQA, as the shape of the CSD obtained from a crystallisation process strongly affects the efficiency of downstream operations such as filtration, washing, and drying (Aamir et al., 2010), and the drug product performance in the patient (Brown et al., 2018). More critical effects of CSD shape are found in the purity, bulk density, flowability, stability, packing properties, tablet dissolution rate and subsequent bioavailability, which are integral for pharmaceutical products (Wibowo et al., 2001; Braatz, 2002; Nagy et al., 2008; Nagy, 2009; Aamir et al., 2010).

On one hand, typically large and uniform crystals (large mean size with narrow CSD) are desired to aid rapid filtration and drying, whereas the presence of a considerable number of fine particles can prolong processing times (Yang et al., 2015). In extreme cases, a poorly-controlled CSD will lead to a total batch rejection and may require extra processing steps such as recrystallisation and milling (Braatz, 2002). On the other hand, smaller crystal sizes increase the *in vitro* drug dissolution rate and bioavailability, as has been demonstrated by Mosharraf and Nystrom (1998), Simakin and Bindeman (2008), and Jinno et al. (2006). A downside of a smaller-sized distribution however, is that the resulting larger total crystal surface makes it easier for impurities to adhere to the surface (Mermann, 2001). Controlling the rate of supersaturation generation to control nucleation and growth rates will control the CSD in a crystallisation system (Jones et al., 1987) for the desired objective.

Multiple methods exist for meeting CSD requirements. Well-known control approaches such as model-based and direct design have been used to affect CSD indirectly by implementing either a temperature or antisolvent profile (Nagy et al., 2008; Majumder et al., 2013; Ridder et al., 2014; Yang et al., 2015). Since variability in final product CSD is mainly caused by uncertainties that plague nucleation, these control approaches attempt to identify operating protocols which provide an acceptable compromise between crystal growth and nucleation (Bakar et al., 2008), improving the crystallisation of products with desired CSD.

One method for specifically achieving small-sized distribution (narrow CSD with small mean size) is through sonocrystallisation, where an applied ultrasound of ~20 kHz or greater produces smaller crystals with a high number density and narrower CSD (Guo et al., 2005; Amara et al., 2004; Sayan et al., 2011). This result is attributed to enhanced nucleation rates due to cavitation, and enhanced micromixing, which accelerates diffusion and reduces agglomeration (Nii and Takayanagi, 2014). The impinging jet crystalliser utilises micromixing

to achieve a uniformly high supersaturated solution for producing small particles with narrow CSD (Woo et al., 2009; Liu et al., 2015). Other methods that could be employed to reduce mean crystal size are wet milling (Yang et al., 2015; 2016) using a high shear rotor-stator device, or inclusion of structurally-related additives in the model compound to hamper growth on certain crystal faces (Saleemi et al., 2013; Powell et al., 2016). In cases where it is desirable to obtain a large mean crystal size, the operating mean residence time can be extended through a periodic flow operation (Powell et al., 2015; Su et al., 2016) to allow for more crystal growth, or solids recycling can be employed (Li et al., 2016), where a fraction of product crystals is returned to the crystalliser for further growth. It is important to note that even though crystal size can be optimised by process control methods such as those mentioned above, maximum attainable sizes are still determined by the crystal molecular structure. In cases where crystal size is limited by molecular structure, spherical agglomeration (where crystals are bound together into agglomerates by a binding liquid) can be employed to successfully optimize product properties (Yang et al., 2015).

An effective approach utilised in this work for controlling CSD is continuous seeding. Seeding helps to avoid the variability of nucleation steps. By seeding a batch or continuous process, supersaturation generated by cooling can be consumed by the growth of well-tailored seeds added, and hence, it can be kept relatively low throughout the process; consequently, secondary nucleation can be avoided. Production of seeds with a consistent mean size, shape, and CSD can be challenging, hence the need to look at wet milling as a method of seed production in this work. Ultimately, with this approach, the most important variables to be manipulated for optimising the crystallisation process and obtaining a well-controlled CSD are the supersaturation trajectory as well as the seed characteristics (Aamir et al., 2010; Eder et al., 2011).

2.4 Polymorphism

Polymorphism is the property of a substance to have more than one crystalline form. Over 80% of marketed pharmaceutical drugs exist in more than one polymorphic form (Snider et al., 2003; Bakar et al., 2011), and this frustrates drug processing because although they have the same chemical composition, their different structures give rise to different physicochemical properties notably solubility, kinetic rates, stability, morphology, tabletability, melting point, heat of fusion, hygroscopicity, density, refractive index, and dissolution rate (Grant, 1999;

Hörter, 2001; Snider et al., 2003; FDA, 2007). The most critical implications of polymorphism are efficacy in the patient and delivery of the intended pharmacological effect, and the altering of the bioavailability of drug products in the human body by primarily affecting dissolution rate (FDA, 2007). It is generally desirable and usual to choose the most stable polymorphic form of a drug substance that delivers the intended pharmacological effect, either by crystallisation from different solvents, slow evaporation, melting, slow/rapid cooling, or seeding (Vippagunta et al., 2000; Hörter, 2001; Snider et al., 2003, Kawabata et al., 2011).

Polymorphs of a compound can be either enantiotropically or monotropically related to each other. In an enantiotropic system, a polymorph is stable below a certain temperature, while the other is metastable (Saleemi, 2011). Any transformations are reversible, with both kinetic and thermodynamic factors determining the interconversion rates of the polymorphs. In the monotropic system investigated in this work, there is no crossover of solubility curves; only one form is stable while the other forms are metastable. Thus, no interconversion of polymorphs is expected.

Polymorph transformations can occur by two mechanisms namely solvent-mediated and solid-state. Solvent-mediated transformation usually involves the dissolution of the unstable phase, followed by nucleation, and growth of the stable form (Kralj et al., 1997). Factors such as temperature, stirring speed, solvent type, pH, seeding have been found to affect the polymorph obtained, with the nucleation or growth rate of the new crystal form usually being the rate-determining step (Lai et al., 2015). Supersaturation also determines the polymorphic form obtained, with high supersaturation ($S > 3$) and rapid nucleation usually yielding metastable polymorphs (Llinàs and Goodman, 2008; Briggs et al., 2015).

Solid-state transformation can happen during formulation and storage processes, and can be influenced by factors such as drying, milling, granulation, tabletting, as well as temperature and humidity (Gao et al., 2017). For this reason, it is necessary to identify drug polymorphic forms offline using traditional characterisation methods such as XRPD, Raman, FTIR (Hu et al., 2005; Hausman et al., 2005) and thermal analysis (DSC, TGA, DTA) (Srinivasan, 2008), or *in situ* using FTIR, Raman spectroscopy (Kobayashi et al., 2006; Simone et al., 2014), FBRM/PVM (where distinct habits exist) (O'Sullivan et al., 2003; Barthe et al., 2008) so that control of polymorphism can be achieved by formulation chemistry, recrystallising from different solvents, manipulating crystalliser temperature and residence time (Lai et al., 2015), seeding (Ni et al., 2004), and even subjecting to thermal and mechanical stresses (Krstulovic and Lee, 1997; Snider et al., 2003; Saleemi, 2011; Kawabata et al., 2011). Table 2.1 lists drug substance CQAs and downstream processes they affect. Polymorphism, crystal size, and crystal

shape affect downstream filtration and drying times, as well as the final drug dissolution profile. The crystalline or amorphous form of the drug affects its bioavailability, while a pure drug substance is critical to patient safety and efficacy.

Table 2.1 Summary of drug substance properties and processes affected

Drug substance CQA	Factors affecting property	Processes affected	References
Polymorphism	Solvent, hydrogen bonding, surfactants, temperature, supersaturation, cooling rate, hydrodynamics, seeding, mechanical stress, drying	Agglomeration, dissolution rate, compaction, filtration, washing, drying, solubility, wettability, safety	Gordon and Amin, 1984; Shankland et al., 1996; Finnie et al., 1999; Vippagunta et al., 2000; Garekani et al., 2001; Cano et al., 2001; Rasenack and Muller, 2002; Li, 2002; Snider et al., 2003; Ni et al., 2004; FDA, 2007; Simone et al., 2014
Crystal size and shape	Solvent, nucleation and growth rate interaction, attrition seed characteristics, hydrodynamics of solution, batch/residence time, impurities	Filtration, washing, deliquoring, drying, handling, storage, compaction, dissolution rate, bioavailability, tablet stability	Chow et al., 1985; Jones et. al, 1987; Chianese et al., 1993; Wibowo et al., 2001; Braatz, 2002; Nagy et al., 2008
Crystalline form, amorphous form	Formulations	Dissolution, solubility, bioavailability	Vippagunta et al., 2000; Blagden et al., 2006; Kabawata et al., 2011
Purity	Solvent inclusion, impurities, additives	Dissolution, toxicity	Braatz, 2002; Fujiwara et al., 2004

2.5 Batch crystallisation processes

The interactions between momentum transport, energy transport, and material transport in both solution and solid phases are affected by mixing and can be critical for success of many batch and continuous crystallisation processes, especially with complex organic compounds (Tung and Paul, 2009). Cooling crystallisation involves the generation of supersaturation in a crystalliser by the direct or indirect heat exchange between a hot solution containing the solute to be crystallised, and a colder fluid usually a liquid. This method of crystallisation is preferably applied to solute-solvent systems exhibiting steep solubility curves, as is the case for over 80%

of pharmaceutical small molecules. The following section discusses mixing in stirred tanks, its effect on basic crystallisation phenomena, and the inherent problems encountered in batch scale-up of cooling crystallisation, which is the method of crystallisation focused on in this thesis.

2.5.1 The problem with mixing and scale-up in stirred tank crystallisers

It is well-documented that crystallisation kinetic processes are greatly influenced by hydrodynamic conditions within the bulk environment (see Figure 2.3). These hydrodynamic conditions are created within an STC usually by the provision of mechanical energy through an impeller with the aim to suspend and distribute crystals and ensure as nearly a homogeneous macroenvironment as possible via turbulent mixing (Mersmann, 2001). The turbulent mixing process occurs at three distinctive scales, proceeding from macro- to meso- to micromixing, with micromixing being the fastest of the three.

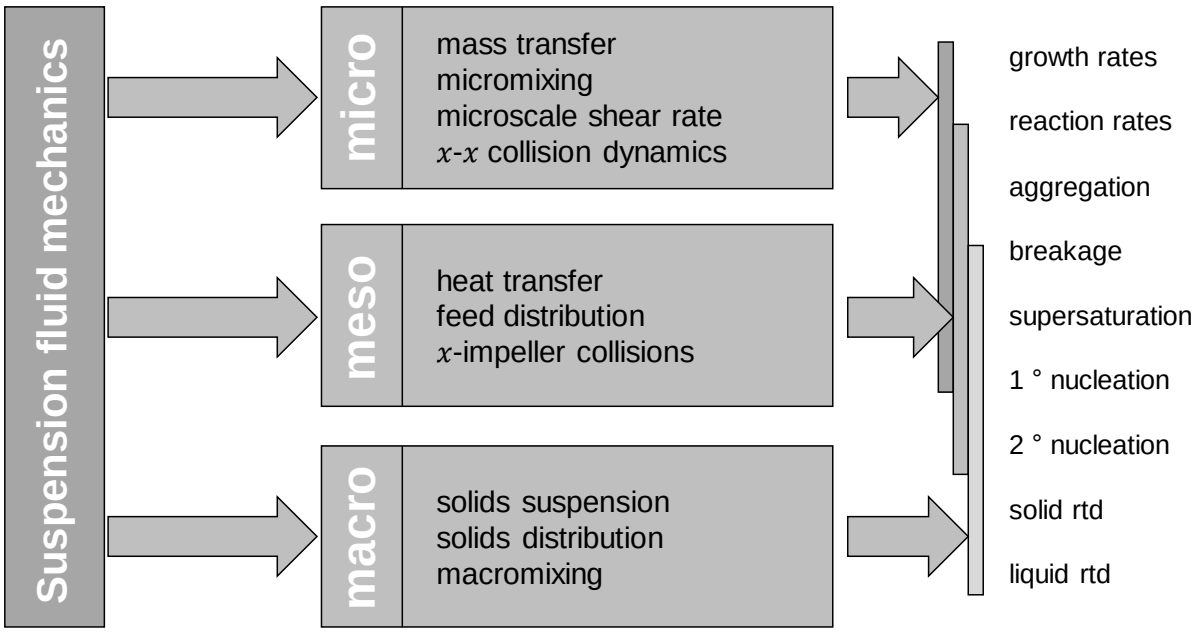

Figure 2.3 Suspension fluid mechanics effects on kinetic processes in a crystalliser, categorised by scale (x: crystal) (adapted from Rielly and Marquis, 2001).

Macromixing is an overall blending on the scale of the crystalliser dimensions that occurs by convection, where large-scale turbulent eddies determine the environment for meso- and micromixing. The fluid mechanics of the mean flow affect the distribution in space of the

fluid and solid phases, imposing a degree of backmixing which determines the solid and liquid RTDs.

Mesoscale fluid mechanics, of the order of the impeller blade width, affect the local liquid concentration distributions of feed reagents, the interactions of the crystals with the impeller and heat transfer rates from crystalliser internals (Rielly and Marquis, 2001). The mechanism of mixing at the mesoscale is described in detail by Baldyga et al. (1994); however, mesomixing can be regarded as an inertial-convective disintegration of large eddies that constitute an environment for micromixing. At this scale, active eddies create large passive eddies which produce large scale segregation and transfer the local mixture properties to the micromixing environment. The micro-environment is therefore governed by mesomixing.

At a molecular scale, of the order of the individual crystals, micromixing is realised by an unsteady molecular diffusion with deforming laminar structures which are embedded within energy dissipating vortices, and it is assumed to be controlled by fluid engulfment (Baldyga and Bourne, 1986). The microscale fluid mechanics affect mass transfer rates, the rate of turbulent collisions between particles and micromixing of chemical reagents. Crystals grow when the microenvironment is supersaturated, stop when it is just saturated, and dissolve when it is undersaturated.

In a cooling crystalliser, the spatial distribution of supersaturation is a coupled effect of the distribution of solute, suspended solids, and the temperature profile in the crystalliser volume; all of which are determined by the specific power input or power density (ε), which is the power input per unit volume or mass of the crystalliser. In practice, while it is relatively straightforward to achieve a homogeneous liquid phase, it is difficult to suspend the solid phase homogeneously at economic power inputs (i.e. impractical power consumption), particularly at larger scale (typically $>$100 litres) (Zwietering, 1958; Nienow, 1985; Plumb, 2005). This is important because processes such as nucleation, growth, and agglomeration which are more directly related to the local supersaturation, are indirectly determined by the suspension fluid mechanics. Local supersaturation is determined by local micromixing, reaction and mass transfer rates.

In an environment where uneven distribution occurs, regions of local supersaturation higher than the vessel average lead to fluctuations in MSZW, variations in nucleation rates, and non-uniform growth of individual crystals throughout the crystalliser; with nucleation and growth occurring more rapidly in regions of high supersaturation. In addition to nucleation and growth, the mechanisms of attrition and agglomeration are sensitive to particle collision rate, which is a function of local particle concentration (Smoluchowski, 1960; Shamlou and

Koutsakos, 1989). Therefore, where particles are not suspended uniformly by sufficient turbulent mixing, much of attrition and agglomeration occurs in relatively small zones of higher particle concentration.

It is clear that individual crystals respond only to their micro-environment, and that mixing determines how the micro- and macro-environments interact as well as their spatial and temporal homogeneity. Thus, mixing determines the ease or difficulty of scaling a crystallisation process. At bench scale (typically <1 litre), where length scales are smaller and circulation/blend times are shorter, homogeneity is easy to achieve. Hence, laboratory scale crystallisation processes can be said to be largely kinetically controlled. At larger scales of operation where mixing is heavily dependent on convection it is almost never possible to achieve uniformity of a crystalliser's key variables (Jones, 2002). For instance, in scaling up a batch process, attempting to maintain a constant blend time in a geometrically-similar system would require impractical increase in power consumption (Plumb, 2005). On the other hand, scaling up using a constant power density will give a practical power consumption; however, the resulting long blend time will prolong the time required to approach homogeneity, causing significant fluctuations in local supersaturation.

Much of the difficulty with scaling up crystalliser mixing is tied to the complex interaction between mixing and the critical process variables that govern crystallisation itself. A minor change in stirred tank diameter (say 5:1) can result in very large volumetric differences (125:1) which increase the likelihood of imperfect macromixing. In addition, SAV which is critical for heat transfer in solution cooling crystallisation decreases dramatically with scale. Therefore, the relative loss of heat transfer area together with non-uniform mixing on scale-up means batch cooling times are much longer at large scale, making cooling profiles problematic to implement in any industrial STC (Lawton et al., 2009; Ni and Liao, 2010).

The conventional approach to the scale-up of processes is based on the principle of similarity, which aims to maintain geometric similarity of equipment shape, flow characteristics, specific power input, and temperature profiles etc. (Green, 2002). Following this approach, it is expected that the physical processes occurring in industrial scale plant should ideally be duplicates of those in the laboratory scale units, but this is virtually impossible to achieve in practice, e.g. increased blend times from maintaining a specific power input. There is no agreement on the set of parameters to be kept constant in scale up, although many 'rules' have been proposed (Zwietering, 1958; Gates et al., 1976; Rieger et al., 1988). Parameters such as impeller tip speed, rotational speed of impeller, stirred tank Reynolds number, power density, impeller-to-vessel diameter ratio, volume-averaged shear rate, mass

transfer coefficient, mean droplet size, outputs of computational dynamic simulation, mixing time have all been used as scale-up parameters in stirred tanks, each presenting its own drawback (Smith et al., 1990; Thoenes, 1994; Nienow et al., 1997; Nauman, 2002).

The rigid criteria for APIs such as the purity, width of the CSD, mean crystal size, and yield further complicate scale-up efforts. Reported problems that usually arise from scale-up failures include increased impurity levels, altered morphology, small crystal size, broad CSD (including bimodal distributions), poor washing and a slow-drying product (Green, 2002; Tung and Paul, 2009). The intricacy of optimising mixing in an industrial STC is that it may satisfy one aspect of the operation while simultaneously having a detrimental effect on another. For example, a high specific power input will achieve good particle suspension, but at the same time promote particle shear damage and secondary nucleation, which worsen the CSD and morphology. Therefore, a trade-off between achieving sufficiently good suspension, while minimizing particle damage and secondary nucleation is inevitable. Achieving uniform particle suspension however is difficult as particles themselves affect velocity profiles and turbulence, leaving only the regions in close proximity to the impeller blades with better mixing (Rielly and Marquis, 2001; Xie et al., 2007). Hence, the usual experience in industrial STCs is non-homogeneity of crystal slurry (Green, 2002; Tung and Paul, 2009). Another problem commonly faced is unsatisfactory discharge/withdrawal of slurry from the stirred tank crystalliser, which leaves excess product crystals behind (otherwise known as classification) (Kougoulos et al., 2005), and results in failure to satisfy the mixed suspension mixed product removal condition described by Randolph and Larson (1988).

Attempts have been made to predict the effects of imperfect mixing on crystalliser performance and engineer alternative vessel configurations to minimise the problem (Mahajan and Kirwan, 1996; Wei and Garside, 1997). It is worth noting that the results of these numerous investigations over the years highlight specifically the geometry of STCs as the intrinsic factor that makes the scale-up of crystallisation processes so difficult, owing to the fact that different shapes and sizes of impellers and baffles can produce very different hydrodynamics (Ayranci et al., 2012).

The complexities associated with the full scale-up of batch crystallisation from laboratory units to industrial plants can be largely avoided through process intensification by adopting a ‘scale-out’ approach. The concept of scaling out or numbering up generally involves using small-scale crystallisers in parallel so that the basic mixing scale is not altered (Plumb, 2005; Poechlauer et al., 2012). Through an intermediate scale-up to pilot scale, the hydrodynamic environment critical to heat and mass transfer processes could be preserved

(Lawton et al., 2009). The number of pilot scale crystallisers can then be multiplied to meet production targets at economic power consumption. Alternatively, scale-up can be replaced by running at longer times or increasing throughput in fixed-size units (Allison et al., 2015). A major benefit of this approach is faster development times, since significant scale-up design and optimisation work involving numerous parameters can be negated during process development (McGlone et al., 2015). This approach may be implemented via continuous crystallisation in tubular devices with practical tube lengths, or in trains of multiple stirred tanks.

2.6 Continuous crystallisation processes

Continuous processes are characterised by variables which are spatially distributed within the entire system and can be unchanging with time i.e. by operating at steady-state conditions. For pharmaceutical crystallisation, two main conventional approaches exist for achieving continuous steady-state processes namely:

a) Operation of a series of well-mixed continuous stirred tanks
b) Tubular devices operating at turbulent flow conditions.

The mixed suspension mixed product removal (MSMPR) crystalliser in single- or multi-stage configurations (Randolph and Larson, 1971; Ferguson et al., 2013; Li et al., 2016; Yang et al., 2017) represents the first approach. The conventional plug flow crystalliser (PFC) (Ferguson et al., 2012; Vetter et al., 2014; Su et al., 2015), and continuous oscillatory baffled crystalliser (COBC) (Caldeira et al., 2009; Siddique et al., 2015; Brown et al., 2015; McGlone et al., 2015) are two most popular examples of the second approach. The PFC is essentially the conventional plug flow reactor (PFR) adapted for crystallisation purposes. Other types of continuous crystallisers which have found more bespoke applications are summarised in Table 2.2. Continuous microfluidic crystallisers, are becoming more popular in continuous crystallisation as fast screening platforms due to their low consumption of material and tight control of supersaturation. They are, however, still largely inapplicable to non-aqueous systems; and they are limited in application to crystallisation processes due to solid handling challenges (McGlone et al., 2015; Wang et al., 2017).

Table 2.2 Other types of continuous crystallisers

Continuous crystalliser	Mechanism	Studies/applications	References
Taylor-Couette crystalliser	Fluid motion induced by rotation of coaxial cylinders	Polymorph transition, agglomeration, inhibition of flocculation, CSD control	Kim et al., 2011; Lee et al., 2011; Mayra and Kim, 2015
Draft tube crystalliser	Draft tube provides different fluid flow fields in tank crystalliser	Evaluation of nucleation and growth kinetics	Soare et al., 2013; Lakerveld et al., 2014; Pan et al., 2016
Microfluidic crystalliser	10 – 500 μm I.D. poly(dimethylsiloxane) tubes	Screening platform for process parameter evaluation; spherical crystallisation from emulsions; nanolitre-scale crystallisation	Marre et al., 2010; Rossi et al., 2015
Fluidized bed crystalliser	Solid/fluid mixture created by pressurised fluid	Continuous preferential crystallisation	Yazdanpanah and Langrish, 2011; Al-Rashed et al., 2013; Binev et al., 2016
Laminar shear crystalliser	Shear force produced by two concentric cylinders	Characterisation of nanostructure of fats	Maleky and Marangoni, 2011; Maleky et al., 2011; Mazzanti et al., 2011
Forced circulation crystalliser	Mother liquor circulated and heated in chamber	Water desalination	Guo et al., 2016
Falling film crystalliser	Concentric tubes inside jacketed tank	Melt crystallisation and purification of products	Jiang et al., 2013; Sun et al., 2013

Laminar shear and Taylor-Couette crystallisers are more or less similar to MSMPR crystallisers because of the long mean residence times they provide. Taylor-Couette crystallisers have been successfully applied to CSD control which is made possible by their narrow RTDs provided by the fast-rotating coaxial cylinders. Fluidized bed crystallisers are commonly used in preferential crystallisation and falling film crystallisers have become popular in continuous crystallisation in recent years.

Table 2.3 compares the pros and cons of batch and continuous operation of crystallisation processes in the pharmaceutical industry. Perhaps the most important advantage of continuous operation is that more degrees of operational freedom are at play across crystalliser configurations than in a single batch STC (Mascia et al., 2013). This allows for product quality attributes that are unavailable in equivalent batch crystallisations to be produced (Gerstlauer and Motz, 2002; Ferguson et al., 2013).

Table 2.3 Some comparisons between batch and continuous operation in the pharmaceutical industry

Continuous operation	Batch operation	References
Plug flow operation ensures every particle has same RTD, nucleation and growth rates	Spatial variation of key variables due to time and global/local conditions are inherent	Green, 2002; Palma and Giudici, 2003; Tung and Paul, 2009; Alvarez et al., 2011; Zhang et al., 2012; Wong et al., 2012
Plug flow operation offers enhanced excellent mixing and heat transfer	Poorer mixing and heat transfer efficiencies at plant scale	Calabrese et al., 2011; Baxendale et al., 2015; Diab and Gerogiorgis, 2017
Operates at steady-state with possibility to improve yield through recycle	Operates at close to equilibrium with usually high yields	Chen et al., 2011; Benyahia et al., 2012; Yang et al., 2016; Diab and Gerogiorgis, 2017
Overall process yield loss can be minimised through integrated end-to-end manufacture	Overall process yield loss over consecutive stages due to cleaning, transfer or poor recovery.	Plumb, 2005; Chen et al., 2011; Wong et al., 2012
Improved control performance for delivery of consistent product quality	Batch-to-batch variation of induction times, nucleation processes, seed/feed material plagues overall product quality and requires further processing	Plumb, 2005; Lawton et al., 2009; Calabrese and Pissavini, 2011; Zhang et al., 2012; Aksu et al., 2012; Su et al., 2015
Shorter process development times requiring simplified scale-up/scale-out	Complex scale-up requires years of process development	Leuenberger, 2001; Plumb, 2005; Buchholz, 2010; Ferguson et al., 2013
Intensified, low cost, compact equipment and operation with high productivity	Large plant size with bigger equipment for bigger batches, or multiple campaigns	Plumb, 2005; Lawton et al., 2009; Schaber et al., 2011; Su et al., 2015; Wang et al., 2017
Steady-state continuous operation minimises downtime, reduces waste	Significant downtime from cleaning and changeover of batches	Gron et al., 2003; Plumb, 2005;
Prone to fouling, encrustation and clogging which could lead to downtimes	Batch operation allows frequent cleaning of equipment between batches	Alvarez et al., 2011; Chen et al., 2011; Powell et al., 2015; Majumder and Nagy, 2015
Start-up times to achieve steady-state could be long	Start-up and shut down effort is minimal	Takiyama and Matsuoka, 2001; Hou et al., 2014; Yang et al., 2015; Yang and Nagy, 2015
Quality-by-design (QbD) approach to product quality, but processes not yet robust	Well-established analytical methods for product quality control, with robust processes	Betz et al., 2003; Calabrese et al., 2011
More degrees of freedom in operation means wider range of particle attributes achievable	Limited to one type of configuration in STR	Ferguson et al., 2013; Gerstlauer and Motz, 2002
Offers flexibility to target small patient populations and faster responses to market demands with smaller inventory	Flexibility of equipment to respond to varying customised design requirements, however slow response to changing market conditions	Su et al., 2015; Mascia et al., 2013
Integrated end-to-end production campaigns eliminate intermediate storage	Disconnected processes, high material inventories and significant intermediate storage	Shah, 2004; Plumb, 2005; Mascia et al., 2013; Adamo et al., 2016

Continuous operation holds undeniable advantages over batch operation in areas of scale-up, product consistency, and equipment footprint; and the pharmaceutical industry has long

understood the advantages of continuous manufacturing for many unit operations, including crystallisation (Biscans, 2011). The industry has however been reluctant to implement continuous technology due to the complex nature of crystallisation. It is generally perceived that concerns about equipment/process robustness, lack of tried-and-tested control methodologies, and an industry bias for already established batch processes and inventory are barriers to the full implementation of this technology (Roberge et al., 2005; Mascia et al., 2013; Ferguson et al., 2013).

2.7 Mixed suspension mixed product removal (MSMPR) crystalliser

Randolph and Larson (1988) are credited with inventing the concept of the MSMPR crystalliser. An immediate advantage of this platform is that at continuous steady-state it is simple to analyse its operation and performance, and it can be used to study nucleation and CSD in continuous crystallisation processes (Sun et al., 2015; Kolbach-Mandel et al., 2015). The operation of the MSMPR crystalliser in theory is such that solution enters the vessel and is well-mixed throughout in terms of composition, having homogeneous temperature and concentration (see Figure 2.4). Supersaturation generated by cooling leads to the formation of nuclei and growth of crystals. Product slurry is continuously withdrawn with the assumption that it has the same solute concentration and CSD as in the vessel i.e. representative withdrawal. Ensuring all particles are suspended is a first step towards achieving uniform solids distribution throughout the crystalliser and avoiding size classification through isokinetic slurry withdrawal. In practice, while it is relatively straightforward to achieve homogeneity of the liquid phase, it is usually difficult to suspend the solid phase homogeneously at economic power inputs (Nienow, 1997). The quality of suspension generally increases with impeller speed, and sufficient mixing is necessary to ensure that crystals as much as possible experience similar hydrodynamics and RTD with the bulk solution i.e. no settling or accumulation of solids.

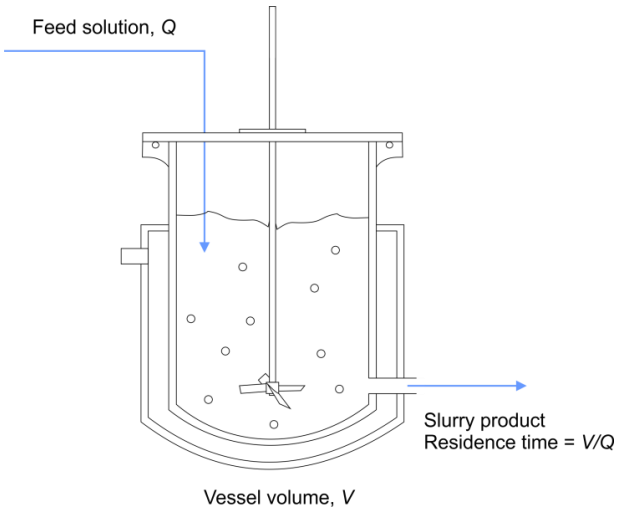

Figure 2.4 Theoretical concept of MSMPR crystalliser.

The just-suspended speed, N_{js}, is the impeller speed at which particles are completely suspended, and no particles remain stationary at the bottom of the vessel for more than 1 – 2 seconds (Zwietering, 1958). Complete suspension of solids is important for crystallisation as it ensures the maximum crystal surface area is presented to the bulk solution for mass transfer and crystal growth (Ayranci and Kresta, 2011; Wadnerkar et al., 2010). Operating at N_{js} provides near optimal mass transfer between solid and liquid phases; above this speed little mass transfer enhancement is gained despite much higher energy input (Kneule, 1956; Nienow, 1997).

The CSD output from an MSMPR can be predicted from basic kinetic rate laws using the population balance equation (PBE) which was formalised and adapted to crystallisation by Randolph and Larson (1988). Since then, PBE models have been used in the design of MSMPR crystallisers (Alvarez et al., 2011; Lai et al., 2015; Li et al., 2016), optimisation of operating conditions (Acevedo et al., 2017; Power et al., 2015) and the avoidance of unwanted problems such as fouling (Hou et al., 2014). The PBE follows similar conservation principles to material and energy balances and is used to account for the size and number of particles in a population of crystals in a crystalliser. The CSD in an MSMPR can be written as (Randolph and Larson, 1988; Marchal et al., 1988):

$$\frac{\partial n}{\partial t} + G(S)\frac{\partial n}{\partial L_c} + n\frac{d(\log V)}{dt} - B_c + D_c + \sum_k \frac{n_k Q_k}{V} = 0 \quad (2.3)$$

where n is the population density function of crystals, which is relative to time and particle size, L_c is the characteristic size of the crystal, and V is the volume of the solution in the crystalliser. B_c is the birth term (for breakage or agglomeration) and D_c is the death term. G is the linear growth rate of the crystal. $\sum_k \frac{n_k Q_k}{V}$ represents the flow of crystals in and out of the crystalliser, where k is the number of influent and effluent streams. This term incorporates and is dependent on the mean residence time of particles in the crystalliser, $\tau = V/Q_k$, where Q_k is the volumetric flow rate of the influent and effluent streams.

Given the assumptions of (1) well-mixed vessel contents i.e. crystal population and size distribution are the same anywhere inside the tank; (2) isothermal behaviour with no crystals in the feed stream i.e. $n_{inlet} = 0$; (3) CSD in the system is continuous, (4) agglomeration and breakage are ignored i.e. $B_c = D_c = 0$; and (5) size-independent growth rate of crystals, the flow of crystals in and out of the crystalliser can be changed as:

$$\sum_k \frac{n_k Q_k}{V} = \frac{n}{\tau} \quad (2.4)$$

When the system reaches a steady-state, n and V no longer change with time, the population density is no longer dynamic but constant, and:

$$\frac{\partial n}{\partial t} = n\frac{d(\log V)}{dt} = 0 \quad (2.5)$$

The population balance in Equation (2.3) reduces to:

$$G(S)\frac{dn}{dL_c} + \frac{n}{\tau} = 0 \quad (2.6)$$

In Equation (2.6), it is assumed that the crystals and solution have the same τ (see section 4.2.3 of Chapter 4), and the equation can be solved by integration to give the final form of the PBE:

$$n = n_0 \exp\left(-\frac{L_c}{G(S)\tau}\right) \quad (2.7)$$

where n_0 is the population of nuclei.

The MSMPR crystalliser is the most popular approach to the design of continuous crystallisation processes as it offers a straightforward technology transfer from batch operations, since the hydrodynamics for both systems can be similar (independent of net flow) (Peña et al., 2017). Also, the MSMPR crystalliser currently offers the most convenient route to continuous operation for the pharmaceutical industry, since stirred tank batch crystallisers abound in the pharma industry and are relatively easy to convert to continuous operation in the form of MSMPR stages (Griffin et al., 2010; Chen et al., 2011; Johnson et al., 2012; Su et al., 2015; Morris et al., 2015; Diab and Gerogiorgis, 2017). MSMPR crystallisers have tolerance for high suspension densities, are accepting of a wide range of crystallisation systems having fast and slow kinetics and can be expanded in capacity and degrees of freedom through cascade operation, thus making the MSMPR one of the more flexible continuous systems.

The back-mixed nature of the MSMPR crystalliser, whereby processed elements intermingle with fresh feed, leads to broad RTDs (see Figure 2.5) and produces broader CSDs than those usually obtained from tubular crystallisers such as the non-mixing PFC or COBC (see section 2.8) (Ferguson et al., 2012). For a CSTR or CSTC (which is one extreme case, the other extreme being a PFR or PFC), a pulse of tracer which enters from the input immediately mixes with the contents and some tracer leaves in the output. All fluid elements in the vessel have an equal probability of leaving. Fresh feed which enters the tank would dilute the tracer already in the tank and cause the exit concentration to fall. There is a broad tail to the output concentration distribution, indicating a wide spread of residence times.

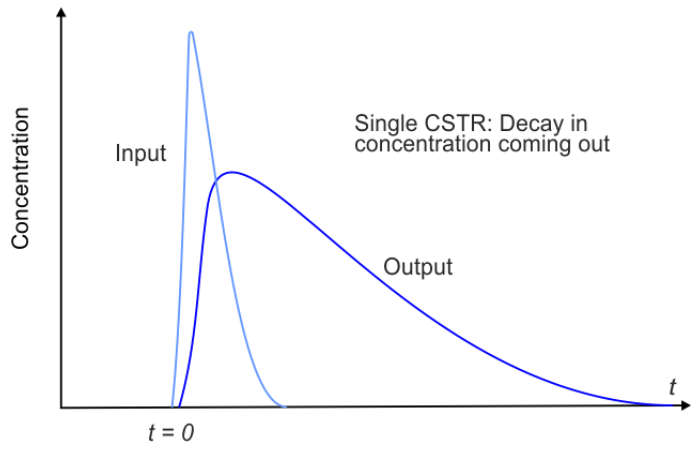

Figure 2.5 Typical CSTR residence time distribution (adapted from Rielly, 2013).

2.7.1 Application of process analytical technology to MSMPR crystallisation

In recent years, the advancement of technology and onset of PAT tools has meant that product critical quality attributes (CQAs) can now be monitored (simultaneously) in-process, and the impact of MSMPR crystalliser process variables on critical particle attributes can be now be better understood. Prior to that, offline analysis has been the common approach to product quality assessment, such as the use of laser diffraction for particle sizing and determination of CSD, liquid chromatography (HPLC) for purity, optical microscopy for visualising crystal morphology, X-ray powder diffraction (XRPD) and offline Raman microscopy for determining polymorphic form. PAT is a key enabler for continuous crystallisation, providing real-time information of CSD, crystal form, and the solution-phase concentration of the active ingredient (Siddique et al., 2015) via tools such as the FBRM, PVM, and Raman, from which conclusions can be extracted (De Beer et al., 2011; Simon et al., 2015). The use of PAT for real-time monitoring of crystallisation processes is progressing well, with more in-line analytical tools being routinely implemented in studies of MSMPR crystallisation. Powell et al. (2016) applied in-line Raman spectroscopy to monitor solution phase concentration in the MSMPR crystallisation of paracetamol from isopropyl alcohol. Raman was also used by Powell et al. (2015) to monitor steady-state operation in a periodic MSMPR crystalliser. Kougoulos et al. (2005a, 2005b) were the first to successfully demonstrate the application of FBRM to steady-state characterisation in a modified MSMPR crystalliser. The FBRM technique was used to estimate crystallisation kinetics. The investigators also made use of an in-line process video imaging (PVI) system for visualising crystal habit and behaviour within the crystalliser. Quon et al. (2012) reported using the FBRM to characterize chord length distributions (CLDs) of the solid product aliskiren hemifumarate in a two-stage MSMPR reactive crystallisation process. More recently, Acevedo et al. (2017) used the FBRM to monitor the continuous operation of an MSMPR integrated with an *in situ* wet mill device in the continuous crystallisation of paracetamol from aqueous isopropanol mixture. Yang et al. (2017) also used Raman microscopy and FBRM for real-time monitoring of polymorphs and CSD in an automated two-stage MSMPR crystallisation of Carbamezepine. A host of other investigators have implemented FBRM technology in identifying and monitoring steady-state continuous operation in MSMPR crystallisers (Alvarez et al., 2011; Ferguson et al., 2013; Morris et al., 2015; Yang and Nagy, 2015; Powell et al., 2015; Yang et al., 2016). While FBRM is well-suited for qualitative monitoring and enabling on-the-fly adjustment of MSMPR operating conditions, it is less commonly used for estimating crystallisation kinetics, since

CLD measurements are strongly influenced by crystal shapes (Agimelen et al., 2015), solids loadings, FBRM probe position in the crystalliser, agitation rate (Hou et al., 2014), as well as fouling (Ferguson et al., 2013). So far, offline laser diffraction measurements are still preferred for accurate determination of steady-state CSD and extraction of crystallisation kinetics (Hou et al., 2014; Power et al., 2015). In this work, real time process monitoring, and the determination of steady-state operation is achieved by monitoring chord length distribution with the aid of an *in situ* FBRM probe.

2.7.2 Studies in alternative configurations of MSMPR crystallisers

For a given operating volume of the MSMPR crystalliser, a key objective is the rapid attainment of a steady-state process with a high yield, which continuously outputs product material of desired CQAs namely CSD, shape, polymorph, and purity. A common challenge associated with the transition from batch to continuous crystallisation is that batch processes discharge at equilibrium, while continuous processes operate at a steady-state in which the discharge is still supersaturated (Chen et al., 2011). Different MSMPR crystalliser configurations have been employed with a chief aim of improving process yield, but also obtaining better CSD. A common way to improve process yield (at least equivalent to batch yield) is to include a mother liquor recycle stream and manipulate the recycle ratio (Alvarez et al., 2011). The mother liquor in the recycle stream can be concentrated to increase the solute concentration. Wong et al. (2012) carried out cooling and anti-solvent-cooling crystallisation of pharmaceutical drugs cyclosporine and deferasirox respectively in two continuous single-stage MSMPR systems with recycle. Their work demonstrated that a single-stage MSMPR recycle system could produce high yield and high purity of product. In such a system however, care must be taken to minimise impurity build-up via a purge in the recycle stream. Improvement of the yield is also usually possible through solids recycling (Li et al., 2015), and by simply extending residence times through slower flow rates. Major challenges with operation at slower flow rates are inefficient material transport, and a high chance of transfer line blockage. Also, longer residence times would lead to lower material throughput (Zhang et al., 2017).

Another configuration used is the multi-stage or cascade MSMPR crystalliser (see Figure 2.6) which is basically two or more MSMPR crystallisers connected in series, for which each MSMPR can be modelled with the population balance in Equation (2.3). A broad RTD,

characteristic of a single MSMPR crystalliser, is undesirable as it widens the product size distribution, causing inefficient downstream filtration, drying, and tableting steps (Kacker et al., 2016). With increasing number of MSMPR stages, the behaviour of the crystallisation process approaches plug flow, and it can operate closer to the batch equilibrium condition. Extending the number of stages is an effective way to increase the overall yield of the process, particularly for systems with slow kinetics, requiring longer residence times. Alvarez et al. (2011) obtained similar yield to a 9-hour batch process by employing a three stage MSMPR cascade, each stage having a 2 hour 56-minute residence time. While the cascade design is suitable for systems that require longer residence times, strong agitation and non-uniform temperature profile in the crystallisers may cause problems for particle size and polymorphism control (Yang et al., 2017). The multi-stage MSMPR crystalliser affords more flexibility in operation than a single-stage MSMPR crystalliser by enabling multiple combinations of operating conditions to achieve certain process and product quality. A cascade design provides a significant advantage of decoupled operation which permits independent control of crystallisation mechanisms in different MSMPR stages. Several investigators have demonstrated this capability in different studies. Peña and Nagy (2015) designed a novel two-stage MSMPR crystalliser for continuous spherical crystallisation in which the first stage was for nucleation and growth, while the second was used for agglomeration. Zhang et al. (2012) applied a cooling process in the first stage of a two-stage MSMPR crystalliser and a combination of cooling and anti-solvent in the second stage to improve the properties of the final crystals. In an interesting study, Vetter et al. (2014) identified regions of particle sizes attainable in a three-stage MSMPR cooling crystallisation of paracetamol. It was observed that the minimum attainable particle size stayed almost constant with varied total residence time. However, the maximum attainable particle size increased with total residence time, owing to the added flexibility in distributing total residence time among the three stages while fulfilling yield constraints. More importantly, the authors found that an MSMPR cascade consisting of many crystallisers has an attainable region similar to that for a PFC; and an MSMPR cascade with few crystallisers allows significantly larger particle sizes to be obtained compared to PFC and semi-batch crystallisers. There have been much earlier studies on multi-stage MSMPR crystallisers, although those studies focused only on the effect of process conditions on crystal size or purity of the product (Nývlt and Broul, 1979; Tavare et al., 1986; Shiau and Berglund, 1987). MSMPR cascades are growing in popularity and have been utilised by many other

investigators to accomplish key process output variables (Lai et al., 2015; Yang and Nagy, 2015; Peña and Nagy, 2015; Power et al., 2015; Galan et al., 2015; Li et al., 2015).

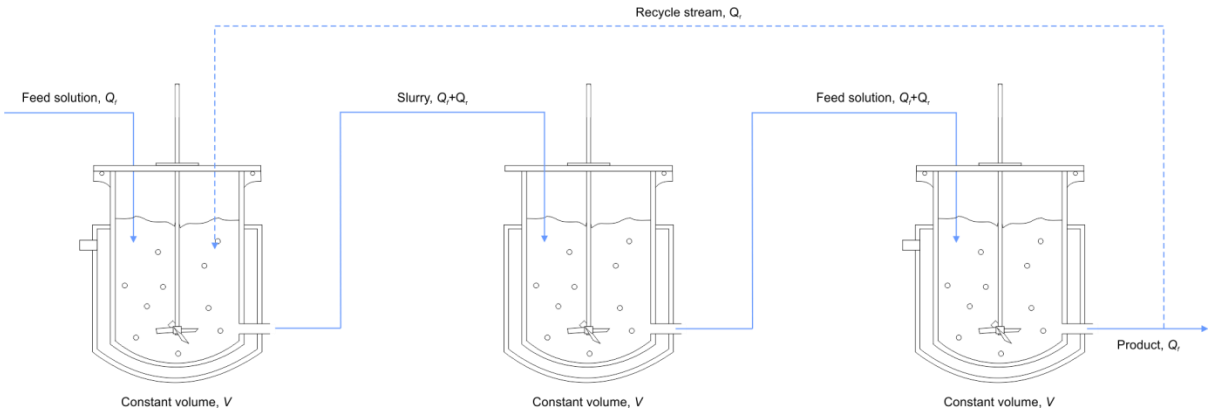

Figure 2.6 A typical multistage MSMPR crystalliser configuration.

The yield of the multi-stage MSMPR system can also be boosted by recycling the mother liquor (see Figure 2.6). Alvarez et al. (2011) found an increase in yield of cyclosporine by 22% with the addition of a recycle stream in a three-stage MSMPR system. However, as mentioned above, impurity build-up was a challenge for the recycle method. For the same cyclosporine study, the purity of the crystals was determined as 96% without recycle, and 94% with recycle. An important consideration for multi-stage MSMPR crystallisers is that the maximum number of stages practically feasible may be limited by laboratory space requirements and costs; and as such, advantages such as narrow RTDs may be difficult to realise in practice.

Studies of MSMPR design strategies and their effects on process and product quality have also been carried out by various researchers. Yang et al. (2015) investigated a novel integrated continuous wet milling-crystallisation (CWMC) process to achieve better control of CSD and yield. The investigators found that applying a wet milling device upstream of the MSMPR as a high shear continuous seed generator significantly improved the yield of the process and provided a narrow size distribution of particles. Another important process quality, the start-up duration, was significantly reduced by the integration of a wet mill compared to operation without. Narducci et al. (2011) also shortened start-up duration in adipic acid MSMPR crystallisation by implementing ultrasonic technology. The ultrasonic irradiation produced smaller crystal sizes at steady-state, increased product yield, reduced agglomeration and improved crystal habit. Hou et al. (2014) compared MSMPR start-ups from saturated solution, equilibrium batch suspension, and product suspension and found the steady-state

product chord length distributions (CLDs) to be independent of the start-up mode. Starting up from saturated solution and equilibrium batch suspension had similar durations to achieve steady-state, however starting up from saturated solution seeded with previously produced MSMPR material offered the quickest route to steady-state operation. Dry seeding is commonly employed to start up batch and continuous crystallisation processes to induce the formation of desired polymorph and trigger secondary nucleation where spontaneous nucleation cannot occur.

The CQAs of an API are dictated by the level of supersaturation within the crystalliser and are known to impact on the efficiency of downstream processes such as filtration, drying, milling, granulation (Peña and Nagy, 2015), and formulation. System design variables namely MSMPR operating temperature, starting feed concentration, feed temperature, mean residence time, and number of MSMPR stages have an impact on the product quality obtained. Power et al. (2015), in the cooling crystallisation of paracetamol from aqueous propanol in a single-stage MSMPR crystalliser, found that increasing the steady-state residence time resulted in a relative decrease in nucleation than growth, and subsequently increased the mean particle size, while decreasing crystal population (total counts). Surprisingly, Ferguson et al. (2013) obtained an inappreciable change in the crystal size and number despite a 300% increase in residence time; suggesting the existence of system-specific optimal residence times, within or beyond which insignificant change in crystal size is obtained. Morris et al. (2015) in the cooling crystallisation of benzoic acid from water-ethanol solution, observed the profound effect of the MSMPR operating temperature on crystal growth rate. At the highest investigated operating temperature of 30 °C, where much lower supersaturation existed, the crystal growth rates were faster than at colder crystalliser temperatures of 0 – 10 °C. In the same work, the nucleation rate was also found to have a high dependency on suspension density, and larger product sizes were obtained for decreasing suspension density (feed concentration and saturated feed temperature). MSMPR operating temperature has also been found to determine the dominant steady-state polymorphic form obtained by altering the solubility and energy barrier (Lai et al., 2015). In this work, the effect of MSMPR operating temperature, mean residence time, and number of MSMPR stages on the mean particle size and yield is investigated. Start-up from equilibrium batch suspension is utilised, with the MSMPR system operated in product recycle mode.

2.7.3 Current challenges with MSMPR operation

Well known operational challenges have hindered the complete adoption of MSMPR crystallisation within the pharmaceutical industry. These challenges discussed below include system-dependent fouling on *in situ* process monitoring equipment, encrustation on vessel walls, slurry transport difficulties, product classification issues, and most especially transfer line encrustation and blockage (Kougoulos et al., 2006; Chen et al., 2011; Powell et al., 2016). Some steps have been taken by investigators to alleviate fouling/encrustation in MSMPR crystallisation, these include periodically purging nitrogen through the transfer lines to prevent fouling (Hou et al., 2014), and introducing additives (Powell et al., 2015) to minimise encrustation. These efforts have successfully enabled extended steady-state MSMPR operation.

A major concern with MSMPR operation is that it is plagued by blockage of transfer lines, fouling and encrustation (of *in situ* PAT probes and vessel walls), and classified product withdrawal (Westhoff et al., 2004; Zarkadas and Sirkar, 2006). Transfer line blockage is possibly the biggest hindrance to prolonged steady-state operation of laboratory scale MSMPR crystallisers (Chen et al., 2011), and is commonly experienced with pump operation (Mullin, 2001; Narducci et al., 2011). In recent times, novel strategies have been employed to resolve some of these limitations and permit prolonged operation of MSMPR crystallisers for robust studies. One such strategy first introduced by Ferguson et al. (2013) is the rapid intermittent withdrawal method to prevent the clogging of transfer lines and non-representative product withdrawal. Intermittent withdrawal involves rapid pneumatic/vacuum slurry withdrawal of up to approximately 10% of the slurry volume every one tenth of a residence time. The rapid transfer achieves isokinetic withdrawal which is key for MSMPR operation, making this technique an effective transfer system essential to multi-stage operations, and allowing for longer residence times to be attained without compromising the continuous operation. Rapid intermittent withdrawal has since been adopted by several investigators of MSMPR crystallisations (Power et al., 2015; Morris et al., 2015; Yang et al., 2015; Cui et al., 2016; Acevedo et al., 2017). Powell et al. (2015) and Su et al. (2017) presented a novel concept known as the periodic flow MSMPR crystalliser, which is based upon an “on-off” peristaltic pump operation across the system. The technique involves a series of rapid addition and withdrawal cycles and a tuneable holding period between, which allows the manipulation of material RTD in the MSMPR crystalliser. High flow rates were applied during additions and withdrawals to prevent sedimentation in transfer lines and enable a more representative slurry

withdrawal. Interestingly, periodic flow operation has been shown to extend mean residence time without overly broadening the material RTD, and larger crystal mean sizes have been obtained for a glycine product compared to a continuous flow operation. The periodic flow operation, however, can be described as a hybrid of batch and continuous crystallisation, as the MSMPR crystalliser responds to periodic but controlled disturbances and achieves a "state of controlled operation" rather than the conventional "steady-state" operation described by Randolph and Larson (1971). Rapid intermittent withdrawal is considered a form of continuous operation since changes in steady-state conditions are negligible when slurry slug size withdrawn is less than 10% of the crystalliser volume. Thus, this work employs a rapid intermittent vacuum transfer method in a single and two-stage MSMPR crystallisation for isokinetic withdrawal from a well-mixed MSMPR and avoidance of crystal breakage during transfer. This transfer method can overcome the limitation of transfer line blockage encountered during pump operation, permitting longer mean residence times and continuous steady-state operation.

2.8 Continuous oscillatory baffled crystalliser (COBC)

Since the early 1990s, numerous studies have demonstrated that tubes that contain periodically-spaced orifice baffles, when subjected to a net flow with an oscillatory component of correct magnitude, can exhibit efficient fluid mixing and a narrow RTD (Van Dijck, 1935; Brunold et al.,1989; Dickens et al., 1989; Howes et al., 1991). Oscillatory flow mixing has existed for many years as a process intensification technology for achieving efficient and controlled mixing in various process operations including liquid-liquid reaction (Ni et al., 1993), polymerisation (Ni et al., 1998), and flocculation (Gao et al., 1998. Their ability to achieve near plug flow RTDs, scale-up more linearly than stirred tanks (Jian and Ni, 2005), and provide efficient fluid mixing and particle suspension characteristics has made continuous oscillatory baffled reactors (COBRs) (McGlone et al., 2015) an attractive state-of-the-art technology, and the second most common approach to continuous crystallisation after the MSMPR crystalliser, a specific purpose for which they are commonly known as continuous oscillatory baffled crystallisers (COBCs).

2.8.1 Operating principles of the COBC

In their basic form, conventional scale (typically >10 mm I.D.) COBCs are tubular devices containing periodically spaced "sharp-edged" constrictions (SEPC) or baffles with oscillatory flow superimposed on a net flow (Harvey et al., 2001; Ni et al., 2002; Harvey et al., 2003). A major strong point of the COBC is that flow patterns can be reproduced at larger scales making laboratory development work much easier to scale up than STCs (Reis et al., 2005). Secondly, the absence of an impeller means crystal-impeller collisions are non-existent, and crystal breakage is less pronounced than in an STC. The working of the COBC is such that the presence of baffle/constriction edges promotes eddy formation (see Figure 2.7), which increases radial mixing in the tube, leading to radial velocities of the same order of magnitude as axial velocities and promoting mass transfer (Ni and Mackley, 1991; Fitch et al., 2005; Reis et al., 2005; Ahmed et al., 2018). Good radial mixing favours heat removal (see section 5.2.2 in Chapter 5), which is crucial for tight control of supersaturation during cooling crystallisation (Palma and Giudici, 2003; Mackley and Stonestreet, 1995; Stephens and Mackley, 2002; Solano et al., 2012). Oscillatory flow follows the Bernoulli principle – of pressure drop in an accelerated stream. As fluid flows from left to right though an orifice of reduced area, A_0, the stream contracts (as shown in Figure 2.7), hence the velocity increases and pressure decreases (Wilkes, 2006). With the superimposition of an unsteady oscillatory flow component to the fluid system, turbulent conditions are generated at high enough oscillatory Reynolds number, Re_o, and micromixing, critical for crystalliser's key variables, is enhanced (Ni et al., 1998). Essentially, the periodic motion of the fully reversing flow accelerates and decelerates according to a sinusoidal velocity-time function. Particle image velocimetry (PIV) and computational fluid dynamics (CFD) have been used in understanding flow patterns within a COBC (Mecklenburgh and Hartland, 1975; Brunold et al., 1989; Dickens et al., 1989; Ni et al., 1995; Ni and Gough, 1997; Manninen et al., 2013; Zheng and Mackley, 2008; Solano et al., 2012). Studies have shown that the vortex mixing mechanism that develops during oscillatory flow is the key factor responsible for the significant enhancement of mixing achieved in COBC systems (Howes, 1988; Mackley and Ni., 1991, 1993; Fitch, 2003; Reis et al., 2005).

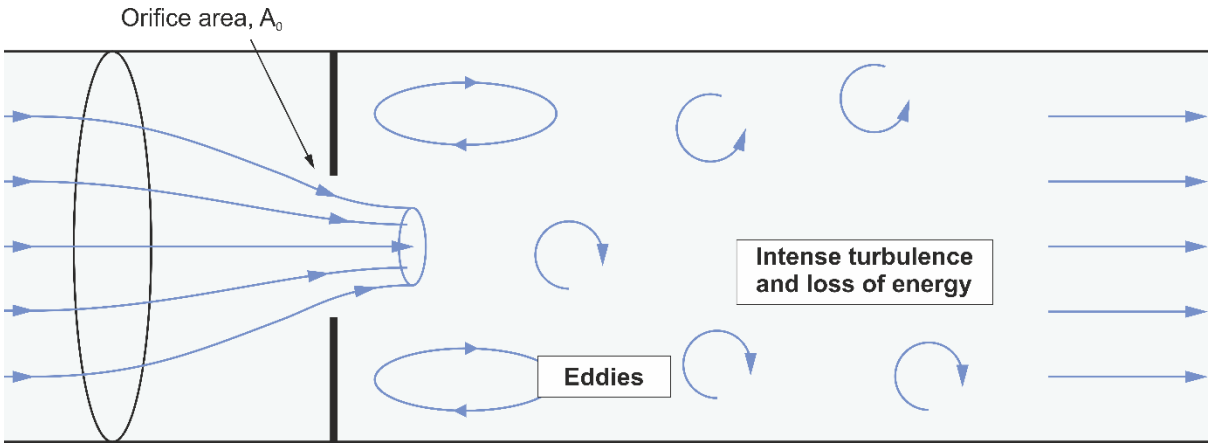

Figure 2.7 Flow through an orifice plate (adapted from Wilkes, 2006).

The mixing mechanism is such that on the start of an up stroke, the formation of vortices behind baffles draws fluid and substance from the walls (See A and B in Figure 2.8). On the start of a down stroke (and flow reversal), the moving fluid and substances from wall are subsequently swept to the centre (see C and D in Figure 2.8). In this way uniform and enhanced mixing within each baffled/constriction cavity as well as along the length of the tube is achieved (Fitch et al., 2005; Ni et al., 1998).

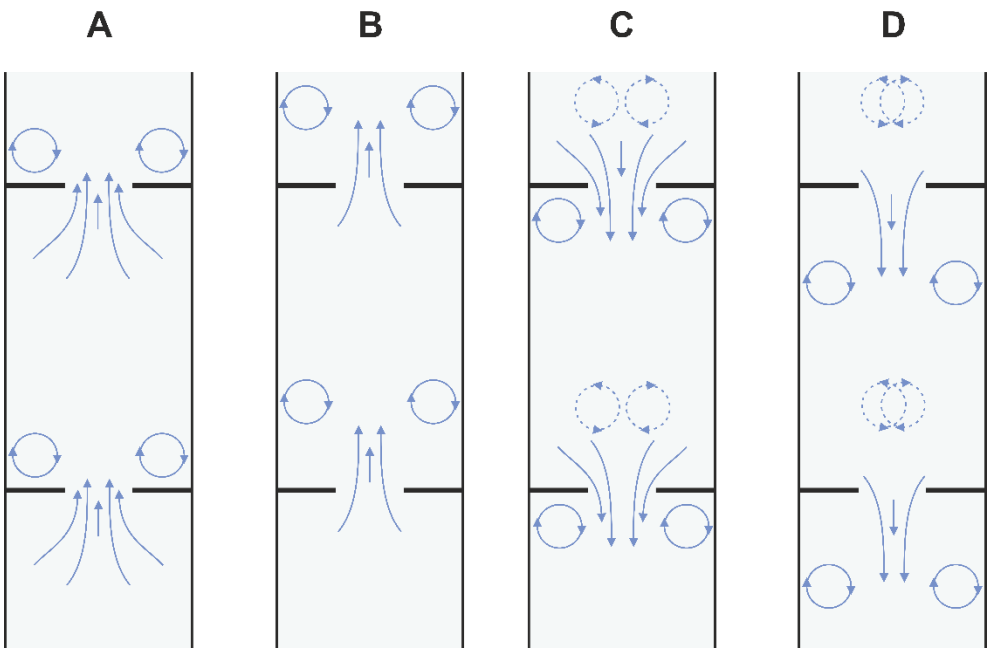

Figure 2.8 Mechanism of mixing in an oscillatory baffled column (adapted from Fitch et al., 2005).

Fluid mechanics in the COBC are governed by three dimensionless groups relating to oscillatory flow namely the oscillatory Reynolds number, Re_o, the net flow Reynolds number, Re_n, and the Strouhal number, St, which are defined as:

$$Re_o = \frac{2\pi f x_0 \rho D}{\mu} \tag{2.8}$$

$$Re_n = \frac{\rho u D}{\mu} \tag{2.9}$$

$$St = \frac{D}{4\pi x_0} \tag{2.10}$$

where ρ is the fluid density, D is the internal diameter of the tube, x_0 is the centre-to-peak oscillation amplitude, f is the oscillation frequency, u is the superficial velocity, and μ is the fluid viscosity. Re_o describes the intensity of mixing applied in the tube, while St is the ratio of tube diameter to stroke length, in other words it characterises the effective eddy propagation (Fitch et al., 2005). When $St = \infty$, the absence of eddy generation to effectively mix the baffle cavity results in flows that are dominated by viscosity and density effects, with high axial dispersion along the length of the tube (Mackley and Ni, 1991). An additional dimensionless group is the velocity ratio, φ, which describes the interdependence of the oscillatory and net flow components:

$$\varphi = \frac{Re_o}{Re_n} \tag{2.11}$$

Usually, oscillatory flow must be dominant for full flow reversal and efficient mixing to occur; for this to happen, φ must be at least greater than 1 (Stonestreet and Van der Veeken, 1999).

2.8.2 Achieving near plug flow for continuous crystallisation in the COBC

In a continuous crystallisation process, plug flow operation is essential for ensuring consistent fluid mechanical conditions and superior heat transfer rates due to increased radial mixing rates. Improved heat transfer under plug flow conditions enables a tight control over the local supersaturation to suppress unwanted nucleation and to achieve uniform growth conditions for crystals. This leads to a highly reliable environment for forming crystals with

reproducible properties i.e. size and shape distribution, and polymorphic form (Lawton et al., 2010). The axial dispersion coefficient is a measure of the degree of deviation in flows from true plug flow behaviour (Fitch, 2003) and is constant throughout a given system. Theoretically for plug flow, the axial dispersion coefficient should be zero. An ideal PFR or PFC exhibits true plug flow behaviour. For this reason, it is referred to as an unmixed flow device as it represents an extreme case (Rielly, 2013). True plug flow behaviour is difficult to achieve practically and an approximation to plug flow is the best that can be achieved by any real reactor or crystalliser. Plug flow is best described in Figure 2.9, by the fact that fluid flow through the reactor is orderly, which means every element moving in the z-direction with a velocity u does not overtake the other. There is perfect mixing in the r-direction, but no mixing in the z-direction along the reactor. Assuming a perfect pulse of tracer is added at $z = 0$, it continues to move through the reactor without spread or change in shape independent of position z and every fluid element has the same residence time, τ (Rielly, 2013). Hence, for an ideal PFC, all crystal and solution elements have the same τ, and experience the same history of supersaturation and hence the same crystal nucleation, growth, and agglomeration rates, which is perfect for crystallisation (Rielly, 2013). Thus τ is an important design parameter for a crystallisation process. By definition, τ is the average length of time spent in the crystalliser, and is calculated as:

$$\tau = \frac{V}{Q} = \frac{L}{u} \tag{2.12}$$

where V is the volume of the crystalliser, Q is the volumetric flow rate through the crystalliser, and L is the length of the crystalliser in consideration.

Usually, long residence times are required in continuous crystallisation processes to obtain substantial yield and growth of crystals. From Equation (2.12), achieving a long residence time in a tubular crystalliser could mean either a very long L or low u. The latter might lead to axial dispersion (at low Re_n) or difficulty in suspending solids. The downside of a PFC of a given length is that plug flow is achieved at very high net flows ($Re_n > 2200$), which results in too short residence times for crystallisation. Also, providing sufficient residence times at high net flows would require impractical crystalliser lengths and large capital costs. For this reason, the COBC is very advantageous since fluid mixing is decoupled from net flow, and can be controlled independently by adjusting oscillatory conditions (Harvey et al., 2001; Phan et al., 2011); hence a close approximation to plug flow behaviour is achievable

for crystallisation purposes at low net flows, with greatly reduced length to diameter ratios. For the COBC however, an RTD exists. And a narrow COBC RTD is crucial for obtaining desired CQAs such as narrow CSDs and bigger mean sizes.

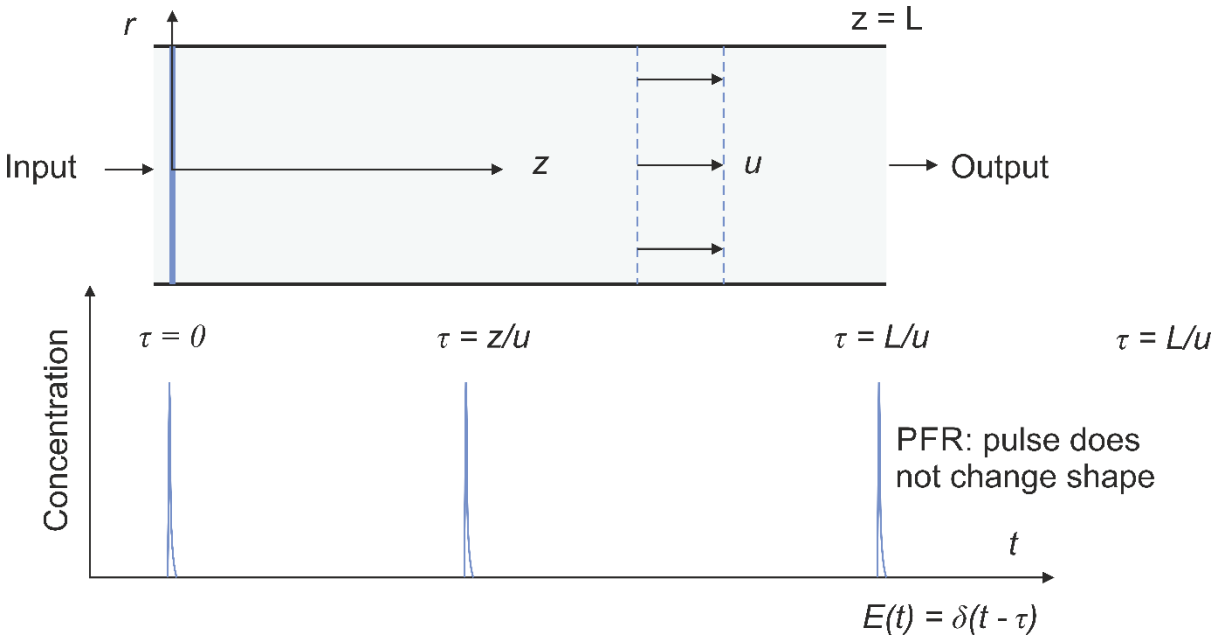

Figure 2.9 An ideal PFR RTD (adapted from Rielly, 2013).

Residence time distribution is a crucial tool for the analysis of real reactors, to detect and quantify non-ideal flow patterns. RTD experiments have been employed in quantifying the deviation of the COBC from plug flow behaviour using tracer input and response tests (pulse or step inputs) (Ni and Mackley, 1991; Stonestreet and Veeken, 1999; Ni et al., 2003; Reis et al., 2004; Phan and Harvey, 2010; Ejim et al., 2017). Models that have been used to describe non-ideal tubular flow include the axial dispersion model (Levenspiel, 1999), tanks-in-series model (Phan and Harvey, 2010), and the differential backmixing model (Reis et al., 2004; 2010; Fitch, 2003). The axial dispersion model describes the mixing behaviour within a test section by superimposing one-dimensional axial dispersion onto convective flow. This model is utilised in this work for its capability to capture the intermediate backmixing state expected for the constricted SPC mesoscale crystalliser when it is operated at different oscillatory flow conditions (Reis et al., 2010). It is therefore suitable for describing the degree of deviation of the SPC mesoscale crystalliser from true plug flow behaviour. The axial dispersion model has been shown to be useful for RTD studies of oscillatory flow mixing (Mackley and Ni, 1993; Palma and Guidici, 2003; Smith and Mackley, 2006; Zheng and Mackley, 2008; Reis et al., 2010; Ejim et al., 2017; Kacker et al., 2017). The tanks-in-series model (Levenspiel, 1999) is

another commonly used model which assumes the constricted tube acts as a series of n equal-sized well-mixed stirred tanks. The tanks-in-series model has also been used in RTD studies of oscillatory flow mixing (Phan and Harvey, 2010; Phan et al, 2011a; 2011b; Reis et al., 2010; Mohd-Rasdi et al., 2012).

Four methods of response data analysis have been most frequently used in reported studies: direct fitting of moments, Laplace transform domain, frequency domain analysis (Fourier analysis), and time domain analysis. Among these methods, the Laplace transform domain analysis has been found to be the least accurate (Himmelblau, 1970; Glennon et al., 1988) whilst time domain analysis has proved to be the most reliable for estimating model parameters (Verlaan et al., 1989; Obradovic et al., 1997). Fitting in the frequency domain has been found to give distorted results due to the large number of numerical operations used in deconvolution and in inverse Fourier transformation. However, frequency domain convolution is a more sophisticated option for dealing with an imperfect input response (Verlaan et al., 1989). Reis et al. (2010) has shown that direct fitting of moments has major drawbacks which limit the applicability to the modelling of flow systems. For instance, in the moments technique, there is a lack of knowledge of the quality of the fit of the model; and emphasis given to the data in the tail of concentration-time curves (C-curves) is usually less accurate (Froment and Bischoff, 1990). Therefore, in this work, the option of convoluting in the frequency domain and fitting in the time domain is selected for estimation of the hydrodynamic model parameters, since it gives nearly the same accuracy as time domain convolution (Verlaan et al., 1989; Obradovic et al., 1997).

2.8.3 Geometric designs and scale-up behaviour of COBCs

Apart from the governing dimensionless groups, the geometric parameters relating to the tube design namely open cross-sectional area (α) and baffle or constriction spacing (l) also influence the fluid mechanics of COBCs (see Figure 2.10). The open cross-sectional area and baffle spacing are given as:

$$\alpha = \left(\frac{d_0}{D}\right)^2 \tag{2.13}$$

$$l = hD \tag{2.14}$$

where d_0 is the orifice or constriction diameter, D is the tube internal diameter, and h is the ratio of the distance between baffles/constrictions to tube internal diameter.

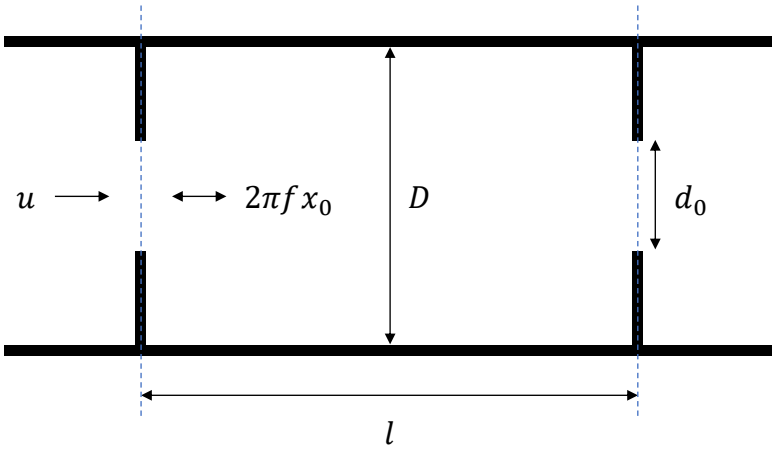

Figure 2.10 Geometric parameters and net flow superimposed with oscillatory motion

Geometric parameters are a basis for different COBC (continuous mode) and OBC (batch mode) designs that exist and are constant for each design. Continuous mode designs are also referred to as moving fluid (MF-OBC), whereby the movement of the oscillating piston produces a movement of the fluid. Moving baffle (MB-OBC) designs are equipped with a structure of baffles and supports periodically moving up and down the tube to produce oscillatory flow. They are most often operated vertically in batch mode (Manninen et al., 2013). Table 2.4 summarises the different COBC and OBC designs currently available. The list goes down from the pilot scale multi-orifice 'rattlesnake' to mesoscale COBCs and OBCs (also known as mesoscale crystallisers). These scales are essentially distinguished by tube internal diameter, D, however $\alpha, l/D$, and baffle/constriction type and shape control the hydrodynamics and particle suspension capability of each design, with α being the most important design parameter (Ejim et al., 2017). There are several fundamental differences between conventional and mesoscale COBCs. For instance, flow separation, which is the point of asymmetric vortex formation, occurs at $Re_o > 50$ for conventional scale COBCs, and $Re_o > 10$ for mesoscale COBCs (Reis et al., 2005), and diffusion plays a significant role in the formation of plug flow at mesoscale (McDonough et al., 2015). More importantly, mesoscale COBCs require more intense mixing and higher power density to generate plug flow than their conventional counterparts; this means that power dissipation decreases with increasing scale, a behaviour that is in direct contrast to STCs (Jian and Ni, 2005; McDonough et al., 2015). Also, the points at which flow symmetry breaks (i.e. flow becomes non-axisymetric and 3-dimensional) for the

conventional scale COBC and mesoscale COBC with smooth constrictions are $Re_o > 250$ (Howes et al., 1991) and $Re_o > 100$ (Reis et al., 2005), respectively.

Table 2.4 Summary of novel OBC/COBC designs

COBC/OBC scale	D (mm)	α (%)	l/D	Baffle/constriction	References
Pilot MB-OBC	76	21	0.68	Annular	McLachlan and Ni, 2016
Pilot (Rattlesnake)	69	25	0.26	Multi-orifice	Siddique et al., 2015
Conventional (DN-50)	50	22	1.5	Annular	Fitch, 2003; Ni and Liao, 2010; Zhao et al., 2014
Conventional (DN-40)	40	21	1.8	Annular	Pereira and Ni, 2001
Conventional (DN-25, MB-OBC)	25	21	1.5	Annular	Manninen et al., 2013
Conventional (DN25, MF-OBC)	25	21	1.5	Annular	Manninen et al., 2013
Conventional (DN-24)	24	25	1.5	SEPC	Harvey et al., 2001; Stonestreet and Veeken, 1999
Conventional (DN-15)	15	25	2	Annular	Brown, 2012; Zhao et al., 2014; Briggs et al., 2015; Brown et al., 2015
Mesoscale (DN-10)	10	12	3	SPC	Ejim et al., 2017
Mesoscale (Helical baffle)	5	30	1.5	Helical coil (sharp-edged, round-edged, sharp-edged with central insert)	Phan and Harvey, 2011; 2012; Solano et al., 2012
Mesoscale (Integral baffle)	5	25	1.5	Smooth baffles	Phan and Harvey, 2010
Mesoscale (SPC)	5	25	1.5	SPC	Mohd-Rasdi et al., 2012
Mesoscale (SPC)	5	16	2.6	SPC	Zheng et al., 2007; Zheng and Mackley, 2008
Mesoscale (SPC)	4.4	13	3	SPC	Reis et al., 2004; 2005; 2006
Mesoscale (Central axial baffle)	4	36	1.5	Axial hexagonal discs	Phan et al., 2012; Mohd-Rasdi et al., 2012

Smith (1999) has shown that the scale-up of COBCs is achieved simply by linear geometric scaling (of α and l/D) and by maintaining hydrodynamic similarity via Re_o, Re_n, and St. This contrasts with the complex and non-linear scale-up of STCs (see section 2.5.1); as such, linear geometric scaling of COBCs cannot be overemphasised as a significant advantage possessed over STCs. Smith and Mackley (2006) in their scale-up of a conventional OBC (24 mm, 54 mm, and 150 mm), found that axial dispersion is independent of tube diameter. Similar dispersion performance was obtained in a 150 mm I.D. multi-orifice baffled tube at lower

oscillation intensities (and power densities). Furthermore, studies of a helical baffled mesoscale COBC have shown that plug flow can be scaled from tubes of 5 mm I.D. to 10 mm and 25 mm I.D. by maintaining the values of Re_o and St, whilst scaling Re_n with diameter i.e. ensuring that $\frac{Re_{n,2}}{Re_{n,1}} \sim \frac{D_2}{D_1}$ (Phan and Harvey, 2013; McDonough et al., 2015). Other works by Reis et al. (2005) and Phan and Harvey (2010) have shown that the eddy mixing mechanism observed at larger scales is also obtained in mesoscale COBCs, and that scale-up of mesoscale COBCs to industrial scales is feasible. This is an important feature of COBC technology, as laboratory scale data can be used to optimise large scale COBCs, demonstrating the linear scale-up capability (Reis et al., 2006a; 2006b) and drastically reducing process development times.

The optimal φ for plug flow performance in conventional scale COBCs is commonly in the region of 2 – 4 (Stonestreet and Van der Veeken, 1999; Kacker et al., 2017). A range of 0.4 – 5 has been reported for the rattlesnake COBC (Siddique et al., 2015). For mesoscale COBCs the range varies with geometric design. The optimal φ has been identified in the range of 4 – 8 and 4 – 10 for the central and integral (smooth baffles) designs respectively (Phan and Harvey, 2010; Phan et al., 2011). The optimum baffle spacing for conventional designs is around $l/D = 1.5$ (Brunold et al., 1989) with a few exceptions which have higher or lower l. For mesoscale COBCs, this goes as high as $l/D = 3$ (Reis, 2006). Ejim et al. (2017) found that mesoscale COBC designs with smooth periodic constrictions (SPC) generally show superior particle suspension performance to their SEPC counterparts and may be better suited for continuous crystallisation processes. This is linked to lower critical amplitudes and the associated power densities required for full suspension of particles in SPC meso-tubes due to the absence of 'dead corners' usually found in SEPC counterparts. Also, SPC designs with small values of α were found to show better RTD performance due to the strong eddies formed at lower values of α. The authors identified an SPC meso-tube geometry having $l/D = 3$, $\alpha = 0.12$ as the best design for solids suspension and minimised axial dispersion. The SPC mesoscale crystalliser investigated in this work has a similar meso-tube geometry to this design with $l/D = 2.6$ and $\alpha = 0.16$.

The dissipation of power in oscillatory flow affects scale-up performance as well as heat transfer, mass transfer and mixing characteristics (McDonough et al., 2015). The power dissipation of SPC and SEPC meso-tubes is linked to differences in spatial arrangement of the constrictions, and this is responsible for the differences in their particle suspension performance. The power density quantifies the power consumption in COBCs and is an important scale-up parameter with economic relevance. It provides an understanding of baffle

geometries based on the fluid oscillation requirement per unit volume for each meso-tube. The power density, ε (W m^{-3}), for an OBC is the power consumption time-averaged over an oscillation cycle divided by the system volume. It can be estimated using a quasi-steady flow model (QSM) which was derived by Baird and Stonestreet (1995) based on a standard pressure drop correlation for flow through an orifice (Equation (2.15).

$$\varepsilon = \frac{P}{V} = \frac{2\rho n_c}{3\pi C_d^2 L}\left(\frac{1-\alpha^2}{\alpha^2}\right) x_0^3 \omega^3 \tag{2.15}$$

where the angular frequency of oscillation, $\omega = 2\pi f$ (rad s^{-1}), C_d is the orifice discharge coefficient usually taken as 0.6 – 0.7 (Mackley and Stonestreet, 1995; Ni and Gao, 1996; Ni et al., 1998), n_c is the number of constrictions, and ρ_s is the solution density. QSM assumes the instantaneous pressure drop in the oscillation cycle is the same as the pressure drop that would be produced in a steady flow with the same velocity (Baird and Stonestreet, 1995). The model is applicable to both OBC and COBCs, since contributions from net flow to power density are negligible (Jimeno et al., 2018). QSM has been shown to under-predict the power density in a conventional OBC for low amplitudes ($x_0 < 6$ mm) and is generally considered more suitable for high amplitudes/low frequencies ($x_0 = 5$ – 30 mm, $f = 0.5$ – 2 Hz) (McDonough et al., 2015). There is also no published work which rigorously assesses the applicability of QSM to mesoscale OBCs and COBCs.

Recently, Jimeno et al. (2018) validated the quasi-steady flow model against CFD simulation results and concluded that power density over-estimations are due to geometric parameters of its formulation not being applicable to modern oscillatory baffled devices. For instance, the values for C_d used in the existing model are typically for a standard orifice made of a sharp-edged thin plate (Mackley and Stonestreet, 1995). Jimeno et al. (2018) proposed a revised QSM that is more applicable to modern OBC/COBCs containing orifices of smooth curvature and optimised baffle/constriction spacing, as is the case in the SPC mesoscale crystalliser. The revised quasi-steady flow model (Equation (2.16)) gives the least error of prediction when $C_d = 0.8$ (for smooth-edged baffles/constrictions) and n_c is replaced by $n_c^{0.7}$.

$$\varepsilon = \frac{P}{V} = \frac{2\rho n_c^{0.7}}{3\pi C_d^2 (V/A_{CS})}\left(\frac{1-\alpha^2}{\alpha^2}\right) x_0^3 \omega^3 \tag{2.16}$$

where A_{CS} is the cross-sectional area of the tube (m^2). L is used in the original QSM equation, as it holds true for tubes containing sharp-edged disk-like baffles. However, the use of the ratio V/A_{CS} is more appropriate for smooth-edged baffles/constrictions, as there is a large discrepancy between V/A_{CS} and L (Jimeno et al., 2018).

2.8.4 Mesoscale continuous oscillatory flow crystallisers (mesoscale crystallisers)

In this research, attention is focused on one of the mesoscale COBCs (4.4 – 5.0 mm I.D.), originally known as mesoscale continuous oscillatory flow reactors (mesoscale OFRs or meso-OFRs). Mesoscale OFRs are primarily developed for laboratory scale processes; they are designed to scale-up to pilot scale directly, or to be used as small-scale production platforms (McDonough, 2015). As shown in Table 2.4, there are four known mesoscale OFR designs namely integral, helical, axial hexagonal (central), and smooth periodic constrictions (SPC) which are smooth curved orifices formed from the glass wall that replace sharp-edged baffle inserts or sharp-edged constrictions (SEPC) in other designs. Mesoscale OFRs pioneered by Reis et al. (2005) offer significant advantages of easy fabrication, reduced material inventory and consumption, and the achievement of near plug flow at very low net flow rates (µl min^{-1} to ml min^{-1}), whereas the conventional scale COBRs cannot (Phan and Harvey, 2010; Phan et al., 2011). As such, they are well-suited for developing laboratory scale continuous crystallisation processes as mesoscale continuous oscillatory flow crystallisers (mesoscale crystallisers) with minimal use of process materials, or for continuous kg-per-day manufacturing of high-value APIs. Mesoscale OFRs with SPC geometries have recently gained attention for application to crystallisation particularly because of their ability to efficiently suspend concentrations of solids at very low net flows (Reis et al., 2005; Ejim et al., 2017). Furthermore, the smooth constrictions in the SPC meso-tube (similar to that shown in Figure 2.11) greatly reduce high shear regions (Reis et al., 2005) and crystal fragmentation (Castro et al., 2018) over other designs, and facilitate gas bubble removal from the meso-tube. Hence the SPC meso-tube is an important design for bioengineering and pharmaceutical applications to be duly explored in this work.

It has previously been demonstrated that an appropriate combination of oscillatory frequency, f, and centre-to-peak amplitude, x_0, can minimise liquid axial dispersion (liquid backmixing) in mesoscale OFRs, making it possible to approach the RTD of an ideal PFR at very low net flows (Reis et al., 2004). However, the oscillatory conditions identified for near

plug flow behaviour can vary according to different sizes, baffle designs (Phan and Harvey, 2010; Phan et al., 2011), and geometries of mesoscale OFRs (Ejim et al., 2017), as well as operating net flows (Stonestreet and Van Der Veeken, 1999; Zheng and Mackley, 2008; Phan et al., 2011). Also, the exact value of hydrodynamic model parameters (i.e. axial dispersion coefficient, D and number of tanks, N) is very dependent on measurement methods (as demonstrated herein) and numerical fitting techniques employed (Froment and Bischoff, 1990; Obradovic et al., 1997; Reis et al., 2010). Therefore, for any continuous process platform development it is an essential first step to critically assess its hydrodynamic performance using suitable methods, rather than relying solely on literature reporting. Table 2.5 summarises the minimum dispersion conditions obtained for different mesoscale OFR designs from literature.

Figure 2.11 SPC design of the mesoscale continuous oscillatory flow crystalliser. SPC meso-tube shown is 30 cm long and has a 5 mm internal diameter.

Mixing and residence times as functions of fluid oscillation conditions have been investigated extensively for several designs of mesoscale OFRs between 4 – 5 mm I.D. (Zheng et al., 2008; Reis et al., 2010; Phan and Harvey, 2010), and the optimal operation of these systems in terms of Re_o and St is well understood. As shown in Table 2.5, a minimum dispersion condition is common across mesoscale OFRs of different geometries and tube diameters. Regardless of flow rate, backmixing is typically minimised at low x_0 between 0.5 – 4 mm and values of $f \leq 12$ Hz where the generation of vortex rings in the inter-constriction regions induces substantial radial mixing and eliminates stagnant zones in the cavities. Also, intrusive techniques (such as fibre optics and conductivity probes) have so far been the most common way of determining mixing performance in mesoscale OFRs. In recent times, non-invasive techniques have been employed by different investigators. Usually, on increasing f and x_0, an optimum condition is rapidly approached where maximum radial mixing is

achieved, and axial dispersion is minimised. Beyond this condition, extended backflow is induced by higher values of f and x_0 producing convective mixing in the direction of flow (Reis et al., 2010). For example, increasing Re_o (at a constant f) beyond the identified optimum condition will approximate mixing to a stirred tank RTD, as higher amplitudes (lower St) will cause vortices to interact with adjacent inter-constriction cavities and render the flow less like discrete tanks-in-series (Phan and Harvey, 2010).

Table 2.5 Minimum dispersion conditions for different mesoscale OFR designs

Meso-OFR I.D. (mm)	Baffle type	Minimum D_{ax}/uL range	Oscillatory range studied	Flow rates (ml min^{-1})	Tracer/ technique	Reference
4.4	SPC	$x_0 = 0.5 – 1$ mm $f = 7.5 – 10$ Hz	$x_0 = 0 – 3$ mm $f = 0 – 20$ Hz	1.94	Indigo carmine/ fibre optic probes	Reis et al., 2004
4.5	SPC	$x_0 = 0.5 – 1$ mm $f = 10$ Hz	$x_0 = 0 – 3$ mm $f = 0 – 20$ Hz	1.94	Indigo carmine/ fibre optic probes	Reis et al., 2010
5	SPC	$x_0 = 0.5 – 1$ mm $f = 10 – 12$ Hz	$x_0 = 0 – 3$ mm $f = 2 – 12$ Hz	2.3 – 13.7	Indigo carmine/ optical probes	Zheng and Mackley, 2008
4	Hexagonal discs	$x_0 = 0.5 – 1$ mm $f = 4$ Hz	$x_0 = 0 – 4$ mm $f = 1 – 6$ Hz	1.0 – 8.0	KCl/ conductivity probes	Phan and Harvey, 2010; Phan et al., 2011
5	Helical coil inserts	$x_0 = 2 – 4$ mm $f = 3$ Hz	$x_0 = 0 – 4$ mm $f = 1 – 6$ Hz	1.0 – 8.0		
5	SPC	$x_0 = 0.5 – 1$ mm $f = 3$ Hz	$x_0 = 0 – 4$ mm $f = 1 – 6$ Hz	1.0 – 8.0		
6	Integral baffles	$x_0 = 1$ mm $f = 1.5$ Hz	$x_0 = 1 – 10$ mm $f = 0.2 – 3$ Hz	10.0 – 30.0	Methylene blue/ microscope camera	Oliva et al., 2018
10	SPC	$x_0 = 0.5 – 3$ mm $f = 7$ Hz	$x_0 = 0 – 3$ mm $f = 0 – 20$ Hz	17.8	PVC particles/ CCD camera	Ejim et al., 2017
10	SEPC	$x_0 = 0.5 – 3$ mm $f = 7$ Hz	$x_0 = 0 – 3$ mm $f = 0 – 20$ Hz	17.8		

While numerous studies clearly show the suitability of mesoscale OFRs for achieving narrow RTDs, these studies have only investigated axial dispersion of the liquid phase, neglecting the solid phase behaviour. Recently, Ejim et al. (2017), employing a washout (step input) experiment of monodispersed polyvinyl chloride (PVC) particles and a single CCD camera, measured the axial dispersion of solid-liquid flow in different geometrical designs of 10 mm I.D. mesoscale OFRs and concluded that the axial dispersion of solid-liquid flow in mesoscale OFRs is comparable to axial dispersion in liquid phase flow. The authors however drew no direct comparison between hydrodynamic parameters of the solid and liquid phase in the 1 m-long 10 mm I.D. meso-tubes investigated. To no surprise, Kacker et al. (2017) using pulse input experiments of melamine crystals and an FBRM probe, showed that in a conventional sharp-

edged COBC (15 mm I.D.) the optimal oscillatory conditions for minimising dispersion are different for the heterogeneous and homogeneous system. The authors utilised *in situ* absorbance spectrophotometry and methylene blue tracer for the homogeneous experiments. In general, particles do not follow exactly the fluid flow, and may not be transported at the same velocity or with the same degree of axial dispersion as the liquid continuous phase for a set of oscillatory conditions. This is mainly for two reasons: (i) particles have inertia and (ii) the drag force causes particles to accelerate towards the local liquid velocity (Rielly and Marquis, 2001).

To address this issue, a dual backlit imaging technique is developed to measure the separate RTDs of the liquid and solid phase in the SPC mesoscale crystalliser. This new image-based method comprising of two HD cameras with backlighting enables direct comparison of the hydrodynamic parameters for the liquid and solid phase without concern for errors that may be introduced by utilising different measurement techniques for each phase. This will help understand the mixing behaviour of crystals in comparison to the bulk liquid under different fluid oscillatory conditions in mesoscale continuous oscillatory flow crystallisers. The technique also overcomes the limitation faced with traditional intrusive measurements, whereby probes can only be fitted into sample ports located at the U-bends. By means of a traversing platform, the cameras can easily be mounted at any distance apart to vary the test section in the mesoscale crystalliser without interfering with the flow. Non-invasive image-based methods have been used by other investigators such as Ejim et al. (2017) to determine RTDs in mesoscale OFRs. Recently, Oliva et al. (2018) utilised a single microscope camera and a novel principal component image analysis to determine the dispersion coefficients in a mesoscale OFR (DN-6) and conventional scale COBR (DN-15). While image-based techniques are growing in use, no direct comparisons with traditional techniques have been made. The dual backlit imaging enables the implementation of an imperfect pulse method to eliminate difficulties associated with an inaccurate pulse injection and measurement, since a perfect input function is difficult to achieve practically. A Fourier transform domain analysis is applied to convolute an input function from an upstream measurement point, with the one-dimensional axial dispersion model, and fit the response to the output function by adjusting model parameters within the axial dispersion model.

Mixing and heat transfer are critical process parameters (CPP) for cooling crystallisation, as they control the spatial distribution of supersaturation which impacts on various properties of the crystal product obtained (Zhao et al., 2014). Efficient mixing required for controlling local crystallisation kinetics is readily achieved in COBCs by superimposing an

oscillatory flow component which provides vigorous eddy mixing inside each baffle or constriction cavity (Mackley et al., 1990). The heat transfer on the other hand is dependent on the mixing conditions inside the tube and is promoted by chaotic flow that results in a high degree of radial mixing. COBCs can achieve superior heat transfer properties for crystallisation than stirred tank reactors due to their higher surface area to volume ratios (SAV) (Zhao et al., 2014). The SAV is a ratio of the outside area of the tube to the volume within the tube and represents the amount of surface area per unit volume of fluid inside the tube. Three well-known studies of a conventional sharp-edged OBR (smooth tube with sharp-edged baffle inserts) (Mackley et al., 1990; Mackley and Stonestreet, 1995; Stephens and Mackley, 2002) have confirmed that significant heat transfer enhancement is obtained when both flow oscillation and baffles are present, compared to non-oscillatory flow in a smooth tube. Mackley and Stonestreet (1995) examined the heat transfer performance of a 12 mm I.D. sharp-edged OBR in a 1 m long stainless-steel shell-and-tube heat exchanger configuration. A 5-fold increase in Nu_t was observed when only baffles were inserted in the tube, and a 30-fold increase was achieved when oscillations were superimposed.

Overall, the heat transfer characteristics of conventional SEPC OBRs are well established and predicted by the Mackley and Stonestreet (1995) correlation. For mesoscale OFRs, which have a variation of baffle configurations (Reis et al., 2005; Phan and Harvey, 2010), their heat transfer characteristics have not been properly investigated, and are still largely speculative (McDonough, 2015). When compared to conventional-sized tubes, the much higher SAV provided by meso-tubes favours enhanced heat transfer for better controlled crystallisation of APIs. So far, no heat transfer investigations have been reported for any of the different geometric designs of mesoscale OFRs, although simulations carried out for non-oscillatory flow in a helical coil meso-tube by Solano et al. (2012) revealed that helical coils, when inserted into a plain meso-tube, would yield a 10% heat transfer augmentation. Furthermore, the authors showed that an increase in Re_o from 10 to 320 caused a 4-fold increase in the mean Nu_t. Although simulation results for the helical coil meso-tube demonstrate a steady increase in Nu_t with Re_o at low net flow, experimental validations of these predictions are yet to be presented. This work will provide an insight into the heat transfer characteristics of the SPC meso-tube, whereby findings may be applicable to other meso-tubes of similar SPC design (Ejim et al., 2017).

2.8.5 Crystallisation studies in OBCs, COBCs, and mesoscale crystallisers

Control of solution cooling crystallisation is a foremost concern addressed by QbD (Nagy, 2009). QbD purports the engineering of a process to produce desired quality objectives, including but not limited to crystal purity, mean size, size distribution, morphology, polymorphic form, and yield. The variables that play a role in controlling the governing states (local supersaturation) for achieving these objectives can vary from one crystallisation platform to the other, and their effects change drastically across operating scales. A good number of crystallisation studies have been performed in conventional (>10 mm I.D.) and pilot scale SEPC COBCs, highlighting the benefits of the technology over traditional batch crystallisation. The COBC has previously been shown to produce consistent crystal size and morphology; reduce crystallisation time, space usage, utility and energy consumption (Lawton et al., 2009); produce a single form of crystal when two forms are possible and produce crystals of higher quality (in terms of CSD and surface characteristics) when compared to that of STCs (Ristic, 2007). Researchers have carried out investigations into the effect of process parameters on the crystallisation of some compounds in OBCs. Ni and Liao (2010) notably studied the effect of mixing intensity, seeding, composition of baffle material and final temperature on the MSZW and crystal polymorph of *L*-glutamic acid in a 50 mm I.D. MB-OBC. They found that the MSZW decreases with increasing mixing intensity; and that metastable α crystals are transformed into stable β crystals with enhanced mixing intensity. The study also highlighted the importance of baffle types used in the OBC; the smoother surface baffle material used exhibited a larger MSZW and favoured metastable crystals, while rougher surface had smaller MSZW with stable crystals dominating. The final cooling temperature also influenced the polymorph obtained, as metastable crystals gradually changed into the stable form when the final cooling temperature in the tube was closer to the stable form nucleation temperature. Ni and Liao (2008) also investigated the effect of cooling rate and solution concentration on the MSZW, nucleation parameters, and crystal polymorphism of *L*-Glutamic acid in a 50 mm I.D. MB-OBC. The investigators reported that the MSZW increased with an increase in cooling rate, while it remained unchanged for different solution concentrations. Solution concentration influenced the polymorph formed with the α crystals favoured for low to medium solution concentration for all cooling rates, while the β crystals were favoured for relatively high solution concentrations. Conventional scale COBCs have also been subjected to crystallisation studies to understand how different variables, and their combinations thereof affect the outcomes of continuous crystallisation processes. Brown et al. (2015) studied the effect of

mixing intensity and supersaturation on experimental steady-states in the anti-solvent crystallisation of salicylic acid in a 15 mm I.D. COBC. Other cooling and anti-solvent crystallisation studies on several organic compounds have investigated the effects of operating conditions such as cooling rate, oscillation intensity, shear rates, starting concentration, impurity, anti-solvent addition rates, holding time, and seeding in both batch and continuous modes of operation (Chew et al., 2004; Ni et al., 2004; Ni and Liao, 2008; Lawton et al., 2009; McLachlan and Ni, 2016). The outcomes of these investigations are generally positive, in most cases showing improvements over crystallisation processes performed in STCs, and with strong correlation between operating variables and CQAs.

The significant reduction of process scale-up and development times is one of the key drivers for continuous manufacturing. Zhao et al. (2014) demonstrated the effectiveness of COBCs for rapid scale-up of crystallisation processes by successfully scaling up the co-crystallisation process of α-lipoic acid with nicotinamide using a 16 mm I.D. COBC, while operating at different spatial temperature profiles in the presence and absence of seeding. Over 1 kg of solid co-crystals was produced at a throughput of 350 g h^{-1} yielding a purity of 99%. Solid content and CSD were monitored from the outlet stream using an FBRM probe. Also, Agnew et al. (2017) recently performed the first continuous crystallisation of the metastable paracetamol form II in a 15 mm I.D. COBC. By rapidly scaling up to the COBC, high polymorphic and solid phase purity and stability was obtained.

Studies focused on seeded continuous cooling crystallisation have also been conducted. Seeding is an effective technique for initiating crystallisation (for compounds difficult to crystallise), controlling polymorphic forms, obtaining high purity, and controlling CSD in continuous crystallisation by avoiding spontaneous nucleation (Mullin, 1993; Narducci et al., 2011). In seeded continuous cooling crystallisation, supersaturation generated by cooling is consumed by the growth of seeds and can be kept low if sufficient seed mass is present, consequently suppressing secondary nucleation (Aamir et al., 2010). If the seed mass is insufficient, then secondary nucleation becomes important and the final CSD will be broad. On the other hand, adding a large quantity of seeds can reduce productivity. It means therefore that the seed surface area available is an important variable that determines the final CSD, and it is determined by the size and mass of seeds used in a crystallisation. Brown (2013) investigated the impact of seed size and seed loading on the final crystal size distribution of an adipic acid – isopropyl alcohol/water system in a COBC. It was found that increasing the seed loading influenced the size of the product crystals, but only when the seeds were of sufficiently small size to offer enough surface area for crystal growth. In seeded cooling crystallisation, it is

necessary to maintain consistency in seed preparation to ensure the seed quality is maintained across different loadings. The temperature profile applied to a cooling crystallisation directly controls the spatial distribution of supersaturation along the crystalliser length. In an ideal seeded crystallisation process, the supersaturation is maintained at a desired constant value through the application of well-designed control algorithms (Aamir et al., 2010). It is well known that in batch crystallisation, a cubic profile can provide better control over CSD than linear or natural cooling (Majumder and Nagy, 2013). Usually, in a cubic profile, the temperature is decreased slowly at the start of the batch, and at a faster rate towards the end to promote crystal growth over nucleation. Where a batch temperature profile can be easily implemented by manipulating the heating/cooling rate in a programmed sequence, replicating such in a continuous process presents its practical challenges. In a tubular crystalliser, the cubic profile is approximated over a plurality of independent temperature-controlled segments based on the mean residence time of the process solution through the crystalliser. The success in closely matching the cubic profile depends on the number of temperature segments employed as well as the degree of freedom of the jacket i.e. single or double liquid filled jacket (Siddique et al., 2015). To follow the cubic cooling curve, a given segment of a continuous crystalliser will be operated at a lower temperature than those preceding it. This approach is applied in this work for seeded cooling crystallisation in the SPC mesoscale crystalliser.

The major challenge facing continuous crystallisation in COBCs is the problematic phenomenon of encrustation. Encrustation manifests as an unpredictable solid formation on internal equipment walls which interferes with heat transfer or PAT measurements and can cause disruption to steady-state operation or complete blockage of the system (Myerson, 2002; Narducci et al., 2011; Biscans, 2012; McGlone et al., 2015; Agnew et al., 2017). Various solutions to the problem have been suggested, such as alternating segments of solution and immiscible transport medium i.e. slug flow (Schiewe and Zierenberg, 2003), stringent temperature profile control and selection of material of construction and coating (Eder et al., 2011), ultrasound (Eder et al., 2012), surface coatings (Zettler et al., 2005), and additives (Middis et al., 1998). Alternative designs to SEPC have been investigated such as the helical baffles, as these generate a ‘swirling flow’ in addition to vortices, which has potential for encrustation mitigation (Phan and Harvey, 2011). Seeding has been employed as an effective strategy for avoiding significant encrustation during a crystallisation process. McGlone et al., (2015) reported operation of a continuously seeded crystallisation process for *L*-glutamic acid in a 15 mm I.D. COBC with glass walls. Attempting to operate without seeding led to significant encrustation and shut down. However, by seeding with β form of *L*-glutamic acid

crystals and maintaining a bulk supersaturation below 3, steady-state operation was maintained for at least 10 hours, thus highlighting the importance of continuous seeding for robust operation.

Despite its suitability for developing small-scale (kg/day) continuous crystallisation processes, there is almost no published work on the use of the SPC mesoscale crystalliser for isolation and purification of APIs; although a paper by Castro et al. (2013a; 2013b) described the continuous precipitation of hydroxyapatite carried out by the authors in a 4.4 mm I.D. mesoscale OFR with similar SPC design. More recently, Castro et al. (2018) also reported the lysozyme crystallisation in a batch mode mesoscale crystalliser. The majority of mesoscale OFRs have found applications over the years in small-scale flow chemistry (Reis et al., 2005; Mohd-Rasdi et al., 2012), gas-liquid mass transfer intensification (Reis et al., 2007; 2008), transesterification (Zheng et al., 2007; Phan et al., 2012), and micro-bioreactions (Reis et al., 2006; 2008). Crystal suspensions are relatively sensitive to mechanical collisions as this leads to crystal breakage. This is especially relevant when focus is on obtaining crystals with a desired shape, size, and distribution. Batch crystallisation studies in stirred tank environments have shown that crystal attrition can directly affect the maximal crystal size of the final product. Loï Mi Lung-Somarriba et al. (2004) in their study on glycine, found that crystal attrition becomes increasingly important as crystals grow towards granular sizes (>1000 μm). Consequently, attrition is a process-limiting phenomenon which restricts crystal growth, in most cases producing bimodal distributions. This brings up a further attraction of the SPC mesoscale crystalliser, which is that the presence of smooth periodic constrictions greatly reduces high shear regions and the probability of crystal attrition.

The performance of the SPC mesoscale crystalliser, however, for seeded continuous cooling crystallisation is still largely untested. Thus, this work systematically investigates the effects of operating variables namely spatial temperature profile, mean residence time, oscillatory conditions, seed size, and seed loading on key process and product particle attributes. Of particular interest is the effect of continuously seeding with different polymorphic forms; since the different polymorphs of the model compound, having different physical properties and crystallisation kinetics, can significantly affect crystallisation process performance and quality of the final product. Therefore, investigations of operating variables are carried out on seed material of both polymorphic forms. Secondly, this work seeks to establish a boundary of operation that is best suited for achieving desired process and product quality as applies to seeded continuous cooling crystallisation of the model compound in the SPC mesoscale crystalliser. This study will utilise *in situ* application of Raman spectroscopy

and FBRM for real-time monitoring of process conditions and detecting the onset of steady-state operation.

2.9 Process analytical technology

Process analytical technology (PAT) is defined by the FDA as "a system for designing, analysing, and controlling manufacturing through timely measurements (i.e. during processing) of critical quality and performance attributes of raw and in-process materials and processes, with the goal of ensuring final product quality" (FDA, 2004b). Usually, PAT measurements are of key process parameters which affect the efficiency of the process and the quality of the final product (Simon et al., 2015). The FDA's initiative on the pharmaceuticals current good manufacturing practice (cGMP) for the 21st Century (FDA, 2004a), aimed to encourage adoption of new technological advances by the pharmaceutical industry, and the subsequent issuance of the FDA PAT guidance of 2004 led to increased impetus and focus on this arena, and raised significant expectations of greater adoption of PAT in all phases of development by the pharmaceutical industry. The value proposition for PAT in early process development, as an enabler of increased mechanistic and process understanding, as well as process control and optimisation, has already been validated by academia and the broader scientific community over decades.

In the last few years, PAT has found a compelling use in continuous crystallisation monitoring. Continuous crystallisation processes benefit significantly from PAT tools as they give real-time feedback of the variations of parameters which is essential for ensuring that the process is within robust control (Wang et al., 2017). Real-time measurement tools and techniques widely used in the last decade include focused beam reflectance measurement (FBRM), nuclear magnetic resonance (NMR), infra-red (IR) spectroscopy, near infra-red (NIR) spectroscopy, attenuated total reflectance (ATR)-UV/Vis, attenuated total reflection (ATR)-Fourier transform infrared (FTIR), Raman spectroscopy, and particle vision microscopy (PVM). These in-line tools help to avoid sample preparation and time delay typical of offline analysis. They can provide effective and efficient means for acquiring information to facilitate process understanding, continuous improvement, and development of risk-mitigation strategies (Simone et al., 2014). They also help to design experiments and obtain data for identification of the crystallisation kinetics, design controllers to maximize product

quality and minimize operating costs, and operate the process within the required performance indicators using suitable feedback control (Nagy et al., 2013).

Recent advances in PAT have made smaller-sized PAT tools available for use with COBC platforms. These have enabled the routine application of tools such as the FBRM, Raman, and FTIR for real-time crystallisation process monitoring. Lawton et al. (2009) investigated the continuous crystallisation of a commercial API in comparison to batch crystallisation, using a 15 mm I.D. COBC fitted with an FBRM probe for real-time CLD measurements. The investigators reported that the COBC offered better control of cooling rates, and API morphology, mean size and CSD than the batch process. Siddique et al. (2015) utilised in-line FBRM and mid-IR to establish thermodynamic and kinetic parameters for sonocrystallisation of lactose in the rattlesnake COBC. The study found the yield of the process was influenced by the sonicator power for seed generation, and that narrower CSD was obtainable in the COBC compared to the batch process. More recently, Peña et al. (2017) used an FBRM probe in the spherical agglomeration/crystallisation of benzoic acid in a 15 mm I.D. COBC.

In this work, Raman spectroscopy and FBRM technology are utilised to monitor real-time solute concentration and particle counts of crystallisation processes. It is common that more than one PAT tool is applied simultaneously to monitor physical and chemical phenomena during processes, resulting in data with high dimensionality. Therefore, multivariate data from these *in situ* process monitoring devices must first be interpreted using Chemometrics (Rajalahti and Kvalheim, 2011). Chemometrics refers to the application of statistical and mathematical methods to handle process data to discover hidden structure of the data. Chemometrics uses multivariate data analysis methods such as multiple linear regression (MLR), principal component analysis (PCA), principal component regression (PCR), partial least squares (PLS) and others (Matero et al., 2013). A brief overview of the capabilities of Raman spectroscopy and FBRM and their limitations is provided in the sections below.

2.9.1 Raman spectroscopy

Most organic molecules present clear and resolved peaks in Raman spectra, offering the possibility to do quantitative and qualitative analysis. For this reason, Raman spectroscopy can be used *in situ* or externally (using non-invasive accessories) to monitor spectral intensity changes corresponding to the composition of the system being monitored (Nagy et al., 2013).

Raman spectroscopy has become a frequently used PAT tool in pharmaceutical research particularly because it can be correlated to other material properties besides concentration, such as polymorph form, particle size, or polymer crystallinity. In particular, Raman enables non-destructive and fast quantitative measurements of solid samples without specific sample preparation. Its ability to distinguish between different polymorphic forms enables its application during crystallisation of chemical species with more than one polymorphic form. It is also advantageous in that it displays more distinct spectral features than other spectral techniques (Simone et al., 2014). However, one of the biggest and frequent challenges to collecting Raman spectra is fluorescence which can disturb measurements. Also, the presence of strong peaks in Raman spectra for organic solvents can interfere with those of the solid/solute (Févotte, 2007). For this reason, water is a preferred solvent used in this work because it does not show peaks in Raman.

The potential of using Raman spectroscopy to quantitatively determine the concentration of polymorphic forms in solutions depends on the possibility of building a good calibration model using a robust experimental approach. PCR and PLS are commonly used multivariate methods (Esmonde-White et al., 2017) that have been successfully applied for Raman solute concentration calibration (Caillet et al., 2006; Hu et al., 2006; Qu et al., 2008), with the PLS approach usually giving better results (Simone et al., 2014). However, many parameters can affect the Raman spectra used to build these models such as temperature, crystal size, solid concentration, solution density, and solute concentration, and these have been studied in detail (Hu et al., 2007; Chen et al., 2008; Simone et al., 2014). Usually, such effects can be compensated using pre-processing techniques such as standard normal variate (SNV), normalisation, baseline corrections, 1st and 2nd order derivatives etc. (Vankeirsbilck et al., 2002; Huang et al., 2010). Ultimately, good calibration practice (GCP) should be applied to ensure high quality non-biased data is obtained from Raman concentration measurements.

2.9.2 Focused beam reflectance measurement (FBRM)

FBRM is widely used in continuous crystallisation as an *in situ* particle monitoring technique for in-line real time measurement of particle size in the range of 0.25 – 1000 µm (Barrett and Glennon 2002; Braatz, 2002; Bakar et al., 2009). A great advantage of this technique is that data is acquired in real time to give particle size data and population trends without the need for sampling, which could potentially cause disturbance to the process

(Kougoulos et al., 2005). FBRM works on the principle of laser backscattering, where a beam of laser light is rotated at a constant speed of 2 m s^{-1} and the backscatter from particles in suspension is measured and represented as a particle chord length. The measured chord lengths are counted, categorised and displayed as a chord length distribution (CLD) with selected size bins. The chord lengths may be represented as non-weighted, linear, square or cube-weighted distributions. Particle counts (#/s) are related to the total number of crystals in the size bins represented. The CLD is proportional to the CSD in the crystalliser, and the mean particle size is represented by the square-weighted mean chord length (SWMCL) which is defined as:

$$\text{SWMCL} = \frac{\sum_{i=1}^{k} n_i L_i^3}{\sum_{i=1}^{k} n_i L_i^2} \tag{2.17}$$

where L_i is the chord length of ith size bin, n_i is the number of counts corresponding to the ith bin, and k is the upper size bin.

A major disadvantage of FBRM is that it does not measure true particle size and is prone to false measurements since a large number of chords of different sizes can be obtained from any given particle (Bakar, 2010; Ferguson et al., 2014). The problem is worsened for strongly non-isometric particles such as needle-like or plate-like particles which are ubiquitous in pharmaceutical manufacturing, especially since CLD geometrical models are largely based on populations of spherical and slightly non-spherical particles (Barrett and Glennon, 1999; Nere et al., 2007; Agimelen et al., 2015). It is even more likely that in suspensions of crystals with a wide variety of morphologies, an even greater number of different chords may be obtained relative to a suspension of crystals with a more uniform shape (Powell et al., 2015). Thus, full CSD information cannot be accurately obtained from CLD measurements. FBRM measurements are also sensitive to surface roughness, noise or disturbance, particle number density, as well as variations in the mixing conditions. For this reason, the FBRM square weighted mean chord length (SWMCL) statistic is often used as a qualitative estimate of the mean crystal size (Yang and Nagy, 2014). Encrustation on FBRM probes and subsequent fouling and adherence of crystals to the probe window is also a major problem encountered in MSMPR crystallisation processes where supersaturation and crystal number densities can be very high. Despite these problems, FBRM total particle counts (#/s) statistic has been used in continuous crystallisation processes for successfully implementing feedback and feedforward control (Yang and Nagy, 2015; Yang et al., 2015b; 2016; Yang et al., 2017), qualitative characterising of steady-state operation (Powell et al., 2015; Yang et al., 2015a; Li et al., 2016),

investigating size classification in MSMPR slurry transfer (Cui et al., 2016), and detecting dissolution and nucleation events (Powell et al., 2016); hence the decision to utilise it in this work. Another challenge faced is the adaptability of FBRM probes to smaller scales of continuous crystallisers such as the mesoscale COBC designs. Although commercially available FBRM probes such as the ParticleTrack G400 can easily be incorporated into conventional scale COBCs, technological capabilities have so far prevented development of smaller diameter probes which suit mesoscale crystallisers. To enable the use of FBRM technology with these crystallisers, specific modifications to meso-tubes would have to be carefully made to accommodate the FBRM probe without significantly disrupting the hydrodynamics. Table 2.6 summarises key advantages and disadvantages of Raman and FBRM technology.

Table 2.6 Summary of advantages and disadvantages of Raman spectroscopy and FBRM

PAT tool/technique	Benefits	Limitations
Raman spectroscopy	Can reliably provide quantitative data through non-destructive analysis	Raman spectra are affected by fluorescence
	Can detect concentration, polymorphic form, particle size	Sensitive to instrument environment and exhibits fluctuations
	In-line Raman enables real-time control of CPPs and process corrections	Immersion probe and window are prone to fouling and encrustation over long periods in high solids concentration
	Sampling versatility via non-contact probes or *in situ* immersion probes	
	Compatible with aqueous environments	
FBRM	Robust for different chemical and solvent environments	Cannot reliably provide CSD information
	Can provide information about nucleation, induction time, and growth, size, dissolution, MSZW, polymorphic transformation, and agglomeration	Highly prone to fouling of probe window over time
		Technological capabilities limit application to small-sized equipment such as mesoscale COBCs or microfluidic crystallisers

2.10 Summary of literature review

This chapter has reviewed the existing technologies that currently offer potential for the development of robust and scalable continuous crystallisation processes, as well as findings from published literature which serve as an important indication of progress made so far in translating pharmaceutical crystallisation processes from batch to continuous operation. A clear distinction between the underlying principles governing batch and continuous processes, as well as the possible benefits of continuous operation over batch has been covered. It is well known that each approach discussed has certain advantages over the other, as well as pitfalls of its own. However, common to both the MSMPR and COBC platforms is the problem of encrustation and blockage (partly caused by poor control of local supersaturation). In the case of MSMPR crystallisation, reports of blockages in transfer lines have been made, limiting the periods to which the 'continuous' process can run. In the COBC, blockage of the baffled tube (usually towards the end) is a common occurrence in all existing designs which must be overcome if ever a truly continuous crystallisation is to be achieved. By industry standards, a fully developed continuous crystallisation process should meet all quality requirements and must have run for at least 2 weeks uninterrupted. With the significant progress made so far in PAT, the next logical step would be bringing together PAT tools to serve as enablers in better understanding continuous crystallisation processes and overcoming the current challenges with crystallisation in these continuous platforms. This is a key objective of this thesis.

Chapter 3 Experimental materials and methods

This chapter gives a detailed description of the batch SPC mesoscale crystalliser, SPC mesoscale crystalliser, MSMPR crystalliser, and the model system investigated in this work. All experimental and modelling methods, materials, and equipment used in characterisation and crystallisation process development on both platforms are outlined in detail. All chemical substances used in crystallisation studies were obtained from approved suppliers. Measures were taken to obtain chemicals from the same supplier where possible. Specific polymorphs of the model compound were ordered from the same supplier but originated from different countries.

3.1 Model system selection

To facilitate cooling crystallisation investigations in both platforms in a non-cGMP (FDA, 2004a) laboratory, a model system with the following characteristics was required:

- Cheap and non-hazardous compound to ease handling and ensure safety.
- Cheap Class 3 solvent or lower (according to the International Council for Harmonisation of Technical Requirements for Pharmaceuticals for Human Use (ICH)) to reduce solvent cost, ease waste solvent management, and minimise environmental impact.
- Strong temperature-dependent solubility of compound in solvent (>0.15 g/g at 40 °C) for cooling crystallisation (Muller et al., 2009).
- Non-volatile solvent (boiling point > 80 °C) to prevent significant solvent loss during heat up.
- Monotropic at temperatures below 60 °C to avoid *in situ* polymorphic changes during cooling crystallisation.
- Relatively fast growth kinetics of model system for observable crystal growth in short residence times.
- Non-needle-like morphology to aid *in situ* FBRM measurements and offline size characterisation by laser diffraction.
- Raman-active solute in a weakly Raman scattering solvent to aid *in situ* solute concentration measurements with a Raman immersion probe.

The glycine-water system was found to satisfy the criteria above. Glycine was selected as a model compound for study as it is relatively safe and cheap, highly soluble in low-cost water, and exhibits multiple polymorphs with fast and slow growth kinetics.

3.2 Materials

2-aminoacetic acid or glycine (herein called GLY) is an amino acid found in the protein of all living organisms. It is widely known for its therapeutic use as a nutrient, buffer agent in cosmetics, and food additive in seasoning and preservatives (Banerjee and Briesen, 2009; Matsumoto et al., 2013). In solution and in solid state, GLY is zwitterionic ($H_3N^+-CH_2-COO^-$) and has specific physical and chemical properties due to the presence of the proton donor carboxyl acid group ($-COOH$) and the proton acceptor amino group ($-NH_2$). The chemical formula and physical properties of GLY are shown in Figure 3.1 and Table 3.1 respectively.

Commercial glycine with ≥99% purity was purchased from Sigma Aldrich UK and used in preparing feed solution for all experiments conducted in this work. Deionised water from a Milli-Q® IQ 7000 Ultrapure Lab Water System was used as the solvent. α-GLY (originating from USA) and γ-GLY (originating from China) were specifically used to prepare seed material for all seeded crystallisation experiments.

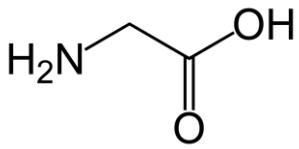

Figure 3.1 Chemical formula of glycine (2-aminoacetic acid).

Glycine exists in 3 known polymorphic forms under atmospheric conditions namely α, γ, and β with a thermodynamic stability in the order $\gamma > \alpha > \beta$ (Marsh, 1958; Srinivsan, 2008). α and β forms are monoclinic, and γ form is trigonal-hexagonal. α-GLY is easily crystallised from pure aqueous solution (Zaccaro et al., 2001; Park et al., 2003), β-GLY is obtained from anti-solvent crystallisation from ethanol (Nii and Takayanagi, 2014; Matsumoto et al., 2013), while γ-GLY can be crystallised from aqueous solution in the presence of a selective additive such as sodium chloride (NaCl) (Narayan Bhat and Dharmaprakash, 2002; Srinivasan and Arumugam, 2007).

α-GLY and γ-GLY exhibit distinct morphological differences; α-GLY crystals have a prismatic shape, and γ-GLY usually appears as square based bipyramid crystals. Although α-GLY is

metastable and γ-GLY is highly stable at ambient conditions, transformation from α- to γ-GLY occurs on long exposure to highly humid ambient conditions (>50% RH). A reversible or irreversible solid-solid transformation from γ- to α-GLY occurs while heating well above room temperature between 165 – 180 °C (10 °C min^{-1} heating rate) (Srinivasan, 2008; Rabesiaka et al., 2010). β-GLY on the other hand is highly unstable, transforming quickly in the open air to α-GLY (Langan et al., 2002) and through solution-mediated phase transformation (Iitaka, 1960; Srinivasan, 2008).

3.3 SPC meso-tube

Figure 3.2(a) shows the exterior of an SPC meso-tube, Figure 3.2(b) shows a cross-section of an SPC meso-tube, and Figure 3.2(c) shows the schematic of the SPC meso-tube.

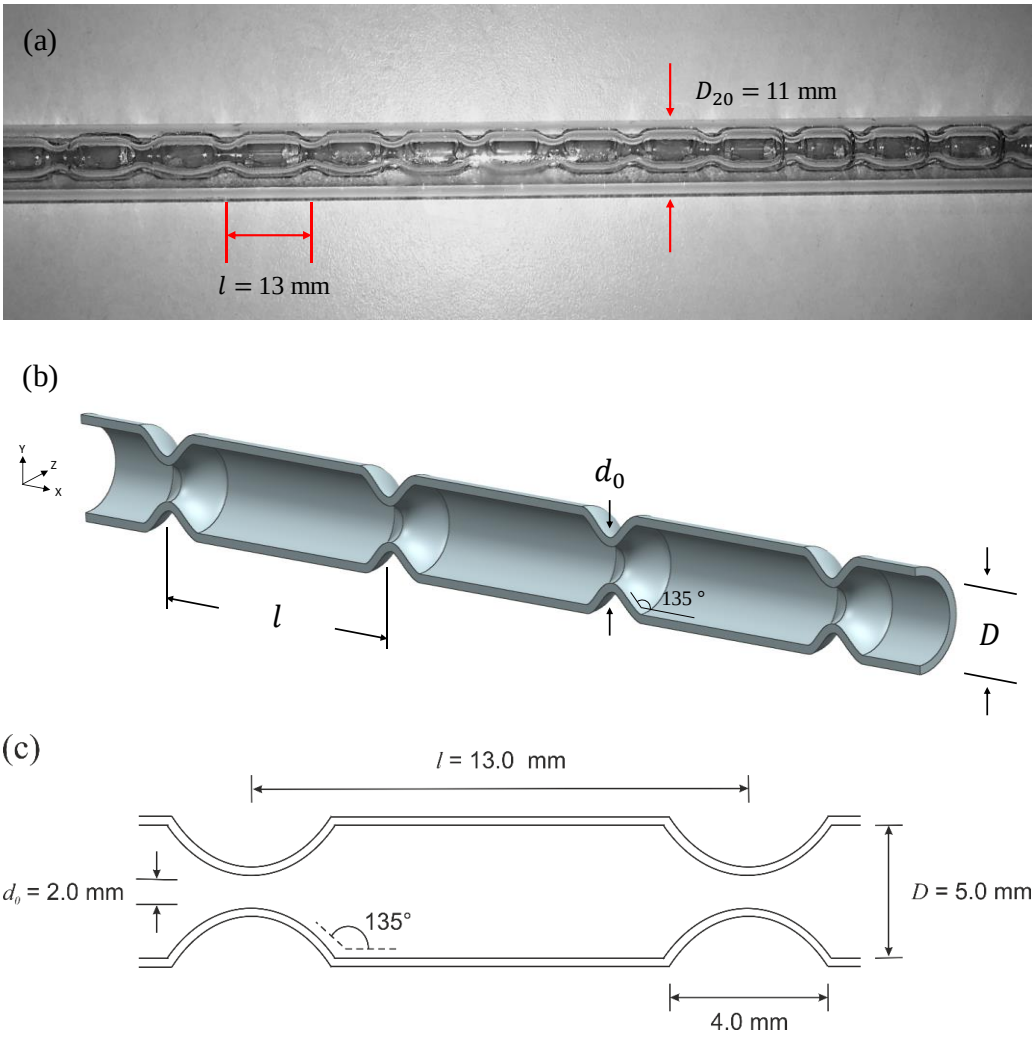

Figure 3.2 (a) section of a jacketed SPC meso-tube (b) internal CFD visualisation of an SPC meso-tube (c) Schematic of SPC meso-tube with labelled dimensions.

The term 'SPC meso-tube' herein refers to a single straight glass tube with an internal diameter, D, of 5 mm, and containing smooth curved orifices known as smooth periodic constrictions. An SPC meso-tube may be jacketed or unjacketed, and has an inner constriction diameter, d_o, of 2.0 mm which gives an open cross-sectional area, α, of 16%. The mean spacing between smooth constrictions, l, is 13 mm, giving a constriction length-to-diameter ratio, l/D, of 2.6, which is significantly higher than ratios of 1.5 – 2 for conventional SEPC COBCs (Brown and Ni, 2012; Zhao et al., 2014).

Table 3.1 Chemical and physical properties of glycine

Molecular weight (g mol^{-1})	75.07
Colour	White powder
Odour	Odourless
Density (g cm^{-3})	1.61
Melting point (°C)	260

3.4 Batch SPC mesoscale crystalliser

Figure 3.3 shows the schematic of the batch SPC mesoscale crystalliser. The batch SPC mesoscale crystalliser consists of a 35 cm long jacketed SPC meso-tube vertically mounted on a piston-driven diaphragm which is connected to an electromagnetic oscillator (LDS, UK).

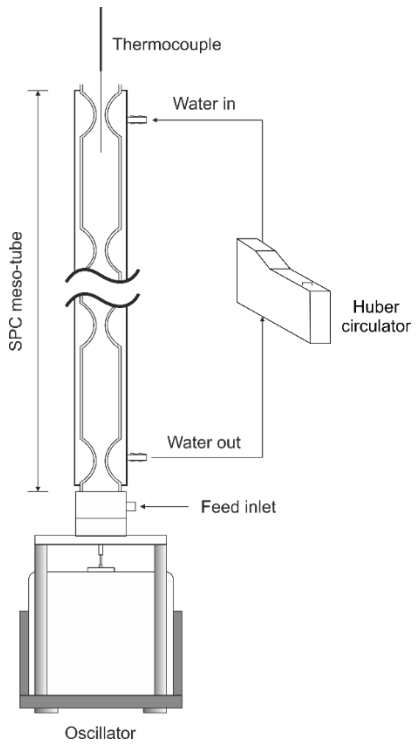

Figure 3.3 Schematic diagram of the vertically-oriented batch SPC mesoscale crystalliser (not drawn to scale).

The SPC meso-tube has an internal diameter, D, of 5 mm, a constriction diameter, d_0, of 2.0 mm, and a total volume of ~4.3 ml. The bottom end of the SPC meso-tube is connected to the piston-driven diaphragm by a mixing chamber containing a feed inlet port. Cooling and heating of the process fluid in the batch SPC mesoscale crystalliser is provided by a Huber Ministat 230 cooling circulator, and a K-type thermocouple (Thermosense) inserted at the top of the SPC meso-tube monitors the process fluid temperature. Oscillations in the range of $x_0 = 0.5 – 3$ mm, $f = 2 – 12$ Hz are provided in the batch SPC mesoscale crystalliser via a signal generator (LDS, UK, PO100) and an amplifier (LDS, UK, PA100E).

3.5 SPC mesoscale crystalliser

A mesoscale continuous oscillatory flow crystalliser with smooth periodic constrictions (herein called SPC mesoscale crystalliser) was assembled for characterisation and development of a small-scale continuous crystallisation process. Figure 3.4 shows the SPC mesoscale crystalliser modified for residence time distribution measurements reported in Chapter 4. The main platform consists of 1 L-shaped unjacketed 90° glass bend (B90) and 6 jacketed SPC meso-tubes (S0 – S5) connected in series by 5 unjacketed U-shaped glass bends (B0 – B4) using PEEK connectors. The total volume and length of the crystalliser is 72 ml and 5.4 m respectively. The first SPC meso-tube, forming the first section of the crystalliser, is 0.796 m in length, and is connected to the oscillator unit by the 90° glass bend. The other 5 sections consist of 0.727 m-long jacketed SPC meso-tubes. The 90° and U-shaped glass bends all have the SPC dimensions given in section 3.3 above. An important design feature of the U-shaped glass bend is that the right end of the bend has 10° orientation to the horizontal plane. This gives each connected straight section a 10° inclination, with the exit of the section higher than the entrance. This degree of inclination was determined by Reis et al. (2005) as the optimal minimum angle for assembling a meso-OFR manufacturing unit which comprises of a number of SPC meso-tubes arranged in series. This optimum inclination minimises gas retention and facilitates bubble washout from the meso-tube.

Fluid oscillations in the SPC mesoscale crystalliser are achieved by a piston-driven diaphragm fixed at the bottom of a mixing chamber and connected to an electromagnetic oscillator (LDS, UK, V406). A signal generator (LDS, UK, PO100) and an amplifier (LDS, UK, PA100E) provide a range of oscillation amplitude and frequency of $x_0 = 0.5 – 3$ mm, $f = 2 – 12$ Hz for the system. Continuous steady flow was supplied by a Labhut Series 1500 dual piston pump, which fed the system with volumetric flow rates of up to 12 ml min^{-1}.

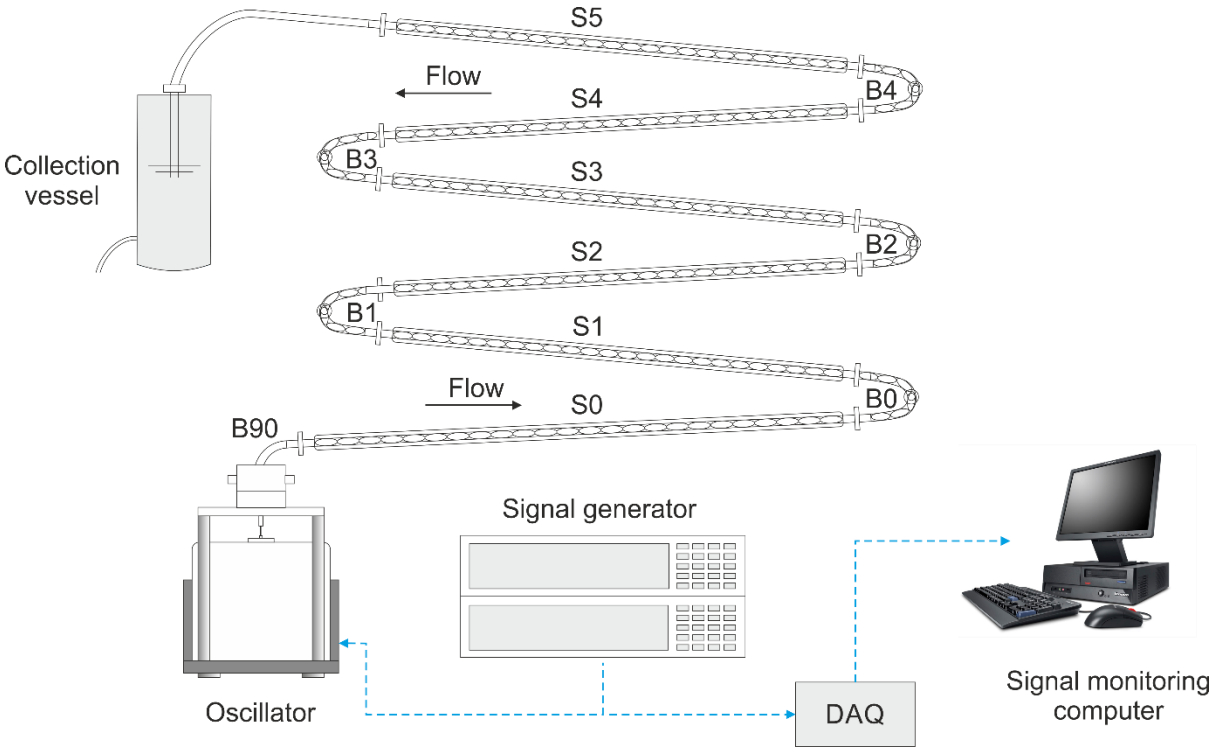

Figure 3.4 Schematic of the SPC mesoscale crystalliser platform (not drawn to scale).

3.6 Offline characterisation methods

3.6.1 Raman spectroscopic analysis

An important property which guided the selection of GLY-water as a model system is that all 24 vibrational modes of GLY are Raman active in the spectral region 400 – 4000 cm^{-1}. Also, since water does not Raman scatter (i.e. polarizability of the water molecule does not change during vibration), real-time solution concentration monitoring of the system can be performed using Raman spectroscopy and robust calibration models (see section 3.7). The vibrational spectrum of GLY has been studied in solid state and in water. Offline analysis of GLY polymorphic forms was performed using a Thermo Scientific™ DXR™ 2 780 nm Raman microscope equipped with OMNIC 8 software. Figure 3.5 shows the full-range solid-state Raman spectra for α-GLY and γ-GLY with the observed bands identified in Table 3.2.

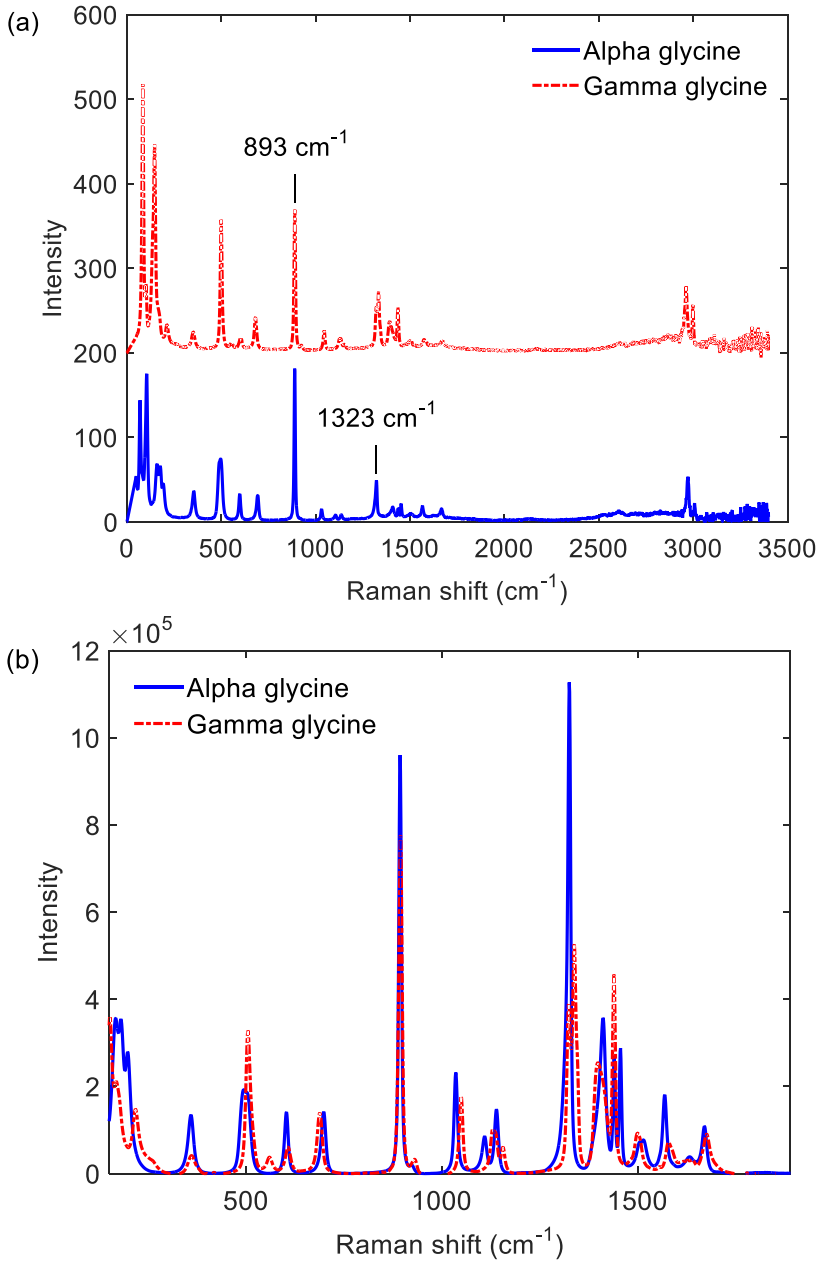

Figure 3.5 (a) Stacked plot of offline solid-state Raman spectra for α- and γ-GLY (0 – 3500 cm^{-1}) and (b) Overlay of zoomed in offline solid-state Raman spectra for α- and γ-GLY (150 – 1890 cm^{-1}).

Table 3.2 shows the 13 GLY bands in the solid-state Raman spectrum and their vibrational assignments (Kumar et al., 2005; Zhu et al., 2011). The bands at 893 and 1323 cm^{-1} are among the most intense in the Raman spectra of the solid and solution GLY and can be considered as the marker of GLY. These two bands are found at 898 and 1330 cm^{-1} in the aqueous GLY solution spectra; however, the band located at 602 cm^{-1} in literature (Zhu et al., 2011) was observed at 508 cm^{-1} in the GLY solution spectra.

Table 3.2 Comparison of observed and literature bands for GLY Raman spectra

Observed α-GLY (cm^{-1})	Observed γ-GLY (cm^{-1})	Observed GLY-water (cm^{-1})	Literature value (cm^{-1})	Assignment
3006	2998	-	3050(m)	Asymmetrical CH stretch
2972	2961	-	2930(s)	Symmetrical CH stretch
-	-	-	2123(w)	Combination band (697 + 1410 cm^{-1})
1667	1675	-	1667(w)	C=O stretch
1566	1573	-	1567(w)	-
1503	1506	-	1508(w)	CH_2 bend + OH bend
1454	-	-	1458(m)	-
1435	1436	1445	1442(m)	Hα −Cα −H
1408	1394	1413	1410(m)	CH_2 scissoring
1322	1322	1330	1323(s)	NH_2 twist + CH2 twist
1032	1045	1033	1033(m)	C−N stretch + C−C vibration
889	890	898	893(s)	NH_2 twist + CH_2 twist
694	682	-	697(w)	NH_2 bend
599	603	508	602(m)	COOH bend + NCCO bend
497	500		497(m)	COO^- bend + CH_2 bend

m = medium, s = strong, w = weak

3.6.2 Powder X-ray diffraction analysis

Powder X-ray diffraction (PXRD) measurements were performed using a benchtop Bruker D2 PHASER diffractometer with Bragg-Brentano focusing optics equipped with Cu Kα of wavelength of 1.5406 Å and a LYNXEYE 1-dimensional detector. Figure 3.6 shows the powder patterns for both polymorphic forms of GLY investigated.

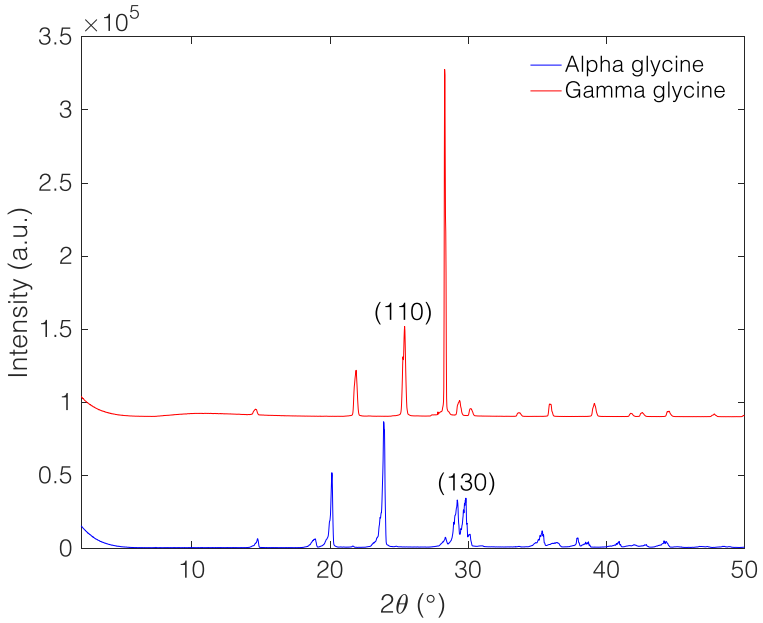

Figure 3.6 Powder diffraction patterns of α- and γ-GLY.

The tube voltage and amperage were set to 30 kV and 10 mA respectively. Samples were measured in the 2θ range of 2 – 50 ° at a step size of 0.02 °. The resulting reflection peaks in the PXRD spectrum known as Bragg peaks correspond to different crystal planes. The Bragg peaks can be indexed and from the values of 2θ, d-spacing, $h\ k\ l$, and relative intensity (I/I_0) of every prominent peak, the lattice parameters of the crystals can be determined. In its diffraction pattern, α-GLY exhibits a Bragg peak corresponding to (130) plane at an angle approximately 30 ° of 2θ, whereas γ-GLY is fingerprinted by its Bragg peak at approximately 26 ° of 2θ corresponding to the (110) plane (Srinivasan, 2008).

3.6.3 Laser diffraction analysis

Offline particle sizing was performed using a Malvern Mastersizer 2000 particle size analyser. The Mastersizer 2000 analyser uses the technique of laser diffraction to measure particle size distributions from 10 nm up to 3.5 mm. In laser diffraction a laser beam passes through a dispersed particulate sample and the angular variation in intensity of the scattered light is measured. The angular scattering intensity data is then analysed to calculate the size of the particles that created the scattering pattern using the Mie theory of light scattering. The particle size is reported as a volume equivalent sphere diameter.

The Mastersizer 2000 analyser was fitted with a wet dispersion unit containing isopropanol as the dispersant fluid. Isopropanol was selected as the dispersant since it does not dissolve GLY. Prior to particle sizing, samples dried overnight were placed in a sonication bath for 1 min to break up agglomerates. For samples analysed immediately after collection from the crystalliser outlet, no sonication was performed. Particle sizing was performed by adding the sample to the wet dispersion unit until an obscuration of between 10 – 12% was achieved. Three measurements of the same sample were taken by the Malvern instrument, after which the raw data was automatically analysed to produce a particle size distribution, herein referred to as the crystal size distribution.

3.7 Multivariate calibration

Calibration refers to the development of a relationship between a set of variables such as spectra to some property(s) of interest e.g. concentration. To facilitate real-time *in situ* GLY solution concentration measurements, a calibration model was developed and validated using a set of experiments and a robust multivariate chemometric method. In multivariate calibration, more than one

response variables are involved. This is particularly helpful if the variability in the independent variable (concentration in this case) can be explained in a better way by using multiple variables (Brereton, 2003; Bakeev, 2010). The linear regression equation takes the form:

$$\boldsymbol{c} = \boldsymbol{X}\boldsymbol{b} + \boldsymbol{e} \tag{3.1}$$

where $\boldsymbol{c}$ is the concentration vector, $\boldsymbol{X}$ is an $n \times m$ matrix of multiple variables such that each row corresponds to a complete spectra recorded at m wavelengths. A column of ones can be introduced to account for the intercept term; in this case $\boldsymbol{X}$ will have $n \times (m + 1)$ dimensions. The vector $\boldsymbol{b}$ ($\boldsymbol{b} = [b_0, b_1, \dots, b_m]$) has all the regression coefficients, each corresponding to a specific variable present in the $\boldsymbol{X}$ matrix. The equation for determining the coefficients is given as:

$$\boldsymbol{b} = (\boldsymbol{X}^{\boldsymbol{T}}\boldsymbol{X})^{-\boldsymbol{1}}\boldsymbol{X}^{\boldsymbol{T}}\boldsymbol{c} \tag{3.2}$$

And the prediction of concentration can be performed with Equation (3.3):

$$\boldsymbol{c}_{\boldsymbol{pred}} = \boldsymbol{X}_{\boldsymbol{meas}}\boldsymbol{b} \tag{3.3}$$

The subscript '$meas$' is used to denote the vectors of measured Raman scatter for the samples with unknown concentrations. Note that the concentration matrix $\boldsymbol{C}$ can also be multivariate, e.g. the concentration of several species in the solution can be predicted simultaneously. In this case $\boldsymbol{C}$ is an $n \times s$ matrix, with s being the number of species for which the concentration is determined from the calibration model.

3.7.1 Partial least squares regression (PLSR)

A necessary condition for multivariate calibration is that the number of samples (n) must be greater than the measured variables (m) otherwise the matrix inversion in Equation (3.2) will not be possible. A disadvantage of multivariate calibration approach comes from the existence of multicollinearity in the data, whereby some of the variables can be expressed as linear functions of some of the other variables. This is particularly true of data produced from spectroscopic measurements like Raman, which produce intensity values in a large number of wavelengths for each concentration. Sometimes part of the data generated is not required or irrelevant and thus can be made

redundant. The presence of such properties in the calibration data can lead to an unstable model with poor prediction capability. To address this, partial least squares regression (PLSR) can be used to improve the efficiency of models developed, through data compression and dimensionality reduction (Adams, 2004; Bakeev, 2010). PLSR simplifies the data structure and still accounts for as much of the total variation in the original data set as possible. In model building, PLSR applies a regression to those variables that account for variance in $\boldsymbol{X}$ and $\boldsymbol{c}$ data. This differs from principal component regression (PCR) which applies regression only to those variables that account for variance in $\boldsymbol{X}$ data.

The first step in performing the PLSR is to pre-process the data to obtain a normalised data matrix $\widetilde{\boldsymbol{X}}$, with zero empirical mean and unit variance, using the scaling parameter vectors $\bar{\boldsymbol{x}} = [\bar{x}_1, \dots, \bar{x}_m]^T$ and $\boldsymbol{\sigma} = [\sigma_1, \dots, \sigma_m]^T$ as the empirical (sample) mean and variance vectors of the process variables in the data matrix, respectively. This normalisation is known as mean centring. The elements of the normalised data matrix are defined as:

$$\tilde{x}_{ij} = \frac{x_{ij} - \bar{x}_j}{\sigma_j} \text{ for } i = 1, \dots, n \text{ and } j = 1, \dots, m \tag{3.4}$$

And the normalised data matrix can be represented as:

$$\widetilde{\boldsymbol{X}} = \boldsymbol{T_1 P^T} + \boldsymbol{E_x} \tag{3.5}$$

and the responses (e.g. concentrations) are represented as:

$$\tilde{\boldsymbol{c}} = \boldsymbol{T_2 q^T} + \boldsymbol{e_c} \tag{3.6}$$

where $\boldsymbol{T}$ is the $n \times q$ latent (or score) matrix, $\widetilde{\boldsymbol{X}}$ has the dimensions $n \times m$, $\tilde{\boldsymbol{c}}$ has $n \times 1$ dimensions, $\boldsymbol{P}$ (latent variables) $m \times q$ and $\boldsymbol{q}$ $1 \times q$ are the loading matrices, and $\boldsymbol{E_x}$ $n \times m$ and $\boldsymbol{e_c}$ $n \times 1$ are the error matrix and error vector respectively, $\boldsymbol{T_1}$ and $\boldsymbol{T_2}$ are the latent (or score) matrices for $\widetilde{\boldsymbol{X}}$ and $\tilde{\boldsymbol{c}}$ respectively, both having dimensions $n \times q$ where $q \ll m$.

PLSR using eigenvalue decomposition is described as follows:
The scores for $\boldsymbol{T_1}$ matrix are calculated as:

$$\boldsymbol{t_1} = \widetilde{\boldsymbol{X}}\boldsymbol{w} \tag{3.7}$$

where $\boldsymbol{w}$ is the eigenvector corresponding to the first eigenvalue of $\widetilde{\boldsymbol{X}}^{\boldsymbol{T}}\tilde{\boldsymbol{c}}\tilde{\boldsymbol{c}}^{\boldsymbol{T}}\widetilde{\boldsymbol{X}}$**.** The first score for $\boldsymbol{T_2}$ is calculated as:

$$\boldsymbol{t_2} = \tilde{\boldsymbol{c}}\boldsymbol{g} \tag{3.8}$$

where $\boldsymbol{g}$ is the eigenvector corresponding to the eigenvalue of $\tilde{\boldsymbol{c}}^{\boldsymbol{T}}\widetilde{\boldsymbol{X}}\widetilde{\boldsymbol{X}}^{\boldsymbol{T}}\tilde{\boldsymbol{c}}$. Once these vectors are calculated, they are subtracted from the original values of $\widetilde{\boldsymbol{X}}$ and $\tilde{\boldsymbol{c}}$ as:

$$\widetilde{\boldsymbol{X}} = \widetilde{\boldsymbol{X}} - \boldsymbol{t_1}\boldsymbol{t_1}^{\boldsymbol{T}}\widetilde{\boldsymbol{X}} \tag{3.9}$$

$$\tilde{\boldsymbol{c}} = \tilde{\boldsymbol{c}} - \boldsymbol{t_2}\boldsymbol{t_2}^{\boldsymbol{T}}\tilde{\boldsymbol{c}} \tag{3.10}$$

The above process is then repeated to extract the second factor and so on and so forth. The latent variables can then be calculated as:

$$\boldsymbol{p_1^T} = (\boldsymbol{t_1^T t_1})^{-1}\boldsymbol{t_1^T}\widetilde{\boldsymbol{X}} = \boldsymbol{t_1^T}\widetilde{\boldsymbol{X}} = \boldsymbol{w_1^T}\widetilde{\boldsymbol{X}}^{\boldsymbol{T}}\boldsymbol{X} \tag{3.11}$$

The final regression coefficients are given by:

$$\boldsymbol{b} = \boldsymbol{W}(\boldsymbol{P}^{\boldsymbol{T}}\boldsymbol{W})^{-1}\boldsymbol{g}^{\boldsymbol{T}} \tag{3.12}$$

The prediction step is then carried out as follows:

1. Take a new measurement $\boldsymbol{X_{meas}}$
2. Calculate normalised measurement matrix $\widetilde{\boldsymbol{X}}_{\boldsymbol{meas}}$ using $\bar{\boldsymbol{x}}$ and $\boldsymbol{\sigma}$
3. Project the measurement data in the reduced space determined by the PLSR

$$\boldsymbol{t_{1meas}} = \widetilde{\boldsymbol{X}}_{\boldsymbol{meas}}\boldsymbol{P} \tag{3.13}$$

4. Calculate predicted concentration

$$\boldsymbol{c_{pred}} = \boldsymbol{t_{1meas}}\boldsymbol{b} \tag{3.14}$$

The root mean square error of prediction (RMSEP) can be used to check the predictive capability of the model as:

$$RMSEP = \sqrt{\frac{\sum_{i=1}^{n}(c_i - \hat{c}_i)^2}{n}} \tag{3.15}$$

3.8 Calibration of *in situ* Raman probe for solution concentration measurements

Raman spectra of dissolved GLY in deionised water were collected using a Kaiser RamanRxn1 spectrometer system accompanied by a Multi-RXN 1-785 probe with a 785 nm laser and 5.5 mm accessory connected to the iC Raman™ 4.1 software. Different concentrations of GLY-water solutions were prepared at saturation temperatures of 5 – 20 °C (0.159 – 0.228 g/g) using the solubility equation of α-GLY in water provided in Equation (3.16). Raman spectra were collected in the range 100 – 3425 cm^{-1} at 60 s measurement intervals. An exposure time of 20 s provided a good signal-to-noise ratio and high-quality spectra.

$$C = 0.0013 \times 10^{-2} T_{sat}^2 + 0.4324 \times 10^{-2} T_{sat} + 13.651 \times 10^{-2} \tag{3.16}$$

where C is the GLY-water solution concentration and T_{sat} is the saturation temperature. All calibration and validation solutions were prepared in a 500 ml temperature-controlled glass vessel and subsequently recirculated through the SPC mesoscale crystalliser which housed the Raman probe via a specially modified U-shaped bend (see Figure 3.8 (a)). The location of the Raman immersion probe in the modified U-shaped bend caused no significant disruption of flow within the SPC mesoscale crystalliser, as only the tip of the probe head (sapphire crystal) needed to be immersed in the flow. An FBRM probe was fitted in the glass vessel to detect complete dissolution of GLY in water. For each concentration, stepped linear cooling in the range 30 – 5 °C (see Figure 3.7) was implemented over a period of 150 min in the SPC mesoscale crystalliser to capture the effect of temperature on the spectra collected. The temperature range for calibration was the working range for all cooling crystallisation experiments in the SPC mesoscale crystalliser. Solution temperature was measured by a 1.5 mm diameter K-type thermocouple (accuracy of $\pm$1.5 °C) inserted into the sample port close to the Raman probe (Figure 3.8 (a)).

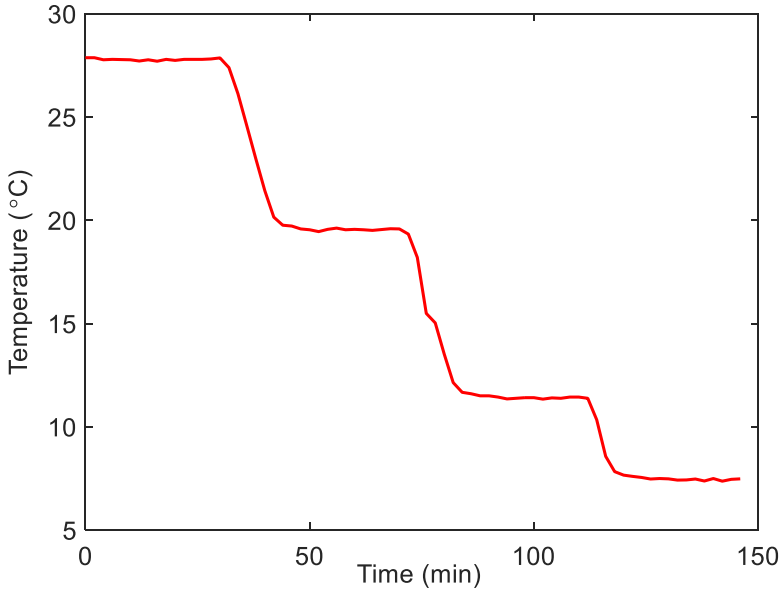

Figure 3.7 Temperature profile implemented in calibration experiments.

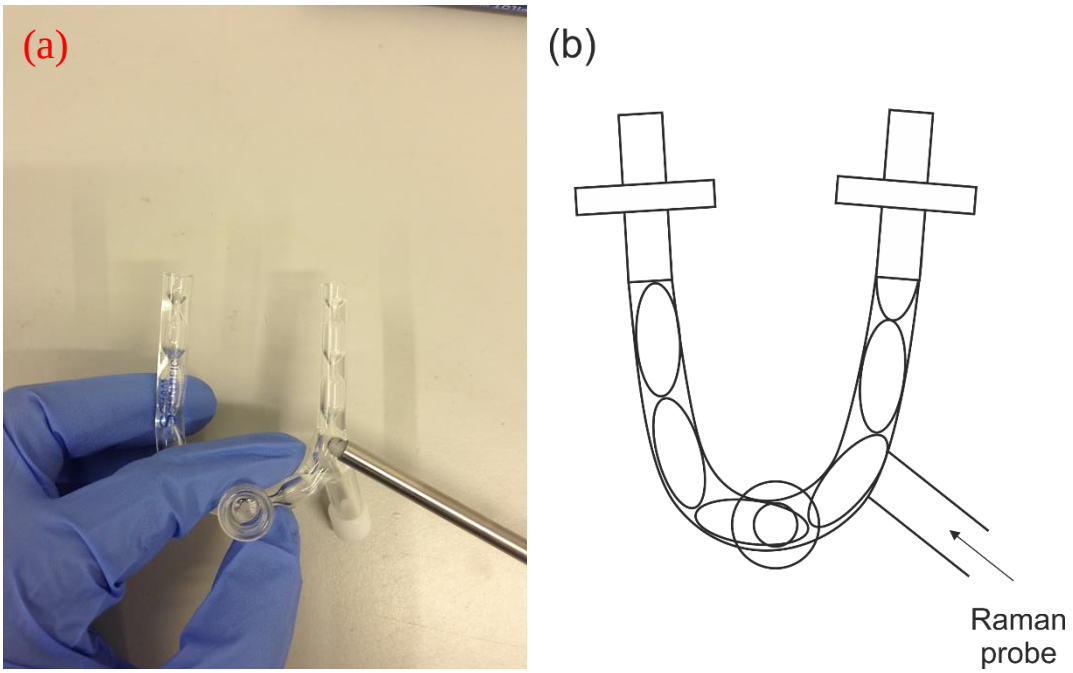

Figure 3.8 (a) modified U-shaped glass bend for Raman immersion probe (b) Schematic of modified U-shaped glass bend showing where Raman probe is inserted.

Figure 3.9 shows the collected Raman spectra of 0.181 g/g GLY-water solution with the strong GLY bands labelled. Overall, temperature did not have a strong effect on Raman intensity in the fingerprint region (150 – 1890 cm^{-1}); an increase in temperature only caused slight decrease of peak intensities in the high frequency region of the spectra (>3000 cm^{-1}), with no peak shifts occurring. A total of 273 calibration standards and 40 solids-free validation standards were used in development of

the calibration model. 4 GLY solution concentrations were included in the calibration data set: 0.228, 0.204, 0.181, and 0.159 g/g. Two validation experiments were performed using concentrations that were not included in the calibration data set: 0.167 g/g (saturated at 7 °C) and 0.214 g/g (saturated at 17 °C) at temperatures of 15 and 10 °C respectively. Two validation standards were chosen at concentrations wide apart in the calibration range and were sufficient to check for linearity of the concentration predictions.

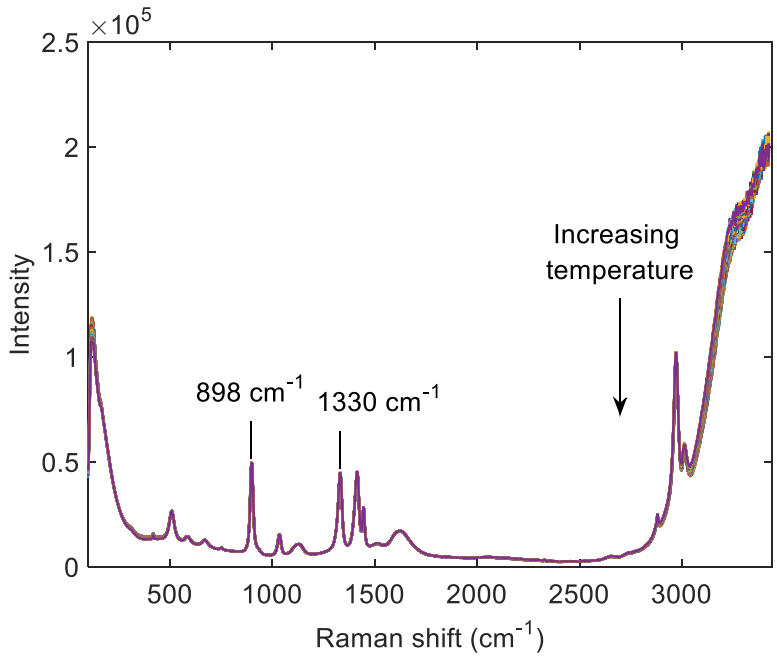

Figure 3.9 Raman spectra of 0.181 g/g GLY-water solution captured in temperature range of 30 – 5 °C showing the strong GLY bands at 898 and 1330 cm^{-1}. Temperature has negligible effect on Raman intensity in fingerprint region (150 – 1890 cm^{-1}).

For spectral pre-processing, mean centring on the mean reference spectra was applied for scatter correction on the Raman signal. Partial least squares regression (PLSR) was used in building the calibration model and a total of five factors were applied, which were sufficient to explain over 95% of the variation between the spectral and concentration data (see Figure 3.10).

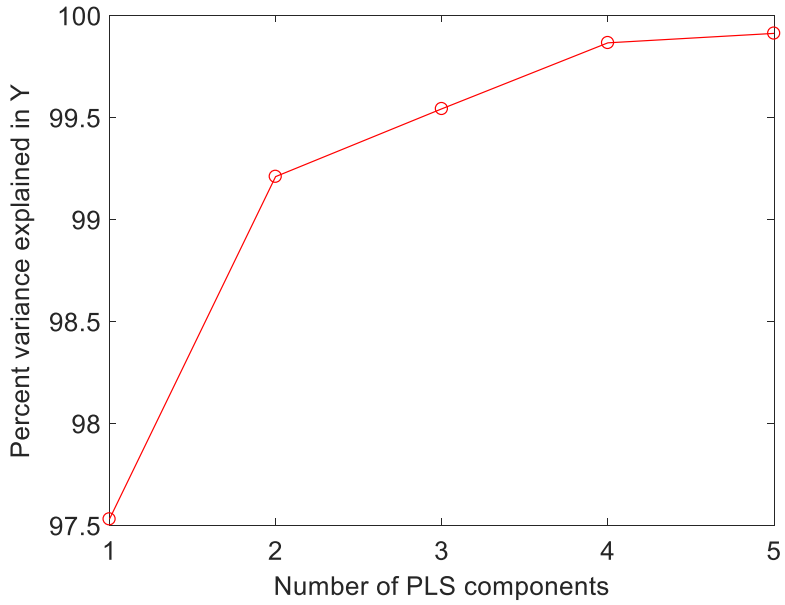

Figure 3.10 Relationship between PLS factors and percent variation spectral data.

Figure 3.11(a) and Figure 3.11(b) show the final PLS model and residual plot for the Raman concentration calibration respectively. A stepwise regression was carried out to identify the subset of independent variables (wavenumbers) with the strongest relationship to the response (concentration) across the temperature range, and a total of 234 wavenumbers between 119 – 3403 cm^{-1} were selected to be included in the model. In each step of the regression, a variable was considered for addition to the set of independent variables based on a prespecified criterion, in this case the strongest relationship to the response. Using a forward selection, no variables were included in the model at the start. Subsequently the addition of each variable was tested using the chosen model fit criterion. A variable that gave the most statistically significant improvement of the fit was included in the model, and this process was repeated until no variable improved the model to a statistically significant extent. The maximum error between the actual concentration and predicted concentration was 1.7%, a highly accurate result. The PLS RMSEP between the calibration and validation data was 0.0017 g/g. All data pre-processing, model development, validation, and prediction were carried out in MATLAB® 2016 software using script files adapted to the calibration experiments.

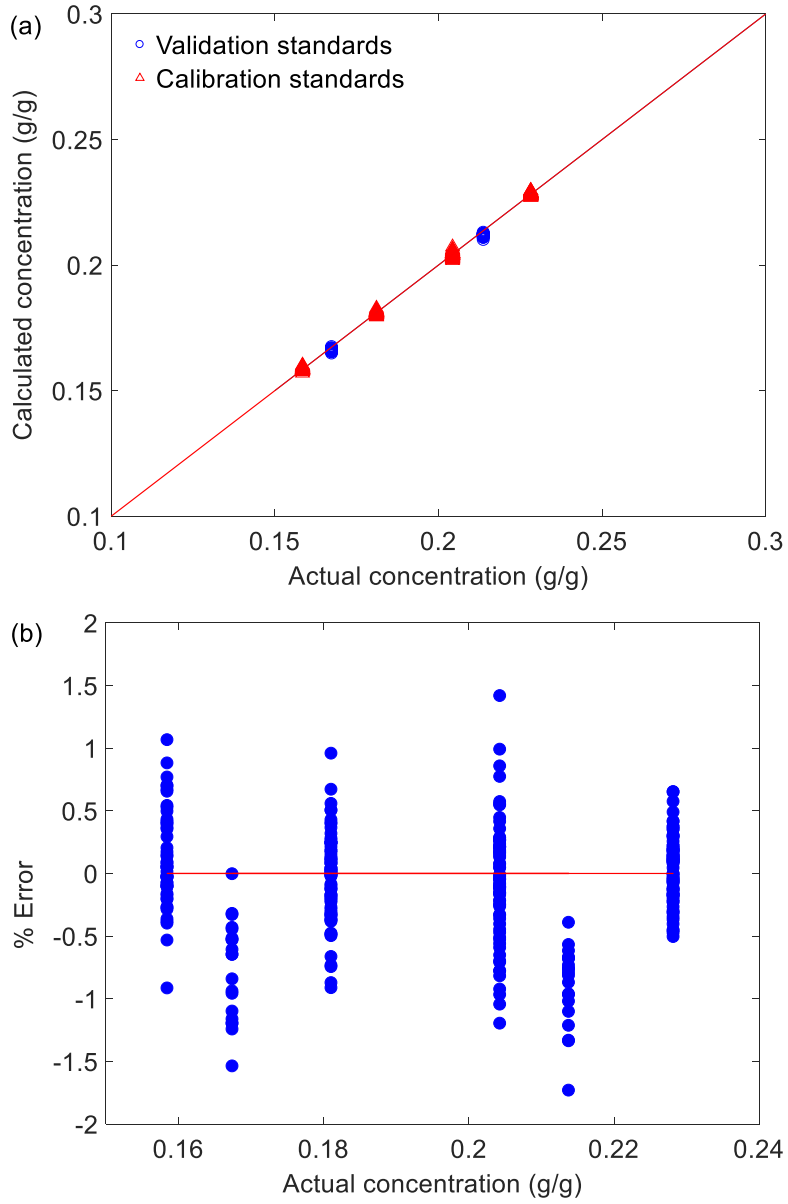

Figure 3.11 (a) PLS model and (b) residual plot for Raman concentration calibration.

3.9 Experimental methods for liquid and solid phase axial dispersion performance of the SPC mesoscale crystalliser

3.9.1 Non-invasive dual backlit imaging technique for liquid and solid RTD measurements

A dual backlit imaging technique was developed for investigating the solid-liquid axial dispersion performance of the SPC mesoscale crystalliser. Backlit imaging is a non-invasive technique that utilises a high-resolution camera to record images of objects which are suspended and transported in flow through an SPC meso-tube. Figure 3.12 shows the schematic for the dual backlit imaging

technique used for RTD measurements in the SPC mesoscale crystalliser. The setup consisted of a box enclosure constructed around a measurement point on an SPC meso-tube to exclude stray light. Each measurement point was backlight by an AC-powered LED light source to provide an even illumination and aid image visualisation in the SPC meso-tube. A HD camera consisting of a Carl Zeiss® lens with 15 megapixels (MP) photo capture, was placed ~1 cm from the wall of SPC meso-tube to maximize the magnification of a single inter-constriction cavity. The HD camera was connected via USB 2.0 to a PC running YAWCAM 0.4.1 software which enabled simultaneous image capture and storage on a computer drive.

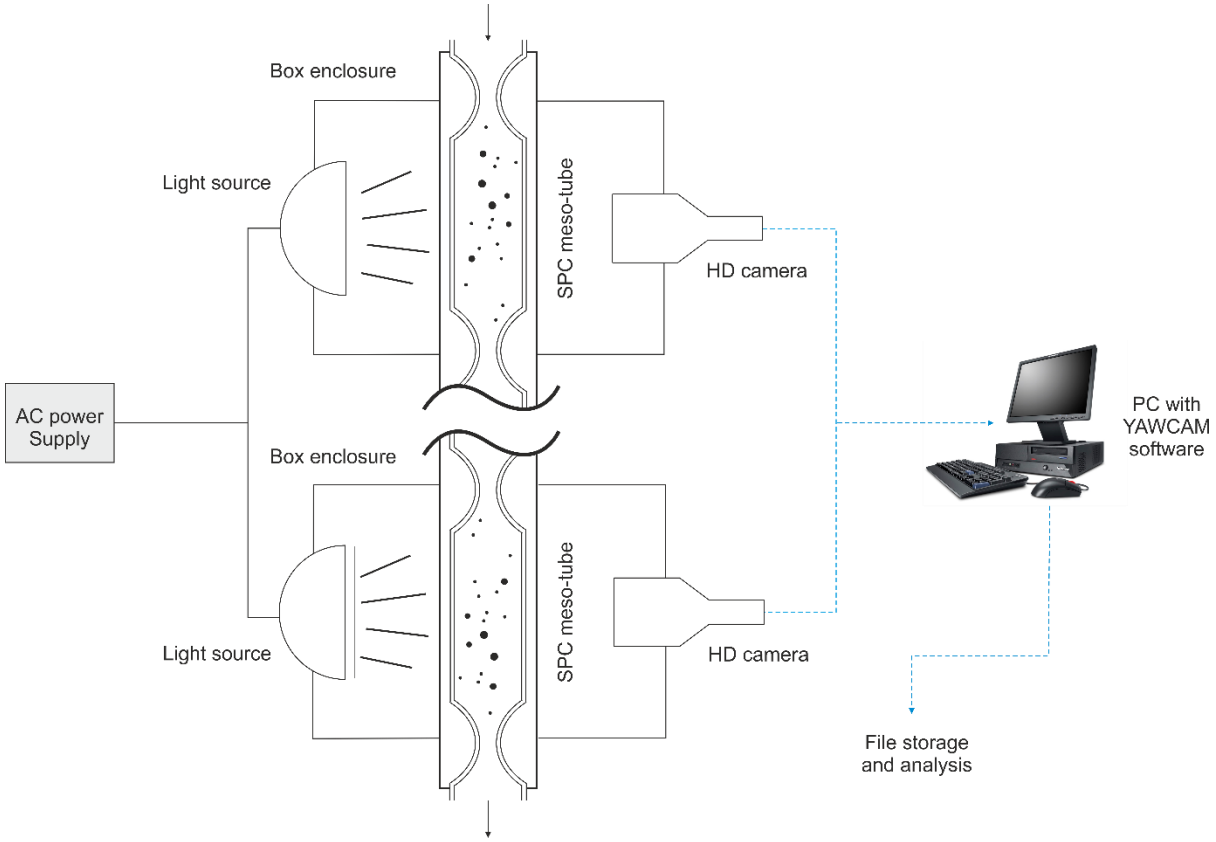

Figure 3.12 Schematic of data acquisition for dual backlit imaging technique.

Two HD cameras (Logitech® HD Pro C920) with 1080p resolution (labelled Cam A and Cam B) were mounted at separate measurement points along the SPC mesoscale crystalliser (see Figure 3.13) to enable RTD determination by the imperfect pulse method (see section 3.9.6). For RTD measurements in the SPC mesoscale crystalliser, a pulse of coloured dye (or a slug of particles) is injected upstream of a first camera, and then flows past a second camera downstream, experiencing a degree of axial dispersion. The images from each camera can be converted to give an input and output

time history of the concentration of dye or particles, from which the liquid or solid phase RTD can be deduced.

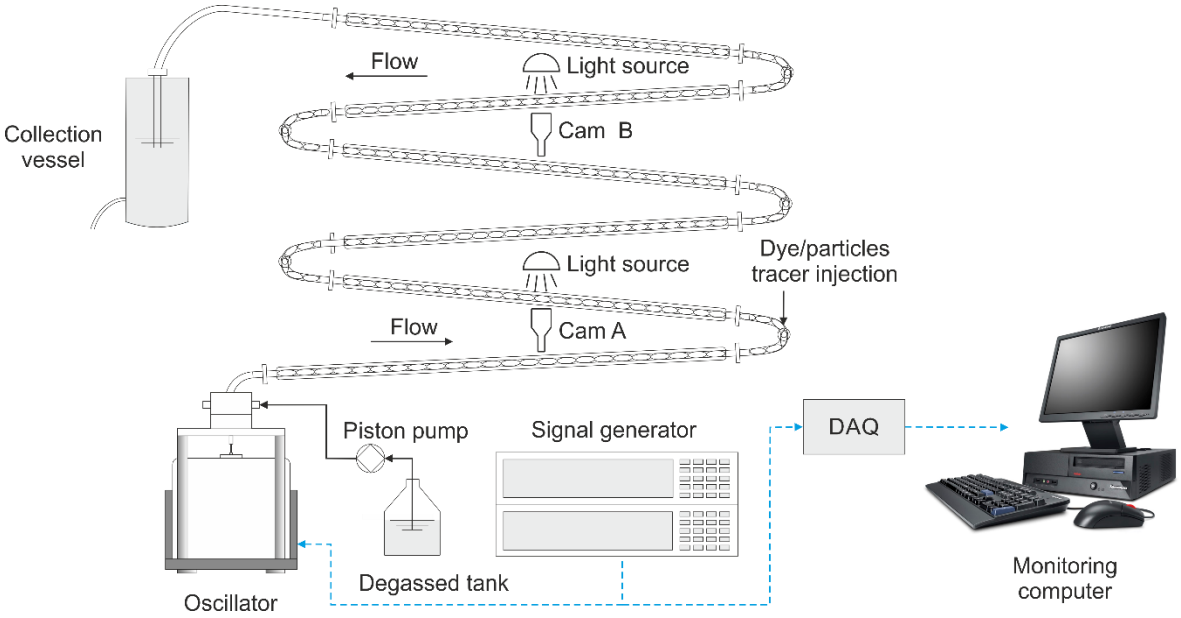

Figure 3.13 Experimental set-up for liquid and solid phase RTD measurements in the SPC mesoscale crystalliser using a non-invasive dual backlit imaging technique (not drawn to scale).

3.9.2 Image analysis for the dual backlit imaging technique

Figure 3.14 shows an example sequence of grayscale images captured from Cam A for a solid RTD experiment using a slug of polystyrene particles. Captured images were stored and processed using a script developed in MATLAB® 2013. True colour images (RGB) from both HD cameras were converted to grayscale images by the MATLAB script.

Each grayscale image had an array of 480 × 640 pixels, and each pixel contained a numerical value for a grayscale intensity ranging from –128 (black) to +127 (white). All grayscale images were cropped into 250 × 110-pixel target images focused on a single backlit cavity in the SPC meso-tube as a region of interest (ROI) (see Figure 3.14), and an average grayscale intensity was calculated for each frame. The background contained information about the camera noise and grayscale intensity observed for the clear liquid and glass wall only. The background was therefore taken as the baseline for normalisation. RTD information was extracted from recorded images in the form of absorbance-time curves. For liquid and solid phase studies, a slug of particles or pulse of coloured dye in water will effectively decrease the intensity of the transmitted beam to the camera in accordance with Beer-Lambert's law:

$$I = I_0 \exp(-\epsilon c l_p) \tag{3.17}$$

where ϵ is the light-scattering cross-section of a particle or wavelength-dependent molar absorptivity coefficient (M^{-1} cm^{-1}), I is the intensity (W m^{-2}) of light transmitted through the suspension or dye (measured intensity), I_0 is the incident light intensity (W m^{-2}), c is the particle or dye concentration (g ml^{-1}), and l_p is the optical path length (m).

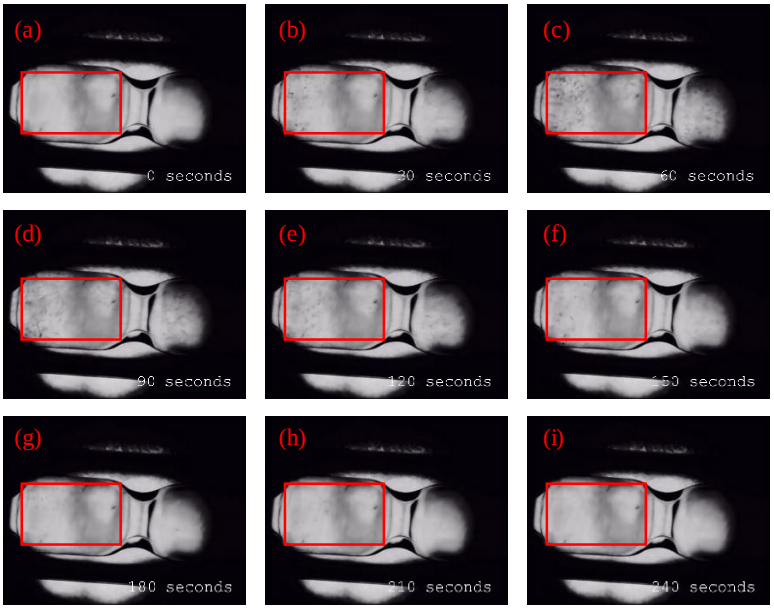

Figure 3.14 Sequence of grayscale images captured from Cam A. $x_0 = 0.5$ mm, $f = 10$ Hz, $Re_n = 21$. Red rectangles indicate the region of interest (ROI) from which grayscale intensities were calculated. From (a) – (i): $t = 0$ s, 30 s, 60 s, 90 s, 120 s, 150 s 180 s, 210 s, 240 s.

Absorbance-time curves for the liquid and solid phase studies were calculated by taking the log of the grayscale intensity to be proportional to concentration according to Equation (3.18):

$$abs = -log\frac{I}{I_0} \tag{3.18}$$

where abs is the absorbance of the species. Both HD cameras were pre-calibrated and returned a linear relationship between measured absorbance and concentration with $R^2 = 0.9979$ for Cam A and 0.9949 for Cam B in the entire range of experiments. The different gradients exhibited by the calibration curves in Figure 3.15 were due to different path lengths of the HD cameras.

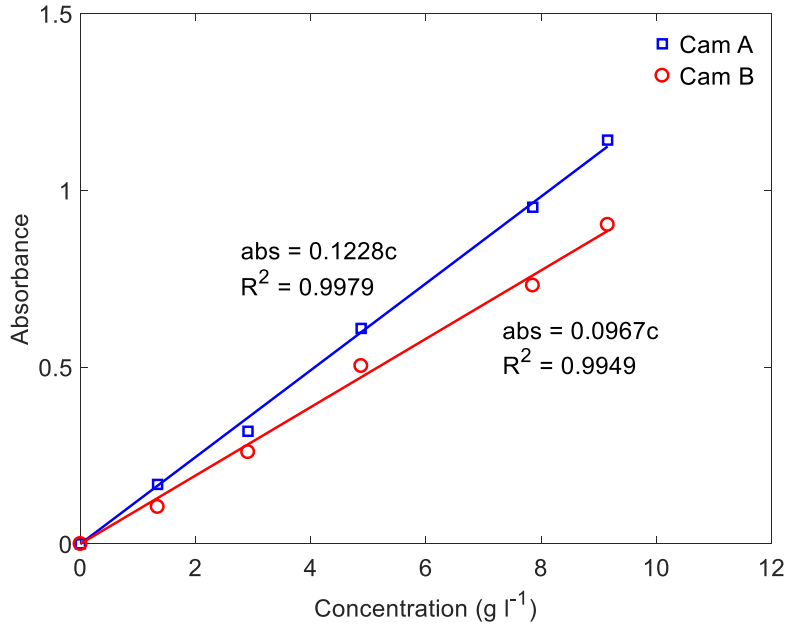

Figure 3.15 Linear relationship established between absorbance (abs) and concentration (c) for both HD cameras.

3.9.3 Dual backlit imaging technique versus traditional conductivity measurement

Initial experiments were performed to evaluate the newly developed non-intrusive imaging technique (see section 3.9.1) against traditional intrusive conductivity measurement for liquid RTD determination. The evaluation criteria were the values of hydrodynamic parameters obtained by both methods i.e. axial dispersion number, mean residence time, and mean axial velocity, as well as the reproducibility of each method for replicated experiments.

For salt tracer injection and response experiments, a pair of calibrated Mettler Toledo InLab® 751-4mm conductivity probes were positioned 2.691 m apart and immersed perpendicular to the flow in the sample ports located at the U-shaped glass bends (see Figure 3.16). The calibration curve for both probes showed a linear relationship with molarity (see Figure 3.17) For dye tracer experiments, two HD cameras were mounted at separate measurement points 2.691 m apart along the SPC mesoscale crystalliser using a traversing platform (see Figure 3.16).

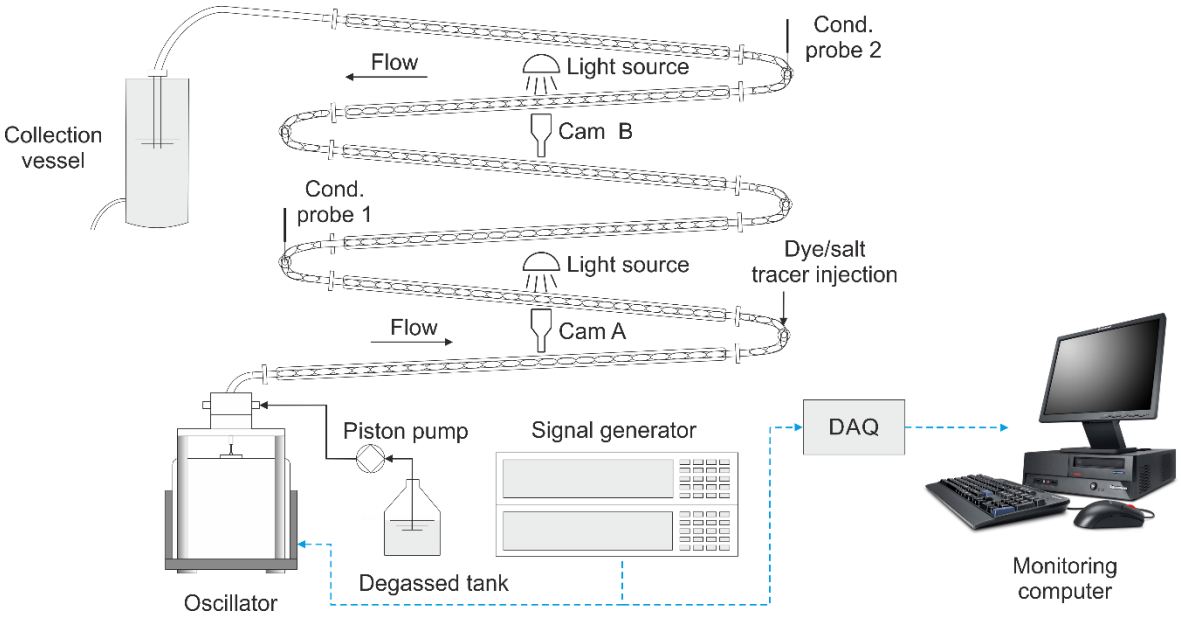

Figure 3.16 Experimental set-up for RTD measurements in the SPC mesoscale crystalliser using the dual backlit imaging technique and traditional conductivity measurements (not drawn to scale).

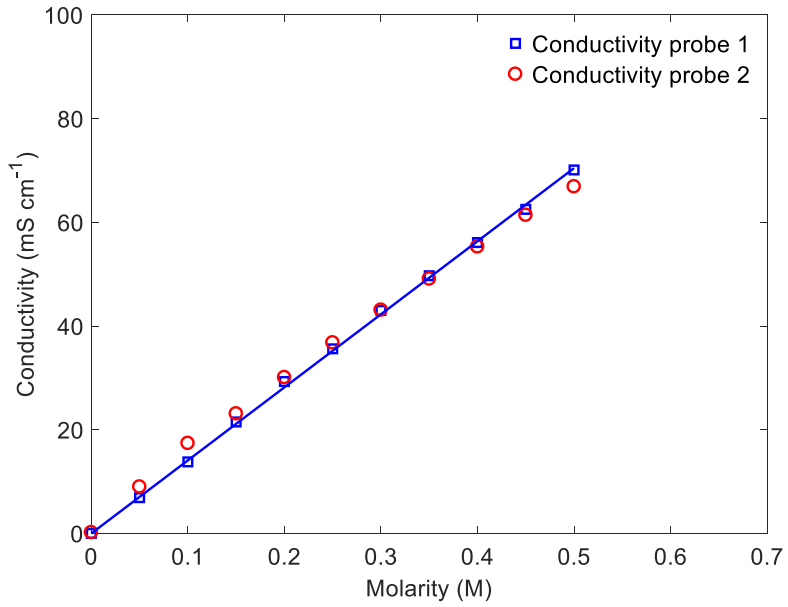

Figure 3.17 Linear relationship established between conductivity and molarity for both conductivity probes.

All experiments were carried out at a room temperature of 20 °C and a net flow of 5 ml min^{-1} (Re_n = 21). The range of frequencies investigated was f = 2 – 12 Hz at a fixed x_0 of 0.5 mm. Before performing an experiment, it was ensured that the SPC mesoscale crystalliser was filled with water and completely bubble-free. Degassing of the system was achieved by operating at $x_0 \geq 2$ mm, $f \leq 2$ Hz to create a sweeping motion through the inter-constriction cavities. The 10 ° inclination of the SPC mesoscale crystalliser aided bubble washout.

At $t = 0$ for salt tracer experiments, a pulse of 0.2 ml containing 0.05 M NaCl with a density of 0.9994 g cm^{-3} (Hai-Lang and Shi-Jun, 1996) was injected by hand into the tracer injection port (see Figure 3.16) in <1 s using a 1 ml syringe. A conductivity meter connected to both probes recorded data at a 1 s interval and was stopped once the conductivity reading returned to background level. During conductivity measurements, the response time of both probes was instantaneous. The distance between the conductivity probes, L, was subsequently reduced to 0.897 m to observe its effect on liquid axial dispersion. The volume in this shorter test section was measured as 12 ml. At $t = 0$ for dye tracer experiments, a pulse of 0.1 ml containing 3.14 g l^{-1} of Procion Red HE-7B dye with a density of 1.003 g cm^{-3} was injected by hand into the tracer injection port in <1 s using a 1 ml syringe. Both HD cameras started image capture simultaneously at a 1 s interval and were stopped once transmittance visibly returned to background level. A lag time of 0.12 s was detected and corrected for in the analysis. This lag time was due to a delay between image capture by the HD cameras and storage of .jpg files on the local drive by the YAWCAM software. All experiments were performed at least in duplicate for both methods.

3.9.4 Liquid phase RTD studies

An aqueous solution of Procion Red HE-7B was used as the dye tracer for liquid phase RTD studies. This dye was selected for not adsorbing to the meso-tube walls. Degassed deionized water formed the continuous phase and was pumped at a steady net flow from a closed reservoir by a pulsation-free dual piston pump. Prior degassing of the continuous phase was necessary to avoid bubble nucleation and oscillation dampening in the SPC mesoscale crystalliser. From literature, minimum dispersion conditions for mesoscale OFRs occur in the range $x_0 = 0.5 – 3$ mm and $f \leq 12$ Hz (see Table 2.5), therefore the continuous phase was oscillated at the conditions $x_0 = 0.5$, 1.0, 2.0 mm and $f = 2$, 4, 6, 8, 10, 12 Hz giving an investigated mixing range of $Re_o = 31 – 740$. Experiments were performed at 2 and 5 ml min^{-1} ($Re_n =$ 8.2 and 21) to compare with data previously obtained by Zheng and Mackley (2008) at similar net flows ($Re_n =$ 10 and 19) for the same mesoscale OFR. These volumetric flow rates corresponded to superficial axial velocities of 2.48×10^{-3} m s^{-1} and 6.19×10^{-3} m s^{-1} respectively in the SPC mesoscale crystalliser. For the SPC meso-tube in which the cross-sectional area varies, the superficial velocity, u, was determined for a mean internal diameter of 4.14 mm. The mean internal diameter for an SPC meso-tube was calculated using Equation (3.19):

$$D_{mean} = 2\sqrt{\frac{V_{SPC}}{\pi L_{SPC}}} \tag{3.19}$$

where V_{SPC} is the measured volume in an SPC meso-tube with a length, L_{SPC}, of 727 mm. Cam A was mounted at measurement point 1, 0.490 m downstream of the tracer injection point (see Figure 3.13). Cam B was mounted at measurement point 2, located 3.181 m downstream of the injection point to give L of 2.691 m (axial distance between measurement point 1 and 2), having a volume of 35 ml. All experiments were carried out at room temperature of 20 °C. Before performing an experiment, it was ensured that the SPC mesoscale crystalliser was filled with water and completely bubble-free. At $t = 0$, a pulse of 0.1 ml containing 3.14 g l^{-1} of dye was injected by hand into the tracer injection port in $<$1 s using a 1 ml syringe.

Different tracer concentrations were tested initially, however lower concentrations were quickly dispersed and too dilute to be detected by the HD cameras. Very high concentrations were too dense, causing excessive tailing in the concentration profiles. An intermediate concentration with a density closer to water (1.003 g cm^{-3}) which was detectable by both HD cameras was finally chosen for experiments. Both HD cameras started image capture simultaneously at 1 s intervals and were stopped once transmittance visibly returned to background level. All experiments were performed at least in duplicate.

3.9.5 Solid phase RTD studies

RTD experiments with paracetamol ($\rho_c = 1.26$ g cm^{-3}) were attempted to study the effects of crystal size, density, and shape on the solid phase axial dispersion. Unfortunately, the sticky paracetamol crystals adhered to the walls of the SPC meso-tube, causing excessive tailing and multi-modal C-curves. Polystyrene particles were chosen for solid phase RTD studies as they had a particle density ($\rho_p = 1.1$ g cm^{-3}) which was close to that of paracetamol crystals. Also, a d_{50} of 70 µm was not far off from the typical mean size of paracetamol crystals obtained from a cooling crystallisation process (Saleemi et al., 2013; Powel et al., 2015). A 0.5 ml slug containing a 2 g ml^{-1} (67% w/w) aqueous suspension of polystyrene particles was injected at $t = 0$ in $<$1 s through the tracer injection port to mimic a stream of particles flowing through the SPC mesoscale crystalliser. Figure 3.18 shows the spherical nature of the polystyrene particles. The maximum steady-state settling velocity, u_p, of the particles was calculated as 0.0044 m s^{-1} using Equation (3.20):

$$u_p = \sqrt{\frac{4}{3}\frac{1}{C_D} g d_p \left(\frac{\rho_p - \rho}{\rho_p}\right)} \tag{3.20}$$

where ρ_p is the density of the particles (kg m^{-3}), ρ is the density of the bulk fluid (kg m^{-3}), g is the acceleration due to gravity (m s^{-2}), d_p is the mean diameter of the particles (m), and C_D is the drag coefficient, which has a value of 2.48 at $Re_n = 21$ (Bird et al., 2007). The oscillatory range investigated was determined from the results of liquid phase RTD measurements. HD cameras mounted at measurement points 1 and 2 were used for image capture at 1 s intervals and stopped once transmittance returned to its background value. All experiments were performed at least in duplicate, and at room temperature of 20 °C.

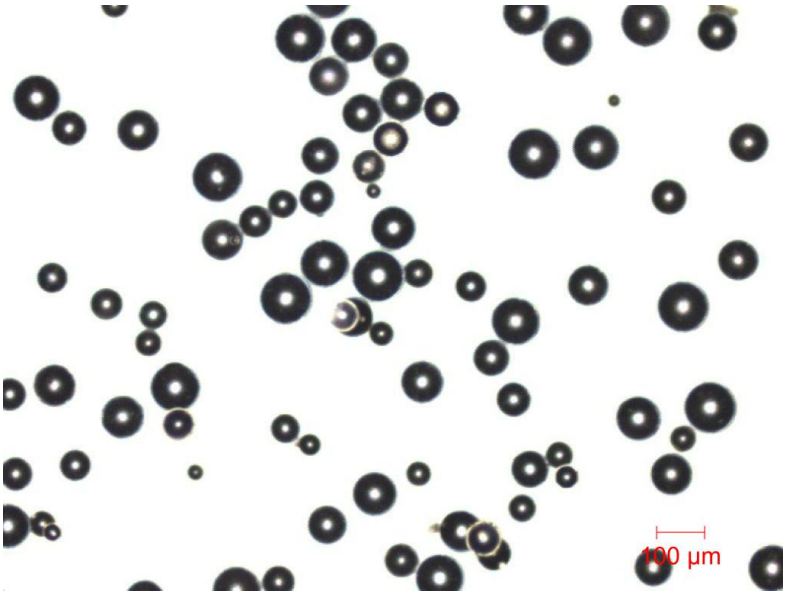

Figure 3.18 Microscope image of spherical polystyrene particles.

3.9.6 Determination of axial dispersion coefficient

All experimental data were fitted to a plug flow with the axial dispersion model (Levenspiel and Smith, 1957). This model was chosen for its capability to capture the intermediate backmixing state expected for the constricted SPC mesoscale crystalliser when operated at different oscillatory flow conditions (Reis et al., 2010). It is therefore suitable for describing the degree of deviation of the SPC mesoscale crystalliser from true plug flow behaviour. The axial dispersion coefficient, D_{ax}, is a measure of the degree of deviation from true plug flow behaviour. In the imperfect pulse method of

the axial dispersion model (Bischoff and Levenspiel, 1962), a tracer is introduced into the flow and a pair of measurement devices (i.e. HD cameras or conductivity probes) detect the upstream and downstream concentration-time history of a tracer, since the input tracer pulse may be far from a perfect Dirac delta function (Levenspiel, 1999) which is very difficult to achieve experimentally. In the section between the two measurement devices, the tracer is further dispersed, so that the concentration-time history detected by the downstream probe is time-shifted and distorted, compared to that detected by the upstream measurement device. For a fixed distance between the upstream and downstream measurement point, the amount of spreading depends on the intensity of dispersion in the system, and this spread can be used to characterise quantitatively the dispersion phenomenon. The imperfect pulse method effectively convolutes the input function from the upstream probe with an axial dispersion model and fits the response to the downstream output function by adjusting the model parameters. The benefit of this method is that the input signal initial shape is arbitrary.

In this analysis it is assumed that the axial dispersion model may be applied to any section of a flow to estimate the local liquid or solid dispersion coefficient. The axial dispersion model describes the mixing behaviour by superimposing one-dimensional axial dispersion onto convective plug flow. The effect of any radial velocity gradients is lumped into the axial dispersion coefficient, as demonstrated by Taylor (1953; 1954). In dimensionless form, the axial dispersion model is represented by the following differential equation:

$$\frac{\partial C^*}{\partial \theta} = \left(\frac{D_{ax}}{uL}\right)\frac{\partial^2 C^*}{\partial z^{*2}} - \frac{\partial C^*}{\partial z^*} \tag{3.21}$$

where $C^* = \frac{(C-C_i)}{\int_0^\infty (C-C_i)dt}$ = dimensionless concentration for tracer (3.22)

$$z^* = \frac{z}{L} = \text{dimensionless length} \tag{3.23}$$

$$\theta = \frac{t}{\tau} = \text{dimensionless time} \tag{3.24}$$

τ is the characteristic time or mean residence time in the test section under consideration. C_i is the initial concentration of species (g l^{-1}) and C is the concentration at any measured time t (s). u is the mean axial velocity (m s^{-1}), z is the position along the axial length (m), L is the length of the test section (m). For the pulse experiment employed, the usual normalisation is to set the initial baseline value to zero and then to divide by the integral of the concentration. The estimates of the degree of liquid and

solid backmixing are so described by the dimensionless axial dispersion number, D_{ax}/uL, and a convective time scale:

$$\tau = L/u \tag{3.25}$$

The dispersion number characterises axial dispersion as the liquid or solid circulates once through the section in terms of an effective dispersion coefficient, D_{ax} (m^2 s^{-1}). This parameter represents axial dispersion in an analogous manner to the way in which molecular diffusivity, as used in Fick's law, represents molecular transport. The value of the dispersion number expresses the degree of axial mixing; if the dispersion number approaches zero, the region's mixing behaviour is close to plug flow, whereas, for large dispersion numbers, the zone is well-mixed. According to Levenspiel (1999), a $D_{ax}/uL > 0.01$ indicates a large deviation from plug flow, while $D_{ax}/uL < 0.01$ indicates a small deviation from plug flow.

The solution of Equation (3.21) depends on the boundary conditions at the inlet and outlet of the fluid section. The *open-open* boundary condition corresponds most closely to the experimental situation here. This means that there is continuity of both the tracer flux and concentration profiles across the boundaries (marked by the position of the measurement devices), which from a physical point of view, is a valid assumption. An advantage of the axial dispersion model is that subject to *open-open* boundary conditions, it can be solved analytically. The solution of Equation (3.21), for an initial Dirac delta function and with *open-open* boundary conditions, was obtained by Levenspiel and Smith (1957):

$$C^*(\theta) = \frac{1}{\sqrt{4\pi(D_{ax}/uL)}}\exp\left[-\frac{(1-\theta)^2}{4\theta(D_{ax}/uL)}\right] \tag{3.26}$$

To study liquid and solid phase dispersion in an individual section of the flow, the imperfect pulse technique is applied, whereby data sets taken from two measuring points a fixed distance, L, apart are compared, and the input signal initial shape is arbitrary. For a linear system, the output response, $C_1^*(\theta)$, can be determined from the convolution integral of the inlet, $C_0^*(\theta)$, and the system transfer function, $M(\theta)$:

$$C_1^*(\theta) = \int_0^\infty M(\theta)C_0^*(\theta - \theta')d\theta \tag{3.27}$$

Using $M(\theta)$, an output signal can be predicted for any arbitrary continuous input signal. The system transfer function is the response to a Dirac pulse; in the case of the axial dispersion model, $M(\theta)$ is given by Equation (3.26). The results of the convolution integral can then be fitted to the measured output concentration-time history, by adjusting the two model parameters τ and D_{ax}/uL. Once the best-fit parameters have been found, D_{ax} may be calculated using Equations (3.28) and (3.29):

$$u = \frac{L}{\tau} \tag{3.28}$$

$$D_{ax} = \left(\frac{D_{ax}}{uL}\right)\frac{L^2}{\tau} \tag{3.29}$$

Previous work by Palma and Giudici (2003) has shown that fitting more than one model parameter gives values of axial dispersion coefficient that are more reliable than when D_{ax} is the only fitted parameter.

3.9.7 Parameter estimation method

Hydrodynamic parameter estimation was performed by convoluting in the frequency domain and fitting in the time domain, since it gives nearly the same accuracy as time domain convolution (Verlaan et al., 1989; Obradovic et al., 1997). Also, complex numerical calculations can efficiently be performed computationally using Discrete Fourier transformation (DFT). An algorithm of the method is provided in Figure 3.19, where an overbar denotes a Fourier transform in the frequency space, ω. After the tracer input signal has been normalised to give $C_0^*(\theta)$, its Fourier transform is calculated using the Fast Fourier Transformation (FFT) method which is a form of DFT. The model output concentration is then obtained by multiplying, in the frequency domain, the model transfer function and the experimental input concentration. According to the convolution theorem, the result of this product in the frequency domain is the Fourier transform of the convolution integral:

$$\int_{-\infty}^{\infty} M(\theta)C_0^*(\theta-\theta')d\theta \;\Leftrightarrow\; \overline{C_0^*}(\omega)\overline{M}(\omega) \tag{3.30}$$

where ⇔ denotes a transform pair. The calculated output concentration is then converted back into the time domain by inverse Fourier transformation (inverse FFT); it is subsequently fitted, in the time domain, to the measured output, by adjusting the characteristic time, τ, and the dispersion number, D_{ax}/uL, in the transfer function. The optimum D_{ax}/uL, τ combination is that which minimises the residual sum of squares (RSS) between model and experiment.

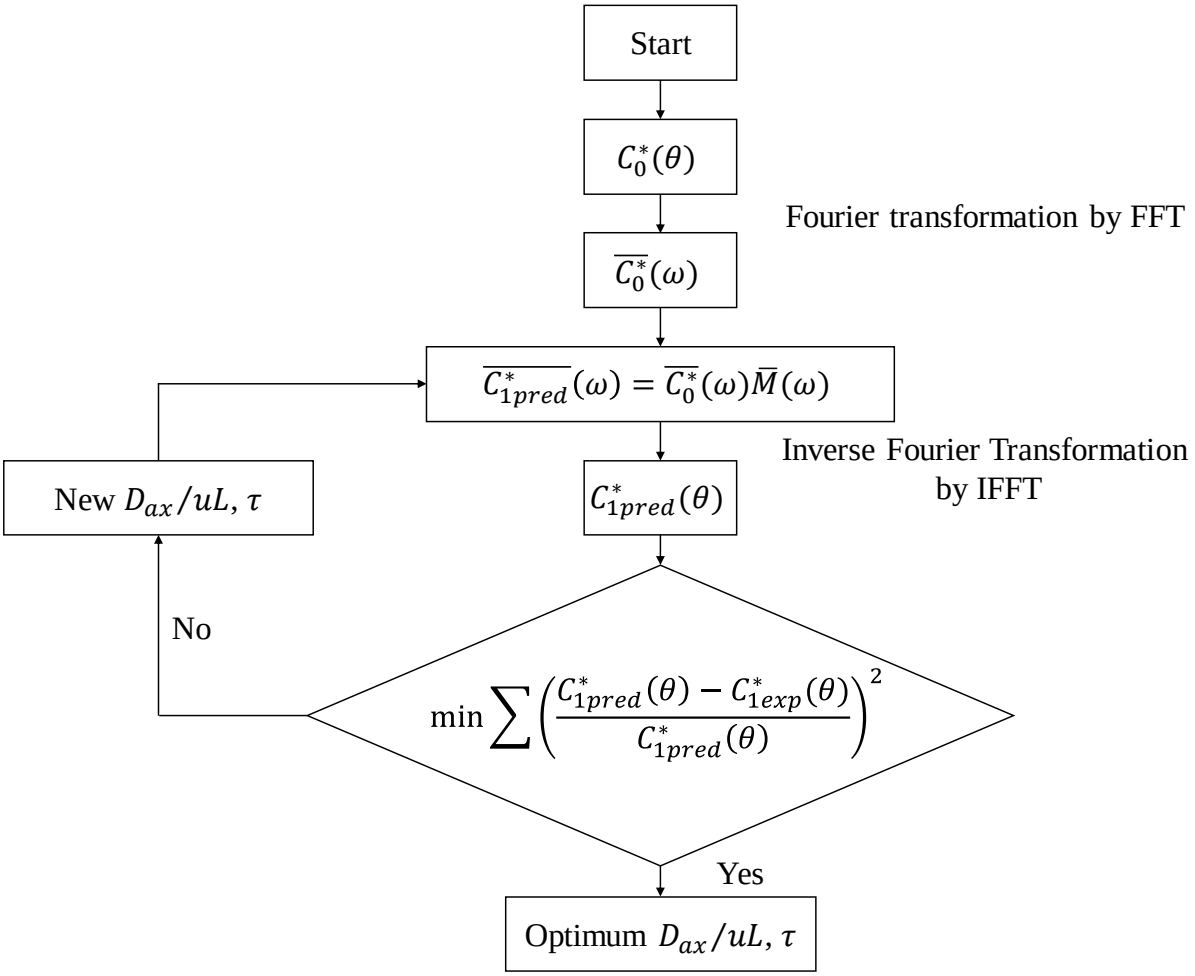

Figure 3.19 Algorithm for the parameter estimation method with convolution in the frequency domain and fitting in the time domain (adapted from Obradovic et al., 1997).

3.9.8 Model implementation

A MATLAB script was written based on the algorithm shown in Figure 3.19 to determine automatically the model parameter giving the best fit between the measured and modelled output signals. An unconstrained optimisation function *fminunc* was used to perform the fitting of the two model parameters with bounds for the parameter searching and starting guesses based on the space time between the measurement points.

3.10 Theory and experimental methods for the heat transfer characteristic of the SPC mesoscale crystalliser

3.10.1 Tube-side Nusselt number determination

The Nusselt number describes the magnitude of convective heat transfer occurring parallel to the surface normal of the boundary layer, and perpendicular to the mean fluid flow within a tube. In other words, it is the ratio of convective heat transfer to conductive heat transfer. Heat transfer performance can be determined by evaluating the dimensionless tube-side Nusselt number, Nu_t, as follows:

$$Nu_t = \frac{h_t D_{1im}}{k_1} \tag{3.31}$$

D_{1im} is the mean internal diameter of the SPC meso-tube given as $2\sqrt{\frac{V_{L1}}{\pi L_1}}$, where L_1 is the active tube length (m) for heat exchange, and V_{L1} is the measured volume in the active tube length (m^3). k_1 is the thermal conductivity of the process fluid (W m^{-1} K^{-1}), and h_t is the tube-side heat transfer coefficient (W m^{-2} K^{-1}). A D_{1im} of 4.24 mm was calculated for the SPC meso-tube due to its undulating internal surface. D_{1im} was used in calculations for Re_n, Re_o, St, and mean velocity, u_m. Nu_t can be determined from measured overall heat transfer coefficient, U_{21} (referred to the outside area of the inner tube), given by Equation (3.32) (Stephens and Mackley, 2002):

$$\frac{1}{U_{21}} = \frac{1}{h_t} + \frac{D_{1im}\ln(D_{1o}/D_{1im})}{2k_g} + \frac{D_{1im}}{D_{1o}h_a} \tag{3.32}$$

where k_g is the thermal conductivity for the inner tube wall material (glass) (W m^{-1} K^{-1}), D_{1o} is the outer diameter of the inner tube (m), h_a is the heat transfer coefficient in the annulus (W m^{-2} K^{-1}), and U_{21} is the overall heat transfer coefficient (W m^{-2} K^{-1}) between the cooling and process fluids. U_{21} is related to heat flux or heat transfer rate as follows:

$$Q_1 = AU_{21}\Delta T_{lm} = \dot{m}_1 C_{p1}\Delta T_1 \tag{3.33}$$

where ΔT_{lm} is the log mean temperature difference (LMTD) of the heat exchanger (temperature driving force), ΔT_1 is the temperature difference of the process fluid over the length of the heat exchanger, $\dot{m}_1$ is the mass flow rate of the process fluid, and A is the outside heat transfer area of the inner tube. The outside heat transfer area of the inner tube was determined as 0.011 m^2 using Equation (3.34) below:

$$A = n_{L1}(A_c + A_s) \tag{3.34}$$

where A_c is the area of a 4 mm-long constriction outer surface estimated by numerical integration, A_s is the area of a 9 mm-long outer straight surface of the inner tube (see Figure 3.2), and n_{L1} is the total number of constriction and straight surfaces in the active length which is 51. Table 3.3 lists the specifications of the concentric tube heat exchanger.

Table 3.3 Specifications of concentric tube heat exchanger

Specifications	
Tube outside diameter, D_{1o} (mm)	7.0
Tube mean inside diameter, D_{1im} (mm)	4.2
Jacket external diameter, D_{2o} (mm)	11.0
Jacket internal diameter, D_{2i} (mm)	9.0
Active tube length, L_1 (mm)	657
Total heat transfer area, A (m^2)	0.011
Heat transfer area per unit length, A_{L1}, (m)	0.02
Hydraulic mean diameter in the annulus, $d_h = d_{2i} - d_{1o}$ (mm)	2.0
Material of construction	Glass
Wall thermal conductivity, k_g (W m^{-1} K^{-1})	1.1

The LMTD is calculated using:

$$\Delta T_{lm} = \frac{\Delta T_2 - \Delta T_1}{\ln[\Delta T_2/\Delta T_1]} = \frac{(T_{1out} - T_{2in}) - (T_{1in} - T_{2out})}{\ln[(T_{1out} - T_{2in})/(T_{1in} - T_{2out})]} \tag{3.35}$$

where T_{1in}, T_{1out} are the process fluid inlet and outlet temperatures, and T_{2in}, T_{2out} are the cooling fluid inlet and outlet temperatures respectively. The high flow rate maintained in the annulus provides a much larger heat capacity rate and heat transfer coefficient than that of the process fluid, enabling the cooling fluid to absorb a large quantity of heat with negligible change in its temperature along the

tube. This results in a special case where the temperature of the cooling fluid remains approximately constant throughout the heat exchanger length, and $T_{2in} = T_{2out} = T_w$. Where T_w is the annulus or wall temperature. Substituting into Equation (3.33) gives an equation for U_{21}:

$$U_{21} = \frac{\dot{m}_1 C_{p1} \Delta T_1}{A} \frac{\ln[(T_{1out} - T_{2in})/(T_{1in} - T_{2out})]}{\Delta T_1 + \Delta T_2} \tag{3.36}$$

U_{21} is obtained from experimental data and Nu_t is calculated using Equation (3.37):

$$\frac{1}{Nu_t} = \frac{k_1}{D_{1im}} \left[\frac{1}{U_{21}} - \frac{D_{1im}}{D_{1o} h_a} - \frac{D_{1im} \ln\left(\frac{D_{1o}}{D_{1im}}\right)}{2\kappa_g} \right] \tag{3.37}$$

The Nusselt number in the annulus was estimated using the Dittus Boelter turbulent flow expression (Equation (3.38)). The heat transfer coefficient h_a, was found to be 13,041 W m^{-2} K^{-1} based on the volumetric flow rate of the cooling fluid and it was assumed constant for all experiments conducted. At such high values, minor changes in the heat transfer coefficient were found to have very little effect on the tube-side Nusselt number calculated.

$$Nu_a = 0.023 Re_n^{0.8} Pr^{0.3} \tag{3.38}$$

3.10.2 Heat transfer model for temperature predictions in the SPC mesoscale crystalliser

Figure 3.20 shows a cross-section of a jacketed SPC meso-tube as a concentric tube heat exchanger, in which heat is exchanged across the boundary between a process fluid contained within an inner tube, and a cooling fluid contained in the annulus. The process and cooling fluids flow counter-currently to each other with mass flow rates $\dot{m}_1$ and $\dot{m}_2$ (kg s^{-1}) respectively. $T_1(x)$ and $T_2(x)$ are the temperatures at a distance x in the inner tube and annulus respectively. T_{1in} and T_{1out} are the inlet and outlet temperatures of the process fluid, while T_{2in} and T_{2out} are the inlet and outlet temperatures of the cooling fluid in the annulus.

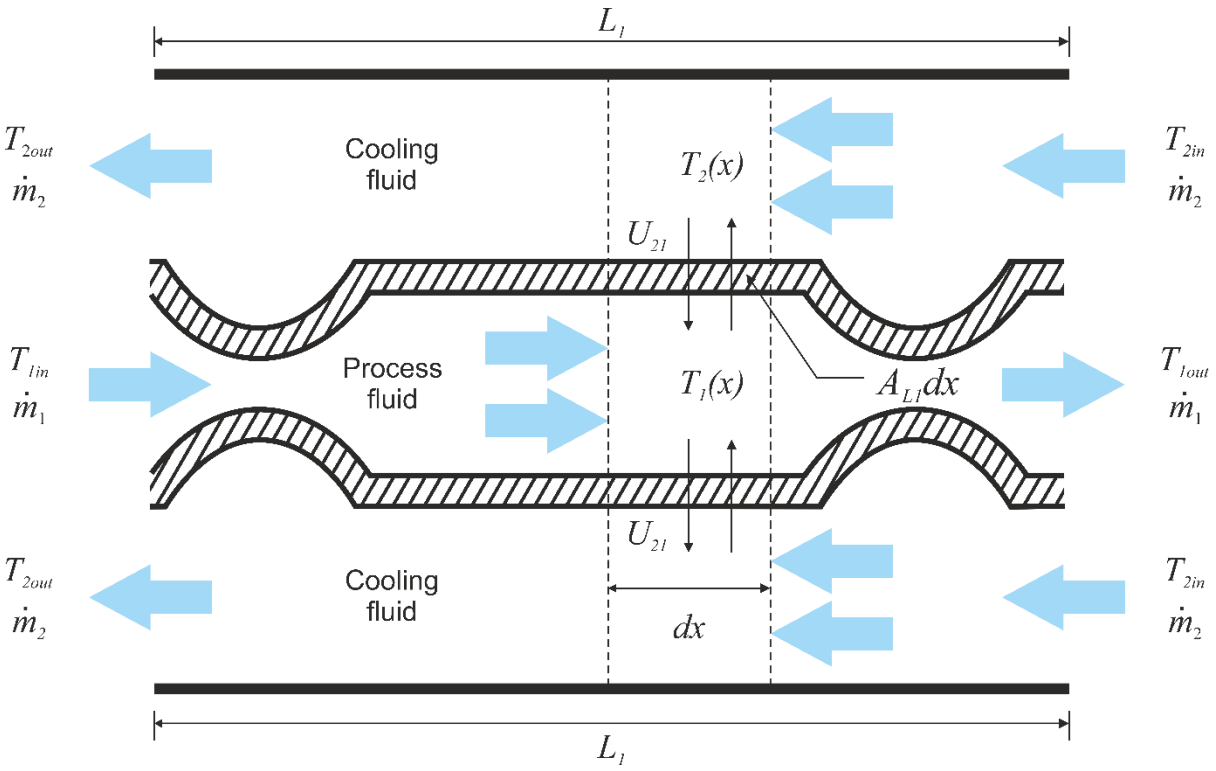

Figure 3.20 Heat exchange process occurring between process and cooling fluids.

Taking a differential length, dx, of this concentric tube heat exchanger, a heat balance can be carried out for the process and cooling fluids that yields Equations (3.39) and (3.40) respectively.

$$\dot{m}_1 C_{p1} \frac{dT_1}{dx} = A_{L1} U_{21} (T_2 - T_1) \tag{3.39}$$

$$\dot{m}_2 C_{p2} \frac{dT_2}{dx} = -A_{L1} U_{21} (T_1 - T_2) \tag{3.40}$$

where C_{p1} and C_{p2} are the specific heat capacities (J kg^{-1} K^{-1}) of the process and cooling fluids respectively, and $A_{L1} = \pi D_{1o}$ is the outside heat transfer area per unit axial length of the inner tube (m). From Figure 3.20,

$$T_1 = T_{1in} \text{ at } x = 0 \tag{3.41}$$

$$T_2 = T_{2in} \text{ at } x = L_1 \tag{3.42}$$

Equations (3.39) and (3.40) are ODEs that can be solved analytically subject to the initial and boundary conditions in Equations (3.41) and (3.42) respectively to give Equations (3.43) and (3.44).

$$T_1 = -C_2 + T_{1in} + C_2 \exp(B_2 x) \tag{3.43}$$

$$T_{2in} = T_{1in} + C_2((X_1 B_2 + 1)\exp(B_2 L_1) - 1) \tag{3.44}$$

where C_2 is an integration constant, $B_2 = -\frac{(X_1 + X_{21})}{X_1 X_{21}}$, $X_1 = \frac{\dot{m}_1 C_{p1}}{A_{L1} U_{21}}$, and $X_{21} = -\frac{\dot{m}_2 C_{p2}}{A_{L1} U_{21}}$.

Equations (3.43) and (3.44) predict the spatial temperature variation of the process and cooling fluids in a jacketed SPC meso-tube by incorporating the mass flow rates and specific heat capacities of both fluids, as well as the heat transfer performance of the SPC meso-tube. Section 3.11.3 explains how Equations (3.43) and (3.44) are used in the spatial approximation of temperature profiles in the SPC mesoscale crystalliser for seeded continuous cooling crystallisation.

3.10.3 Experimental apparatus

The setup for heat transfer experiments consisted of two identical jacketed SPC meso-tubes connected as concentric tube heat exchangers by an unjacketed U-shaped bend and operated in counter-current mode (see Figure 3.21). The thickness of the glass wall was ca. 1 mm and the active tube length, L_1, was 0.66 m. The process and cooling fluids were deionized water with temperature-dependent thermophysical properties (specified in Table 3.4) based on their mean bulk temperatures $\left(\frac{T_{in} + T_{out}}{2}\right)$ in the active length of the heat exchanger which were 32.5 °C and 3 °C respectively. The cooling fluid was pumped at a constant flow rate of ~6 L min^{-1}, and the process fluid was pumped continuously by a Labhut Series 1500 Dual Piston Pump from a de-gassed reservoir. A constant temperature, T_w, was maintained in the annulus by a Huber Ministat 230 temperature control bath.

Table 3.4 Temperature-dependent thermophysical properties of cooling and process fluids (Perry et al., 1999)

Physical properties	Process fluid at 32.5 °C	Cooling fluid at 3°C
Density, ρ (kg m^{-3})	992.80	1005
Viscosity, μ (Pa s)	7.87×10^{-4}	1.5×10^{-3}
Thermal conductivity, k (W m^{-1} K^{-1})	0.614	0.579
Specific heat capacity, C_p (J kg^{-1} K^{-1})	4188	4185
Prandlt number, Pr	5.37	10.67

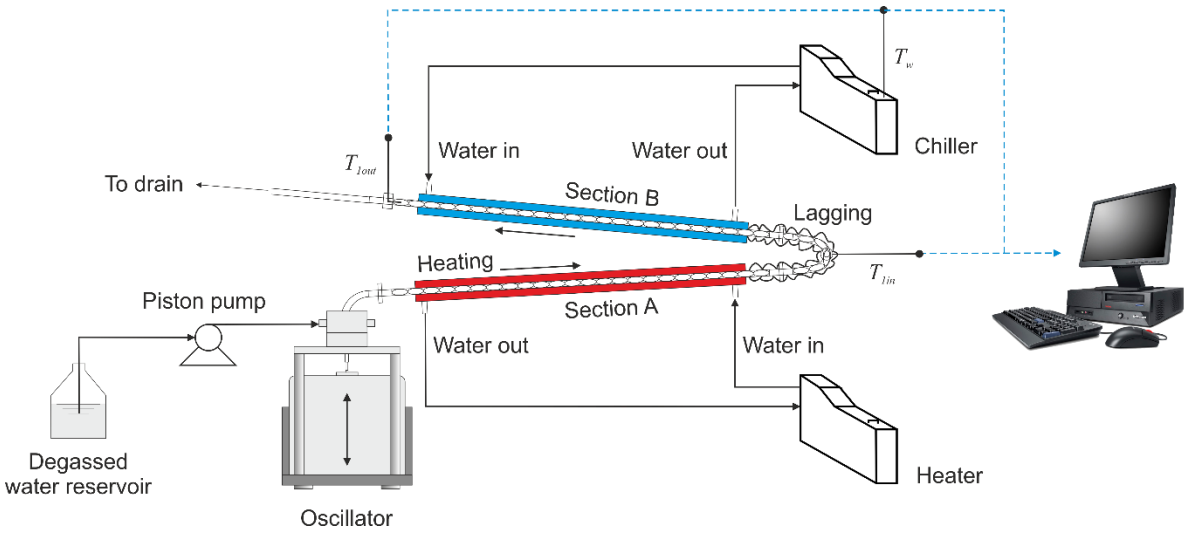

Figure 3.21 Schematic diagram of the heat transfer apparatus.

T_{1in}, T_{1out}, and T_w were measured using 3 K-type thermocouples with mineral insulated sensors (Thermosense) inserted into the U-shaped bend, tube exit, and the temperature control bath respectively. The entire section connecting the heat exchangers was sufficiently lagged such that heat loss to the surrounding was negligible and the temperature measured at the bend could be taken as the inlet temperature $T_{1_{in}}$. Each thermocouple was calibrated for linearity before installation. The thermocouples were connected to a computer via an Advantech USB-4718 data acquisition module.

3.10.4 Heat transfer experiment

At the start of an experiment, deionized water was pumped at a steady net flow rate into Section A (see Figure 3.21) where it was heated to a desired inlet temperature, T_{1in} of 55 °C. The resulting hot water was then cooled in Section B to an outlet temperature, T_{1out} which is measured at the exit of the heat exchanger. The annulus of the heat exchanger was maintained at a constant temperature, T_w of ~3.5 °C by a constant turbulent flow of water (3.9 m s^{-1}) with a much greater heat capacity rate ($C_1 =$ 416 J K^{-1} s^{-1}) than that of the process fluid ($C_2 = 0.14 – 0.8$ J K^{-1} s^{-1}). The wall resistance, R_w, was found to be 7.5×10^{-4} m^2 K W^{-1}, and the resistance to convective heat transfer from the wall to the cooling fluid, $R_{conv,c}$, was found to be 5.2×10^{-5} m^2 K W^{-1}.

A set of steady flow experiments were first conducted in a plain meso-tube. The plain meso-tube is a straight-walled meso-tube with no constrictions and has a 5 mm mean inside diameter. A second set of steady flow experiments were then conducted in the SPC meso-tube. The oscillatory x_0 and f were varied for different unsteady flow experiments subsequently carried out in the SPC meso-

tube. For every oscillatory and net flow condition, the mean Nu_t was calculated from recorded data corresponding to steady-state operation i.e. when temperature values had become steady. Experiments were performed in the range Re_n = 10.79 – 53.97 (2 – 10 ml min^{-1}).

3.11 Experimental methods for continuous cooling crystallisation in the SPC mesoscale crystalliser

3.11.1 Determination of metastable zone width

Accurately measuring the MSZW is essential to define an appropriate seeding point within the metastable zone and a spatial temperature profile that avoids spontaneous nucleation. Batch experiments (i.e. zero net flow) were performed to determine the MSZW of GLY-water solution in the batch SPC mesoscale crystalliser (see description in section 3.4). The batch SPC mesoscale crystalliser has identical meso-tube geometry and wall material to the SPC mesoscale crystalliser, meaning that the hydrodynamics and heat transfer characteristics in both platforms are essentially the same. Therefore, the MSZW in the batch SPC mesoscale crystalliser is applicable to the SPC mesoscale crystalliser for seeded continuous cooling crystallisation.

A polythermal method was used to measure the MSZW in the batch SPC mesoscale crystalliser under different mixing and cooling conditions. With the aid of a dark background, naked eye observation was employed to detect the onset of cloudiness, indicating the metastable limit. Visual observation was used here as the available 9 mm FBRM probe could not be fitted into the small-diameter batch SPC mesoscale crystalliser. For MSZW measurements in the 500 ml STC, a Mettler Toledo ParticleTrack™ G400 with iC FBRM™ software was used. The polythermal method is based on the determination of the maximum supercooling, ΔT_{max}, therefore, for all experiments performed the MSZW was defined as:

$$\Delta T_{max} = T_{sat} - T_{lim} \tag{3.45}$$

where T_{sat} is the saturation temperature (°C) and T_{lim} is the temperature at which cloudiness is detected.

In the first set of polythermal experiments performed, the batch SPC mesoscale crystalliser was operated at the oscillatory condition $x_0 = 0.5$ mm, $f = 12$ Hz. Four different solutions saturated at 20 °C, 30 °C, 40 °C and 50 °C with concentrations of 0.228 g/g, 0.278 g/g, 0.330 g/g and 0.385 g/g respectively were heated to 10 °C above their saturation temperatures for 30 min, and then cooled at –

1 °C min^{-1} until cloudiness appeared. A second set of experiments were performed for a 0.278 g/g solution (saturated at 30 °C) to investigate the combined effect of cooling rate and mixing intensity on the MSZW. Cooling rates of –0.5 °C min^{-1} and –1 °C min^{-1} were investigated at Re_o of 31, 123, 185, 740.

3.11.2 Power density calculations

For each mixing intensity investigated in the MSZW experiments, the corresponding power density was evaluated to determine its effect on MSZW, and to quantitatively assess the mixing efficiency of the batch SPC mesoscale crystalliser against a 500 ml STC. The mixing mechanisms in the SPC mesoscale crystalliser and STC are very different, as such, hydrodynamic conditions in both systems are not directly comparable. As mentioned in section 2.8.3, the power density quantifies the power consumption for a given system volume; therefore, the power density can provide useful insight, by assessing the energy efficiency of both platforms in terms of the MSZW. For each oscillatory condition investigated, the power density for the batch SPC mesoscale crystalliser was calculated using the revised quasi-steady flow model (Jimeno et al., 2018):

$$\varepsilon_{SPC} = \frac{2\rho n_c^{0.7}}{3\pi C_d^2 (V/A_{CS})}\left(\frac{1-\alpha^2}{\alpha^2}\right) x_0^3 \omega^3 \tag{3.46}$$

where C_d is 0.8 for a smooth baffle/constriction as applies to the batch SPC mesoscale crystalliser (Jimeno et al., 2018), n_c is 26, V is measured as 4.3 ml, and V/A_{CS} is 0.22. The power density for the 500 ml STC, having an impeller diameter of 5.08 cm and an impeller rotational speed of 400 rpm, was calculated using Equation (3.47) (Ni et al. 1995):

$$\varepsilon_{STC} = \frac{P_0 \rho N_i^3 D_i^5}{V} \tag{3.47}$$

where P_0 is the impeller power number estimated as 1.3 for the retreat curve impeller (Rielly, 2006), N_i is the rotational speed of the impeller (rps), D_i is the diameter of the impeller (m).

3.11.3 Prediction of spatial temperature profiles in the SPC mesoscale crystalliser

For the continuous cooling crystallisation process, it was necessary to understand how the temperature of the feed solution would vary along the crystalliser length for different oscillatory and net flow operating conditions. To achieve this, a heat transfer model was developed in section 3.10.2 to predict the temperatures of the process and cooling fluids at a given axial position or distance, x, in each temperature-controlled segment of the SPC mesoscale crystalliser. The input variables to the model included the mass flow rates and specific heat capacities of both fluids, and the overall heat transfer coefficient, U_{21}. For a given oscillatory and net flow condition, the tube-side Nusselt number, Nu_t, was estimated by a newly derived empirical correlation (see section 5.3 of Chapter 5) and used in calculating U_{21}. This enabled accurate predictions of outlet temperatures for the process fluid in each segment. More importantly, with the heat transfer model, a mathematical approximation to a desired temperature profile could be made prior to physical implementation in the crystalliser. This aided rapid process development.

For full-length temperature predictions, the SPC mesoscale crystalliser was modelled in a Microsoft Excel® worksheet as four independent temperature-controlled segments consisting of 5 straight sections (S1 – S5). The active tube length, L_1 of each segment was divided into 24 discrete axial positions. The first three segments consisted of sections S1 – S3, each having an active length of 0.657 m. The final segment consisted of sections S4 and S5 and had a length of 1.314 m. The length of the final segment was doubled to maximise crystal growth at the final temperature. For a desired flow rate, inlet temperature (at seeding point), T_{1in}, and final temperature, T_{1f}, the spatial temperature profile of the process fluid in the crystalliser could be visualised and modified by independently manipulating the flow rate and inlet temperature, T_{2in}, of the cooling fluid in each segment.

Two temperature profiles were implemented for seeded continuous cooling crystallisation in the SPC mesoscale crystalliser, namely a stepped linear profile, and a cubic profile, T_{cubic}, given by Equation (3.48).

$$T_{cubic} = T_{1in} - (T_{1in} - T_{1f})\left(\frac{x}{L_{1tot}}\right)^3 \tag{3.48}$$

where L_{1tot} is the total active tube length of all temperature-controlled segments in the crystalliser. A stepped linear profile involved cooling from an inlet temperature of 17 °C to a final temperature of 11 °C by providing 2 °C drops between segments. Using an Excel® GRG Nonlinear Solver, a cubic profile was spatially approximated in the SPC mesoscale crystalliser by manipulating the flow rate and

inlet temperature of the cooling fluid in each temperature-controlled segment to minimise the sum of squared errors (SSE) between T_{cubic} and T_1.

3.11.4 Unseeded continuous cooling crystallisation approach

Attempts at unseeded continuous cooling crystallisation were made in the SPC mesoscale crystalliser. The crystalliser was modified into four temperature-controlled segments consisting of four straight sections (S0 – S3) (see Figure 3.22). Different GLY-water solutions saturated at 20 °C (0.228 g/g), 30 °C (0.278 g/g), and 40 °C (0.330 g/g) were continuously pumped at 5.39 g min^{-1} from a 500 ml feed vessel into the SPC mesoscale crystalliser using a HPLC pump. In each run, the temperature of the feed vessel was maintained at the saturation temperature of the GLY-water solution. The spatial temperature profile of the process fluid was modified for each trial run by manipulating jacket temperatures T_{J0} – T_{J3}. Each temperature profile was based on the MSZW determined for the GLY-water system in the batch SPC mesoscale crystalliser.

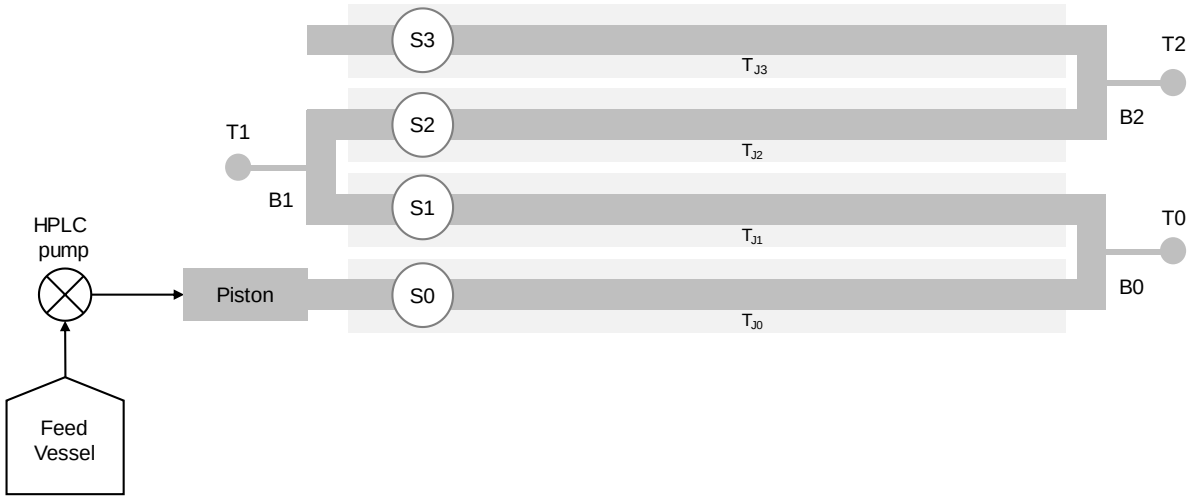

Figure 3.22 Experimental set-up for unseeded continuous cooling crystallisation (not drawn to scale).

3.11.5 Seed preparation and tailoring studies

To perform controlled reproducible seeded continuous cooling crystallisation experiments and ensure delivery of accurate seed mass to the SPC mesoscale crystalliser, a wet milling approach to seed preparation was investigated. Wet milling was performed using a laboratory scale magic LAB® high-shear wet mill (IKA, Germany) configured into a three-stage Dispax Reactor® (DR) module with a '2G – 6F – 6F' rotor-stator combination i.e. a 'course-toothed – fine-toothed – fine-toothed' generator

arrangement (see Figure 3.23). A rotor-stator wet mill was chosen for particle size reduction as it has been shown to avoid undesired polymorphic and amorphous transformations, introduction of crystal lattice disorders, broad bimodal CSDs, and loss of yield which are commonly experienced with dry mills (Kim et al., 2003; Variankaval et al., 2008; Anderson, 2012). In the study, wet milling of recrystallised α-GLY material was carried out isothermally to determine the milling times sufficient to achieve target mean particle sizes for seeding requirements. The process was performed at a constant temperature within a pre-determined metastable zone (see section 3.11.1) to ensure that secondary nucleation was not triggered, and that mechanisms resulting from the wet milling process could be easily identified. 800 ml of a 0.228 g/g GLY-water solution (saturated at 20 °C) was prepared in a 1 L jacketed glass vessel and cooled to 13 °C (well within the metastable zone).

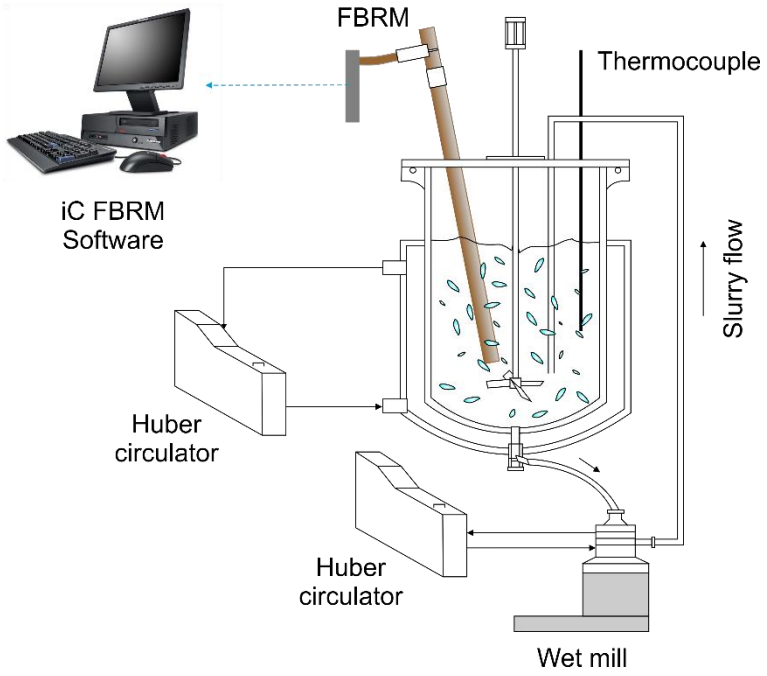

Figure 3.23 IKA magic LAB® high-shear wet milling device used for seed preparation and tailoring.

Afterwards, a pre-weighed amount of recrystallised α-GLY material (37 g) required to make up 7% w/w seed loading in the SPC mesoscale crystalliser (according to Equation (3.49)) was added as dry powder to the saturated solution and kept suspended by impeller agitation at 400 rpm. In this work, the seed or solids loading in the SPC mesoscale crystalliser is defined on a mass flow rate basis as given below:

$$Seed\ loading = \frac{mass\ flow\ rate\ of\ solid\ seeds\ added}{mass\ flow\ rate\ of\ total\ dissolved\ GLY\ in\ the\ feed\ and\ seed\ stream} \qquad (3.49)$$

Prior to the milling process, a recycle loop was created between the DR module and the 1 L jacketed glass vessel using Masterflex® L/S 17 platinum-cured silicone tubing with an internal diameter of 6.4 mm. To mitigate excessive heat generation from the milling process, and prevent the dissolution of milled crystals, a water bath at ~10 °C was connected to the jacket of the DR module to maintain the outlet slurry temperature well below 20 °C. A Mettler Toledo ParticleTrack™ G400 with iC FBRM™ software was used to monitor particle counts and mean chord length in the jacketed glass vessel as milling progressed. At the start of the experiment, a suspension of recrystallised α-GLY material was transferred under gravity into the DR module for milling. Wet milling was carried out at a constant temperature of 13 °C, and the DR module was operated at a rotational speed of 10,000 rpm, which provided continuous recirculation of the suspension for the duration of the experiment. The hydraulic residence time through the DR module, known as a single pass was measured as ~60 s. Samples were taken from the jacketed glass vessel at time intervals of 1 min, 20 min, 60 min, 90 min, and 120 min. Each milled sample was filtered in under 30 s, and the CSD was measured in the Malvern Mastersizer 2000 wet dispersion unit to obtain a volume mean diameter, $d_{4,3}$. Milled seeds were subsequently checked by offline Raman spectroscopy for possible polymorphic transformation due to high shear milling.

3.11.6 Experimental setup for seeded continuous cooling crystallisation

Figure 3.24 shows a schematic of the full-length SPC mesoscale crystalliser for seeded continuous cooling crystallisation studies on the GLY-water system. The SPC mesoscale crystalliser consisted of 6 straight sections (S0 – S5) consisting of jacketed SPC meso-tubes and 5 U-shaped glass bends (B0 – B4) with sample ports. The jacket of each section was connected to a Huber Ministat 230 cooling circulator (not shown in schematic) to enable independent temperature control of the process fluid by counter-current heating/cooling. Four K-type thermocouples with mineral insulated sensors (Thermosense) (T0 – T4) were inserted into the sample ports at bends B0 – B4 and connected to a monitoring computer via a DAQ module (Advantech USB-4718) to record process fluid temperatures exiting sections S0 – S4 of the crystalliser. The cooling fluid in each section had a fixed temperature which was pre-determined by the heat transfer model based on a desired spatial temperature profile for the process fluid (see section 3.11.3 for details).

Degassed feed solution was pumped continuously into the crystalliser from a closed 2 L Duran® bottle. Degassing of the feed solution was necessary to prevent bubble formation when oscillated. A 1 L temperature-controlled agitated glass vessel was used for preparing and holding seed suspension

(see section 3.11.5). Tailored seed suspension was pumped from the seed vessel into bend B1 by a peristaltic pump (Masterflex® L/S Precision Console Pump) using Masterflex® L/S 13 platinum-cured silicone tubing with an internal diameter of 0.8 mm. There was no crystallisation in section S0, as this section was used to equilibrate incoming feed solution to a temperature 1 – 2 °C below that of the seed vessel. This provided sufficient supersaturation at the seed entry point (B0) to keep seed crystals from dissolving. Also, it was crucial to maintain section S0 free of seed suspension to prevent clogging of the oscillator piston by crystals and possible encrustation. An Elveflow® bubble trap with 44 µL internal volume was installed between the peristaltic pump and the seed entry point for in-line removal of bubbles during seed transfer (see Figure 3.24). By expelling bubbles through a porous PTFE membrane (10 µm pores) the device prevented the accumulation of bubbles in the SPC mesoscale crystalliser, which could dampen oscillation propagation and potentially shut down operation. Figure 3.25 shows the working principle of the bubble trap. For the duration of all experiments, no fouling or blockage occurred in the PTFE membrane. Final product material was collected at the outlet of the crystalliser in a collection vessel at room temperature.

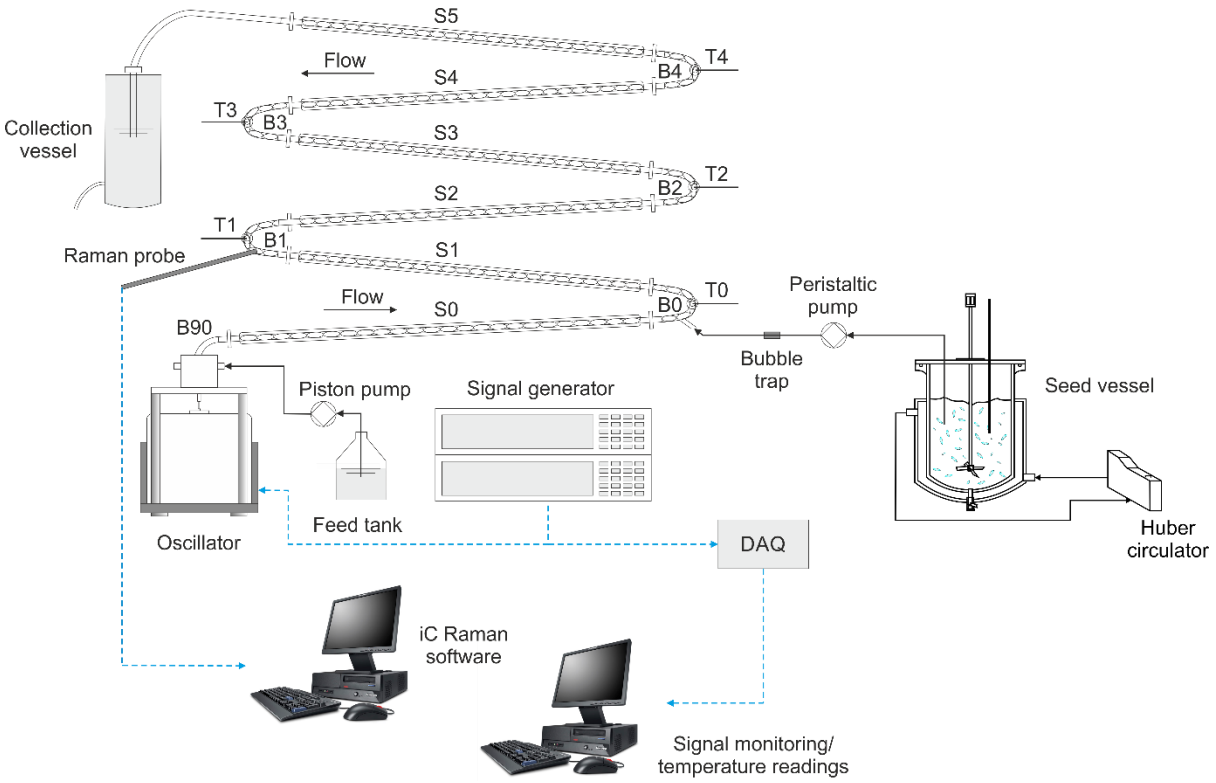

Figure 3.24 Experimental set-up for seeded continuous cooling crystallisation (not drawn to scale).

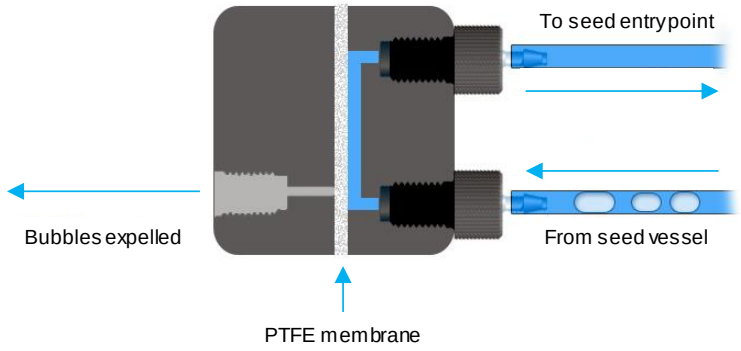

Figure 3.25 Schematic representation showing working principle of the bubble trap.

3.11.7 Experimental procedure for seeded continuous cooling crystallisation

1 L of 0.228 g/g GLY-water solution (saturated at 20 °C) was prepared and held in a 2 L feed tank for the duration of each experiment. 1 L of 0.223 g/g GLY-water solution (saturated at 19 °C) was prepared in the seed vessel. On complete dissolution, the solution was cooled to 13 °C, dry seeded with a known amount of α- or γ-GLY (33 g, 37 g, and 50 g for 4% w/w, 7% w/w and 12% w/w respectively) and milled for an appropriate time to prepare a tailored seed suspension (according to section 3.11.5). After milling, the seed suspension was held at 19 °C for 30 min to allow equilibration and 'healing' of highly strained seed crystals (Ristić et al., 1988). Prior to start-up, gentle oscillations were switched on, and the crystalliser was flushed with deionised water to prime out all air bubbles and dissolve any residual material. The jacket temperatures of sections S0 – S5 were seaqt per the desired temperature profile which was either a stepped linear profile of 2 °C temperature drops between segments or an approximation to a cubic profile (see detailed descriptions in section 3.11.3). The temperatures at bends B0 – B4 were continuously recorded for the duration of each experiment.

At start-up, oscillations were adjusted to the required x_0 and f. The feed solution (feed stream) and seed suspension (seed stream) were pumped simultaneously at calibrated flow rates to deliver the appropriate seed loading and achieve the desired mean residence time in the crystalliser. A calibrated Raman immersion probe positioned at bend B1 was used for *in situ* solution concentration measurement to detect the onset of steady-state operation. Samples collected from the outlet during steady-state were microscope-imaged and filtered in under 1 min, subsequently washed, and dried overnight in an oven. Steady-state concentration of the mother liquor was determined gravimetrically, and the fractional yield was calculated as the amount of product obtained from the crystalliser relative to available supersaturation using Equation (3.50):

$$Fractional\ Yield = \frac{C_f f_0 + C_s f_s - C_1 f_1}{C_f f_0 + C_s f_s - C_{sat} f_1} \times 100 \quad (3.50)$$

where C_f is the feed stream concentration expressed as mass of dissolved GLY per mass of water (g/g), C_s is the seed stream concentration (g/g), C_{sat} is the equilibrium concentration (g/g) at the final operating temperature in the crystalliser, and C_1 is the steady-state concentration of the outlet stream in the crystalliser. f_0, f_s, and f_1 are the mass flow rates of water in the feed stream, seed stream, and outlet stream respectively, and $f_i = X_i \dot{m}_i$ where X_i is the mass fraction of water in each flow stream i and $\dot{m}_i$ is the total mass flow rate of each flow stream i.

Prior to size characterisation, dried samples were sonicated to break up any agglomerates formed while drying. CSD was measured by laser diffraction in the Malvern Mastersizer® 2000 using isopropanol as dispersant, with an obscuration between 10 and 20% for each measurement. Triplicate measurements were taken, and product mean sizes were presented as $d_{4,3}$. The product polymorphic form was analysed using an offline Thermo Scientific™ DXR™ 2 Raman microscope to check for any solution-mediated polymorphic transformation of seed material during the crystallisation process, although this was not expected. The Raman spectroscopic measurements are shown in Figure 6.8 and Figure 6.9 in Chapter 6.

3.11.8 Effect of mean residence time

The effect of mean residence time, τ, on α- and γ-GLY seeded cooling crystallisation was examined by operating the SPC mesoscale crystalliser at a practically attainable 'long' and 'short' mean residence time of 7.3 min and 2.8 min respectively. Here, the mean residence time refers to the time spent by crystals in sections S1 – S5, where seeded cooling crystallisation occurred. Each residence time was achieved by changing the mass flow rates of the feed and seed streams, while ensuring that a seed loading of 7% w/w was maintained in the crystalliser. For a 'short' residence time of 2.8 min, the flow rates of the feed and seed streams were set to 13 g min^{-1} and 7.9 g min^{-1} respectively. For a 'long' mean residence time of 7.3 min, the flow rates of the feed and seed streams were 5 g min^{-1} and 3 g min^{-1} respectively. A stepped linear profile with 2 °C drops between segments was implemented to cool from 17 °C at the seed inlet, to a final temperature of 11 °C in the final segment. To ensure adequate suspension of heavy GLY crystals ($\rho_c = 1.61$ g cm^{-3}) throughout the crystalliser, a mixing intensity of $R_{eo} = 306$ ($x_0 = 1$ mm, $f = 10$ Hz) was applied. The effect of mean residence time was assessed by measuring the mean crystal size, distribution span, and yield of the GLY product obtained.

3.11.9 Effect of oscillatory condition

Investigations were carried out to understand how mixing conditions translate into the crystallisation environment within the SPC mesoscale crystalliser and impact on the attributes of the steady-state product. The effect of oscillatory condition on the crystallisation of α- and γ-GLY was studied by performing seeded cooling crystallisation at three different mixing conditions, $Re_o = 62$, 123, and 308, and measuring the steady-state mean crystal size, distribution span, and yield of the GLY product obtained. A stepped linear profile was implemented, and the crystalliser was operated at τ of 7.3 min with 7% w/w seed loading.

3.11.10 Effect of temperature profile

The effect of temperature profile on the steady-state CSD and yield of steady-state α- and γ-GLY product was investigated by applying a stepped linear profile and a spatially approximated cubic profile in the SPC mesoscale crystalliser. The crystalliser was operated at τ of 7.3 min with a seed loading of 7% w/w.

3.11.11 Effect of seed size and loading

The effect of seed size and loading on the steady-state CSD and yield of α- and γ-GLY was investigated by varying the seed loading in the crystalliser between 4, 7 and 12% w/w at two distinct seed sizes achieved through wet milling of both polymorphic forms. For α-GLY, seed sizes of 57 ± 1.2 µm and 87 ± 1.7 µm were used, while for γ-GLY 88 ± 2.89 µm and 102 ± 0.7 µm seed sizes were used. Sizes closer to those of α-GLY seeds could not be achieved for γ-GLY in the same milling time due to a lower occurrence of mass fracture. For all experiments, a stepped linear cooling profile was implemented, and the mean residence time in the crystalliser was 7.3 min. For each seeding condition investigated, the available seed surface area was calculated as follows (Loï Mi Lung-Somarriba et al., 2004):

$$S_c = \frac{W_s \eta}{\rho_c k_v L_s} \tag{3.51}$$

where S_c is the seed surface area (cm^2), W_s is the seed mass (g), η is the surface shape factor, ρ_c is the crystal density (g cm^{-3}), k_v is the volumetric shape factor, and L_s is the initial seed mean size (cm).

For a glycine tetrahedral bipyramid crystal, the volumetric shape factor and the surface shape factor are 0.17 and 1.75 respectively (Loï Mi Lung-Somarriba, 2003).

3.12 Experimental methods for continuous cooling crystallisation in the MSMPR crystalliser

3.12.1 Experimental setup

Figure 3.26 and Figure 3.27 show the schematic of the product recycle single- and two-stage MSMPR configurations respectively. Two identical 100 ml jacketed glass vessels (model ADAV manufactured by HWS-Labortechnik Mainz) were used as MSMPR 1 and MSMPR 2. Both vessels were unbaffled, had an internal diameter of 60 mm (DN-60), and were each fitted with a 3-bladed retreat curve impeller (RCI) of 30 mm diameter. A 500 ml DN-100 jacketed glass vessel served as the feed/dissolution vessel. For the seeded experiment, the feed/dissolution vessel was replaced by a 1000 ml DN-100 jacketed glass vessel which served as the seed vessel. Independent heating and cooling of all vessel jackets was provided by three Julabo recirculating oil baths. The circulating fluid used was Swansil 10 cSt (25 °C) silicone oil with a working range of –40 – 140 °C. Programming of vessel temperature profiles and temperature data logging were achieved via a Labgear software (version 1.2) connected to the oil baths.

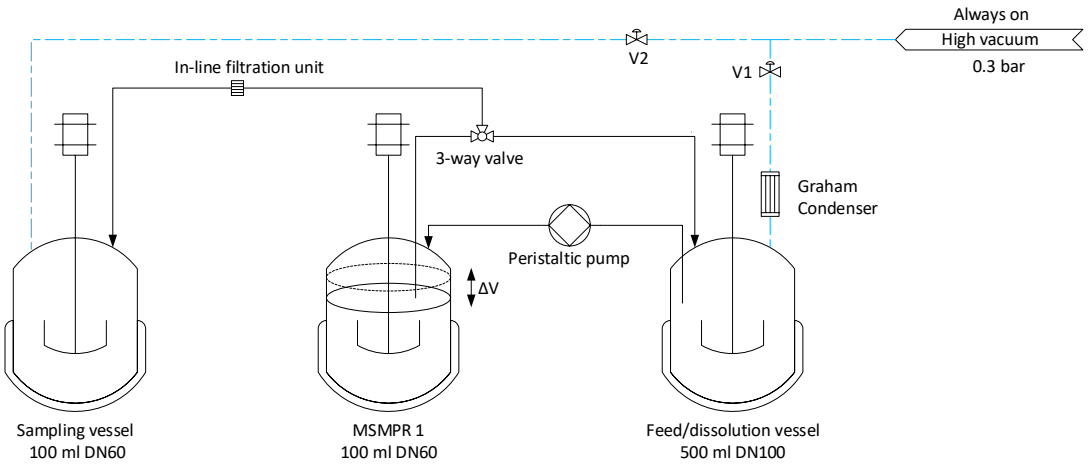

Figure 3.26 Vacuum connections (dashed) and transfer lines (solid) for the single-stage MSMPR configuration.

Rapid intermittent withdrawal was implemented using a high vacuum source controlled via two-way valves (V1, V2, V3) to transfer slurry in the sequence MSMPR 1 → feed/dissolution vessel in the single-stage configuration, and MSMPR 1 → MSMPR 2 → feed/dissolution vessel in the two-stage

configuration. This technique enabled isokinetic withdrawal of suspension in under 2 s from the MSMPR crystallisers.

A calibrated Masterflex® L/S® peristaltic pump was used to continuously transfer clear feed solution (or seed suspension) from the feed/dissolution vessel (or seed vessel) to MSMPR 1 in all experiments. The temperature in the feed/dissolution vessel was maintained at 20 °C above saturation temperature for all experiments, with a condenser attached to minimize solvent loss by evaporation. This ensured fines were absent from the hot feed solution, so that the likelihood of crystal build-up and blockage in the feed line to MSMPR 1 was negligible for the duration of experimental runs. A Mettler Toledo S400 FBRM probe (connected to Mettler Toledo FBRM software version 6.7.0) was placed in MSMPR 1 for the single-stage configuration and moved to MSMPR 2 for the two-stage MSMPR experiments.

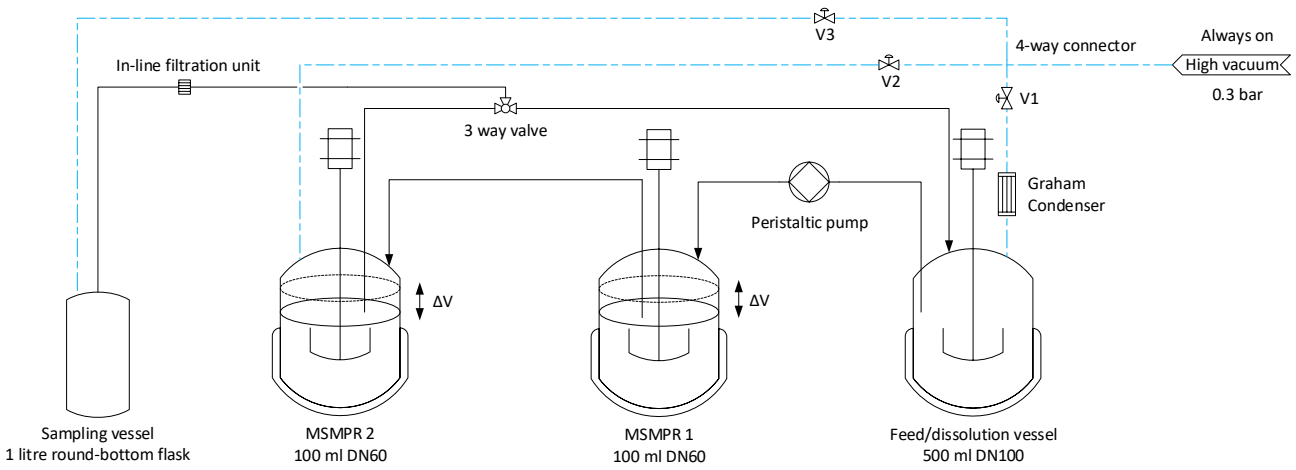

Figure 3.27 Vacuum connections (dashed) and transfer lines (solid) for the two-stage MSMPR configuration.

3.12.2 Liquid RTD characterisation of the MSMPR system

The effect of volumetric flow rate, mixing intensity (impeller agitation speed), and number of stages on the RTD of the MSMPR system was investigated under continuous steady flow operation. RTD was determined using intrusive pulse tracer measurements, whereby a NaCl tracer was used, and a pair of conductivity probes (Mettler Toledo InLab® 751-4mm) were positioned as indicated in Figure 3.28 and Figure 3.29. This was to enable characterisation by imperfect pulse method which has been shown to be a more accurate way of determining axial dispersion in continuous systems (Ni et al., 2003; Zheng and Mackley, 2008). In all RTD experiments MSMPR 1 and MSMPR 2 were operated

at 100 ml of DI water, while the feed/dissolution vessel was operated at 250 ml of DI water (operating below 250 ml was not possible due to impeller clearance limitations).

The RTD performance of a single-stage MSMPR (Figure 3.28) was determined for different conditions from a test section consisting of MSMPR 1 and MSMPR 2 connected in series by silicone tubing (Masterflex® L/S® platinum-cured) and peristaltic pumps (Masterflex® L/S® Standard Digital Pump). A conductivity probe placed in MSMPR 1 measured the pulse input to the test section, while a second probe placed in MSMPR 2 measured the output tracer concentration from MSMPR 1 (i.e. the output from MSMPR 1 was sampled at MSMPR 2 for dispersion).

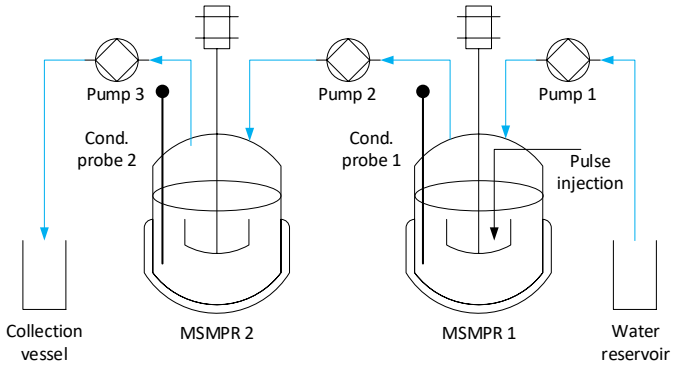

Figure 3.28 Experimental setup for liquid RTD characterisation of the single-stage MSMPR system.

Subsequently, the RTD of a two-stage MSMPR system was measured from a test section consisting of the feed/dissolution vessel, MSMPR 1, and MSMPR 2 connected in series according to Figure 3.29. A conductivity probe was placed in the feed/dissolution vessel to measure the pulse input to the section, and the second conductivity probe in MSMPR 2 measured the tracer exit concentration from MSMPR 1. The interpretation of fitted RTD curves from the measurement points was performed to provide information on the overall extent of axial dispersion in the test section, based on the dimensionless dispersion number, D_{ax}/uL.

At time zero for all experiments, a pulse of 0.5 ml containing 1 M NaCl tracer with a density of 1.0364 g cm^{-3} (Hai-Lang and Shi-Jun, 1996) was injected subsurface close to the impeller in the first vessel in under 1 s using a 1 ml syringe fitted with a flexible capillary tube. 1 M NaCl concentration was used here to provide a good signal from both conductivity probes in a larger total operating volume. Both conductivity probes were started simultaneously via the conductivity meter to record the upstream and downstream response curves (concentration-time curves) at 1 s intervals. Data recording was stopped once readings from both conductivity probes had returned to zero, indicating that the entire tracer had exited the test section. Experiments were conducted at volumetric flowrates

of 25, 50, and 70 ml min^{-1} to vary the mean residence time, τ_L, in the test section (i.e. distance between the measurement points). Impeller speeds were set to 200 and 400 rpm to vary the mixing time in the MSMPR vessels; however, the feed/dissolution vessel could only be operated at an impeller speed of 250 rpm due to vortex formation at higher rpm.

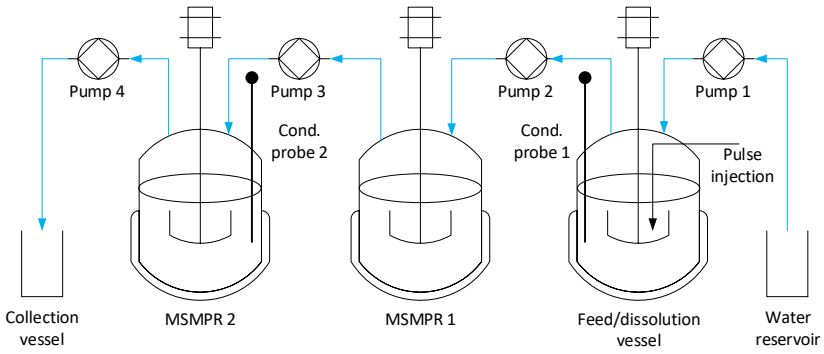

Figure 3.29 Experimental setup for liquid RTD characterisation of the two-stage MSMPR system.

The impeller Reynolds number for the MSMPR was calculated using Equation (3.52):

$$N_{Re} = \frac{\rho N_i D_i^2}{\mu} \tag{3.52}$$

where N_i is the impeller rotation speed (rps), and D_i is the impeller diameter (m), μ is the fluid viscosity (Pa s), ρ is the bulk fluid density (kg m^{-3}).

3.12.3 Determination of axial dispersion coefficient

The axial dispersion coefficient was determined in a similar way to described in section 3.9.6. The estimates of the degree of backmixing were described by the dimensionless axial dispersion number, D_{ax}/uL, and a convective time scale:

$$\tau_L = L/u \tag{3.53}$$

where L is the fixed distance or length of tubing between the measuring conductivity probes (m) in this case, and u is the mean axial velocity (m s^{-1}). The axial dispersion model for an *open-open* boundary condition was employed as given in Equation (3.11) in section 3.9.6. Hydrodynamic parameter estimation was performed according to the algorithm outlined in Figure 3.19, and the results

of the convolution integral were fitted to the measured output concentration-time history by adjusting the two model parameters τ_L and D_{ax}/uL. The tanks-in-series model describes the test section as N equal-sized tanks in series, thus assuming all tank volumes are identical, and therefore space times are identical. The number of tanks in series, N, that best fits the RTD data was then calculated from D_{ax}/uL using Equation (3.54) (Fogler, 1999):

$$N = {uL}/{2D_{ax}} + 1 \tag{3.54}$$

3.12.4 Estimation of just-suspended speed for solids suspension

To facilitate rapid process development, N_{js} was estimated using the Dynochem® solid-liquid mixing utility (Scale-up Systems Ltd.), which is a process development and modelling tool for evaluating vessel mixing performance and scale-up. Results of the estimation were confirmed by visual observation at the start of crystallisation experiments. Determining N_{js} involved selecting the appropriate vessel and impeller geometry from the utility database and specifying the solid-liquid properties and solids concentration. Based on this information, the utility estimated the impeller speed required for complete suspension of solid particles in the MSMPR. The Dynochem® solid-liquid mixing utility calculates N_{js} based on Zwietering's correlation for solids suspension in stirred tanks (Zwietering, 1958):

$$N_{js} = s\nu^{0.1}\left(\frac{g(\rho_p-\rho)}{\rho}\right)^{0.45} \mathrm{X}^{0.13} d_p^{0.2} {D_i}^{-0.85} \tag{3.55}$$

where s is the impeller geometrical constant dependent on impeller type, diameter, and clearance, ν is the liquid kinematic viscosity (m^2 s), g is the acceleration due to gravity (m s^{-2}), ρ_p is the particle density (kg m^{-3}), X is the mass ratio of solid to liquid, d_p is the diameter of spherical particles (m), and D_i is the impeller diameter (m). While the Zwietering correlation has been tested for a wide range of impeller types and solid-liquid properties in vessels of differing scales (Rielly et al., 2007) it is known to have several limitations which can affect the accuracy of its predictions (Ayranci and Kresta, 2011; 2014; Blais et al., 2017). A mean particle size of 100 µm was specified for the calculations, as this was the approximate mean size of crystals in the equilibrated start-up batch suspension. The total GLY mass added to the MSMPR for the preparation of the equilibrium batch suspension (saturated at 40 °C) was taken to calculate a weight fraction, X, of 24.8%.

3.12.5 Critical mean residence time for heat transfer

The critical mean residence time, $\tau_{critical}$, is the minimum time required to cool an incoming feed stream to the desired operating temperature of the MSMPR crystalliser and indicates the cooling capacity of the crystalliser. Here, τ refers to the mean residence time of material in the MSMPR crystalliser. When operating at a mean residence time, $\tau < \tau_{critical}$, the MSMPR crystalliser may attain a steady-state at undesired supersaturation levels, resulting in unexpected product specification; and the time to attain steady-state may be prolonged. The critical mean residence time for both MSMPR crystallisers was determined using Equation (3.56) below:

$$\tau_{critical} = \frac{V_{cr}\rho_s C_p(T_f - T_j)}{UA(T_{cr} - T_j)} \tag{3.56}$$

Where U is the overall heat transfer coefficient between the feed solution and the circulating fluid, V_{cr} is the crystalliser operating volume, ρ_s is the solution density, C_p is the specific heat capacity of the solution at the incoming feed temperature, T_f is the feed temperature, T_j is the MSMPR jacket temperature, T_{cr} is the desired operating temperature of the MSMPR.

3.12.6 Single-stage unseeded MSMPR crystallisation

Unseeded crystallisation experiments were performed in the single-stage MSMPR to investigate the effect of mean residence time and MSMPR operating temperature on steady-state mean crystal size, CSD, and yield of α-GLY. The mean residence time in MSMPR 1 was adjusted by changing the volumetric flow rate of the pump. Prior to start-up, 260 ml of a 0.275 g/g GLY-water solution (saturated at 40 °C) was held at 60 °C in the feed/dissolution vessel. In MSMPR 1, 90 ml of a 0.275 g/g suspension was heated to 50 °C (10 °C above saturation temperature) and held for 30 min to ensure complete dissolution as indicated by FBRM total counts. The clear solution was cooled to an operating temperature of 20 °C to create a batch suspension, and the impeller speed was set to the required rpm to meet hydrodynamic suspension conditions (as determined in section 3.12.4). Once the batch suspension had equilibrated and FBRM total counts were steady, a start-up sequence was initiated. At start-up, hot feed solution (at 60 °C) was continuously pumped into MSMPR 1 until 10 ml of solution was transferred, filling it to a volume of 100 ml. Immediately, an intermittent withdrawal of slurry from MSMPR 1 was initiated through a vacuum operation in which ~10% of the crystalliser volume was transferred via a dip pipe to the feed/dissolution vessel every 1/10th of τ. The average

working volume in MSMPR 1 and the feed/dissolution vessel was 90 ml and 250 ml respectively, with ~10 ml transferred between both vessels. On attainment of steady-state, a sample was isolated by means of an integrated sampling and filtration arrangement which rapidly separated product crystals from mother liquor. The CSD of the product crystals was measured in a Malvern Mastersizer® 2000 using a wet dispersion unit with isopropanol as dispersant. The final steady-state concentration of the mother liquor was determined gravimetrically, and the process yield was calculated for each experiment as the amount of product obtained from the crystalliser relative to the amount of available supersaturation using Equation (3.57):

$$Yield = \frac{C_f - C_{ss}^i}{C_f - C_{sat}} \times 100 \tag{3.57}$$

where C_f is the feed concentration to MSMPR 1, C_{sat} is the equilibrium concentration at the specified operating temperature, and C_{ss}^i is the steady-state concentration in the ith crystalliser. The supersaturation is defined as C_{ss}^i/C_{sat}. Steady-state operation was attained when the total counts and SWMCL showed no significant increasing or decreasing trend. This signified that the rate of generation of crystal mass due to secondary nucleation and/or attrition equalled the removal rate of crystals from the MSMPR crystalliser. The total time from start-up to steady-state operation was expressed in terms of a dimensionless quantity, t/τ, known as the mean residence times to steady-state.

3.12.7 Single-stage seeded MSMPR crystallisation

A seeded cooling crystallisation experiment was performed in the single-stage MSMPR to compare the crystallisation process dynamics with that of unseeded cooling crystallisation experiments and assess the seeding effect on steady-state mean crystal size, CSD, and yield of α-GLY. Prior to start-up of the seeded crystallisation experiment, 810 ml of a 0.180 g/g GLY-water solution (saturated at 20 °C) was held at 19 °C in the seed vessel. 90 ml of a 0.180 g/g GLY-water solution was held in MSMPR 1 at 11 °C, well within the metastable zone for GLY-water in an STC (see section 6.2.1 of Chapter 6). 14.6 g (10% w/w of GLY feed solution concentration) of dry-milled α-GLY seeds with a mean size of 41 $\pm$ 0.9 µm were added to the seed vessel and agitated at 400 rpm to distribute evenly throughout the vessel. An impeller speed of 400 rpm was also applied in MSMPR 1 to completely suspend crystals. Once the seed suspension had equilibrated for 30 min, intermittent slurry withdrawal

was initiated in which seed suspension was continuously pumped into MSMPR 1, and ~10% of the crystalliser volume was transferred via a dip pipe to a collection vessel every $1/10^{th}$ of τ. On attainment of steady-state, a sample was isolated via the integrated sampling and filtration arrangement for CSD and imaging analysis, and the final steady-state concentration was determined gravimetrically.

3.12.8 Two-stage MSMPR crystallisation

Unseeded crystallisation experiments were performed in the two-stage MSMPR to investigate the effect of the number of MSMPR stages on steady-state mean crystal size, CSD, and yield of α-GLY. For the cascade study, feed solution and batch suspension preparation were similar to those employed in the single-stage unseeded MSMPR crystallisation. Each MSMPR crystalliser contained a 90 ml GLY-water suspension of 0.275 g/g (saturated at 40 °C) which was heated to 50 °C and held for 30 min for complete dissolution. The clear solutions in MSMPR 1 and 2 were cooled to 20 °C and 10 °C respectively to create the starting batch suspensions. The impeller speed in each MSMPR crystalliser was set to the required rpm for effective mixing, and real-time monitoring of the crystallisation process was via an FBRM probe positioned in MSMPR 2. At steady-state operation, samples were taken from both MSMPR stages for final concentration, CSD, and image analysis.

Chapter 4 Liquid and solid phase axial dispersion performance of the SPC mesoscale crystalliser

4.1 Introduction

Since crystallisation processes deal with slurries of varying density, solids loading, particle size and shape, liquid phase RTD alone provides limited insight into the hydrodynamic experience of particles in continuous flow. Surprisingly, many crystallisation simulations are often performed with the assumption that crystals experience the exact flow conditions as the bulk liquid and share the same RTD, whereas in practice this may not be the case. Zheng and Mackley (2008) previously reported an optimum oscillatory range of $x_0 = 0.5 – 1$ mm and $f = 10$ Hz for liquid phase plug flow in the same platform herein presented. The authors did not, however, investigate the corresponding solid phase axial dispersion at these conditions.

This chapter extends the work by Zheng and Mackley (2008). It presents the detailed characterisation of the liquid and solid phase axial dispersion performance of the SPC mesoscale crystalliser is performed to understand how oscillatory flow conditions can be manipulated to control RTD and approach the behaviour of a perfect PFC, which is essential for providing a uniform hydrodynamic environment for crystals in continuous crystallisation. A newly developed non-intrusive dual backlit imaging technique is benchmarked against traditional conductivity measurements and utilised for homogeneous and heterogeneous RTD experiments. The liquid phase axial dispersion number is determined as a function of Re_o, Re_n, St, and length of the test section, L, using an imperfect pulse injection technique and the axial dispersion model. The solid phase axial dispersion is investigated using heterogeneous experiments and compared with liquid phase dispersion to address the knowledge gap in the handling of solids in the SPC mesoscale crystalliser and identify an optimum oscillatory range for solid-liquid plug flow.

Firstly, an interpretation of fitted RTD curves is performed to provide information on the backmixing behaviour of the SPC mesoscale crystalliser, and an optimal range of oscillatory conditions is identified based on the liquid axial dispersion number estimated. A similar procedure is carried out to determine the corresponding solid axial dispersion in the same range of operating conditions identified for the liquid phase. While comparisons may be made between model parameters determined here for the solid phase and those previously determined by Zheng and Mackley (2008) for the liquid phase, the integrity of the comparisons would be in doubt, since the authors utilised a different measurement technique (intrusive optical probes) and numerical analysis to that employed here.

4.2 Results and discussion

4.2.1 Axial dispersion from dual backlit imaging and conductivity measurements

A typical normalised input curve, output curve and corresponding fitted response curve is shown in Figure 4.1 as determined by the non-invasive dual backlit imaging for a net flow rate of 5 ml min^{-1} ($Re_n = 21$) and $Re_o = 154$ ($x_0 = 0.5$ mm, $f = 10$ Hz). Note that the green-coloured fitted response curve is completely overlaid on the red output curve.

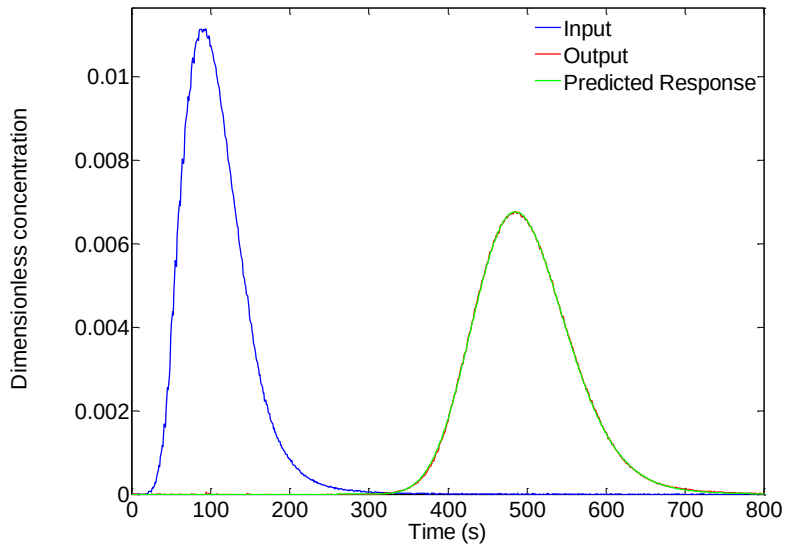

Figure 4.1 Normalised input (blue), output (red), and corresponding fitted response curve (green) from dye tracer backlit imaging measurement. $Re_n = 21$, $Re_o = 154$, $St = 0.8$.

Figure 4.2 shows normalised input and output curves obtained from salt tracer conductivity measurements for oscillatory conditions of $Re_o = 31 - 185$ at $Re_n = 21$. Concentration-time curves (C-curves) obtained from intrusive conductivity probe measurements were significantly broader than those from non-intrusive dual backlit imaging measurements (see Figure 4.5).

Figure 4.3 shows fitted D_{ax}/uL as a function of Re_o for different values of L at $Re_n = 21$. Re_o was varied at a fixed St by changing f. It was observed that tripling the length of the test section lowered D_{ax}/uL measured in the system by a factor of 3.7 ± 0.8, with values approaching near plug flow at higher f. The expression D_{ax}/uL is such that for a given u and D_{ax}, D_{ax}/uL decreases with an increasing test section, L; therefore, the RTD approaches that of a plug in the limit of very long pipe lengths, where advective transport of physical quantities becomes dominant over diffusive transport.

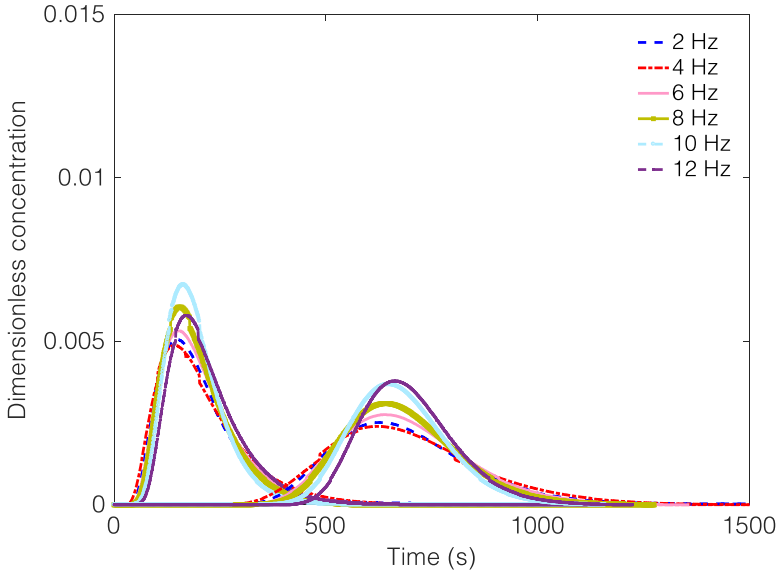

Figure 4.2 Normalised input and output curves from salt tracer measurements. $Re_n = 21$, $Re_o = 31 - 185$, $St = 0.8$.

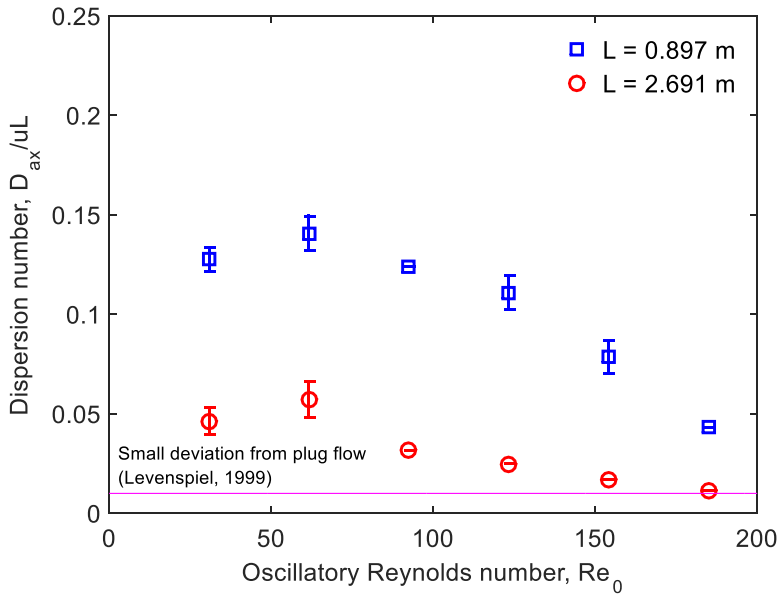

Figure 4.3 D_{ax}/uL determined from conductivity measurements as a function of Re_o for values of L. $Re_n = 21$, $St = 0.8$.

The salt tracer in conductivity measurements was found to have an experimental mean residence time, τ, of 455 $\pm$ 14 s and mean superficial velocity, u, of 5.6 $\times$ 10^{-3} m s^{-1}. The dye tracer in dual backlit imaging measurements had an experimental τ of 443 $\pm$ 12 s and u of 5.9 $\times$ 10^{-3} m s^{-1}. Despite the close matching values for τ and u for both measurement methods, D_{ax}/uL values obtained from the non-intrusive imaging technique were much lower for the same L and Re_n, and fell well within the plug flow region at $Re_o > 93$ (see Figure 4.4). Also, at $Re_o < 93$, large variations in measured D_{ax}/uL were obtained in intrusive conductivity measurements. Higher D_{ax}/uL values from

intrusive conductivity measurements were the result of significantly broader RTD curves. The reason for broader curves is likely due to a time lag in signal change in the probes. This may be caused by repeated salt deposition on the surface of electrodes which decreases the sensitivity of the probes over time. Issues with conductivity measurements have previously been reported by Fitch and Ni (2003), where mass deposition onto electrodes was also experienced. Contrarily, the pixel-based measurements of the dual backlit imaging technique are highly sensitive to subtle changes in transmitted light, thus making it possible to precisely capture concentration changes through the SPC meso-tube wall without delay.

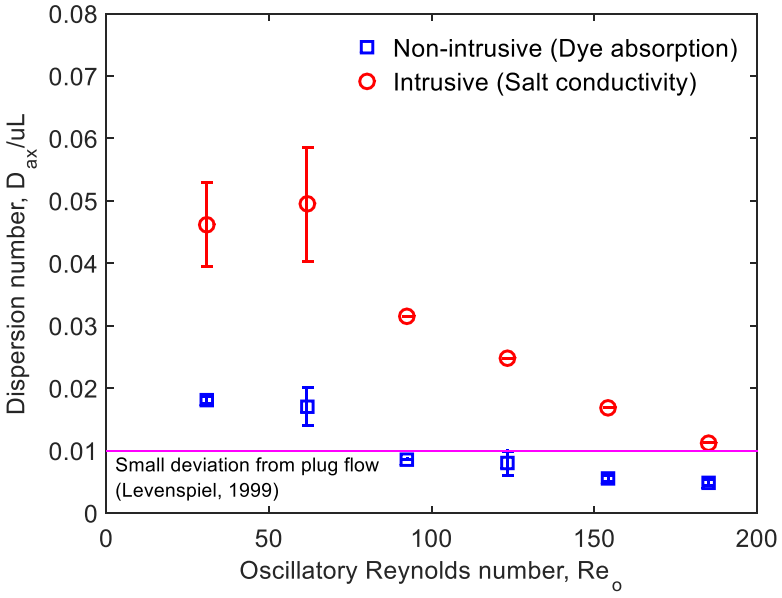

Figure 4.4 Comparison of D_{ax}/uL values obtained from conductivity measurements and dual backlit imaging technique. $Re_n = 21$, $L = 2.691$ m, $St = 0.8$.

The results of the comparative study confirmed non-intrusive dual backlit imaging as a more reliable technique for determining hydrodynamic model parameters. Other benefits of the technique include non-disturbance of the fluid flow and the avoidance of probe fouling which are commonly experienced with traditional conductivity measurements (Ni et al., 2002; Fitch and Ni, 2003). Additionally, the technique may be utilised for solid phase RTD studies, which is a shortcoming of conductivity measurements. In view of its demonstrated reliability, the dual backlit imaging technique was utilised for all liquid and solid phase RTD studies carried out in this work. Other non-intrusive and intrusive techniques such as laser induced fluorescence (Fitch and Ni, 2003) and absorbance spectrometry (Reis et al., 2004; 2010; Palma and Giudici, 2003; Zheng and Mackley, 2008; Siddique et al., 2015; Kacker et al., 2017) respectively, have been employed as preferred alternatives to conductivity measurements for liquid RTD determination.

4.2.2 Liquid phase RTD studies

Experimental C-curves for over sixty experiments were derived from dye absorption measurements, and the effects of Re_o, Re_n, and St on the liquid phase axial dispersion performance were investigated. Figure 4.5 and Figure 4.6 show the normalised input and output curves and corresponding model response $M(\theta)$ obtained from dye tracer measurements over the range of oscillations $Re_o = 31 – 185$ ($St = 0.8$, $f = 2 – 12$ Hz).

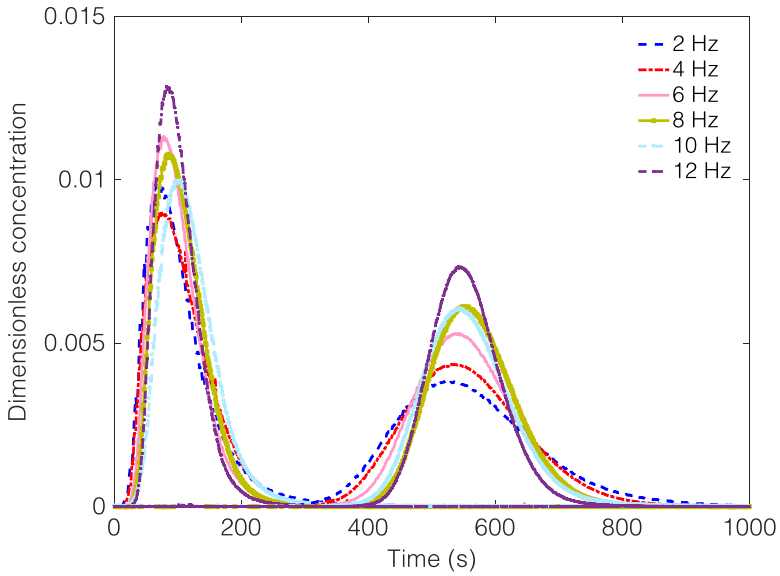

Figure 4.5 Normalised input and output curves from dye tracer measurements. $Re_n = 21$, $Re_o = 31 – 185$, $St = 0.8$.

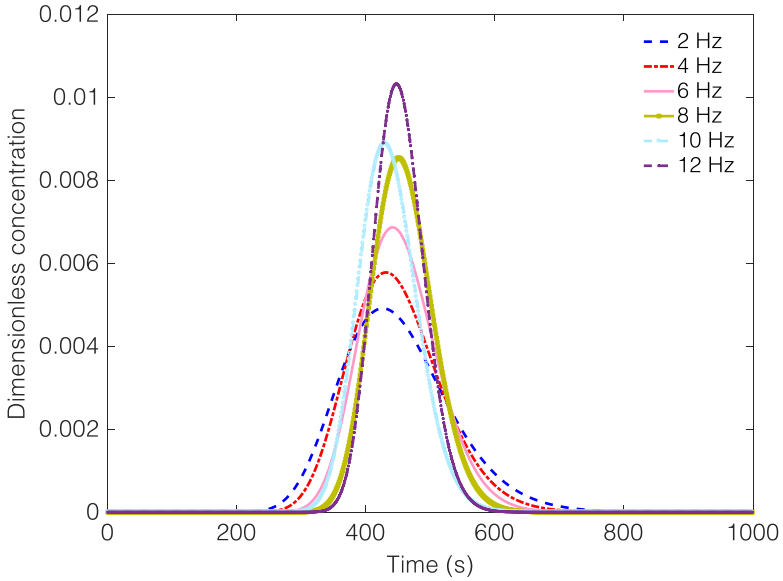

Figure 4.6 Model response, $M(\theta)$, for the liquid phase. $Re_n = 21$, $Re_o = 31 – 185$, $St = 0.8$.

On increasing f, the output curves showed less broadening, indicating a reduction in the spread of the tracer within the test section. This is easier to observe in the $M(\theta)$ curves (Figure 4.6) which are unaffected by different pulse input shapes, as they are calculated response curves for a Dirac pulse input. $M(\theta)$ curves were calculated by the axial dispersion model using the estimated D_{ax}/uL and τ as inputs. Figure 4.7 summarises the experimental mean residence times, τ, of the tracer for different oscillation conditions at Re_n of 21. It was concluded that τ remains approximately constant for all oscillatory conditions, with an average of 442 $\pm$ 11 secs. The flow rate used corresponds to a hydraulic time of ca. 421 secs in the test section, which is 5% shorter than the average experimentally determined τ for the tracer. A value of τ similar to the hydraulic residence time means that the mean residence time of the dye tracer is similar to the mean liquid hydraulic residence time, whereas values of $\tau \gg$ hydraulic residence time suggest that the tracer is delayed within the test section. The average superficial velocity, $u = L/\tau$, for all oscillatory conditions was experimentally determined as 6.0 × 10^{-3} $\pm$ 0.0002 m s^{-1}, which corresponded to a volumetric flow rate of 5 ml min^{-1}. For experiments performed at 2 ml min^{-1}, the average superficial velocity was experimentally determined to be 2.7 × 10^{-3} $\pm$ 0.0001 m s^{-1}.

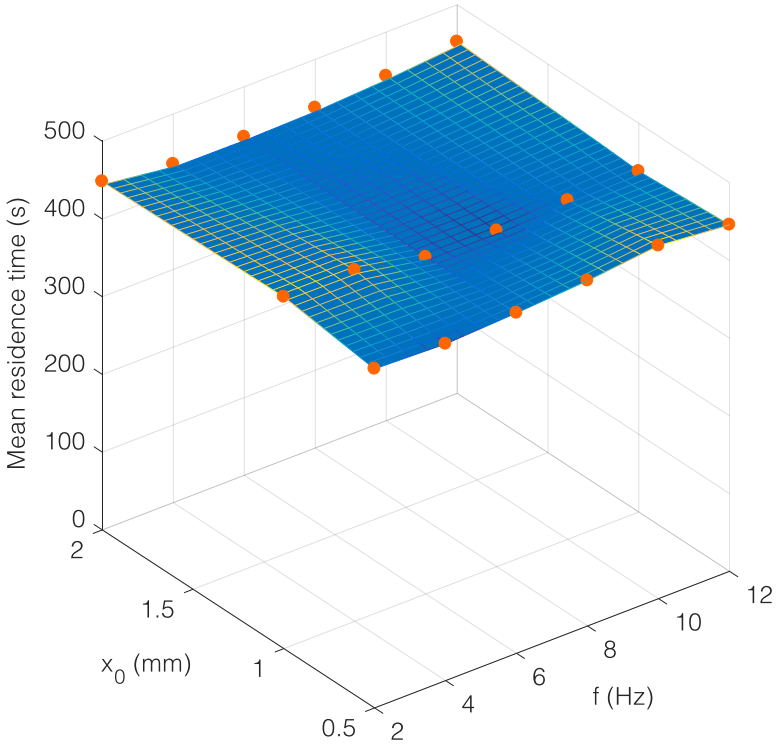

Figure 4.7 Averaged mean residence time of dye tracer for various values of x_0 and f. $Re_n = 21$.

Figure 4.8 shows the effect of net flow on D_{ax}/uL. At higher Re_n, D_{ax}/uL decreased across the range of Re_o investigated. This confirms that increasing net flow improves the overall RTD performance in the SPC mesoscale crystalliser. Interestingly, increasing Re_n to 21 provided greater reductions in D_{ax}/uL at $Re_o < 100$. However, beyond Re_o of 100 the differences in D_{ax}/uL for both net flows were much smaller. This shows that as oscillations become more intense, the radial mixing within the meso-tube is increasingly controlled by oscillatory flow than net flow. In this manner, fluid mixing is decoupled from net flow in this device.

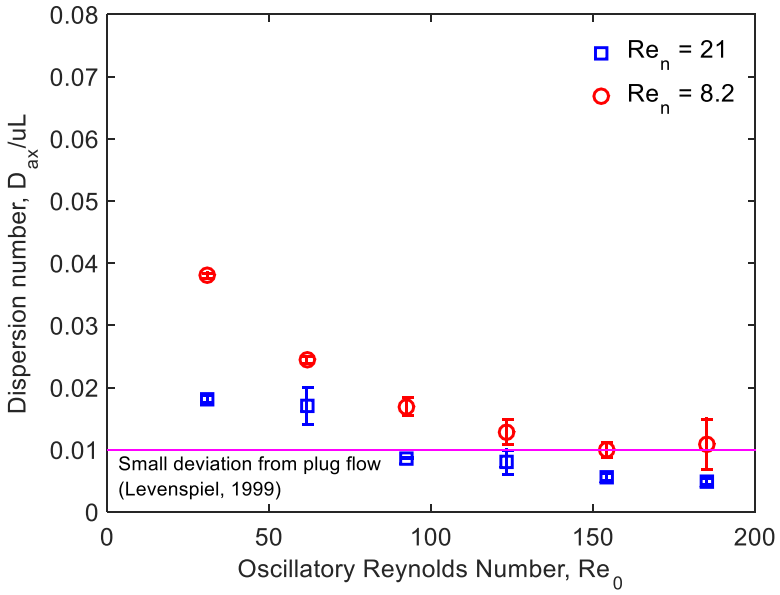

Figure 4.8 D_{ax}/uL determined from dye tracer measurements as a function of Re_o for different net flows. $St = 0.8$; $f = 2$ – 12 Hz.

Figure 4.9 shows the effect of St on D_{ax}/uL. In the case of no oscillation, a D_{ax}/uL of 0.064 was obtained indicating that dispersive transport was dominant in the test section. For such condition, the flow is laminar and significant axial velocity gradients exist between the wall and centre of the meso-tube, hence RTD is broad. The coupling of net flow with a smooth fluid oscillation at $Re_o = 31$ ($St = 0.8$, $f = 2$ Hz) drastically reduced D_{ax}/uL to 0.0182, highlighting the benefits of oscillatory flow for improved RTD performance. With the introduction of a small fluid oscillation, vortices are formed in the inter-constriction regions, which disrupt axial velocity profiles and induce radial mixing; in this way dispersive transport is limited. The SPC mesoscale crystalliser was found to show more sensitivity to changes in St than f, as opposed to a conventional sharp-edged OBR (Stonestreet and Van Der Veeken, 1999). For instance, at $f = 2$ Hz, halving St from 0.8 ($Re_o = 31$) to 0.4 ($Re_o = 62$) increased D_{ax}/uL by 0.0088; doubling f from 2 Hz ($Re_o = 31$, St = 0.4) to 4 Hz ($Re_o = 62$, St = 0.4)

only decreased D_{ax}/uL by 0.0011. Again, halving St from 0.4 to 0.2 also increased D_{ax}/uL for the range of $Re_o = 62 – 185$, however for $Re_o > 185$, this St effect on D_{ax}/uL was less pronounced.

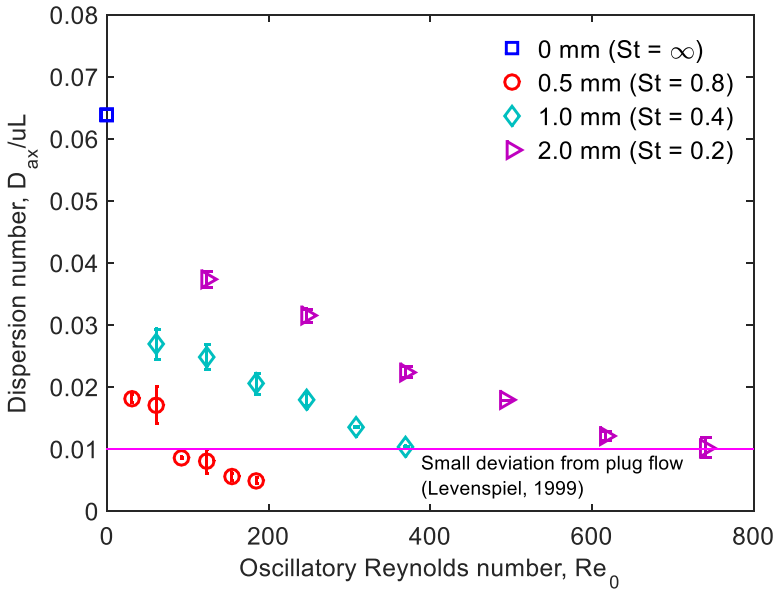

Figure 4.9 D_{ax}/uL determined from dye tracer measurements as a function of Re_o at different Strouhal numbers. $Re_n = 21$; $f = 2 – 12$ Hz.

The effect of St on axial dispersion is such that an effective minimum is achieved at $St = 0.8$ ($x_0 = 0.5$ mm), followed by a gradual worsening with decreasing St. This is similar behaviour to that observed by Zheng and Mackley (2008) for the same platform in the range of $Re_n = 10 – 19$. The results also confirm findings by Mohd-Rasdi et al. (2012) for a similar SPC design where optimum plug flow was obtained at $St = 0.8$. At $St < 0.8$ the size of eddies generated is bigger, and vortices tend to propagate into the adjacent inter-constriction cavity thereby creating axial dispersion. On the other hand, a gradual increase in f narrows the RTD by reducing D_{ax}/uL for all St. Minimum dispersion was obtained at 12 Hz for all St investigated. This corresponds to findings by Zheng and Mackley (2008), where minimum D_{ax}/uL values occurred between $f = 10 – 12$ Hz. Previous work by Reis et al. (2010) has shown that above 12 Hz significant worsening of RTD performance occurs for $St = 0.8$; thus, a point of inflection is observed. Minimum D_{ax}/uL values of $4.9 – 8.6 \times 10^{-3}$ were obtained in the region of $Re_o = 93 – 185$ for different oscillation f at $St = 0.8$. This corresponded to a φ of 4 – 9 which is in the range reported for optimal plug flow performance in mesoscale OFRs (Phan et al., 2011). As expected, minimum D_{ax}/uL values obtained by Zheng and Mackley (2008) were in a lower range of $1.0 – 2.0 \times 10^{-3}$ for a test section ~2.6 times greater than the length of L used in this work. This suggests that for the full-length SPC mesoscale crystalliser ($L\sim$ 5.4 m) utilised in Chapter 6, plug flow operation will be achieved for oscillation $f > 6$ Hz for all St investigated here.

Interestingly, for $St < 0.8$, higher oscillation frequencies were required to achieve similar D_{ax}/uL values to those obtained for $St = 0.8$, suggesting an undesired lower efficiency of mixing at lower St.

The behaviour of the SPC mesoscale crystalliser suggests that operating at low x_0 and high f minimises axial dispersion and favours plug flow like performance. Numerous results have shown that for conventional SEPC OBRs (12 – 69 mm I.D.), relatively higher x_0 and lower f favour plug flow behaviour (Stonestreet and Veeken, 1999; Harvey et al., 2001; Smith and Mackley, 2006; Phan and Harvey, 2010; Siddique et al., 2015). This contrast is mainly attributed to differences in the fluid oscillation requirement with respect to volume. It follows that larger volume (conventional) SEPCs require higher input axial velocities (at the same f) to generate substantial radial velocities that have any significant effect on axial dispersion. On the contrary, small-volume mesoscale OFRs like the SPC mesoscale crystalliser would require only a small x_0 to generate sufficient radial velocities. Since oscillation f governs the rate of eddy generation, small-volume OFRs can handle higher f without creating an imbalance between eddy generation and propagation; as increasing f only serves to optimise the radial distribution of the tracer within inter-constriction cavities. However, with higher x_0 required for effective eddy propagation in large-volume SEPCs, it is possible that high f create an imbalance and radial mixing breaks down (Smith and Mackley, 2006).

4.2.3 Solid phase RTD studies

Results from liquid phase RTD studies identified $St = 0.8$ ($x_0 = 0.5$ mm) as most favourable for minimising axial dispersion in the SPC mesoscale crystalliser. Accordingly, it was necessary to determine the axial dispersion experienced by a suspension of polystyrene particles for a range of frequencies at this St. Therefore, experiments were performed at a flow rate of 5 ml min^{-1} ($Re_n = 21$) and at oscillatory conditions $x_0 = 0.5$ mm and $f = 2$, 4, 6, 8, 10, 12 Hz giving an investigated mixing range of $Re_o = 31$ – 185. In the absence of oscillatory flow, particles injected into the test section settled to the bottom of the meso-tube due to insufficient radial velocity to overcome particle settling velocity ($u_p = 0.0044$ m s^{-1}). The introduction of sufficient fluid oscillation achieved off-bottom suspension of particles in all experiments i.e. peak oscillatory velocity, $u(t)_{max} = 2\pi f x_0$, required for particle suspension ranged from 0.0063 – 0.0377 m s^{-1}. Figure 4.10 and Figure 4.11 show the normalised input and output curves and the corresponding model response curves, $M(\theta)$, obtained from particle tracer measurements over the range of $Re_o = 31$ – 185 ($St = 0.8$, $f = 2$ – 12 Hz). A similar trend is observed in that the $M(\theta)$ curves become increasingly narrower as f is increased, indicating less spread of solid particles in the test section.

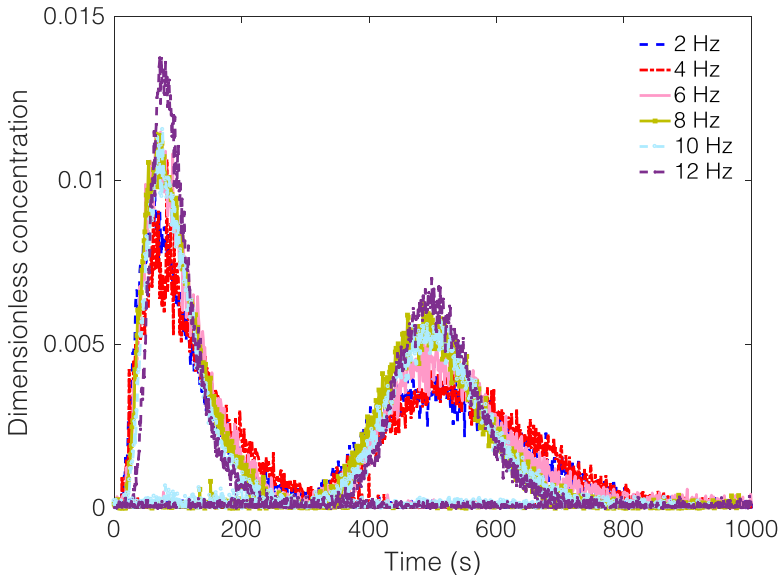

Figure 4.10 Normalised input and output curves from particle tracer measurements. $Re_n = 21$, $Re_o = 31 – 185$, $St = 0.8$.

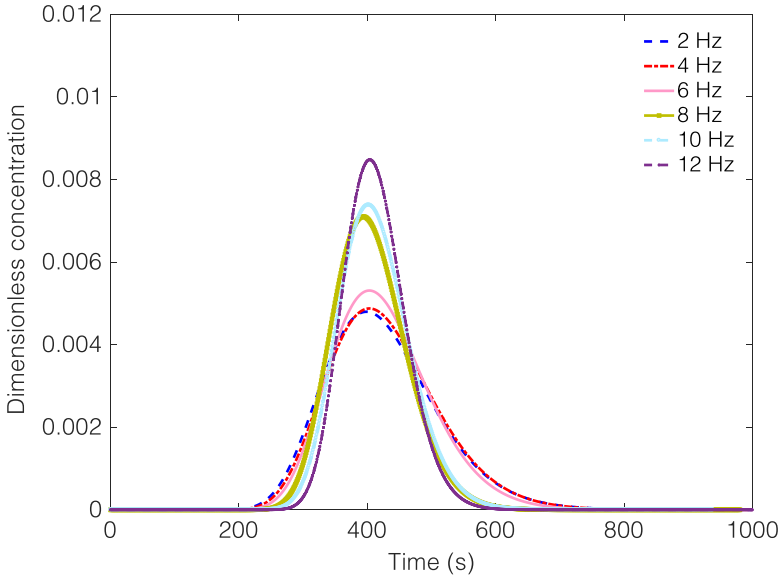

Figure 4.11 Model response, $M(\theta)$, for the solid phase. $Re_n = 21$, $Re_o = 31 – 185$, $St = 0.8$.

Figure 4.12 shows D_{ax}/uL of the liquid and solid phase as a function of Re_o. At a relatively low Re_o of 31 ($f = 2$ Hz), particles experience much more dispersion than the continuous phase due to poor radial mixing in the tube. With poor radial mixing, the particle settling velocity dominates, and particles do not flow with the bulk fluid. The fluid radial velocity must therefore be significantly higher than the particle settling velocity to achieve efficient suspension. It is evident that increasing oscillation f facilitates better particle suspension and allows particles experience similar flow conditions to the

liquid phase. At $Re_o = 185$, where $u(t)_{max}$ is more than sufficient to effectively suspend particles, D_{ax}/uL of the solid phase falls well within the plug flow region and close to the value for the liquid phase. This indicates that density effects are largely suppressed, although not completely overcome since the solid phase is unable to experience the same low degree of dispersion as the liquid phase. Since both phases sharing the same RTD is not of paramount importance, as long as they are within the region of plug flow, operating at Re_o of 185 would be less efficient since it requires a higher energy input. A trade-off with a lower energy input is therefore achievable by operating at an optimum Re_o of 93 ($St = 0.8$, $f = 6$ Hz) in the full-length SPC mesoscale crystalliser having an L of 5.4 m.

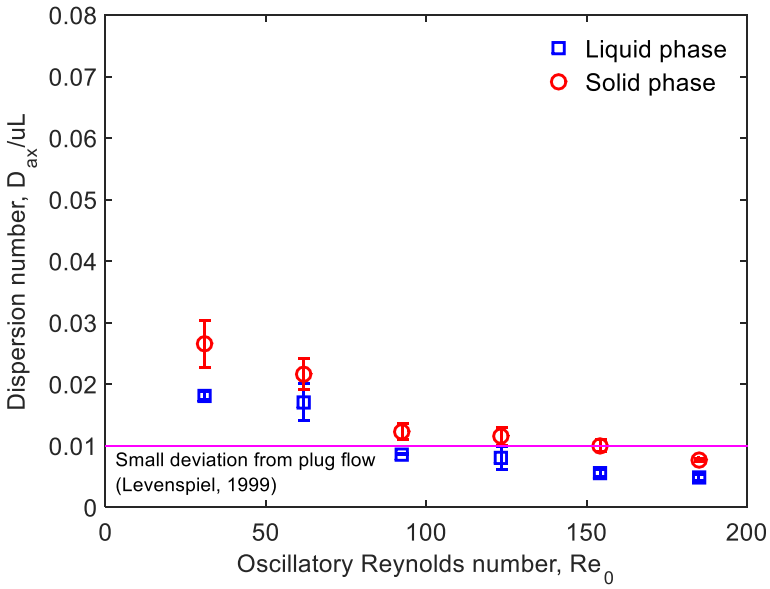

Figure 4.12 D_{ax}/uL as a function of Re_o for the liquid and solid phase. $Re_n = 21$, $St = 0.8$.

Figure 4.13 shows that polystyrene particles spent more time in the test section for all frequencies investigated, with the longest mean residence times occurring at lower f. As expected at higher f, the time spent in the test section was closer to that of the dye tracer. It is worth stating that these results are for solids with a density closer to that of water. For APIs with much higher crystal densities and settling velocities, we can expect greater differences in the mean residence times and axial dispersions experienced by the solid and liquid phase.

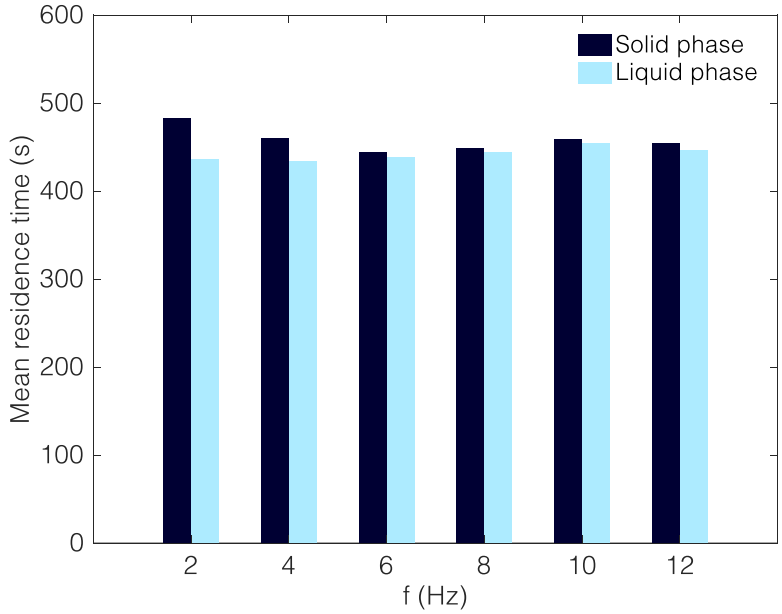

Figure 4.13 Mean residence times of the solid and liquid phase for different f. $Re_n = 21$, $St = 0.8$.

4.3 Conclusions

This chapter has presented the SPC mesoscale crystalliser as a tubular device capable of achieving good plug flow mixing at low net flows. It has been established that low x_0 and high f favour near plug flow performance in the SPC mesoscale crystalliser, in sharp contrast to relatively higher x_0 and lower f preferred by conventional SEPC OBRs. Speculations about the flow behaviour of solids have been put to rest as injected particles were found to have a different RTD to the continuous phase in the range of Re_0 determined for optimum liquid axial dispersion performance. Particles were also found to spend longer times in the system compared to the liquid. A suitable operating range was therefore identified for solid and liquid plug flow as $Re_0 = 93 – 185$ ($\varphi = 4 – 9$). The results and conclusion herein confirm that the SPC mesoscale crystalliser can provide plug flow like RTDs for slurries. Importantly, this work demonstrates that even for small and less dense particles, there are significant differences between liquid and solid phase axial dispersion at low mixing intensities, however at plug flow conditions where radial velocities are higher, particles may experience almost similar dispersion characteristics as the bulk liquid or solution in a crystallisation process.

Overall, the results for the homogeneous and heterogeneous phases show that the SPC mesoscale crystalliser gives precise control of the hydrodynamic experience through careful manipulation of oscillatory conditions and net flow. This is essential for effectively operating continuous crystallisation processes to obtain consistent particle attributes. In this chapter, an understanding of how oscillatory flow impacts on axial dispersion has been gained; in the next chapter, the relationship between

oscillatory conditions and the heat transfer performance of the SPC mesoscale crystalliser will be investigated. This will identify the optimum hydrodynamic conditions for creating a highly reliable environment for crystal formation and growth.

Chapter 5 Heat transfer characteristics of the SPC mesoscale crystalliser

5.1 Introduction

The work presented in this chapter was published as a journal article in the International Journal of Heat and Mass Transfer (Onyemelukwe et al., 2018a). The heat transfer performance of the SPC meso-tube is reported for the first time for both steady flow and unsteady oscillatory flow conditions. A detailed geometric description of the SPC meso-tube is provided in section 3.3 of Chapter 3. Experimental values of the tube-side Nusselt number, Nu_t, are determined using steady-state heat transfer experiments, accompanied by an estimability analysis to identify the factors governing tube-side heat transfer performance in the SPC meso-tube. A new empirical correlation is for the first time developed to describe the heat transfer characteristics of the SPC meso-tube, and accurately predict the tube-side Nusselt number. This chapter will provide more insight into the effect of oscillatory flow conditions on heat transfer performance of the SPC meso-tube for cooling crystallisation.

The SPC meso-tube is herein considered as a concentric tube heat exchanger for heat transfer experiments. The geometry of the SPC meso-tube differs drastically from the sharp-edged baffled tube for which Mackley and Stonestreet (1995) derived a general Nu_t correlation provided in Equation (5.1). The contrasting baffle type and scale of these tubes are chiefly responsible for limiting applicability of the Mackley-Stonestreet correlation to the SPC meso-tube. The sharp-edged baffled tube investigated by the authors had a D of 12 mm, a d_0 of 7 mm ($\alpha = 0.34$), and a baffle spacing of 18 mm, giving it an l/D of 1.5.

$$Nu_t = 0.0035{Re_n}^{1.3}Pr^{0.3} + 0.3\left[\frac{{Re_o}^{2.2}}{(Re_n+800)^{1.25}}\right] \tag{5.1}$$

where Pr is the Prandtl number.

A tube of its scale, as previously mentioned in section 4.2.2 of Chapter 4, requires much stronger oscillations than the SPC meso-tube to provide efficient mixing and near plug flow behaviour. The Mackley-Stonestreet correlation was derived from experiments in the range $Re_n = 100 – 1200$ and $Re_o = 300 – 800$, an operating range deemed impractical for the SPC meso-tube, since most of its advantages for crystallisation would be lost.

5.2 Results and discussion

5.2.1 Heat transfer at steady flow conditions

Heat transfer experiments were performed in a plain meso-tube and the SPC meso-tube to evaluate the effect of smooth periodic constrictions on the heat transfer performance for the case of steady non-oscillatory flow conditions. Both tubes had an internal diameter of 5 mm. Figure 5.1 shows Nu_t as a function of Re_n for steady non-oscillatory flow, and the corresponding prediction by the Mackley-Stonestreet general correlation given in Equation (5.1). For the plain meso-tube, an increase in Nu_t was observed as Re_n increased, confirming a contribution to heat transfer that is expected from an increase in forced convection within the tube.

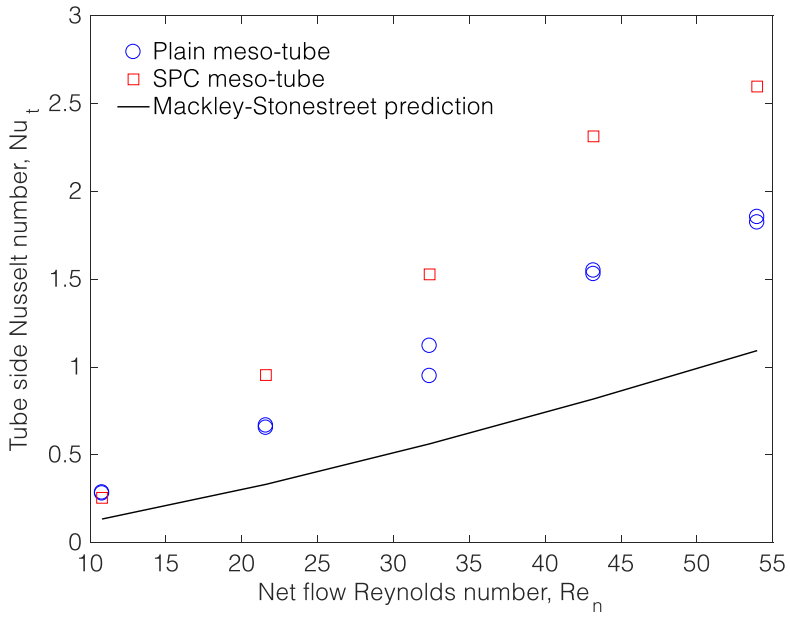

Figure 5.1 Nu_t values obtained for steady flow in a plain meso-tube and the SPC meso-tube, compared with Mackley-Stonestreet predicted values. $Re_o = 0$; Re_n = 10.79 – 53.97.

Comparisons could not be made between Nu_t values for the plain meso-tube and standard literature correlations for laminar flow in circular smooth-walled tubes. For instance, the experimental range of applicability of the empirical Sieder-Tate correlation for smooth tubes (Sieder and Tate, 1936) does not extend to such low Re_n ranges for which Nu_t values were determined in the plain meso-tube. Hausen's correlation (Hausen, 1959) for a broad range of Graetz numbers, $Gr = (Re_n Pr \frac{D}{L_1})$, was equally not applicable since fully developed flow had not been achieved in the plain meso-tube, a condition for which $Nu_t \approx 3.66$.

For the SPC meso-tube, a stronger increase in Nu_t was obtained with increasing Re_n; this is not only attributed to the increased SAV from the presence of smooth constrictions in the tube, but also to a level of secondary mixing resulting from the formation of recirculation zones between the constrictions, as reported by Reis et al. (2005). Smooth constrictions restrict fluid flow and promote eddy formation; consequently, fluid velocities are increased at regions around the constrictions thus enhancing the heat transfer coefficient. From Figure 5.1, a maximum Nu_t of 1.86 was achieved in the plain meso-tube at a maximum Re_n of 53.97. This Nu_t value was found to be ~10 times lower than the maximum value obtained by Mackley and Stonestreet (1995) in a 12 mm I.D. plain tube at a significantly higher Re_n of ~1200. Re_n beyond 53.97 could not be achieved in the SPC meso-tube due to pump limitations. The maximum Nu_t obtained for steady non-oscillatory flow in the SPC meso-tube was 2.60 at Re_n = 53.97, which is 1.4-fold improvement over the Nu_t obtained in the plain meso-tube for the same value of Re_n. At the lowest Re_n investigated, the SPC meso-tube and plain meso-tube provided the same Nu_t. Although the SPC meso-tube had a smaller overall heat transfer area (A_{SPC} = 0.011 m^2) compared to the plain meso-tube (A_{plain} = 0.014 m^2), the resulting SAV was higher at 1190 m^{-1} compared to 1138 m^{-1} for the plain meso-tube. The significant heat transfer enhancement arising from a higher SAV and presence of smooth constrictions in the SPC meso-tube is in general agreement with behaviour observed in the conventional sharp-edged baffled tube by Mackley and Stonestreet (1995). Simulation results obtained by Solano et al. (2012) for similar non-oscillatory conditions (Re_n = 10, Re_o = 0, Pr = 5.5) in a 5 mm I.D. meso-tube, showed a heat transfer augmentation of 10% when helical coil inserts were included.

When applied to predict steady non-oscillatory flow heat transfer performance in the SPC meso-tube for the range Re_n = 10.79 – 53.97, the Mackley-Stonestreet correlation (Equation (5.1)) was found to significantly under-predict Nu_t values by an average of 58% (see Figure 5.1). For unsteady flow heat transfer in the range Re_o = 39 – 197, the correlation under-predicted Nu_t by as much as 65% at the lowest Re_o, and over-predicted Nu_t by as much as 1974% at the highest Re_o. This suggested the SPC meso-tube displayed a different relationship to that described by the Mackley-Stonestreet correlation.

5.2.2 Heat transfer at unsteady oscillatory flow conditions

A second set of experiments was performed to investigate what effect an unsteady oscillatory flow would have on the heat transfer performance of the SPC meso-tube relative to steady non-oscillatory flow. For each Re_n, f was varied from 0 – 10 Hz to give a range of Re_o at a fixed St of 0.8

($x_0 = 0.5$ mm). Figure 5.2 shows the heat transfer obtained in the SPC meso-tube for increasing values of Re_o at Re_n = 10.79. The introduction of a small oscillatory element ($Re_o = 39$) caused a 22% improvement in heat transfer performance ($Nu_t = 0.337$) from the case with no oscillation ($Nu_t = 0.276$). A maximum 31% improvement was obtained at $Re_o = 118$, after which Nu_t plateaued off, and no further heat transfer enhancement (increment in U_{21}) was detected in the system from measured steady-state data.

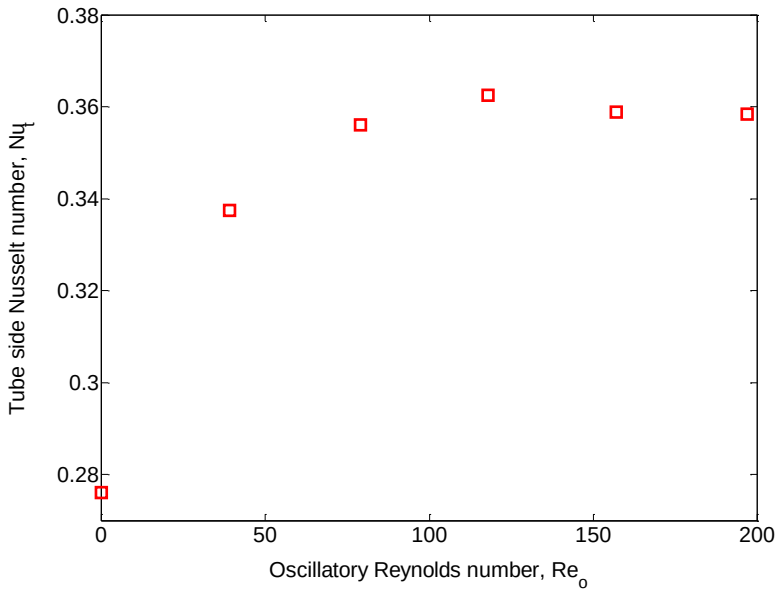

Figure 5.2 Nu_t as a function of Re_o. Re_n= 10.79, St = 0.8.

Subsequent fixed net flow experiments reproduced this limited effect of oscillation on heat transfer enhancement. A stacked plot of these experiments in Figure 5.3 highlights a weaker sensitivity of Nu_t to Re_o, and shows that changing Re_n has a stronger effect on heat transfer performance than changing Re_o. Higher values of Nu_t were obtained at higher Re_n, again highlighting the steady flow contribution to higher rates of heat transfer. Figure 5.3 and Figure 5.4 signify that adding an oscillatory component onto a steady net flow contributes an inappreciable difference to heat transfer performance in the SPC meso-tube. Table 5.1 demonstrates the diminishing effect of oscillations that is exhibited when net flow is increased.

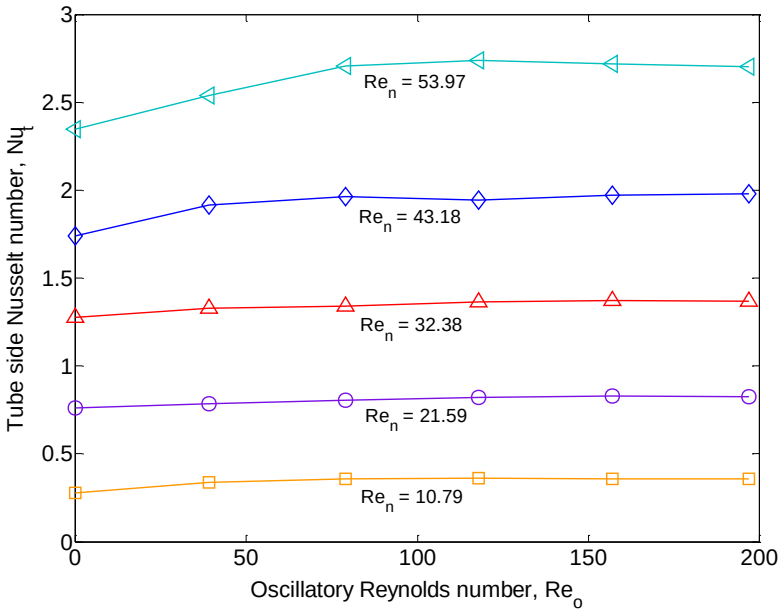

Figure 5.3 Nu_t as a function of Re_o. f = 0 – 10 Hz, Re_n= 10.79 – 53.97, St = 0.8.

Table 5.1 % improvement in Nu_t versus non-oscillatory case

Re_n	Re_o = 39		Re_o = 79		Re_o = 118		Re_o = 157		Re_o = 197	
	φ	% imp	φ	% imp	φ	% imp	φ	% imp	φ	% imp
10.79	3.6	22.2	7.3	29.0	10.9	31.3	14.6	29.9	18.3	29.8
21.59	1.8	2.9	3.7	5.6	5.5	7.7	7.3	8.5	9.1	8.2
32.38	1.2	4.0	2.4	4.9	3.6	6.7	4.8	7.4	6.1	7.1
43.18	0.9	10.2	1.8	12.8	2.7	11.7	3.6	13.3	4.6	13.7
53.97	0.7	8.2	1.5	15.3	2.2	16.8	2.9	15.8	3.7	15.2

Velocity ratio, $\varphi = Re_o/Re_n$

On inspecting Table 5.1, three observations are made:

i. For each set of Re_o the greatest % improvement to heat transfer occurred at the lowest Re_n (or highest velocity ratio, φ). Interestingly, the % improvement dropped off drastically for lower values of φ.

ii. For almost all sets of Re_n, the maximum % improvement appeared to be attained between Re_o = 118 – 157.

iii. It could be argued for all sets of Re_n that beyond Re_o of 39 (f = 2 Hz), the % improvement obtained with respect to oscillatory velocity is insignificant (see Figure 5.5), indicating no further room for heat transfer enhancement in the SPC meso-tube.

The maximum Nu_t obtained was of the order 2.74 at Re_o = 118, which was a 1.2-fold increase over the non-oscillatory result at the same Re_n of 53.97. The effect of oscillation f on the heat transfer performance in the SPC meso-tube contrasts sharply from what has been observed in the sharp-edged

baffled tube. Experimental results by Mackley and Stonestreet (1995) for the baffled tube showed that varying f (at constant St) has a strong effect on heat transfer, and that Nu_t increases almost linearly with Re_o. On the other hand, variations in St had only a small effect on the heat transfer performance. This dissimilarity can be attributed to the difference in scale of the tubes. The smaller-diameter SPC meso-tube has a greater surface area to volume ratio (SAV = 1190 m^{-1}) than the baffled tube (SAV ≈ 389 m^{-1}). As the hot process fluid enters the SPC meso-tube, the abundant heat transfer surface area facilitates rapid heat transfer to the annulus fluid and a depletion of temperature driving force occurs exponentially along the tube according to the heat transfer model (see section 3.10.2 of Chapter 3). The introduction of an oscillatory element improves radial velocities and convective heat transfer, thus leading to faster temperature decay in a shorter distance. The pseudo-plateauing of Nu_t with Re_o is a caused by the insufficient driving force available for further heat transfer due to the process fluid temperature closely approaching the wall temperature at the tube outlet. Since Nu_t is only dependent on the fluid dynamics, its time-averaged value should be the same throughout the meso-tube and should increase with Re_o. However, due to the driving force becoming too small to measure accurately at the outlet, accuracy is lost in determining Nu_t. In view of this, significant heat transfer augmentation from oscillatory flow would only be detectable in a much shorter SPC meso-tube where the approach temperature is not too small, and temperature driving force can be more accurately measured. Due to practical limitations, it was not possible to capture temperature readings at intermediate points along the SPC meso-tube.

Figure 5.4 reveals the dependency of oscillatory flow heat transfer enhancement on the steady flow component. The greatest % improvement from steady flow was obtained by doubling Re_n from 10.79 – 21.59. This corresponded to the greatest decline in % improvement from oscillatory flow. As net flow increased, the % improvement to Nu_t from the steady flow component briefly passed through a maximum and subsequently plateaued owing to further depletion of temperature driving force at higher Re_n in the SPC meso-tube.

The dependency observed is such that a stronger steady flow contribution to heat transfer is accompanied by a weaker oscillatory flow contribution and vice versa, as dictated by the overall driving force available. Also, since the overall driving force becomes increasingly limited as Re_n is increased, the heat transfer enhancement due to oscillatory flow is effectively damped at higher Re_n.

The effect of St on the heat transfer performance was also studied by varying x_0. Figure 5.5 shows Nu_t as a function of the maximum oscillatory velocity, $2\pi f x_0$ (m s^{-1}). For this scale, it is evident that the heat transfer performance has minimal dependence on oscillatory velocity and is impaired by lower St.

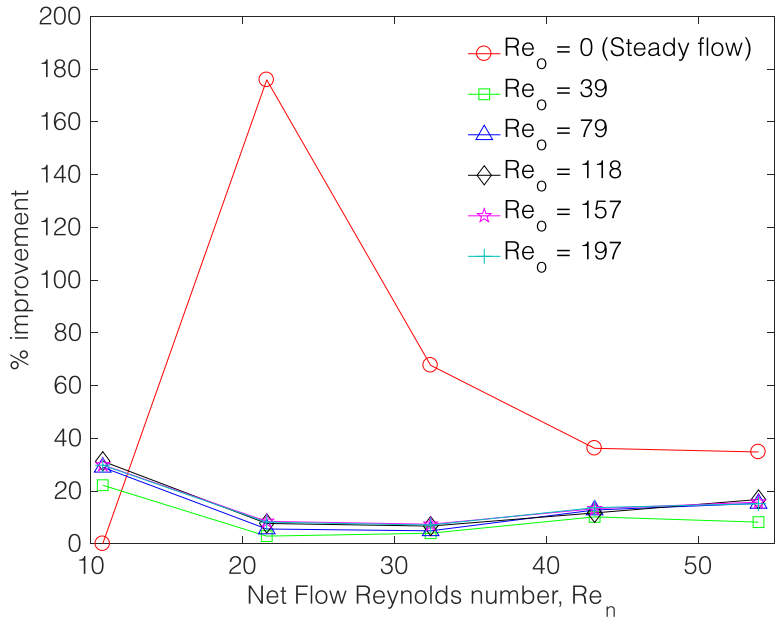

Figure 5.4 % improvement in Nu_t as function of Re_n. Re_o= 0 – 197, St = 0.8.

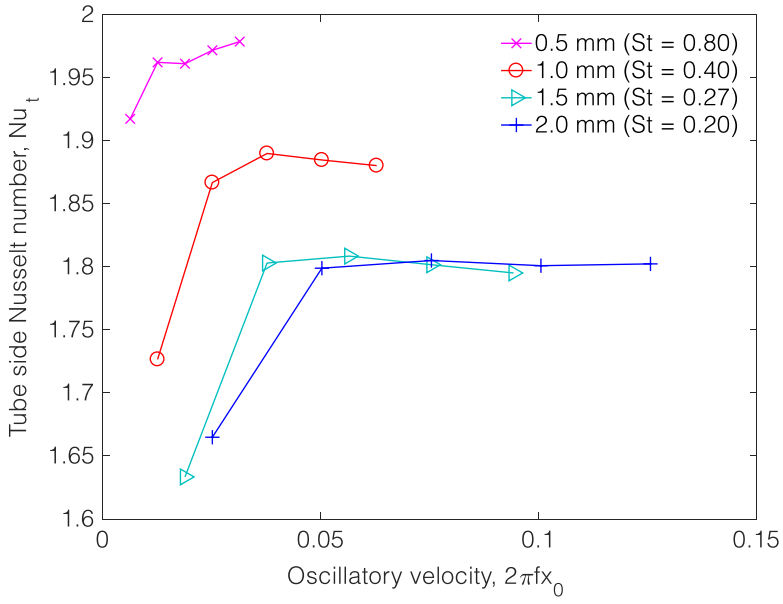

Figure 5.5 Tube-side heat transfer as a function of $2\pi f x_0$ for oscillatory flow. Re_n = 43.18. f = 2 – 10 Hz, St = 0.2 – 0.8.

In Figure 5.5, the SPC meso-tube exhibited a sharp increase in Nu_t (between 2 – 10% depending on St), followed by a plateauing beyond $f = 6$ Hz. Unsurprisingly, the maximum Nu_t was obtained at St of 0.8 ($x_0 = 0.5$ mm), which coincides with the optimal St identified in 0 for good plug flow mixing in the SPC meso-tube. For such small magnitudes of Nu_t, the Strouhal number can be said to have a significant effect on heat transfer in the SPC meso-tube. Moreover, studies have shown that the fluid mechanics in mesoscale OFRs are much more sensitive to St (Phan and Harvey, 2010).

5.3 Empirical correlation for the tube-side Nusselt number

5.3.1 Identification of parameters and experimental fitting

Figure 5.6 describes the relationship between the tube-side heat transfer, steady flow, and unsteady oscillatory flow in the SPC meso-tube. Re_n was varied from 10.79 – 53.97 and the sets of Re_o = 39, 79, 118, 157, 197 on the plot correspond to f = 2, 4, 6, 8, 10 Hz respectively. Overall, in the SPC meso-tube higher rates of heat transfer were achieved at higher Re_n values by superimposing an oscillatory element on steady net flow. At higher Re_n, the oscillatory curves diverge from the steady flow curve. This is in stark contrast to the relationship observed in the conventional sharp-edged baffled tube, where at larger values of Re_n, the best-fitted oscillatory curves tend asymptotically towards the best-fitted steady flow curves (Mackley and Stonestreet, 1995).

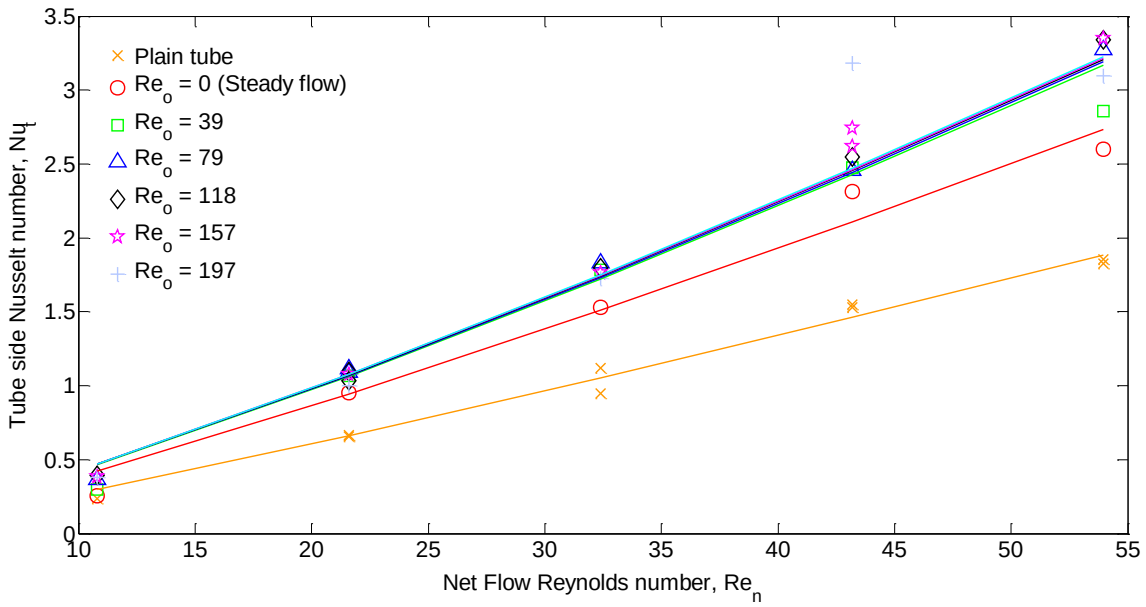

Figure 5.6 Experimental and best-fitted Nu_t as a function of Re_o and Re_n for the SPC meso-tube. St = 0.8.

An empirical correlation was developed to describe the dependency of Nu_t on steady flow and oscillatory flow in the SPC meso-tube. Equation (5.2) shows the structure of this correlation which is based upon the Mackley-Stonestreet correlation in Equation (5.1). A total of 7 parameters that were considered and represented as $a, b, c, \alpha, \beta, \gamma, \theta$.

$$Nu_t = aRe_n{}^{\alpha} Pr^{\beta} + b\left[Re_o{}^{\gamma} Re_n{}^{\theta} \frac{St}{c}\right] \tag{5.2}$$

The identification of the complete set of 7 parameters, without distinction, using the experimental data available, can lead to poor parameter estimates that degrade the prediction capability of the correlation. This is commonly due to the correlation between parameters or their effects within the selected experimental space, and/or the weak effect of some parameters on the output prediction, in this case Nu_t. To address this issue, it was necessary to determine the optimal subset of parameters and their estimates that capture effectively the experimental data and maximise the prediction capability of the correlation. One of the effective ways to achieve this objective was to implement an estimability analysis (also called practical identifiability) (Yao et al., 2003; Benyahia et al., 2013).

5.3.2 Estimability analysis

Prior to the parameter identification step, it was necessary to determine the subset of parameters with the strongest influence on the measured output based on available data, as well as the correlation between the parameter effects using the method of estimability or practical identifiability analysis. The result of an estimability analysis is usually a number of parameters that are sufficient to represent the information provided by the experimental data and reliably predict the output, in this case Nu_t. Usually, the non-estimable parameters are set to nominal values, or the entire correlation can be redefined to remove these parameters (Yao et al., 2003). Accurate estimation of the correlation parameters is required to obtain reliable predictions of Nu_t, and consequently the heat transfer performance of the SPC meso-tube. What limits or reduces the estimability potential of the parameters is their weak influence on the outputs and/or the correlation between the parameters effects. Due to their poor accuracy, the estimation of these parameters can lead to significant degradation in the predictive capability of the correlation (Benyahia et al. 2013). The sequential orthogonalization estimability analysis was performed on the newly developed Nu_t correlation (Equation (5.2)) according to the algorithm below (see Figure 5.7):

Let $\boldsymbol{s}_i$ be the sensitivity vector corresponding to the parameter p_i, $\boldsymbol{r}_i$ the orthogonal projection of $\boldsymbol{s}_i$, $\boldsymbol{X}_j$ the matrix of the selected parameters vectors at the jth stage; $\wp$ the set of estimable parameters, and λ the cut-off value.

1. Selection of the parameter with the highest effect: find the index k such that,

   $$k = \arg\max_i (\boldsymbol{s}_i)^T \boldsymbol{s}_i, i \in I_0 = \{1, \dots, n_p\}$$

   if $(\boldsymbol{s}_k)^T \boldsymbol{s}_k \geq \lambda$ set $\wp_1 = \{p_k\}$ and $X_1 = \boldsymbol{s}_k$

   otherwise stop

2. Orthogonalization: Compute the orthogonal projection of the matrix $\boldsymbol{Z}$:

$$R^j = (I - X_j(X_j^T X_j)^{-1} X_j^T)\boldsymbol{Z}$$

3. Select the next parameter with the highest effect:

$$l = \arg\max_i (\boldsymbol{r}_i^j)^T \boldsymbol{r}_i^j, i \in \boldsymbol{I}_j = \left(\boldsymbol{I}_{j-1} - \{k, \dots\}\right)$$

if $(\boldsymbol{r}_l^j)^T \boldsymbol{r}_l^j \geq \lambda$ set $\wp_j = \left\{\wp_{j-1}, p_l\right\}$ and $X_{j+1} = \left\{X_j, \boldsymbol{s}_l\right\}$

return to step 2

otherwise Stop

The development of an effective solution to the parameter selection problem required the quantification of the influence of each parameter on the measured output (Nu_t). This approach indicates which parameters are the most important and most likely to affect predictions of the correlation. The first step of the method is the evaluation of the sensitivity coefficients:

$$S_{ij} = \frac{\partial \hat{y}_i}{\partial p_j} \approx \frac{\hat{y}_i(t, p_j) - \hat{y}_i(t, p_j - \Delta p_j)}{\Delta p_j}, j = 1,2, \dots n_p \tag{5.3}$$

where n_p is the number of parameters, p_j is the vector of the jth parameter, $\hat{y}_i$ is the vector of the numerically calculated aspect ratio at kth point in time.

Because of the different orders of magnitude of the various parameters in the correlation, it is necessary to normalize the sensitivity coefficients with respect to the nominal values of the parameters and their corresponding output predicted by the correlation. This will allow for a reliable comparison between the effects of different parameters on the predictions of the correlation.

$$S_{ij}\big|_{t=t_k} = \frac{\bar{p}_j}{\bar{y}_i|_{t=t_k}} \frac{\partial \hat{y}_i}{\partial \hat{p}_j}\bigg|_{t=t_k} \tag{5.4}$$

where $\bar{p}_j$ is the nominal value of the jth parameter and $\bar{y}_i|_{t=t_k}$ is the correlation prediction of the ith output evaluated at a sampling time t_k using the nominal vector of the parameters ($\overline{\boldsymbol{p}}$).

The overall sensitivities of the different outputs with respect to the full set of parameters was summarised in a matrix of sensitivity coefficients ($\boldsymbol{Z}$). Each column of this matrix evaluates the global effect of a given parameter on the process outputs at different measurement times, whereas each row represents the effect of the full set of parameters on a given output at a fixed time of measurement.

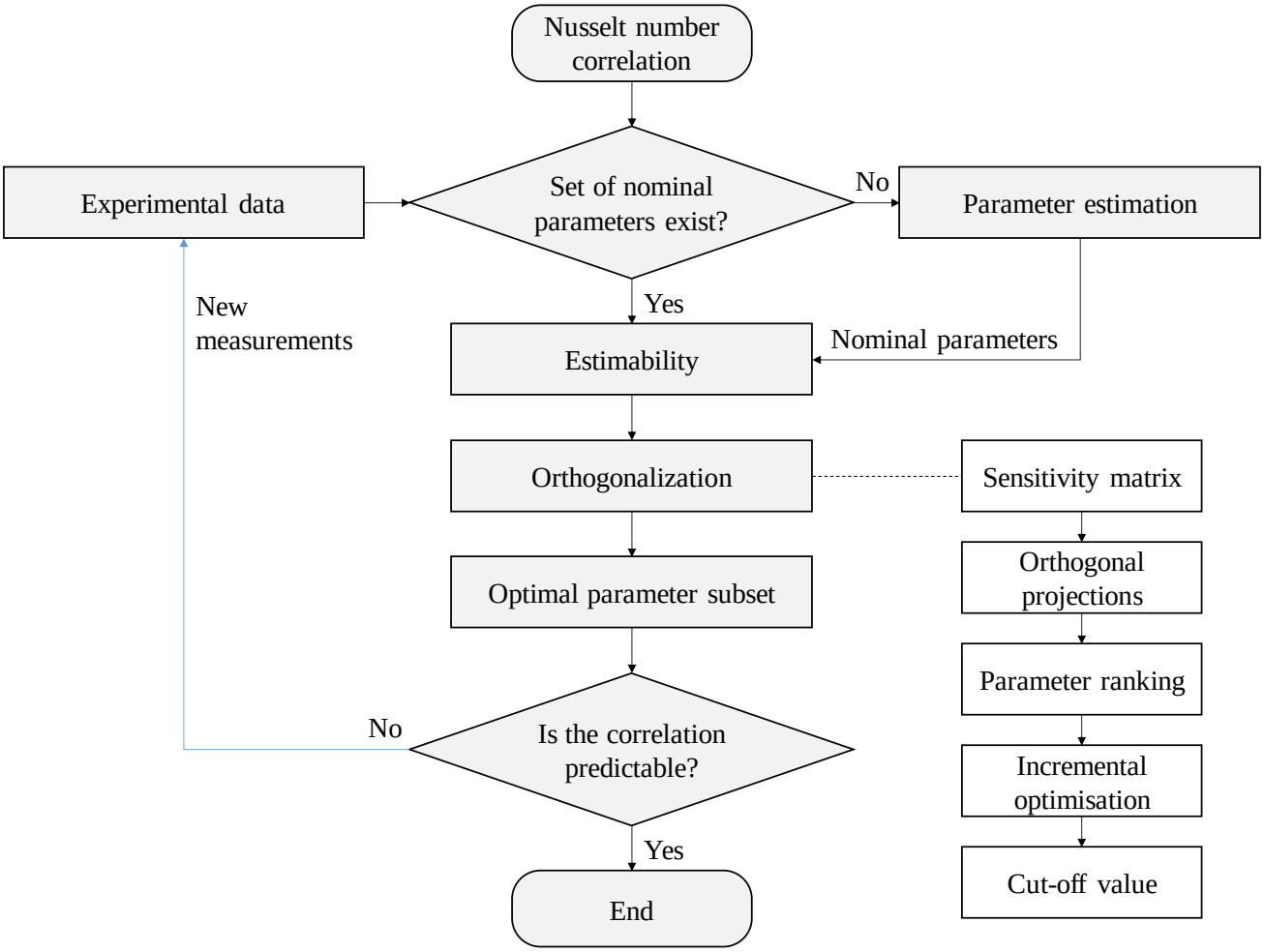

Figure 5.7 Schematic of parameter identification and estimability framework.

$$\boldsymbol{Z} = \begin{bmatrix} S_{11}|_{t=t_1} & \cdots & S_{1n_p}\big|_{t=t_1} \\ \vdots & \ddots & \vdots \\ S_{n_y1}\big|_{t=t_1} & \cdots & S_{n_yn_p}\big|_{t=t_1} \\ S_{11}|_{t=t_2} & \cdots & S_{1n_p}\big|_{t=t_2} \\ \vdots & \ddots & \vdots \\ S_{n_y1}\big|_{t=t_{n_m}} & \cdots & S_{n_yn_p}\big|_{t=t_{n_m}} \end{bmatrix} \tag{5.4}$$

After the selection of the nominal values of the parameters from parameter estimation (Table 5.2), the sensitivity matrix was computed numerically in MATLAB® 2016, based on a sequential orthogonalisation algorithm (Benyahia, 2010). In this work, $\boldsymbol{Z}$ has 7 columns, each column corresponding to one of the 7 model parameters. Each of the 60 rows of $\boldsymbol{Z}$ corresponds to a particular output response at a particular net flow and frequency, rather than sampling time.

Table 5.2 Nominal values of the correlation parameters

Parameter	Value
a	0.01616
b	0.0016
c	1.136
α	1.16
β	0.3
γ	0.08
θ	1.42

The resulting correlation for the tube-side Nusselt number is shown in Equation (5.5):

$$Nu_t = 0.01616 {Re_n}^{1.16} Pr^{0.3} + 0.0016 \left[{Re_o}^{0.08} {Re_n}^{1.42} \frac{St}{1.136} \right] \tag{5.5}$$

The first term of the correlation represents the steady flow contribution to heat transfer, while the second term is the augmentation provided when an oscillatory component is superimposed on steady net flow. Note the inclusion of the dimensionless Strouhal number in the oscillatory term, as this was found to have a separate effect from Re_o on Nu_t. Much of the contribution to heat transfer comes from the steady net flow, as is indicated by the higher coefficient of the first term. The steady flow term is an analogue of the Dittus Boelter turbulent flow equation, as is the first term of the Mackley-Stonestreet correlation. The exponent of Re_n accounts for the presence of smooth periodic constrictions; this value is lower than that of the Mackley-Stonestreet correlation and represents the less chaotic conditions created by smooth constrictions and steady flow in this range of Re_n investigated.

The oscillatory term in the new correlation suggests that the effect of oscillation is multiplied by the steady flow, and that oscillations by themselves have a negligible effect. Thus, for a fixed Re_o, higher values of Nu_t are achieved by increasing Re_n. The opposite is observed in the Mackley-Stonestreet correlation, where for $Re_o \gg Re_n$, the effect of oscillation is superimposed on steady behaviour. The effect of *St* is captured by the relationship with its coefficient; such that for smaller *St*, the heat transfer contribution from the oscillatory term diminishes regardless of Re_o, and values of Nu_t fall closer to those for steady non-oscillatory flow in the SPC meso-tube. In the absence of oscillations, Equation (5.5) simplifies to the first term only and corresponds to the best-fitted curve for steady flow in Figure 5.6. It is important to state that this correlation was derived for an SPC meso-tube with diameter-to-length ratio, D/L_1, of 0.0076, and fitted for measured Nu_t values within the experimental range of Re_n and Re_o defined earlier.

On implementing the orthogonalisation algorithm, the parameters were ranked according to their estimability potential. The most estimable parameters present the highest effect (the column of

the matrix $\boldsymbol{Z}$ with the highest magnitude or Euclidean norm) and lowest pairwise correlation coefficients. Cut-off values (λ) were identified to help determine the set of parameters that capture more reliably, the information contained in the experimental data and, consequently, maximise the prediction capability of the correlation. The choice of cut-off value was somewhat arbitrary, and depending on the selected cut-off value, different parameter sets could be obtained (Table 5.3). An initial cut-off value of 15.4 was selected to obtain a single estimable parameter that influences only one response variable. Table 5.4 shows that the parameter with the highest estimability potential in the correlation is α, which is the exponent of Re_n in the steady term. The second parameter is θ, corresponding to the Re_n exponent in the oscillatory term; and the third most estimable parameter is a, the coefficient of Re_n in the steady term.

Table 5.3 Subsets of the most estimable parameters obtained for different cut-off values

Cut-off value, λ	Subset						
15.4	α						
1.83	α	θ					
0.02	α	θ	a				
4×10^{-3}	α	θ	a	b			
17×10^{-4}	α	θ	a	b	c		
9×10^{-17}	α	θ	a	b	c	γ	
4.2×10^{-18}	α	θ	a	b	c	γ	β

The selection of α as the strongest parameter emphasises the paramount importance of the smooth constrictions to the heat transfer characteristics of the SPC meso-tube as demonstrated by Figure 5.1.

Table 5.4 Ranking of the parameters with the highest estimability potential

Parameter	Rank
α	1
θ	2
a	3
b	4
c	5
γ	6
β	7

Aside from Table 5.3, the effect of the cut-off value on the optimal number of required parameters is depicted in Figure 5.8. This indicates that three parameters would be sufficient to explain the heat transfer behaviour in the SPC meso-tube. To further refine and maximise the outcomes of the estimability method, we need to quantify the effect of the number of parameters to be identified, or the size of the optimal set of the most estimable parameters, on the model prediction performance

compared to the experimental data. This effect is depicted in Figure 5.9 as the optimal value of the maximum likelihood criterion versus set size of the most estimable parameters, starting from one parameter (i.e. the most estimable parameter α). Again, Figure 5.9 shows that 3 parameters provide a sufficient set to build a reliable correlation for the tube-side Nusselt number. However, a further improvement of the agreement between the predictions and experimental measurements was obtained by selecting more parameters to minimize the maximum likelihood criterion (Walter and Pronzato, 1994), which in this case is the sum of square differences between the experimental measurements and the correlation predictions. A satisfactory trade-off between a minimum number of parameters and high accuracy of the model prediction was finally met with 6 parameters selected among the 7 correlation parameters. The selection of γ as the sixth parameter once again highlights the weak influence of oscillations on heat transfer augmentation in the SPC meso-tube.

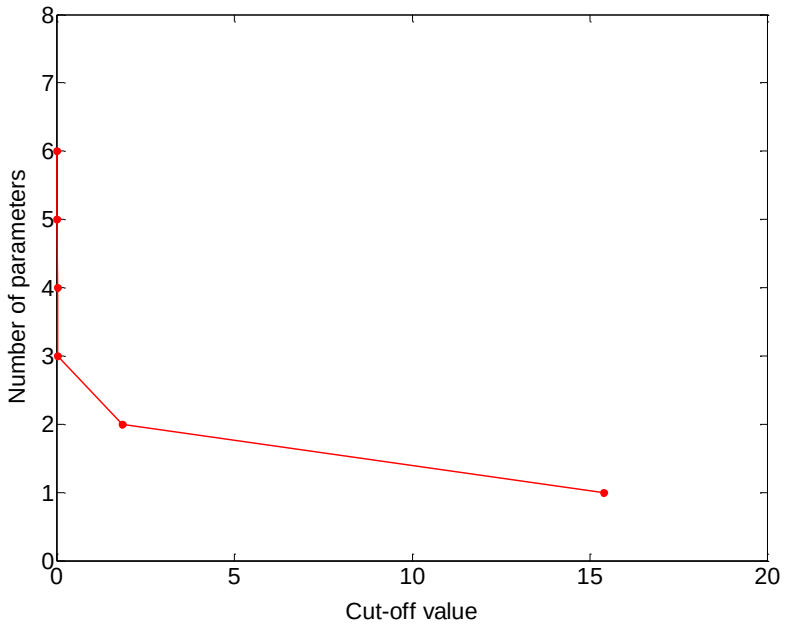

Figure 5.8 Number of selected parameters vs. cut-off value in tube-side Nusselt number correlation.

The selection of c as the fifth parameter points out that St plays a more significant role than oscillation f. θ, an exponent of Re_n in the oscillatory term, was ranked as the second strongest parameter; this affirms that the total contribution from the oscillatory term is largely provided by the net flow component. This also agrees with experimental findings that varying Re_n has a stronger effect on heat transfer than varying f. Overall, from the ranking of parameters, it is now clear that the control of heat transfer in the SPC meso-tube is dictated by the smooth constrictions and net flow velocity.

The parameter β, which corresponds to the exponent of the Prandlt number, Pr, was found to have an infinitesimal effect on Nu_t, and as a result was not selected in the final subset of estimable parameters in Figure 5.9. β was kept fixed at its nominal value, as the dependence of Nu_t on Pr (i.e. varying the process fluid) was not investigated. This means that the correlation may be re-parameterized to exclude β, without compromising on the accuracy of predictions of Nu_t.

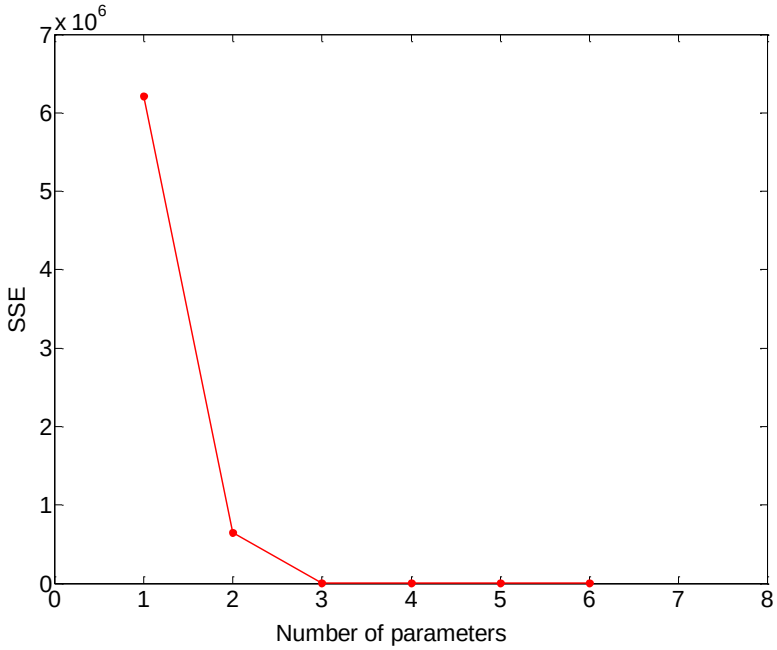

Figure 5.9 Effect of minimizing the maximum likelihood criterion on the number of parameters.

5.4 Conclusions

Experimental investigations into the heat transfer performance of the SPC meso-tube showed that smooth constrictions within the SPC meso-tube significantly enhance the tube-side heat transfer, a behaviour consistent with general observations in conventional SEPC OBRs. An estimability analysis revealed the strong dependency of heat transfer rate on the smooth constrictions and bulk (net) flow velocity, rather than oscillatory flow as established in the SEPC OBRs. For the SPC meso-tube investigated, it was found that oscillations provided a limited heat transfer augmentation, however oscillatory flow is expected to provide further heat transfer enhancement in tubes of higher diameter-to-length ratio ($D/L_1 > 0.0076$). For the experimental conditions investigated, heat transfer rate was found to be weakly dependent on the oscillatory velocity; instead, having a strong dependency on the steady net flow. The heat transfer rate was found to show more sensitivity to the Strouhal number than oscillation frequency, with the SPC meso-tube showing poorer heat transfer performance for $St < 0.8$;

a contrasting behaviour to that observed by Mackley and Stonestreet (1995) for the sharp-edged baffled tube.

The data presented here highlights the similarities and differences of the heat transfer characteristics in the SPC meso-tube and SEPC OBRs. A correlation to describe the heat transfer behaviour of the SPC meso-tube was fitted to experimental data for a range of $Re_n = 10.79 – 53.97$ and $Re_o = 0 – 197$, and a systematic and rigorous approach based on parameter estimability enhanced understanding of the relative importance of the terms in the correlation. The relationship described by the correlation suggests that the effect of oscillation is multiplied by steady flow, and that oscillations by themselves have a negligible effect. The opposite is observed in the Mackley-Stonestreet correlation, where for $Re_0 \gg Re_n$, the effect of oscillation is superimposed on steady behaviour. While the correlation can reliably predict the tube-side Nusselt number within this range of experimental conditions, its veracity is dependent on the baffle type present in the tube, in this case smooth periodic constrictions. Its predictions will also hold true for SPC meso-tubes of similar diameter-to-length ratio.

This chapter has provided an in-depth understanding of the heat transfer characteristics of the SPC mesoscale crystalliser. With the newly developed correlation, overall heat transfer coefficients can be determined for different oscillatory and steady flow conditions, and incorporated into a heat balance equation, alongside physical and material properties, to accurately predict spatial temperature profiles in the SPC mesoscale crystalliser for continuous cooling crystallisation.

Chapter 6 Seeded continuous cooling crystallisation in the SPC mesoscale crystalliser

6.1 Introduction

In the previous two chapters, it has been demonstrated that the SPC mesoscale crystalliser is uniquely capable of achieving near plug flow operation at low net flows (ml h^{-1}) (see Chapter 4); and possesses excellent heat transfer capabilities (see Chapter 5), both of which are essential for the control of crystallisation. From RTD experiments in Chapter 4, it was concluded that solid-liquid plug flow is achievable in the 5.2 m long SPC mesoscale crystalliser at an oscillatory range of $x_0 = 0.5 – 2$ mm and $f > 6$ Hz. Therefore, oscillatory conditions in this range were chosen for plug flow crystallisation in the SPC mesoscale crystalliser. At these plug flow conditions, the desired spatial temperature profile for cooling crystallisation in the SPC mesoscale crystalliser was predicted by a heat transfer model. Details of the heat transfer model and spatial temperature predictions are presented in sections 3.10.2 and 3.11.3 of Chapter 3.

In this chapter, the seeded continuous cooling crystallisation of GLY in the SPC mesoscale crystalliser is reported for the first time. A systematic study is conducted on the effects of mean residence time, axial dispersion, spatial temperature profile, seed size, and seed loading on steady-state product CSD and yield of α- and γ-GLY. The objective of the study is to identify an operating strategy for the SPC mesoscale crystalliser that is suitable for delivering GLY product with large mean size and narrow CSD, which is a common objective of crystallisation processes (Yang and Nagy, 2014). This chapter will also lay the groundwork for future optimisation of the SPC mesoscale crystalliser as a small-scale process development and continuous production platform.

6.2 Results and discussion

6.2.1 Metastable zone width determination

An accurately determined MSZW is vital for the design and control of a cooling crystallisation process. A system with a broad MSZW means that a large supersaturation is required for nucleation to occur, and that the system nucleates slowly. This is desired for a seeded crystallisation as it increases the design space across which seeds can be added. On the other hand, a very narrow MSZW (<2 °C) presents practical challenges for seeding (Brown et al., 2018). The MSZW therefore informs the

temperature profile and seeding point within the metastable zone for a seeded cooling crystallisation. Due to its linear scale-up capability (Ejim et al., 2017), the suitability of the SPC mesoscale crystalliser for solution crystallisation was investigated by measuring the MSZW of GLY-water solution in the batch SPC mesoscale crystalliser following the methodology described in section 3.11.1 of Chapter 3.

Figure 6.1 shows the corresponding metastable limits (nucleation points) detected in the batch SPC mesoscale crystalliser for saturation temperatures of 20 °C, 30 °C, 40 °C and 50 °C at a cooling rate of –1 °C min^{-1}. The solid black line in Figure 6.1 is the solubility curve for GLY in water given by Equation (3.1). Nucleation occurred at higher temperatures (smaller MSZW) in the batch SPC mesoscale crystalliser than in the 500 ml STC. This would have significant influence on the nucleation rate and resultant crystal morphology due to a lower supersaturation ($S = 1.24 \pm 0.03$) than in the 500 ml STC ($S = 1.41 \pm 0.12$). The average MSZW for the solution concentrations investigated remained consistent at 12.0 $\pm$ 0.2 °C for a plug flow oscillatory condition of $Re_o = 185$ ($x_0 = 0.5$ mm, $f = 12$ Hz). A significantly wider MSZW of 18.3 $\pm$ 1.2 °C was obtained in the 500 ml STC for an agitation speed of 400 rpm. Note that an actual cooling rate of –1 °C min^{-1} was not achieved in the 500 ml STC due to heat transfer limitations.

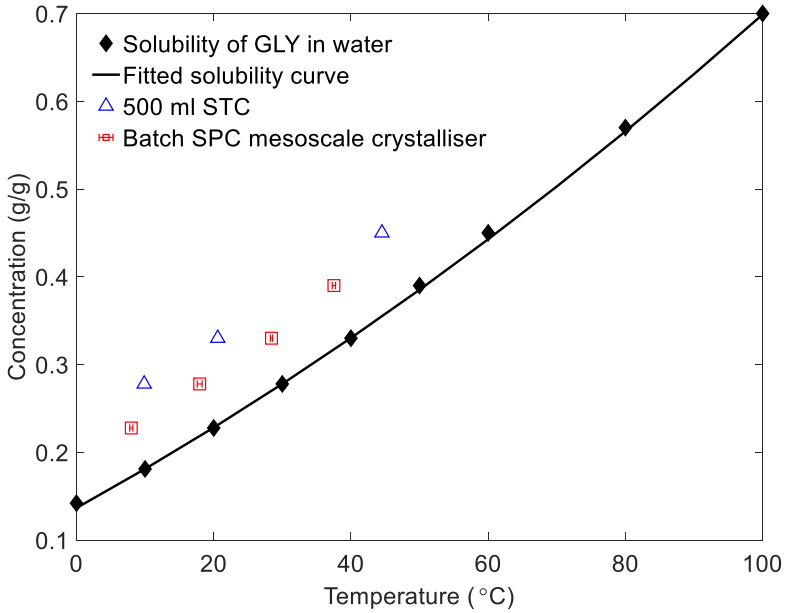

Figure 6.1 Metastable limit of GLY-water solution in the batch SPC mesoscale crystalliser at –1.0 °C min^{-1} cooling rate compared to the STC (–0.83 °C min^{-1}). $x_0 = 0.5$ mm, $f = 12$ Hz. GLY solubility obtained from Mullin (2001).

As earlier mentioned, the MSZW is a nucleation kinetic limited parameter that is highly dependent on mixing conditions (Ni and Liao, 2010; Liang et al., 2004). As such, the uniform mixing and efficient heat transfer provided by the hydrodynamic environment in the small-volume batch SPC

mesoscale crystalliser yielded a reproducible narrower MSZW than obtained in the 500 ml STC (Sermage, 2002). This supports previous findings by Ni et al. (2004), Ni and Liao (2008), Castro et al. (2013) which show that for a specific supersaturation ratio, OBCs are more effective in promoting nucleation than STCs. This can be attributed to the different mechanisms of mixing in OBCs and STCs. While STCs rely on agitation to provide mixing, mixing proceeds mostly through fluid shear forces in OBCs (Ni et al., 2004), as these devices possess shear-inducing mechanical parts such as moving baffles, pistons, or bellows. Mean shear strain rates generated in OBCs are lower than in conventional STCs (Mazubert et al., 2016). However, at these reduced shear rates, effective mixing is achieved in smaller fluid volumes by vortex formation as fluid is forced through each periodic constriction (Ejim et al., 2018). The effect of shear rate on nucleation kinetics has been shown to decrease with increasing volume and plateaus when the volume becomes too large (Steendam et al., 2018).

Figure 6.2(a) highlights the additive effect of mixing intensity and linear cooling rate on GLY-water MSZW in the batch SPC mesoscale crystalliser. The widest MSZW of 16.2 °C was obtained for a cooling rate of –0.5 °C min^{-1} at the lowest mixing intensity of $Re_o = 31$ ($x_0 = 0.5$ mm, $f = 2$ Hz). At such 'soft' mixing intensity, there is an absence strong vortex formation and inefficient mixing which would otherwise promote primary nucleation. In addition, poor radial mixing and associated heat transfer (as evidenced by results in Chapter 4 and Chapter 5) would lead to slower mass transfer rates and uneven distribution of supersaturation, further delaying growth of nuclei to a detectable size. Doubling the cooling rate (i.e. rate of supersaturation generation) to –1.0 °C min^{-1} at the same Re_o had negligible effect on MSZW, suggesting that at low mixing intensities, primary nucleation is independent of cooling rate, and shear rate is the controlling parameter (Steendam et al., 2018).

Increasing the mixing intensity to Re_o of 185 ($x_0 = 0.5$ mm, $f = 12$ Hz) narrowed the MSZW to 15. 2 °C for a cooling rate of –0.5 °C min^{-1} (Figure 6.2(a)). This is to be expected since improved radial mixing at higher frequency will increase mass transfer rates (Ferreira et al., 2017) and promote nuclei growth, leading to earlier detection (Brown and Ni, 2011; Castro et al., 2016). An increase in mixing intensity has been shown to reduce the MSZW and cause faster nucleation in conventional and mesoscale COBCs (Ni and Liao, 2008; Brown and Ni, 2012; Yang et al., 2018; Castro et al., 2016; 2018). Quite surprisingly, doubling the cooling rate to –1.0 °C min^{-1} at the same Re_o of 185 narrowed the MSZW significantly. This is a contrasting behaviour to observations by Ni and Liao (2008; 2010) in a 50 mm I.D. OBC and Brown and Ni (2011) in a 32 mm I.D. OBC, whereby faster rates of supersaturation generation (by cooling and anti-solvent addition rate respectively) resulted in wider MSZWs at the same mixing intensity. It also contradicts results for STCs which show that wider MSZWs are obtained for faster cooling rates (Fujiwara et al., 2002; Liang et al., 2004). Clearly, further

work is required to identify the mechanism for this profound difference observed in the batch SPC mesoscale crystalliser.

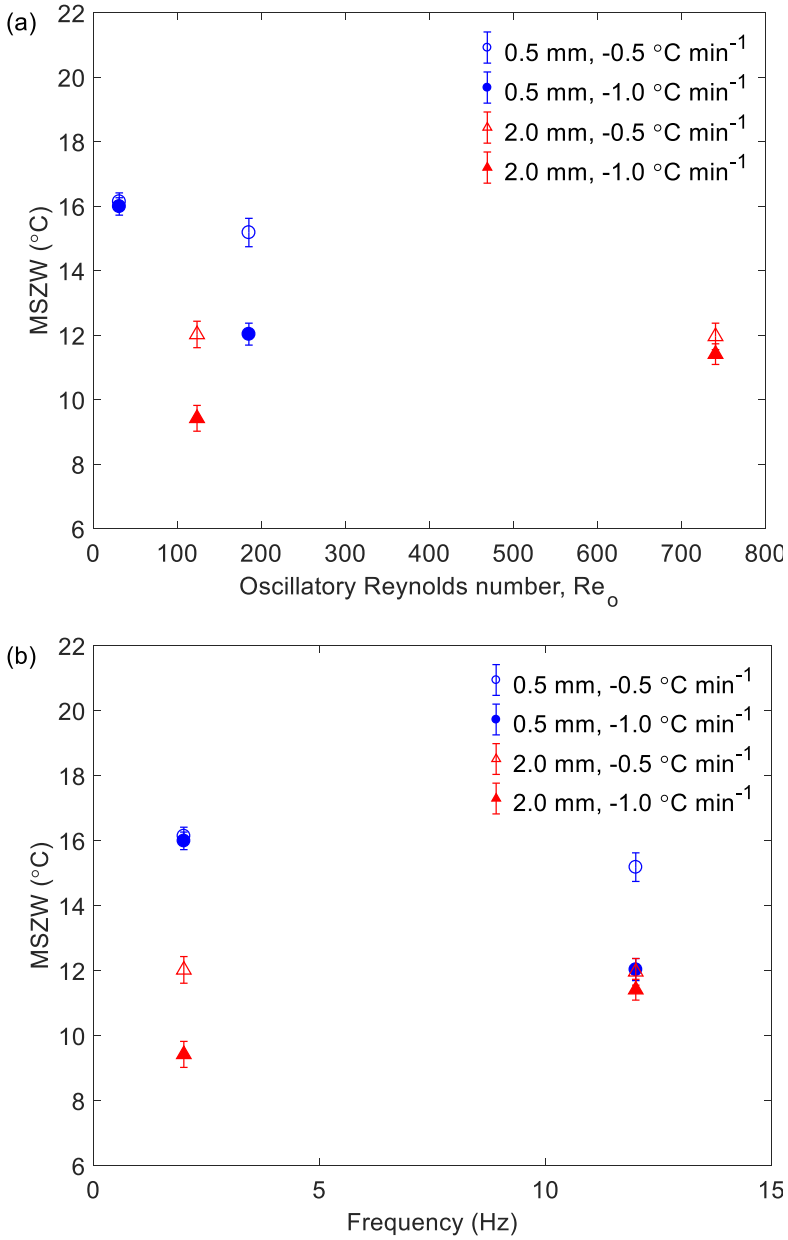

Figure 6.2 Effect of mixing intensity and cooling rate on the MSZW in the batch SPC mesoscale crystalliser saturated at 30 °C. Oscillatory conditions at $x_0 = 0.5$ mm ($Re_o = 31$, 185) and 2.0 mm ($Re_o = 123$, 740); $f = 2$ Hz, 12 Hz.

The dependency of primary nucleation on high fluid shear was demonstrated by a higher x_0 of 2 mm ($Re_o = 123$, $f = 2$ Hz) significantly narrowing the MSZW to 12.0 °C for the same cooling rate of –0.5 °C min^{-1}, despite having an $Re_o < 185$. This behaviour has also been observed by Yang et al. (2018) in a 3 mm I.D. batch oscillatory flow crystalliser. At this mixing intensity, higher input axial velocities contribute to both axial and radial mixing. The high fluid shear generated at constrictions

will promote collision and agglomeration of GLY pre-nucleation clusters in solution, thus, increasing the nucleation probability (Steendam et al., 2018). A minimum reduction in MSZW was obtained at $Re_o = 123$ by doubling the cooling rate to –1.0 °C min^{-1}.

However, increasing mixing intensity beyond $Re_o = 123$ for the same cooling rate increased the MSZW i.e. at $Re_o = 185$ and 740. This is more easily understood by examining Figure 6.2(b) which plots the MSZW as a function of oscillatory frequency, f. At low frequency of $f = 2$ Hz, the MSZW is strongly dependent on oscillatory amplitude for each cooling rate. At a high frequency of $f = 12$ Hz, there is much less dependence on oscillation amplitude or cooling rate and the MSZW is similar for almost all conditions. This suggests that at low frequencies of oscillation, higher fluid shear is generated from the sweeping motion of the bulk fluid as vortices propagate into adjacent inter-constriction cavities; while a smaller amplitude provides poorer mixing and insufficient fluid shear necessary for primary nucleation. At high-frequency conditions, shear-induced primary nucleation is impeded by limited shear at constrictions, however, radial mixing and heat transfer are improved. At high frequency and amplitude, very intense non-axisymmetric mixing (approaching mixed flow conditions) dominates the inter-constriction cavities, with little or no eddy propagation into adjacent cavities (Ni et al., 2003) and as a result, nucleation becomes independent of cooling rate. In between these two frequency extremes, a cooling rate effect is observed.

In Figure 6.3, the MSZW reaches a minimum at a power density of 8.8 W m^{-3} ($Re_o = 123$) for both cooling rates, after which it increases and eventually plateaus.

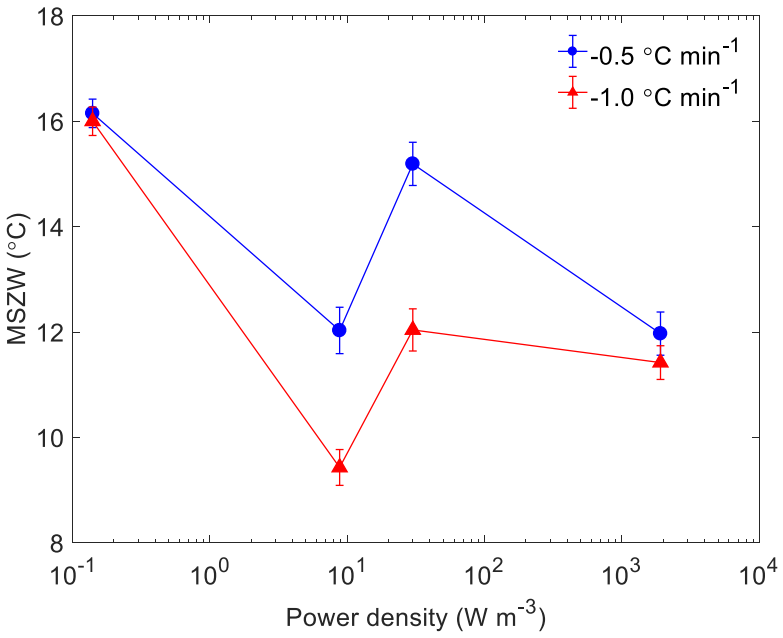

Figure 6.3 Relationship between power density and MSZW in the batch SPC mesoscale crystalliser. Saturated at 30 °C.

This suggests that an optimum power density exists for obtaining a minimum MSZW in the batch SPC mesoscale crystalliser, and that higher energy input can impede primary nucleation. It therefore highlights the stronger influence of oscillatory amplitude on primary nucleation and MSZW compared to oscillatory frequency. Overall, it can be concluded that higher fluid shear (amplitudes) enhances primary nucleation in the batch SPC mesoscale crystalliser.

Table 6.1 compares the power densities obtained in the batch SPC mesoscale crystalliser and the STC. Interestingly, a power density two orders of magnitude lower than that in the STC was sufficient to produce a narrower MSZW in the batch SPC mesoscale crystalliser. The efficient mixing and heat transfer obtained in the batch SPC mesoscale crystalliser at such low energy inputs is responsible for the narrow MSZWs obtained.

Table 6.1 Power densities (mixing intensities) and corresponding MSZW in the STC and batch SPC mesoscale crystalliser

	Mixing intensity (rpm/Re_o)	x_0 (mm)	f (Hz)	Power density (W m^{-3})	MSZW (°C)[‡]
STC	400	-	-	261	[ɟ]20.1
Batch mesoscale	31	0.5	2	0.14	16.0 ± 0.47
	185	0.5	12	30	12.0 ± 0.61
	123	2	2	8.8	9.4 ± 0.69
	740	2	12	1907	11.42 ± 0.55

[‡]Saturated at 30 °C, cooling rate of –1 °C min^{-1}, [ɟ]cooling rate of –0.71 °C min^{-1}

6.2.2 Spatial temperature profiles in the SPC mesoscale crystalliser

Figure 6.4 shows the stepped linear profile implemented for seeded cooling crystallisation in the SPC mesoscale crystalliser. Stepped cooling was achieved in the crystalliser by dropping the temperature of the cooling fluid in successive segments according to the profile 17 °C – 15 °C – 13 °C – 11 °C. The spatial temperature variation of the process and cooling fluids in each temperature-controlled segment was predicted by heat transfer model. The model assumes that in each segment the process fluid follows an exponential decay and equilibrates to an outlet temperature, while the cooling fluid temperature remains almost constant owing to its much higher heat capacity rate. Due to practical limitations, the process fluid temperature could only be measured at the outlet of each segment by K-type thermocouples inserted into U-shaped glass bends (see section 3.11.6 of Chapter 3). Temperature readings corresponded closely with the desired outlet temperatures, as shown in Figure 6.12.

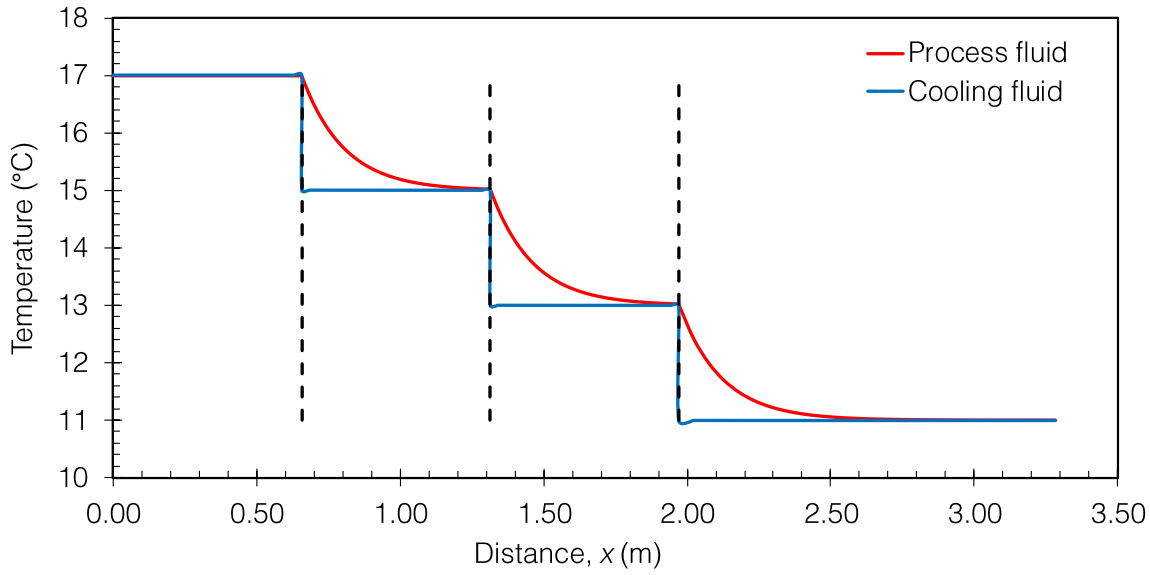

Figure 6.4 Stepped linear profile implemented in the SPC mesoscale crystalliser.

Figure 6.5 shows the result of a spatial approximation to a cubic profile in the SPC mesoscale crystalliser. The black dashed line is the cubic profile predicted by Equation (3.48). The temperature profile along the SPC mesoscale crystalliser is approximated by assuming that in each segment the process fluid temperature follows an exponential profile starting from the inlet temperature to reach the outlet temperature.

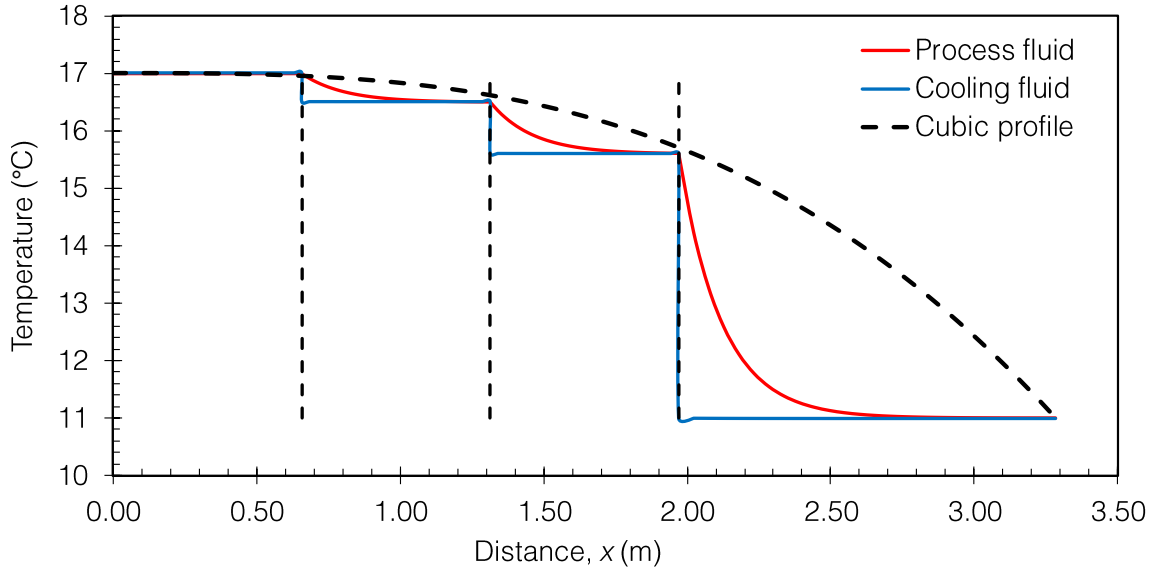

Figure 6.5 Approximation a cubic profile in the SPC mesoscale crystalliser.

Again, the cooling fluid temperature remains approximately constant due to its heat capacity rate. The spatial temperature profile of the process and cooling fluid is the result of a minimized objective

function (SSE $= 1.33 \times 10^2$) by the Excel® GRG Nonlinear Solver. The solver, however, produced a suboptimal solution, as the process fluid temperature profile significantly deviates from the cubic profile in the final segment. This spatially approximated profile increases supersaturation gradually in segments 1 – 3, and sharply in the final segment; thus, risking the occurrence of secondary nucleation and encrustation. To achieve a closer approximation to the cubic profile, a greater number of independent temperature-controlled segments would be required, at the cost of higher energy consumption. Majumder and Nagy (2013) found 25 independent temperature-controlled segments to be an optimum number for closely matching a cubic profile in the PFC.

6.2.3 Unseeded continuous cooling crystallisation approach

Unseeded continuous cooling crystallisation was attempted in the SPC mesoscale crystalliser as described in section 3.11.4 of Chapter 3. Initial runs with solution saturated at 40 °C resulted in blockages in the piston chamber due to rapid temperature drop triggering spontaneous nucleation. For Trial 1 – 5 (see Table 6.2), a 0.278 g/g GLY-water solution (saturated and maintained at 30 °C) was used, and the mixing intensity in the crystalliser was maintained at a plug flow oscillatory condition of $Re_o = 370$ ($x_0 = 1$ mm, $f = 12$ Hz) (as identified in Chapter 4). At this mixing intensity, radial velocities generated would be sufficient to suspend heavier α-GLY crystals that would be obtained near the crystalliser outlet. Also, T_{J0} was maintained at 35 °C to prevent any nucleation in section S0 (see Figure 6.6), since crystals travelling by backmixing would clog the piston chamber.

In Trial 1 (Figure 6.6), primary nucleation was induced, and crystals were detected in section S3. After ~6 min of operation, excessive encrustation on the walls of the U-shaped glass bend B2 was observed. This quickly dampened oscillations, leading to blockage of bend B2 and a complete shutdown of the crystalliser.

Table 6.2 Summary of operating conditions and results for Trial 1 - 5 in the SPC mesoscale crystalliser.

Trial	Temperature profile (°C)[ɬ]	Re_o (-)	Flow rate (g min^{-1})	Run time (min)	Blockage zone	Nature of blockage
1	35 – 17 – 14 – 10	370	5.39	6	Bend B2	Encrustation
2	35 – 16 – 16 – 16	370	5.39	7	Nucleation zone S1	Wall crystals
3	35 – 17 – 25 – 25	370	5.39	11	Nucleation zone S1	Wall crystals
4	35 – 25 – 18 – 22	370	5.39	9	Nucleation zone S2	Wall crystals
5	35 – 5 – 20 – 23	370	5.39	6	Bend B1	Encrustation

[ɬ]Temperature profile in order of segments S0 – S1 – S2 – S3.

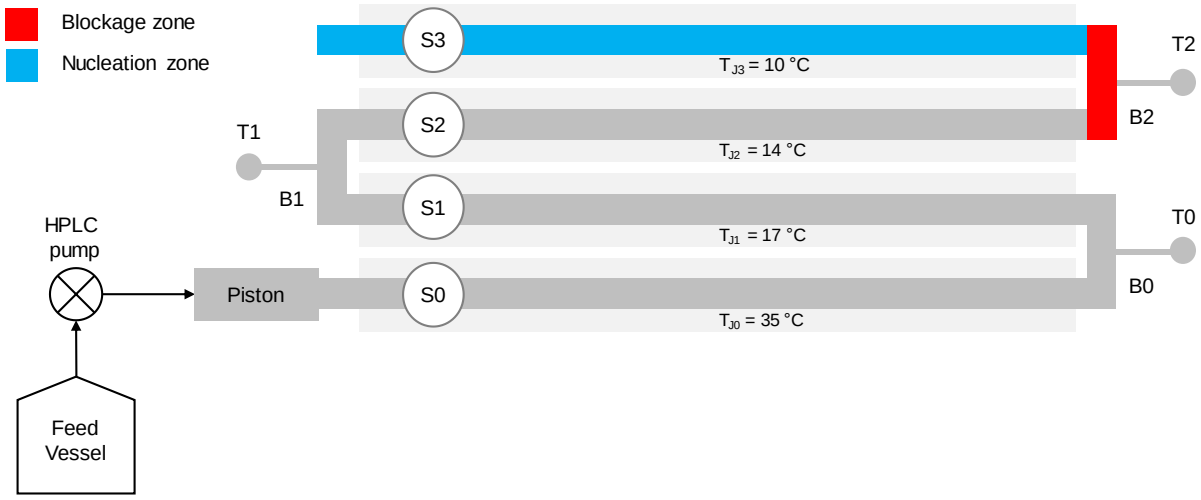

Figure 6.6 Temperature profile for Trial 1 showing nucleation and blockage zones in the SPC mesoscale crystalliser.

Subsequent runs were attempted in the SPC mesoscale crystalliser using different temperature profiles as summarised in Table 6.2. In Trial 2 – 4, primary nucleation occurred in sections S1 and S2 which were at temperatures corresponding to the MSZW determined in the batch SPC mesoscale crystalliser for a 0.277 g/g (saturated at 30 °C) GLY-water solution. This confirmed that the GLY-water MSZW fully translates between both platforms. In all trial runs, blockages occurred either by 'wall crystals' forming around the constrictions in the nucleation zone, or by encrustation in the adjacent bend (see Figure 6.7). The phenomenon of 'wall crystals' was attributed to surface-induced heterogeneous nucleation occurring on the wall surfaces around the smooth constrictions, where the strongest turbulent kinetic energy is present (Liang, 2002). It is reasonable to conclude that newly formed nuclei attach to the glass wall surfaces and continuously grow as freshly supersaturated solution is transported to the region (see Figure 6.7(a)). As these nuclei grow to larger crystal sizes, some are washed off wall surfaces by strong fluid shear forces and dispersed further down the crystalliser to trigger more secondary nucleation. This sequence continues until the constrictions become blocked by 'wall crystals' that have grown very large.

Encrustation occurring in adjacent bends was due to high levels of local supersaturation generated by sharp temperature drops as the saturated solution flowed into a colder section of the crystalliser. From Table 6.2, encrustation in bends B1 and B2 resulted in the shortest run times. Excessive nucleation from high supersaturation levels triggered the rapid deposition of solids on the walls of bends B1 and B2. A further complication was the inability to apply rapid temperature cycling to mitigate encrustation, as there was no form of temperature control in both unjacketed bends. In a short period of time, the crusts broke off and blocked the constrictions, leading to a shutdown of the crystalliser.

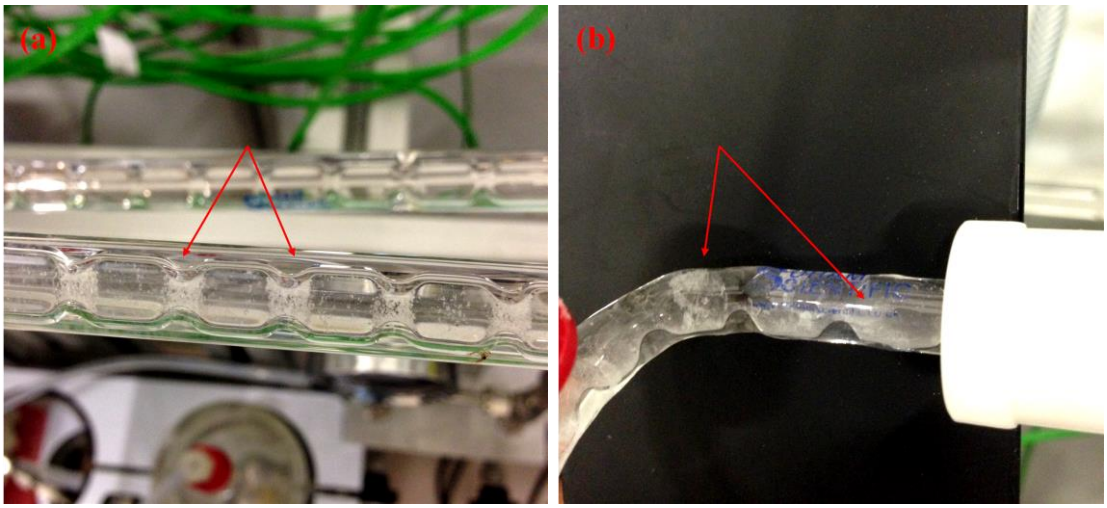

Figure 6.7 (a) 'Wall crystals' formed around smooth constrictions (b) Encrustation in an unjacketed bend.

Trial runs revealed the complexities of performing unseeded continuous cooling crystallisation in the SPC mesoscale crystalliser in its current state, with nucleation control being the most difficult. It was therefore concluded that avoiding primary and secondary nucleation would reduce the likelihood of encrustation in the crystalliser. Also, to avoid any blockages of the bends, it was crucial that a threshold solids concentration was always maintained in the crystalliser, knowing fully well that this would compromise on process yield.

6.2.4 Seed preparation and tailoring studies

Implementing a seeded continuous cooling crystallisation approach successfully mitigated the practical challenges encountered in unseeded cooling crystallisation approach, and enabled steady-state operation for a total run time of 140 min. However, operating continuously at a non-plug flow condition of $Re_o = 31$ ($x_0 = 0.5$ mm, $f = 2$ Hz) and 1% w/w solids loading yielded sub-optimal crystallisation performance. It was therefore necessary to systematically identify an operational window of process variables in which desired product CQAs would be met in the SPC mesoscale crystalliser.

As a first step towards achieving the above objective, a seed tailoring study was performed on recrystallised α-GLY material to determine the milling times sufficient to achieve target mean seed sizes, as this would enable reproducible seeded continuous cooling crystallisation experiments. The benefits of particle size reduction using the wet mill included a unimodal narrow size distribution, small mean size, complete suspension of seeds in the seed vessel (at 400 rpm), and improved seed

transport by eliminating transfer line blockages, which ensured accurate seed loading in the crystalliser. Offline Raman spectroscopic analysis of milled seeds showed that wet milling did not cause any polymorphic transformation of GLY (see Figure 6.8 and Figure 6.9).

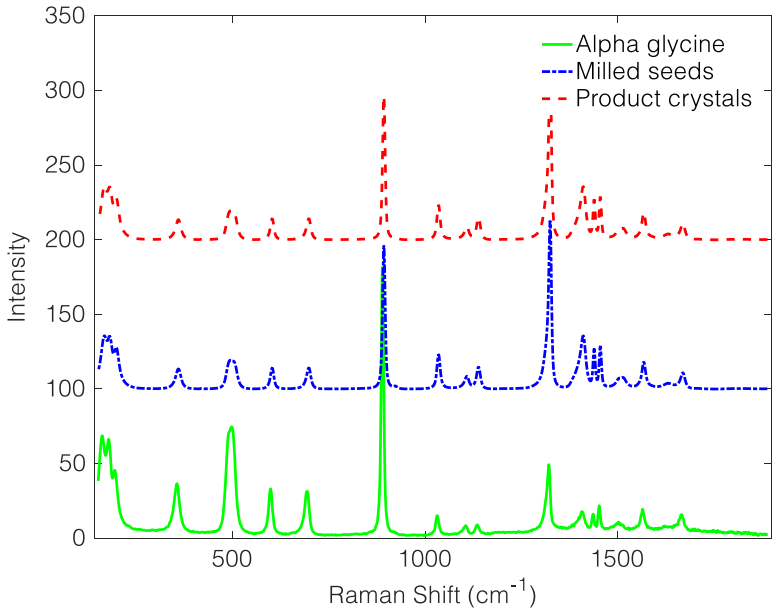

Figure 6.8 Offline Raman spectra for α-GLY raw material, milled seeds, and product crystals.

Figure 6.10 highlights the quality of seed material produced by the wet milling process. The starting raw material had predominantly coarse crystals with a mean size of 544 µm and a span of 2.32. The span of the distribution was calculated using Equation (6.1).

$$Span = \frac{d_{90} - d_{10}}{d_{50}} \tag{6.1}$$

where d_{10} is the diameter below which 10% of the population lies, d_{50} is the diameter below which 50% of the population lies, and d_{90} is the diameter below which 90% of the population lies. After a minute of milling, the span of the distribution was slightly increased to 2.38 by the creation of a fines fraction due to 'mass fracture' (Engstrom et al., 2013) of larger particles. Successive samples showed a gradual shift of the distribution from right to left, and a tightening of the span into a unimodal log-normal distribution at 120 min.

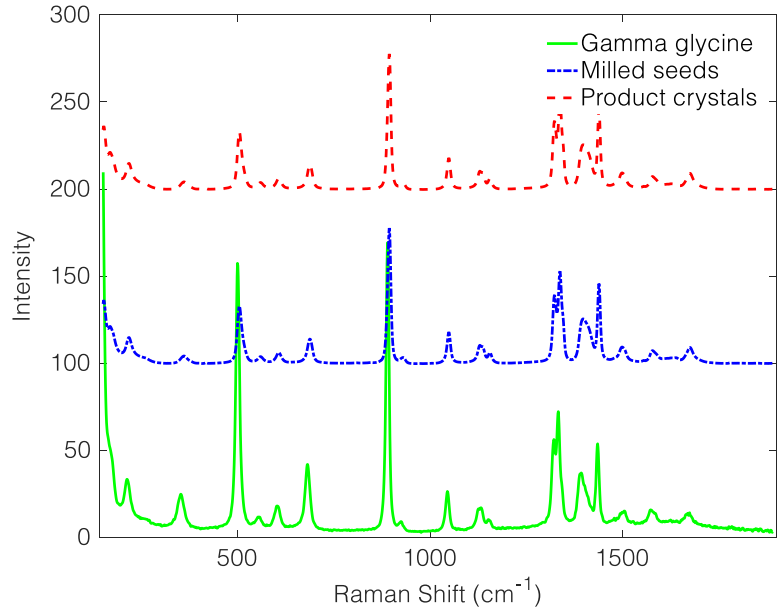

Figure 6.9 Offline Raman spectra for γ-GLY raw material, milled seeds, and product crystals.

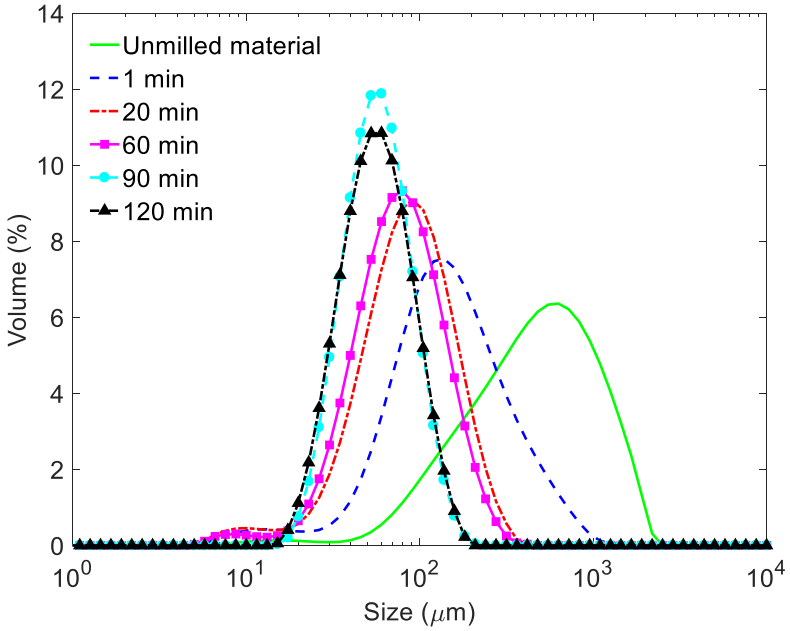

Figure 6.10 Evolution of α-GLY CSD during isothermal wet milling in DR module at 10,000 rpm.

It is evident from a plot of the volume mean diameter, $d_{4,3}$ (see Figure 6.11) that particle size reduction and creation of surface area slows down as milling time progresses. This is due to a transition from a dominant mass fracture mechanism, whereby large particles are fractured by colliding with the mill teeth, to attrition, where particle size is reduced by chipping (Lee et al., 2004); therefore, more energy is required to achieve further size reduction (Donovan, 2003; Engstrom et al., 2013).

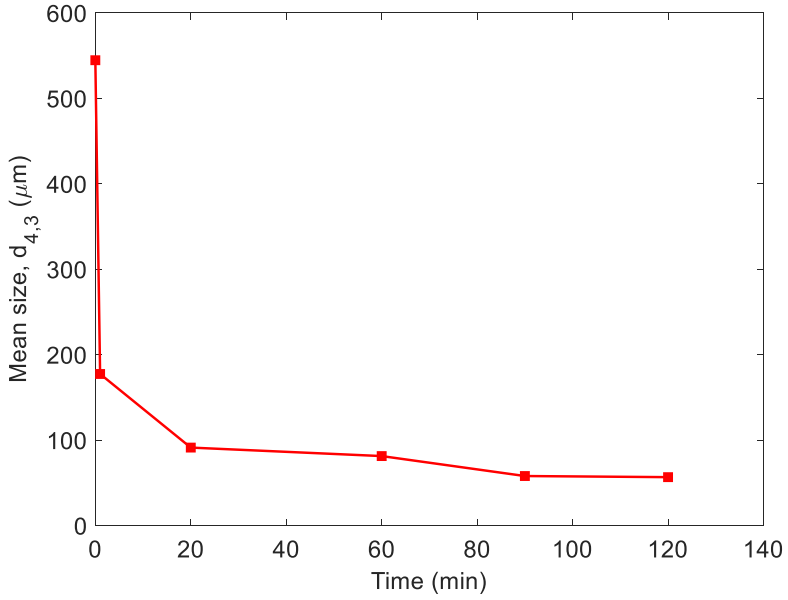

Figure 6.11 Evolution of α-GLY mean size during isothermal wet milling in DR module at 10,000 rpm.

It is also worth noting that the characteristic broad RTD of a CSTR (see section 7.2.1) will cause various fractions of the bulk suspension to undergo varying degrees of milling. However, as a way of balancing out the broad RTD effect, smaller size fractions would undergo less size reduction than larger size fractions, and the distribution will eventually converge to a single mode. The biggest size reduction (67%) was obtained after 1 min of milling (Table 6.3), and an overall size reduction of 90% was achieved after 120 min of milling.

Table 6.3 Summary of CSD properties for wet milling process

Milling time (min)	α-GLY span	α-GLY mean size, $d_{4,3}$ (μm)	% mean size reduction
0	2.32	544.6	-
1	2.38	177.5	67.4
20	1.65	91.3	48.6
60	1.60	81.3	10.9
90	1.21	58.0	28.7
120	1.32	56.7	2.27

From Figure 6.11 and Table 6.3, milling beyond 90 min is energy inefficient since negligible size reduction is obtained. Therefore, 90 min was selected as a suitable milling time for achieving a mean size of ~60 μm for the α-GLY starting seed material. This milling time was also applied to the γ-GLY starting seed material.

6.2.5 Steady-state operation in the SPC mesoscale crystalliser

For the crystallisation experiment shown in Figure 6.12, process fluid temperatures T0 – T4 were measured in bends B0 – B4 (see Figure 3.24 in Chapter 3). Due to the absence of temperature control in these unjacketed bends, slight deviations in measured temperatures (of an average of 0.6 °C) were observed. This, however, did not pose a serious concern. A stepped linear profile was implemented across four temperature-controlled segments as follows 17 °C – 15 °C – 13 °C – 11 °C (see section 3.11.3 in Chapter 3 for details). T0 is the process fluid temperature at the seed entry point, T1 is the process fluid temperature between sections S1 and S2, T2 is the process fluid temperature between sections S2 and S3, T3 is the process fluid temperature between sections S3 and S4, and T4 is the process fluid temperature between sections S4 and S5.

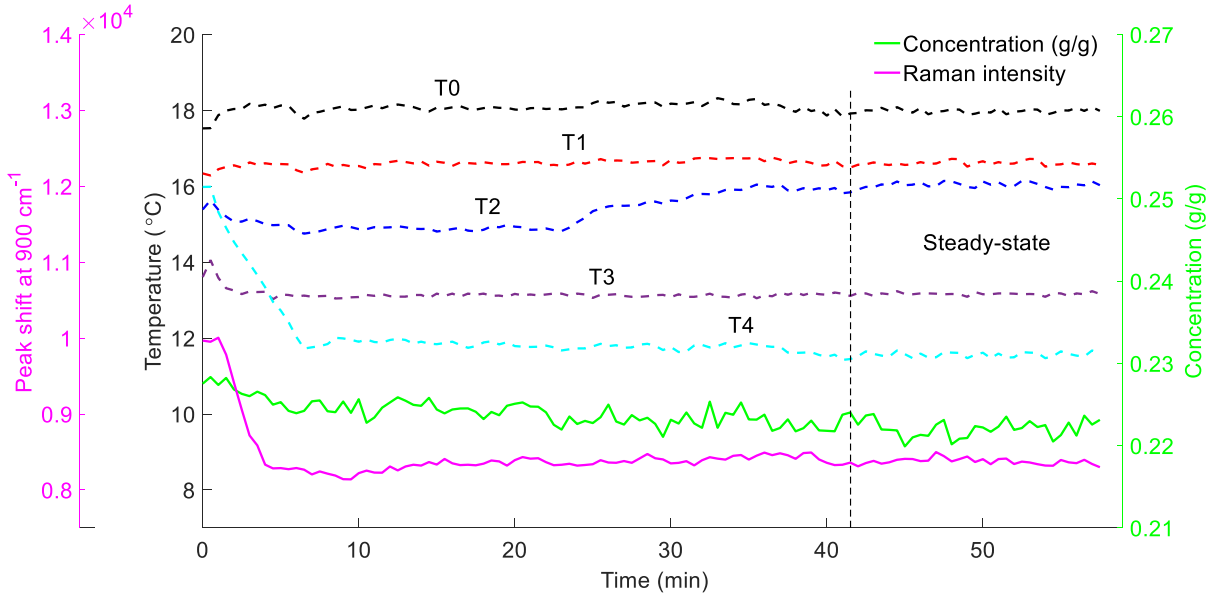

Figure 6.12 Process time diagram for seeded continuous cooling crystallisation of GLY from water. Seed loading: 7% w/w; residence time: 7.3 min; oscillatory conditions: $x_0 = 1$ mm, $f = 10$ Hz; temperature profile: stepped linear. Steady-state achieved after 5 residence times.

Steady-state operation was achieved at about 42 min (after 5 residence times) when all process fluid temperatures (T0 – T4) and solution concentration were steady, with no rapidly increasing or decreasing trends (see Figure 6.12). As seed crystals travel through the crystalliser, they grow by consuming available supersaturation created by the temperature gradient, thus depleting the concentration of GLY in solution. The significance of a steady concentration is that in the absence of new crystal formation, the total crystal mass passing through the Raman probe location is constant at any point in time, however the total mass of crystals varies along the length of the crystalliser. Thus,

any significant fluctuations in Raman intensity (at 900 cm^{-1}) or solution concentration would indicate issues with the incoming seed stream.

6.2.6 Effect of mean residence time (net flow)

The mean residence time controls the average time spent by crystals in the crystalliser, and therefore can influence the final size crystals grow to. To study the effect of mean residence time, the SPC mesoscale crystalliser was operated at a near plug flow oscillatory condition of $R_{eo} = 306$ ($x_0 =$ 1 mm, $f =$ 10 Hz), which was earlier identified in Chapter 4. Table 6.4 summarises the operating conditions and results obtained for the mean residence time effect on GLY crystallisation.

Table 6.4 Summary of experimental conditions and results for the residence time effect on the crystallisation of GLY

	α-GLY		γ-GLY	
Mean residence time, τ (min)	2.8	7.3	2.8	7.3
Crystalliser final temperature (°C)	11	11	11	11
Seed stream concentration (g/g)	0.223	0.223	0.223	0.223
Feed stream concentration (g/g)	0.228	0.228	0.228	0.228
Supersaturation at seed entry point (-)	1.07	1.07	1.07	1.07
Starting seed size, $d_{4,3}$ (µm)	66 ± 0.3	69 ± 0.2	78 ± 0.2	ǂ89 ± 0.1
Starting seed span (-)	1.52	1.47	1.38	1.20
Steady-state mean product size, $d_{4,3}$ (µm)	98 ± 2	200 ± 14	98 ± 2.8	107 ± 3.1
Normalised product size, L_p/L_s (-)	1.48	2.86	1.25	1.20
Steady-state exit concentration (g/g)	0.202	0.197	0.208	0.208
Span (-)	1.41	1.64	1.31	1.32
Fractional yield (%)	58.8	71.5	45.7	45.5

ǂStarting seeds from different batch of milled material

Figure 6.13 demonstrates that the mean residence time controls the size of the steady-state product for α-GLY. The extent of crystal growth in the crystalliser was quantified by comparing the $d_{4,3}$ of the steady-state product (L_p) and the starting seed material (L_s), otherwise known as the normalised product size, L_p/L_s. While 2.8 min was sufficient for significant growth of α-GLY crystals, extending τ to 7.3 min provided a 1.9-fold increment to the normalised product size, and increased fractional yield to 71.5% (see Table 6.4). A fractional yield of 71.5% implies that the solution did not equilibrate in each crystalliser segment.

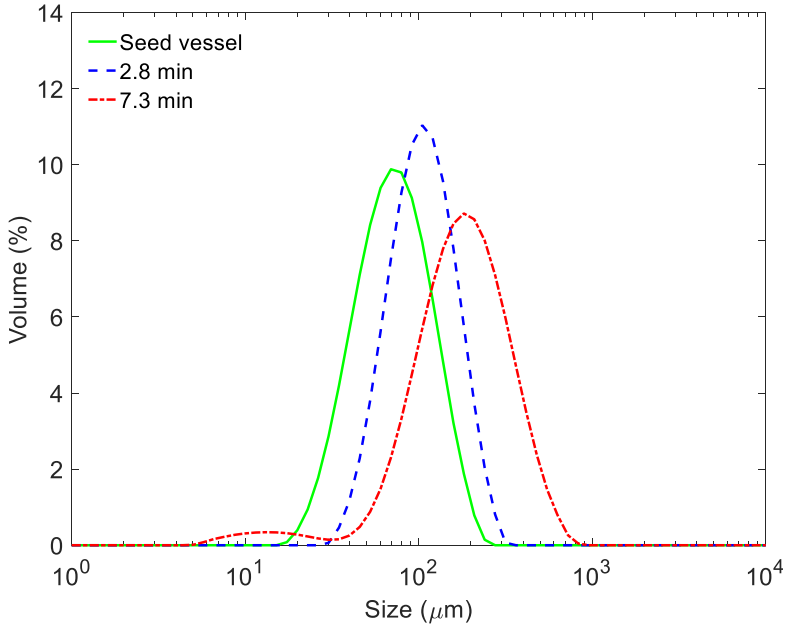

Figure 6.13 CSD of α-GLY seed and steady-state product for τ of 2.8 min and 7.3 min.

The benefit of a well-tailored seed material is evident in Figure 6.13, whereby a unimodal seed distribution translated into a unimodal steady-state α-GLY product CSD for both mean residence times. Unimodality was maintained as the size distribution shifted to the right with increasing τ. This suggests that crystal growth was the dominant crystallisation mechanism in the crystalliser. This is evidenced by microscope images in Figure 6.14(b) and Figure 6.14(c) which show the absence of significant fines and agglomerates in the steady-state α-GLY product for both runs, indicating an absence of secondary nucleation. Also, the regular and well-faceted crystals of α-GLY product indicate that significant attrition did not occur in the crystallisation process. The propensity for attrition depends on the suspension density, crystal size, fluid shear rates, and presence of high shear regions. Crystal attrition is commonly experienced in agitated vessels e.g. MSMPRs where crystal-crystal and crystal-impeller collisions are promoted at high agitation speeds (high shear rates) (Brown et al., 2018; Onyemelukwe et al., 2018). The absence of crystal attrition in this seeded crystallisation process is a major advantage of the geometry and mixing mechanism in the SPC mesoscale crystalliser. The presence of smooth, rather than sharp constrictions reduces high shear regions compared to conventional SEPC COBCs (Reis et al., 2005). Also, the reliance on oscillatory flow mixing rather than agitation means that crystal-impeller collisions are absent, and significantly lower shear strain rates are generated in the SPC mesoscale crystalliser (Mazubert et al., 2016; Ejim et al., 2017). It is important to note that laser diffraction measurements for all steady-state α-GLY product in this work appeared to have bimodal distributions containing populations of particles with much smaller size modes than were present in sample images. These smaller particle fractions were identified as artefacts

caused by the laser diffraction software applying a default scattering model for spherical particles to strongly prismatic particles of α-GLY (Agimelen et al., 2017). The corresponding laser diffraction measurements for γ-GLY samples were unimodal and without artefacts.

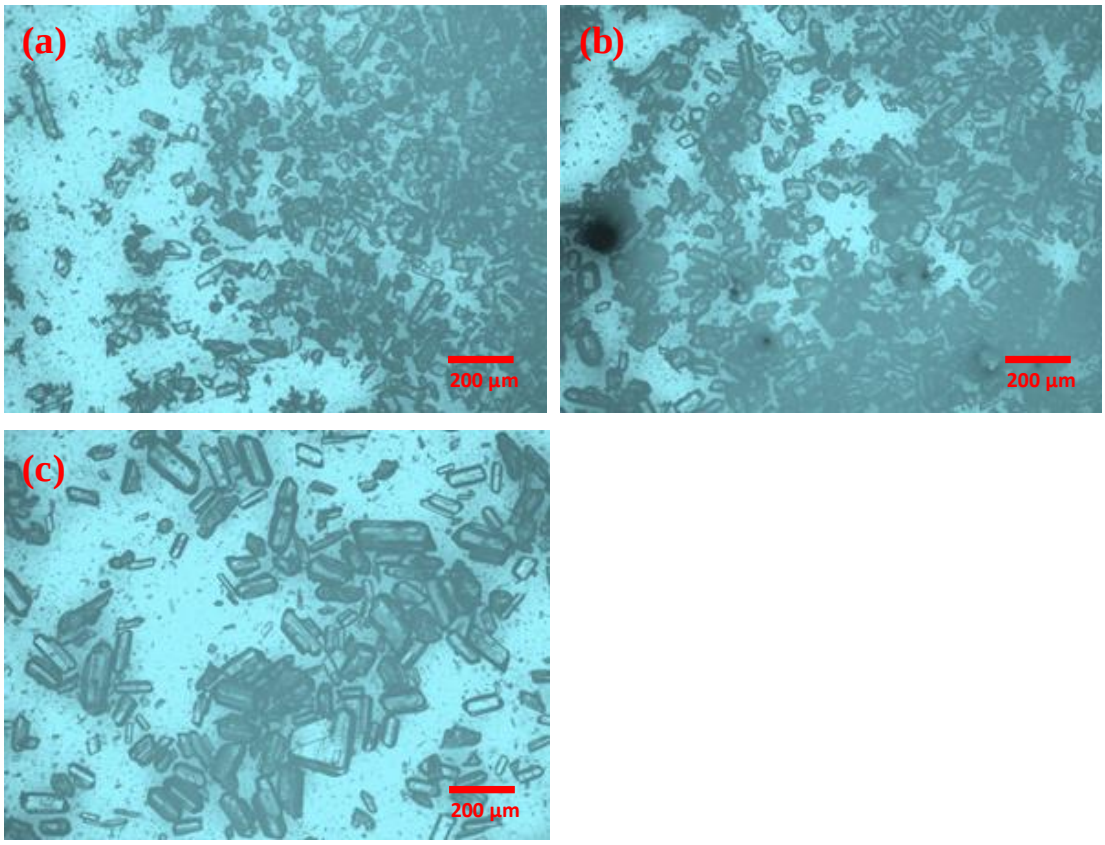

Figure 6.14 Microscope images of α-GLY crystals (a) from seed vessel, (b) at steady-state for τ of 2.8 min, (c) at steady-state for τ of 7.3 min.

For a τ of 2.8 min (20.9 g min^{-1}), less crystal growth was obtained, however, the span of the α-GLY seed material was reduced to 1.41 in the steady-state α-GLY product (see Table 6.4). This is the result of a plug flow-like RTD in the SPC mesoscale crystalliser providing crystals with similar supersaturation histories. Extending τ to 7.3 min by reducing the mass flow rate to 8 g min^{-1} provided much more crystal growth at the expense of a broader α-GLY product distribution with a span of 1.64 (see Figure 6.13). This agrees with findings in section 4.2.2 of Chapter 4, which show an increase in D_{ax}/uL at a lower Re_n. With increased axial dispersion, there is more of a spread of supersaturation histories and a wider distribution of crystal sizes. This is evidence that crystalliser axial dispersion strongly influences the CSD of α-GLY.

The effect of τ on γ-GLY was less discernible due to its much slower growth kinetics. Previous work by Srinivasan (2008) has shown that the γ-GLY crystal exhibits normal unidirectional growth

along one of its 'c' directions, but has almost no growth in its other directions, hence its possession of a trigonal end. The α-GLY crystal on the other hand, has almost equal growth rates along both 'c' directions, with [011] being the fastest growing direction among other growth directions of the crystal. This is easy to observe in Figure 6.14(a) and Figure 6.14(b) where more rounded crystals grow into the distinct α-GLY prismatic morphology with increasing τ. Figure 6.15 shows a less pronounced shift of the γ-GLY product distribution to the right despite a longer mean residence time. This slower growth rate of γ-GLY was detrimental to process performance, as a fractional yield of only 45% was attained for both mean residence times. Figure 6.16 shows the bi-pyramidal morphology of smaller γ-GLY product crystals. The absence of significant fines and agglomerates suggest that secondary nucleation and attrition did not occur in the crystallisation process. In a similar fashion to α-GLY, the span of the γ-GLY seed material was also reduced for a τ of 2.8 min (see Table 6.4) due to near plug flow operation in the crystalliser.

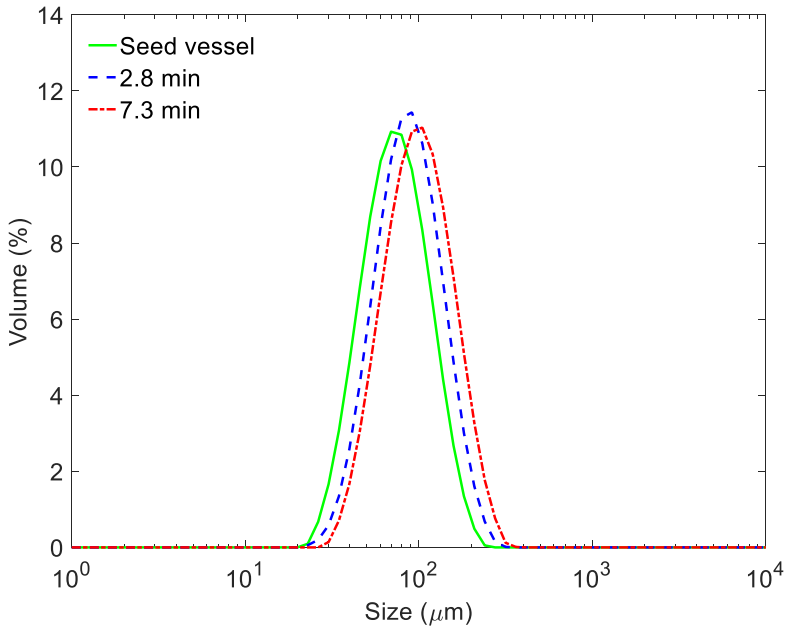

Figure 6.15 CSD of γ-GLY seed and steady-state product for τ of 2.8 min and 7.3 min.

However, lowering the mass flow rate to 8 g min^{-1} (τ of 7.3 min) had negligible effect on the normalised size and span of the γ-GLY product. This once again emphasised the role of growth kinetics in crystallisation.

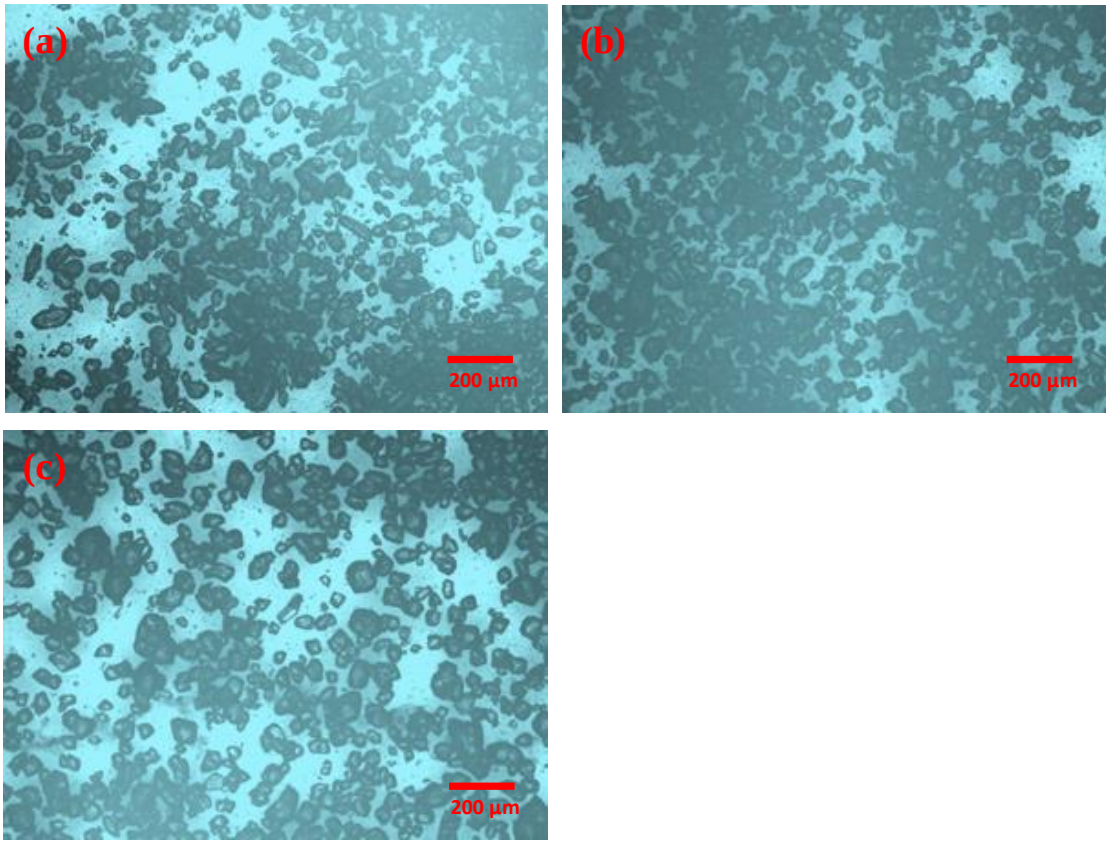

Figure 6.16 Microscope images of γ-GLY crystals (a) from seed vessel, (b) at steady-state for τ of 2.8 min, (c) at steady-state for τ of 7.3 min.

Figure 6.17 highlights the insensitivity of γ-GLY product size to changes in mean residence time. A 2.6-fold increase in τ (by changing the mass flow rate) had negligible effect on γ-GLY normalised product size owing to its slow growth kinetics. γ-GLY also showed no sensitivity to a change in axial dispersion with flow rate, as the steady-state product CSD for both mean residence times had almost identical spans. For this polymorph, extending the length of the SPC mesoscale crystalliser to gain additional mean residence time would be impractical, and unlikely to provide a consequential improvement to crystal growth and yield. Therefore, γ-GLY may be better suited for MSMPR crystallisation.

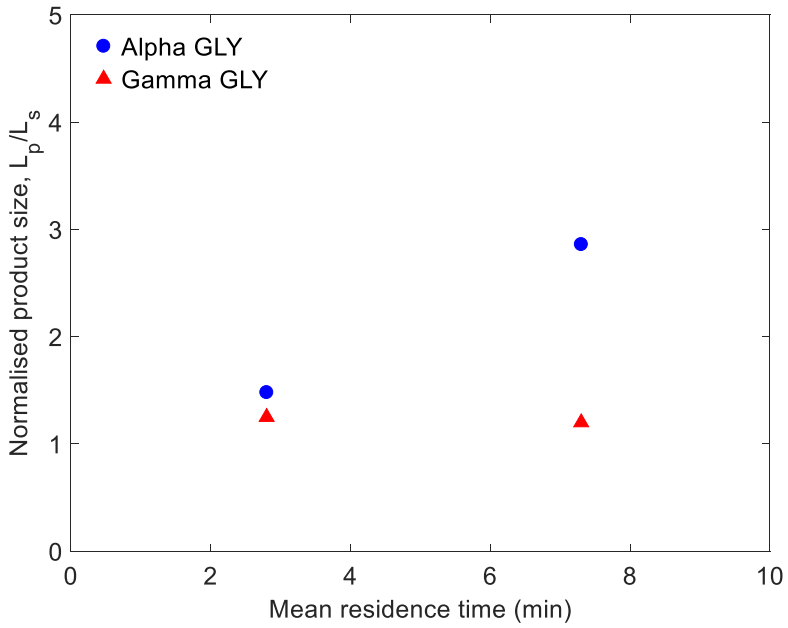

Figure 6.17 Effect of mean residence time on the steady-state normalised product size.

6.2.7 Effect of oscillatory condition

Oscillatory conditions have been shown to directly control the hydrodynamic conditions within the SPC mesoscale crystalliser. It is therefore important to understand how different hydrodynamic conditions affect crystallisation process performance and final product attributes. The effect of oscillatory condition on the crystallisation of α- and γ-GLY was studied by performing experiments at three different mixing conditions Re_o = 62, 123, and 308. The axial dispersion coefficient, D_{ax}, for each condition was evaluated from liquid and solid phase RTD studies in Chapter 4 using Equation (6.2). Accordingly, an Re_o of 62 (x_0 = 1 mm, f = 2 Hz) corresponded to a D_{ax} of 4.8×10^{-4} m^2 s^{-1}. An Re_o of 123 (x_0 = 2 mm, f = 2 Hz) provided the greatest deviation from plug flow in the crystalliser (Levenspiel, 1999) with a D_{ax} of 6.2×10^{-4} m^2 s^{-1}. At an Re_o of 308 (x_0 = 1 mm, f = 10 Hz), near plug flow operation was achieved in the crystalliser with a D_{ax} of 2.2×10^{-4} m^2 s^{-1}. Table 6.5 summarises the x_0, f, D_{ax}/uL and D_{ax} at these mixing intensities.

$$D_{ax} = \left(\frac{D_{ax}}{uL}\right)\frac{L^2}{\tau} \tag{6.2}$$

Figure 6.18 shows that the steady-state α-GLY product CSD is sensitive to mixing conditions inside the SPC mesoscale crystalliser. Operating at a near plug flow condition (x_0 = 1 mm, f = 10 Hz) provided the greatest size increase with a factor of 2.86 (see Table 6.5) as indicated by the most

right-shifted distribution. The least growth in the system was obtained at an Re_o of 123 ($x_0 = 2$ mm, $f = 2$ Hz), a condition which generated significant axial dispersion in the crystalliser.

Table 6.5 Summary of experimental conditions and results for the effect of oscillatory condition on the crystallisation of GLY

	α-GLY			γ-GLY		
Mean residence time, τ (min)	7.3	7.3	7.3	7.3	7.3	7.3
Centre-to-peak amplitude, x_0 (mm)	1	1	2	1	1	2
Frequency, f (Hz)	2	10	2	2	10	2
Oscillatory Reynolds number, Re_o (-)	62	308	123	62	308	123
Axial dispersion number, D_{ax}/uL (-)	0.03	0.01	0.04	0.03	0.01	0.04
Dispersion coefficient, D_{ax} ($m^2 s^{-1}$)	4.8×10^{-4}	2.2×10^{-4}	6.2×10^{-4}	4.8×10^{-4}	2.2×10^{-4}	6.2×10^{-4}
Starting seed size, $d_{4,3}$ (µm)	66 ± 0.3	69 ± 0.2	59 ± 0.2	93 ± 1.0	89 ± 0.1	87 ± 0.1
Starting seed span (-)	1.96	1.47	1.37	1.42	1.20	1.08
Steady-state mean product size, $d_{4,3}$ (µm)	138 ± 1.3	200 ± 14.8	116 ± 9	114 ± 0.2	112 ± 0.0	102 ± 8.4
Normalised product size, L_p/L_s (-)	2.08	2.86	1.96	1.22	1.24	1.18
Steady-state exit concentration (g/g)	0.198	0.197	0.120	0.208	0.208	0.208
Span (-)	1.84	1.64	1.69	1.21	1.31	1.14
Yield (%)	69.2	71.5	65.7	45.0	45.5	44.5

Previous work in Chapter 4 has shown that for a fixed flow rate, operating at different oscillatory conditions does not significantly change the mean residence time in the crystalliser. This means that the changes in steady-state CSD observed in Figure 6.18 are more related to the hydrodynamic conditions created within the crystalliser at these different conditions and their associated effects on crystallisation kinetics. For the SPC mesoscale crystalliser, it has been shown in Chapter 5 that higher radial velocities promote higher rates of convective heat transfer, which reduce radial temperature variations and consequently supersaturation gradients throughout the bulk solution. It has also been shown that mass transfer coefficient is enhanced by the extent of radial mixing in the SPC design (Reis et al., 2008; Ahmed et al., 2018). These higher radial velocities are achieved in the SPC mesoscale crystalliser at combinations of high oscillatory f and low x_0, corresponding to low D_{ax} values and narrower RTDs (see section 4.2.2 of Chapter 4). In a two-step growth mechanism consisting of volume-diffusion and surface integration, the volume-diffusion of solute from the bulk solution to the solution-crystal interface is the first step of crystal growth and can be computed by means of Equation (6.3) (Mullin, 2001).

$$G(L_c) = k_d(L_c)\left[\frac{C - C_l(L_c)}{\rho_c}\right] \tag{6.3}$$

where k_d is the mass transfer coefficient or volume diffusion rate constant (m s^{-1}), G is the linear growth rate (m s^{-1}), L_c is the characteristic length or size of the crystal (m), C is the concentration of solute in the bulk liquid phase (mol m^{-3}), C_l is the concentration of solute in the liquid phase at the

crystal surface (mol m^{-3}), ρ_c is the molar density of the crystal phase (mol m^{-3}). When k_d is small, volume-diffusion becomes the rate-limiting step for crystal growth. Furthermore, growth rate is governed by the crystal surface area exposed to the bulk fluid, and this depends on the quality of crystal suspension. It follows therefore, that at near plug flow oscillatory conditions, uniform mixing provides homogeneous crystal suspension and uniform distribution of supersaturation, thus enhancing crystal growth rates. A higher yield was obtained for the near plug flow condition than at other conditions. With no evidence of secondary nucleation in the steady-state α-GLY product CSDs (Figure 6.18), it can be concluded that the improved yield is linked to faster growth rates in the crystalliser. Interestingly, the oscillatory condition $x_0 = 2$ mm, $f = 2$ Hz provided the least growth of all three conditions despite having the second highest mixing intensity ($Re_o = 123$). This further emphasises that effective mass transfer is promoted more by radial velocities related to higher oscillatory f than axial velocities within the system.

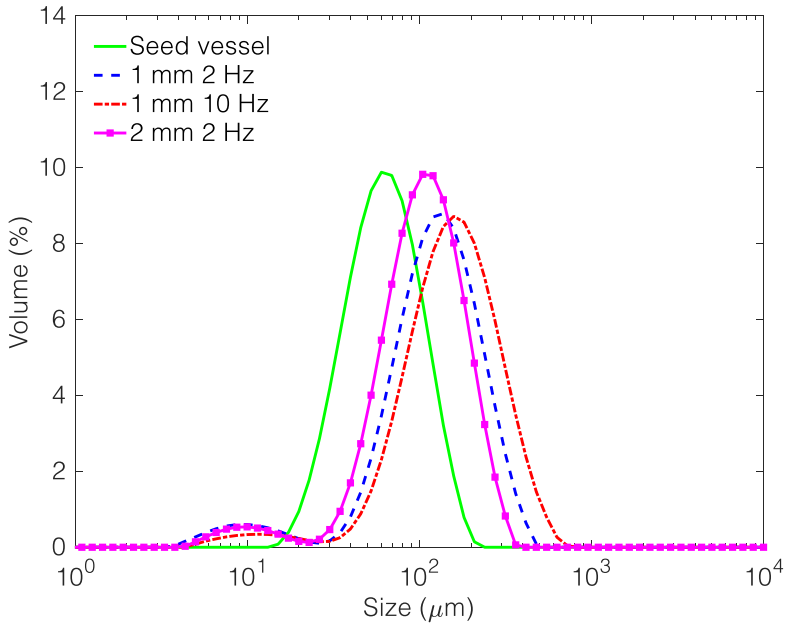

Figure 6.18 CSD of α-GLY seed and steady-state product for different oscillatory conditions.

A less discernible but similar trend was observed in Figure 6.19 for the slow-growing γ-GLY, again demonstrating the importance of plug flow performance for growth rate enhancement. Interestingly, tighter spans were obtained in γ-GLY product CSDs in comparison to α-GLY for the same extents of dispersion. This revealed the bigger role played by inherent growth kinetics of different polymorphic forms in shaping the steady-state CSD. For the same values of D_{ax}, more pronounced size-dependent growth rate dispersion (Girolami and Rousseau, 1985; Mydlarz and Briedis, 1992) contributed to broadening the CSD of α-GLY product. The combined effect of crystal growth rate

dispersion and crystalliser axial dispersion is also responsible for the variations in span amongst steady-state products of each polymorph, and between steady-state products and their respective starting seed material.

Figure 6.20 highlights the strong dependency of α-GLY growth kinetics on the hydrodynamics in the SPC mesoscale crystalliser.

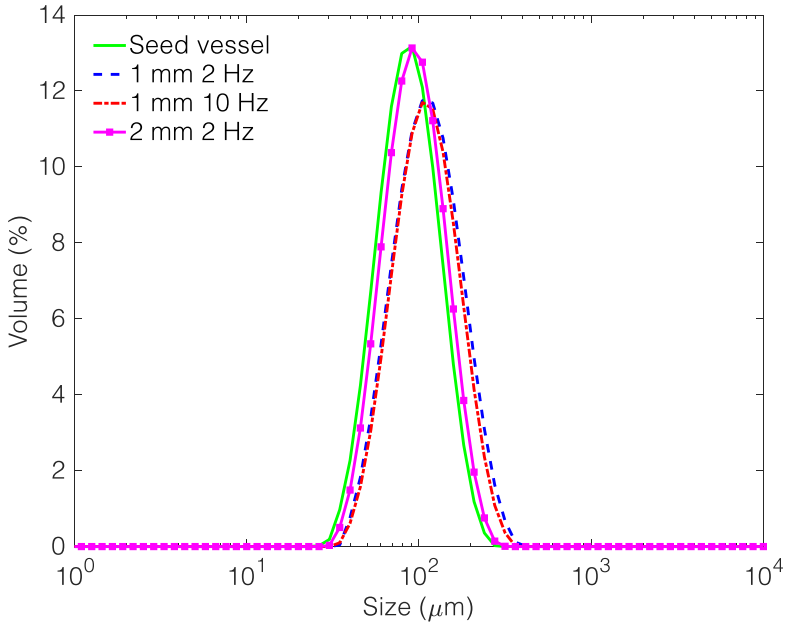

Figure 6.19 CSD of γ-GLY seed and steady-state product for different oscillatory conditions.

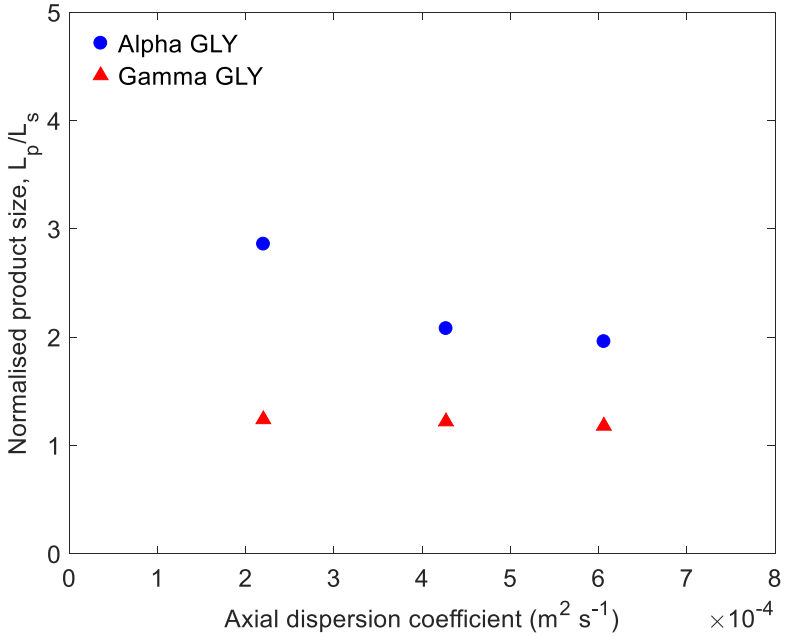

Figure 6.20 Relationship between crystalliser axial dispersion and growth kinetics.

The plot shows that higher degrees of axial dispersion impede crystal growth in the SPC mesoscale crystalliser; however, this relationship is not linear, and appears to plateau with increasing D_{ax}. On the other hand, a very weak dependency exists for γ-GLY as inherently slow growth kinetics dominate. These two polymorphs have morphological differences which greatly influence their growth rates. The unidirectional growth exhibited by γ-GLY means that there is much slower integration of GLY molecules onto the surfaces of γ-GLY seed crystals than α-GLY crystals. This means that surface integration is the controlling step for γ-GLY crystal growth.

6.2.8 Effect of temperature profile

It is well known in batch crystallisation that a cubic profile can provide better control over final CSD than linear or natural cooling (Majumder and Nagy, 2013). Usually, in a cubic profile the temperature is decreased slowly at the start of the batch to control supersaturation generation, and at a faster rate towards the end to promote growth onto available crystal surface area. Aamir et al. (2010) previously demonstrated in a batch crystallisation that a combination of an appropriate seed loading with a cubic profile can avoid secondary nucleation and yield larger, more uniform crystals containing few fines and agglomerates. The effect of temperature profile on steady-state state CSD of α- and γ-GLY was investigated using a stepped linear profile and a spatially approximated cubic profile (see details in section 3.11.3 of Chapter 3). Table 6.6 summarises the experimental conditions and results obtained for the temperature profile effect on GLY crystallisation.

Table 6.6 Summary of experimental conditions and results for the effect of temperature profile on the crystallisation of GLY from water

	α-GLY		γ-GLY	
Mean residence time, τ (min)	7.3	7.3	7.3	7.3
Seed loading (%)	7	7	7	7
Temperature profile	Stepped linear	Cubic	Stepped linear	Cubic
Starting seed size, $d_{4,3}$ (µm)	58 ± 0.03	59 ± 0.03	89 ± 0.1	83 ± 2.6
Starting seed span (-)	1.24	1.38	1.20	1.20
Steady-state mean product size, $d_{4,3}$ (µm)	119 ± 8.6	133 ± 2.7	107 ± 3.2	112 ± 0.1
Normalised product size, L_p/L_s, (-)	2.03	2.24	1.20	1.36
Steady-state exit concentration (g/g)	0.200	0.198	0.208	0.208
Span (-)	1.92	1.36	1.28	1.21
Yield (%)	64.2	69.8	44.7	45.2

Steady-state product distributions in Figure 6.21 show that for the same τ, mixing condition, and seed loading, more growth and yield was obtained in α-GLY crystals subjected to an approximated

cubic profile (see Table 6.6). The gradual spatial temperature variation (°C m^{-1}) in the initial segments gently increased supersaturation which favoured crystal growth over nucleation.

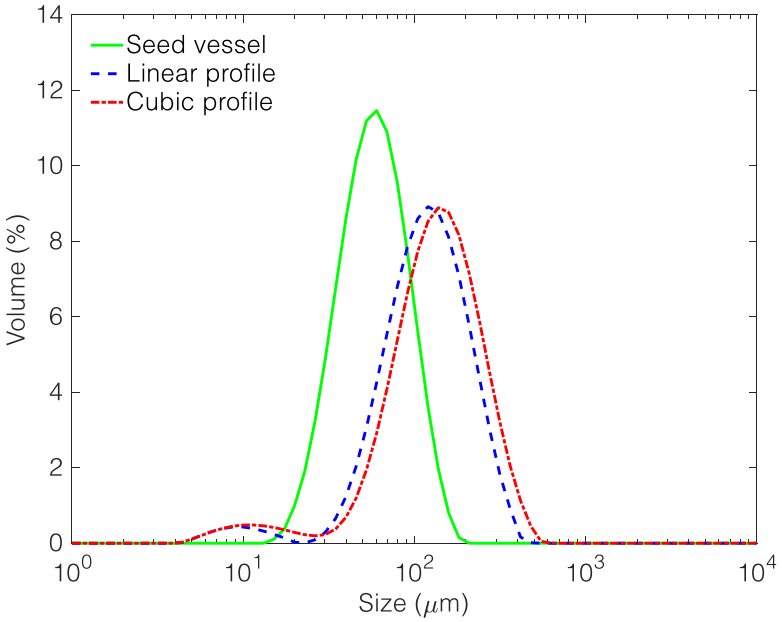

Figure 6.21 CSD of α-GLY seed and steady-state product obtained from stepped linear and approximated cubic profiles.

Secondary nucleation was avoided due to sufficient seed loading, however, a high supersaturation generated in the final segment eventually led to encrustation forming over time on the crystalliser walls. The occurrence of encrustation in the final segment suggests that the current approximation to the cubic profile may not be suitable for prolonged operation, since the avoidance of any encrustation is extremely important for uninterrupted steady-state operation. A closer approximation to the cubic profile using additional segments could provide better control of supersaturation, thereby preventing encrustation and further improving crystal growth.

A marginal improvement was obtained for γ-GLY (Figure 6.22), where slow crystal growth rate once again overshadowed the benefits of the approximated cubic profile. For both polymorphic forms, a tighter CSD span was obtained in steady-state products subjected to an approximated cubic profile. This is could be due to smaller crystals growing at faster rates than larger crystals, which leads to a slight narrowing of the steady-state distribution (Loï Mi Lung-Somarriba et al., 2004).

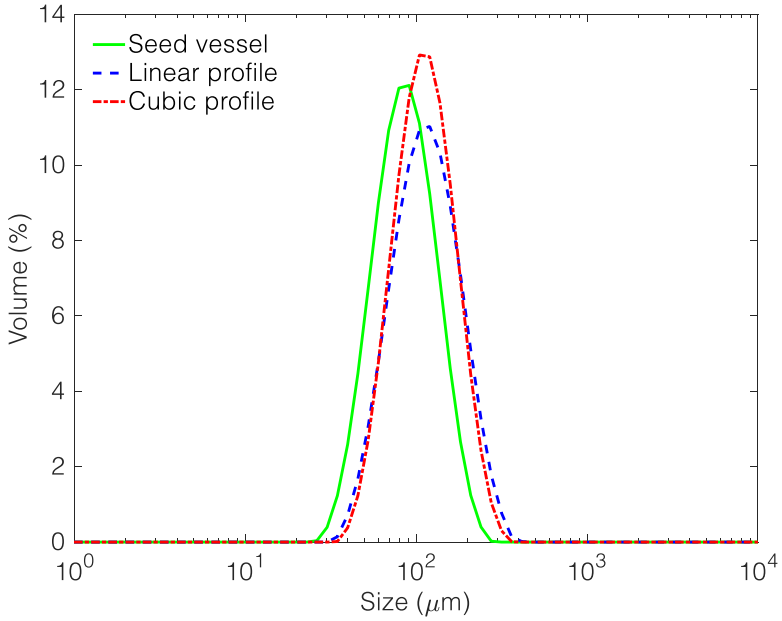

Figure 6.22 CSD of γ-GLY seed and steady-state product obtained from stepped linear and approximated cubic profiles.

6.2.9 Effect of seed size and loading

The seed size and loading control the seed surface area available for growth. Thus, it is necessary to understand the relationship between seed surface area and final product size. The effect of seed size and loading on the steady-state mean size, CSD, and yield of α- and γ-GLY was investigated according to the methodology described in section 3.11.11 of Chapter 3. Seed loadings of 4, 7 and 12% w/w were investigated at two distinct seed sizes for each GLY polymorph. For α-GLY, seed sizes of 57 ± 1.2 µm and 87 ± 1.7 µm were used, while for γ-GLY 88 ± 2.89 µm and 102 ± 0.7 µm seed sizes were used. Table 6.7 gives the seed surface area corresponding to each seed size and loading for the α-GLY polymorph.

Table 6.7 Seed loadings and corresponding seed surface area for α-GLY

Seed size, $d_{4,3}$ (µm)	Seed loading (%)	†Seed mass, W_s (g)	Seed surface area, S_c (cm^2)	Mean product size, $d_{4,3}$ (µm)	L_p/L_s (-)	Yield (%)	% yield improvement
57 ± 1.2	4	0.49	550	240.9	4.27	36.84	-
	7	0.81	909	131.0	2.23	69.83	89.5
	12	1.35	1515	103.6	1.86	79.84	14.3
87 ± 1.7	4	0.49	360	274.3	3.23	17.90	-
	7	0.81	594	231.9	2.66	65.94	268.4
	12	1.35	990	136.6	1.53	71.37	8.2

†Steady-state seed mass in crystalliser based on one mean residence time

Figure 6.23 and Figure 6.24 display an expected trend where an increase in seed loading shifts the steady-state α-GLY distribution to the left. A seed loading of 12% w/w resulted in the smallest steady-state α-GLY product owing to more seed crystals competing for supersaturation.

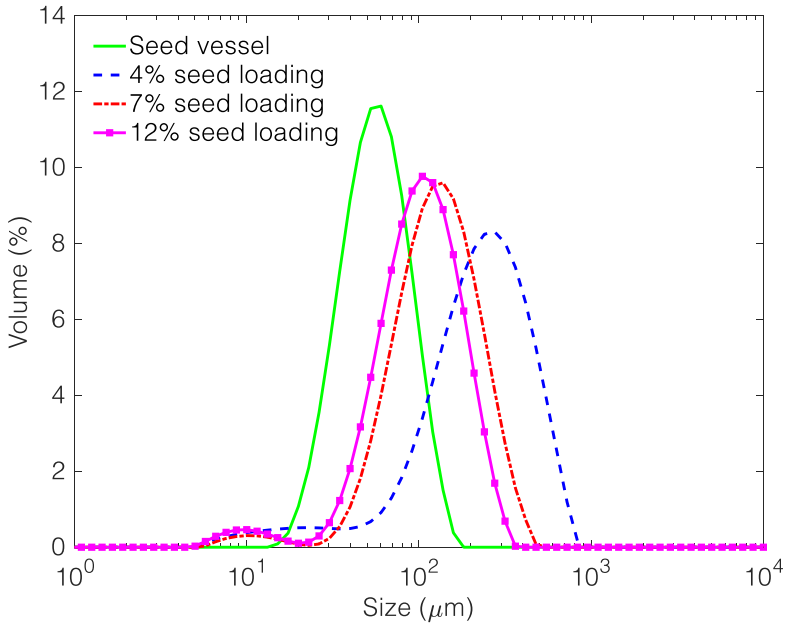

Figure 6.23 CSD of α-GLY seed and steady-state product at different seed loadings for 57 $\pm$ 1.2 µm seeds.

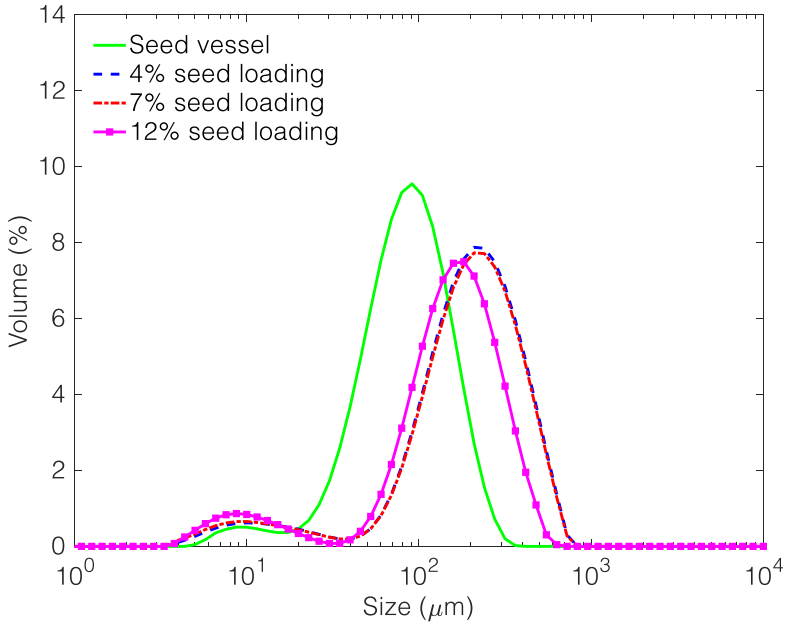

Figure 6.24 CSD of α-GLY seed and steady-state product at different seed loadings for 87 $\pm$ 1.7 µm seeds.

While a seed loading of 4% w/w resulted in the most right-shifted steady-state distribution. This is confirmed by microscope images (Figure 6.25) showing a decrease in steady-state product size with increasing seed loading, with few fines present in the product obtained from 4% w/w seed loading.

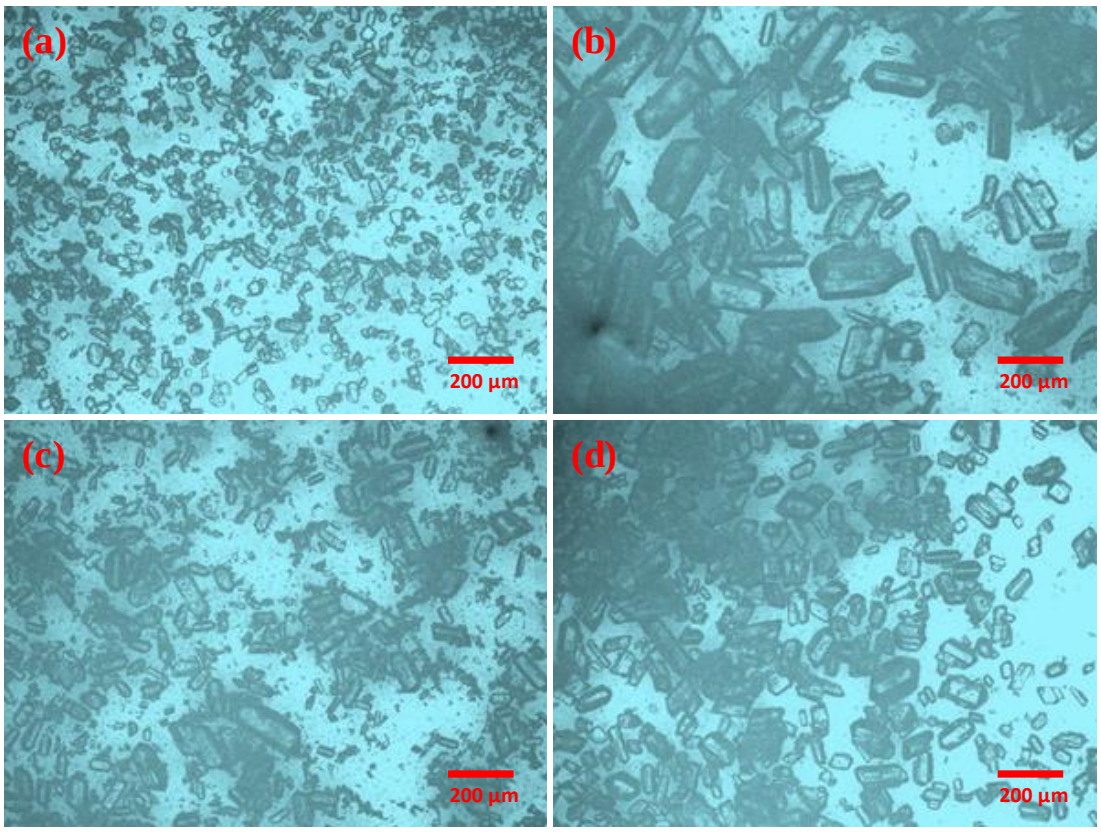

Figure 6.25 Microscope images of α-GLY crystals (a) from seed vessel, (b) from 4% w/w seed loading, (c) from 7% w/w seed loading, (d) from 12% w/w seed loading. Seed size $= 57 \pm 1.2$ µm.

Previous work by Narducci et al. (2011) in an STC showed that if seed mean size was maintained, increasing seed loading decreased the normalised product size (L_p/L_s). It follows therefore, that for a fixed number of crystals which grow to a certain size limited by available supersaturation, increasing the number of crystals at the same supersaturation will form the same mass of new material spread over a larger number of crystals, and thus each crystal will grow to a smaller final size than if there were fewer crystals. As seed loading was increased at a fixed seed size, more seed surface area was available for growth, and an increase in fractional yield was observed for α-GLY (see Table 6.8).

Figure 6.26 highlights the coupled effect of seed size and loading on the normalised product size for α-GLY. For both seed sizes, an increase in seed loading decreased steady-state product size. It is possible that a slower growth rate exhibited by the bigger 87 ± 1.7 µm seeds was responsible for lower normalised product sizes obtained despite having smaller seed surface areas (see Table 6.7). Loï Mi Lung-Somarriba et al. (2004) have shown that α-GLY crystal growth rate is greatly dependent on

crystal size. It decreases rapidly with increasing size and becomes constant for crystal sizes larger than 1600 µm. To achieve higher normalised product sizes with bigger seed sizes, a longer mean residence time would be required in the crystalliser.

Table 6.8 Summary of experimental conditions and results for the effect of seed size and loading on the crystallisation of α-GLY from water

	α-GLY					
Mean residence time, τ (min)	7.3	7.3	7.3	7.3	7.3	7.3
Seed loading (%)	4	4	7	7	12	12
Starting seed size, $d_{4,3}$ (µm)	56 ± 0.8	85 ± 1.3	58 ± 0.01	87 ± 4.7	55 ± 0.1	89 ± 1.2
Starting seed span (-)	1.21	1.48	1.24	1.52	1.36	1.49
Steady-state mean product size, $d_{4,3}$ (µm)	240 ± 0.6	274 ± 16	131 ± 2.7	231 ± 33	103 ± 2.2	136 ± 24
Normalised product size, L_p/L_s (-)	4.27	3.23	2.23	2.66	1.86	1.53
Steady-state exit concentration (g/g)	0.211	0.219	0.198	0.200	0.194	0.197
Span (-)	1.76	2.13	1.51	2.13	1.50	2.17
Yield (%)	36.84	17.90	69.83	65.94	79.84	71.37

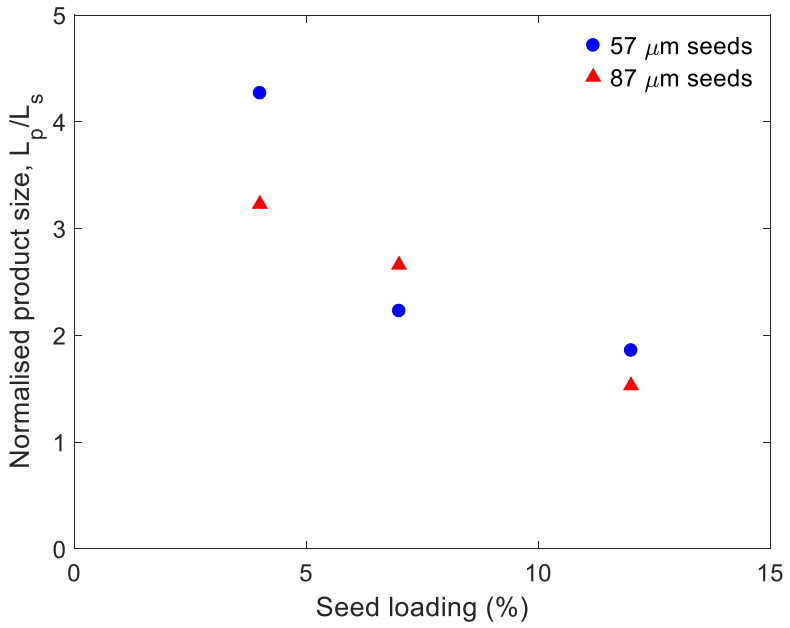

Figure 6.26 Effect of seed size and loading on the normalised product size for α-GLY.

An important requirement for a crystallisation process is to maintain a good balance between the desired product attributes and high yield. The selection of an appropriate seed size and loading would therefore rely on a trade-off between final product size and yield. Figure 6.27 vividly illustrates this relationship with seed surface area. While unimodal CSDs with large normalised product sizes are achievable at low surface areas, the corresponding yields are impractical. A close inspection of Figure 6.27 shows that for 57 ± 1.2 µm seeds, higher yields were obtained for each seed loading in comparison to 87 ± 1.7 µm; this suggests that seeding with smaller α-GLY seeds is better for productivity. For both seed sizes, the biggest % increase in yield was obtained by increasing seed loading to 7% w/w

loading. Beyond this loading, a marginal yield improvement was obtained at the cost of smaller sized product. This suggests that a diminishing relationship exists between seed surface area, normalised product size, and yield for α-GLY. Depending on yield constraints, and downstream processing and formulation requirements, an appropriate seed loading/surface area may be selected along the seed response curve for seeded continuous cooling crystallisations of α-GLY. Ultimately, the yield and product size at chosen seeding conditions may be improved by increasing the mean residence time in the SPC mesoscale crystalliser beyond 7.3 min. For an outlined objective of delivering GLY product with a suitably large mean size and narrow CSD, operating at a seed surface area, S_c, of 1515 cm^2 (12% w/w) would be unsatisfactory, as it compromises too greatly on product size. Operating at S_c of 900 cm^2 (7% w/w) gives a good compromise between process yield (70%) and mean product size (131 µm). Therefore, the crystallisation may be seeded at this condition.

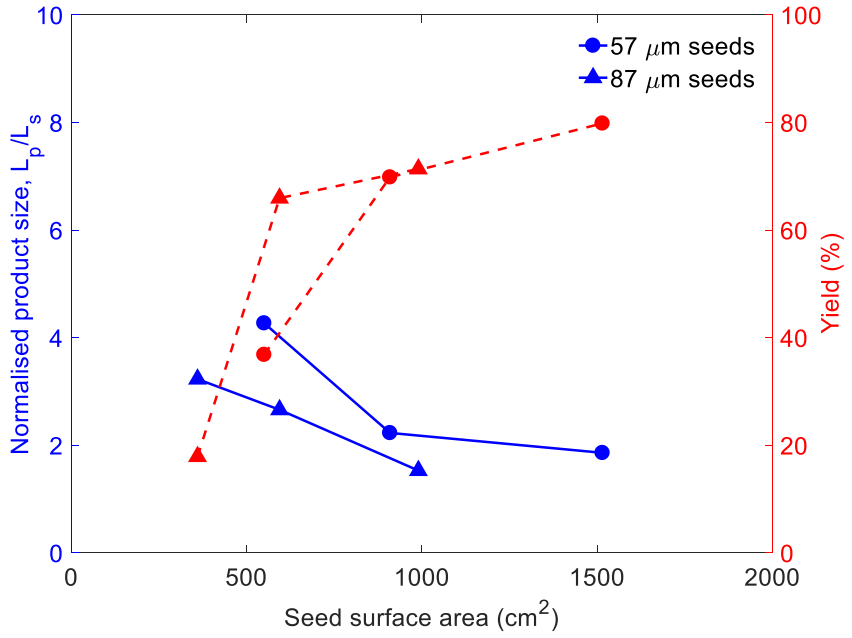

Figure 6.27 Relationship between yield (dashed red lines), normalised product size (solid blue lines), and seed surface area for α-GLY.

Figure 6.28 and Figure 6.29 show the marginal increase in γ-GLY product size obtained by seeding with 4% w/w seed mass compared to 7% w/w for both seed sizes. Once again, seeding with 12% w/w seed loading produced the smallest steady-state product. Table 6.9 summarises the experimental conditions and results for the γ-GLY polymorph.

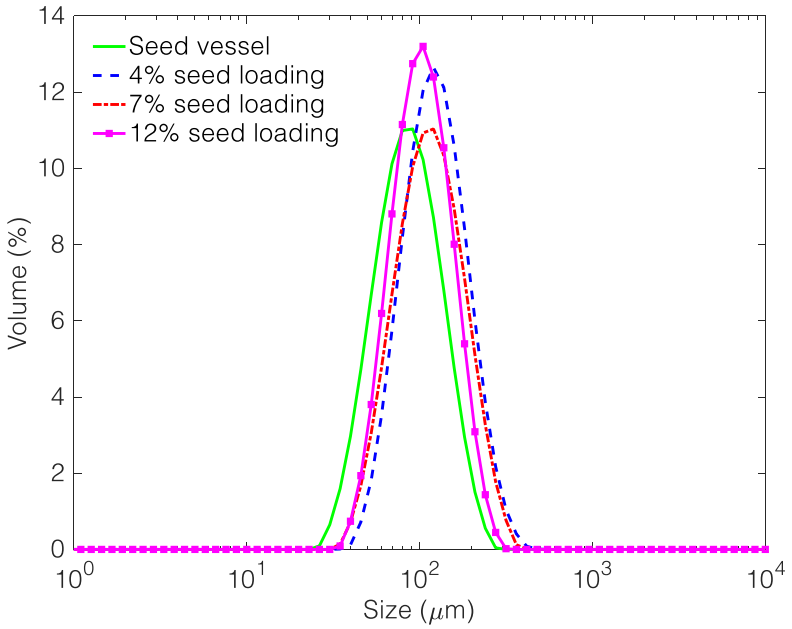

Figure 6.28 CSD of γ-GLY seed and steady-state product at different seed loadings for 88 $\pm$ 2.9 µm seeds.

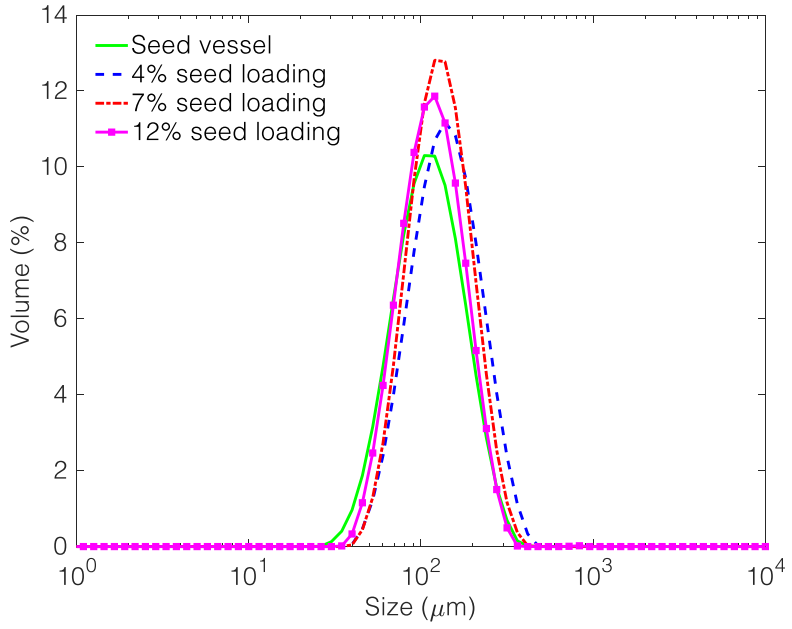

Figure 6.29 CSD of γ-GLY seed and steady-state product at different seed loadings for 102 $\pm$ 0.7 µm seeds.

Microscope images in Figure 6.30 show the much smaller and rounded product crystals obtained for γ-GLY. For both seed sizes, increasing the seed loading had negligible effect on normalised product size (Figure 6.31), but provided a modest improvement to the process yield (Table 6.9) owing to increased seed surface area. A change in seed size from 88 $\pm$ 2.9 µm to 102 $\pm$ 0.7 µm had no discernible effect on the normalised product size and yield, suggesting that the growth rate for γ-GLY

is less sensitive to seed crystal size than α-GLY. These results therefore suggest that seeding the crystallisation process with γ-GLY would be detrimental to final product size and productivity.

Table 6.9 Summary of experimental conditions and results for the effect of seed size and loading on the crystallisation of γ-GLY from water

	γ-GLY					
Mean residence time, τ (min)	7.3	7.3	7.3	7.3	7.3	7.3
Seed loading (%)	4	4	7	7	12	12
Starting seed size, $d_{4,3}$ (µm)	90 ± 1.8	102 ± 10.3	89 ± 0.1	102 ± 0.3	84 ± 1.9	101 ± 3.1
Starting seed span (-)	1.34	1.43	1.20	1.63	1.33	1.50
Steady-state mean crystal size, $d_{4,3}$ (µm)	120 ± 4.3	133 ± 10.5	110 ± 0.03	129 ± 0.1	103 ± 0.3	112 ± 0.1
Normalised product size, L_p/L_s (-)	1.32	1.30	1.24	1.26	1.23	1.11
Steady-state exit concentration (g/g)	0.221	0.223	0.208	0.208	0.207	0.208
Span (-)	1.11	1.18	1.31	1.11	1.07	1.22
Yield (%)	13.88	9.20	44.58	43.01	47.60	45.70

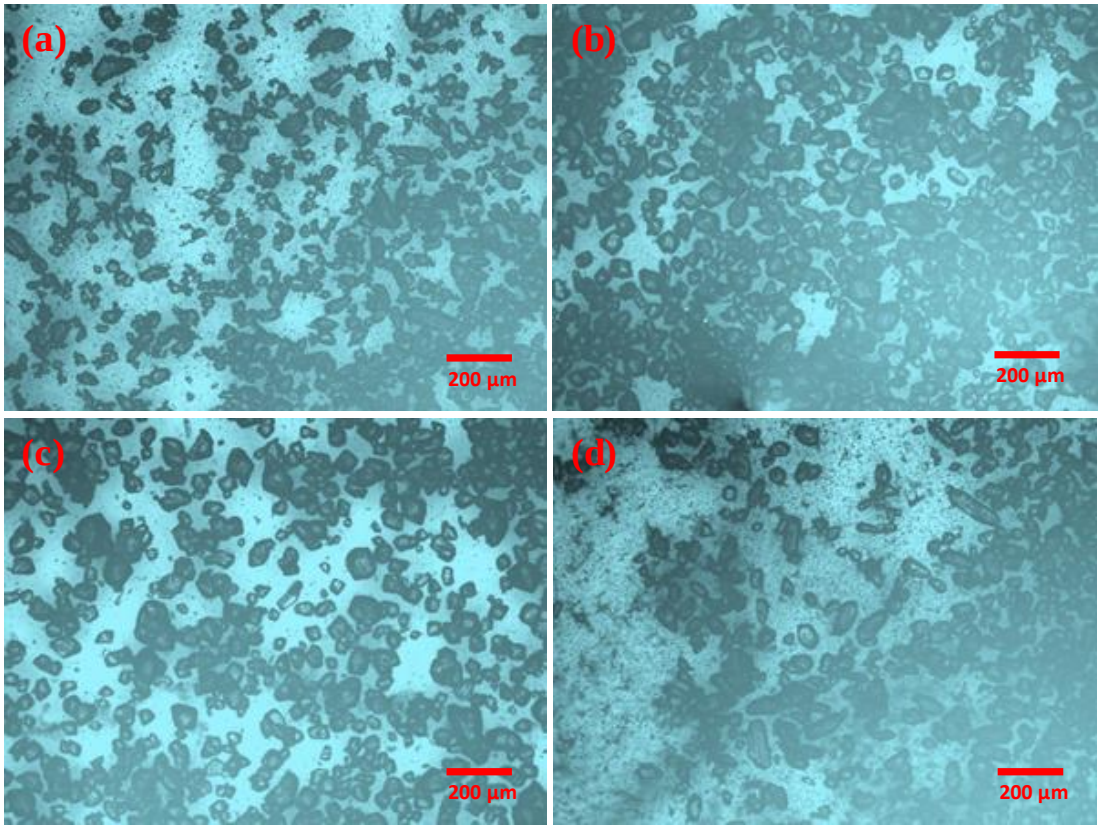

Figure 6.30 Microscope images of γ-GLY crystals (a) from seed vessel, (b) from 4% w/w seed loading, (c) from 7% w/w seed loading, (d) from 12% w/w seed loading. Seed size $= 88 \pm 2.9$ µm.

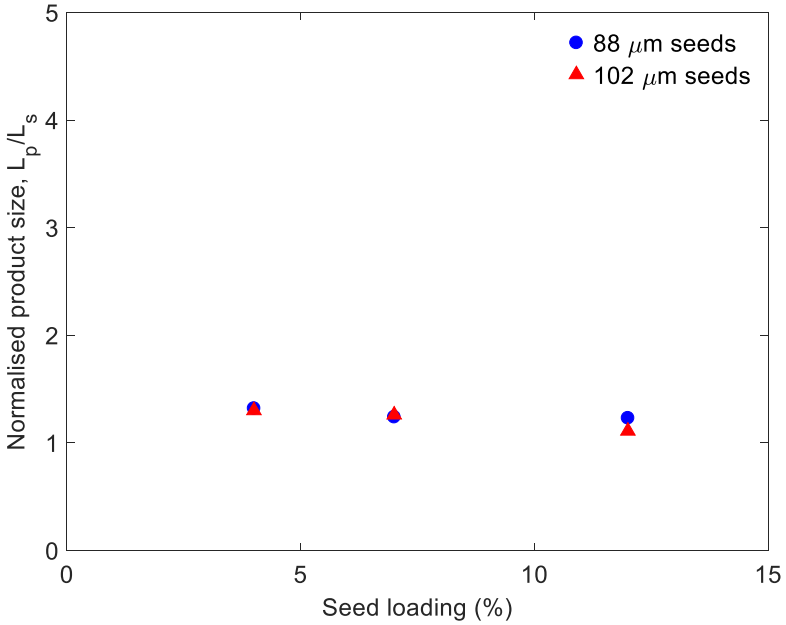

Figure 6.31 Effect of seed size and loading on the normalised product size for γ-GLY.

6.3 Conclusions

The systematic study carried out in this chapter has revealed the importance of mean residence time, temperature profile, oscillatory condition, seed size and loading as key operating variables which affect the outcome of a GLY crystallisation process in the SPC mesoscale crystalliser. It was established that extending the mean residence time by decreasing mass flow rate in the crystalliser increases product crystal size and yield, but also broadens CSD. It follows therefore that extending the mean residence time by 'numbering up' to reasonable lengths will retain a narrow CSD in the final product, provided supersaturation is well distributed along the crystalliser via an optimised spatial temperature profile. Near plug flow operation was proven to be essential for ensuring maximum crystal growth rates are achieved during crystallisation through better control of local supersaturation and enhancement of mass transfer rates. An initial spatial approximation of a cubic profile in this work has shown that successfully mimicking a cubic temperature profile by optimising the number and length of independent temperature-controlled segments can provide substantial improvements to the final CSD over a stepped linear profile. The seed size and loading were found to strongly affect the steady-state product size and yield, with bigger seeds reducing the available seed surface area for supersaturation consumption. As such, seeding with small seeds is advised because it allows to obtain large, good-quality crystals, and satisfactory yield. Finally, the most critical aspect of seeding in industrial applications – polymorphic control, was demonstrated throughout this study. Seeding is an effective approach to controlling polymorphic form and ensuring right physicochemical properties in

the final API. In all experiments performed, offline Raman analysis confirmed that wet milling had no effect on polymorphic form; also, seeds of a polymorphic form yielded product crystals of the same form. The importance of seeding with the right polymorph was emphasised by the insensitivity to operating conditions, and ultimately detrimental effect of unfavourable inherent γ-GLY growth kinetics on the final product size and yield. This highlighted the impact of raw material attributes on process performance and the importance of ensuring variability from raw materials is minimised.

Overall, the SPC mesoscale crystalliser has demonstrated its suitability for performing steady-state seeded continuous cooling crystallisations. The efficient mixing and heat transfer of this platform provide homogeneous suspension of crystals and a tight control of supersaturation for crystallisation. Evidence shows that the hydrodynamics created within the SPC mesoscale crystalliser has a strong influence on the crystallisation environment. This means that the SPC mesoscale crystalliser is uniquely capable of providing exquisite control of particle attributes by fine-tuning the net flow, frequency, and amplitude of oscillations. In the next chapter, a continuous cooling crystallisation process will be developed for GLY using the second conventional approach to continuous crystallisation.

Chapter 7 Continuous cooling crystallisation in a mixed suspension mixed product removal (MSMPR) crystalliser

7.1 Introduction

This chapter covers experimental work performed within Pharmaceutical Technology and Development (PT&D), as part of a 3-month industrial secondment with AstraZeneca UK at its manufacturing site in Macclesfield, Cheshire. The work reported here has been successfully published in the Journal of Crystal Growth & Design (Onyemelukwe et al., 2018b). In the work reported, a single- and two-stage MSMPR crystalliser with integrated vacuum transfer and FBRM is developed to investigate the continuous steady-state crystallisation of α-GLY from water. Characterisation of the RTD, solids suspension, and heat transfer performance of the MSMPR system are completed using both experimental and modelling tools to speed up process development. A rapid intermittent transfer technique is applied to successfully solve transfer line blockage issues usually encountered with peristaltic pump operation, and therefore allow continuous steady-state operation for extended periods. The effect of MSMPR operating temperature, mean residence time, and number of MSMPR stages on the mean crystal size, CSD, and yield of the GLY product is subsequently studied. Real-time monitoring of crystallisation process dynamics, and determination of steady-state operation is achieved by monitoring the particle counts and chord length distribution (CLD) with the aid of an *in situ* focused beam reflectance measurement (FBRM) probe.

7.2 Results and discussion

7.2.1 Liquid RTD characterisation

Figure 7.1 shows the normalised input and output response curves (C-curves) for an experiment performed at a flow rate of 70 ml min^{-1} and 400 rpm. The tracer input to MSMPR 2 was taken as the output concentration from MSMPR 1 (red curve). This represents the RTD of material going into the next stage. Figure 7.1 shows a good fit with experimental data using the transfer function of the imperfect method. The green curve is the model-predicted response fitted to the output response from MSMPR 1 to determine the number of equal-sized tanks, N,

that give approximately the same RTD as the test section considered. In this case, N was determined as 1.4.

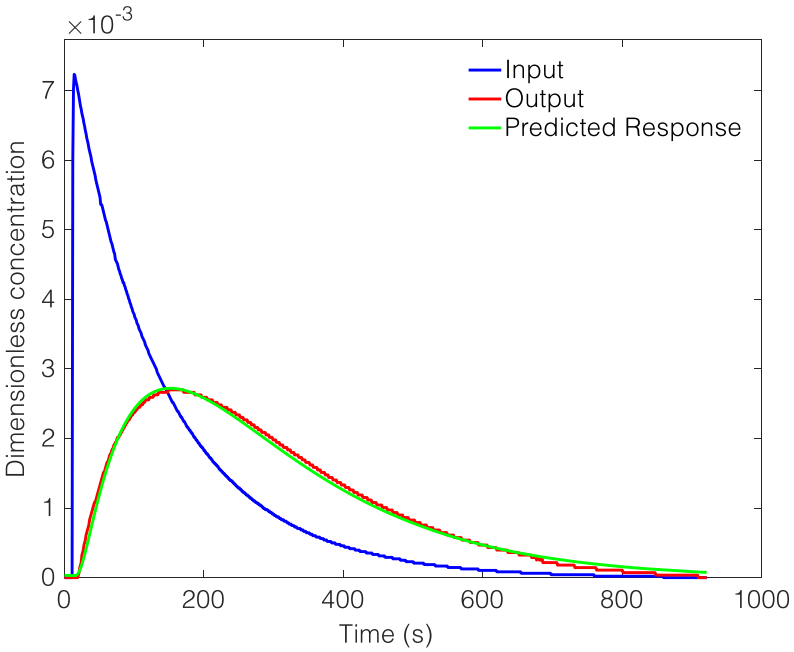

Figure 7.1 Normalised input and output curves for the single-stage MSMPR configuration with dispersion model fitting for imperfect pulse method. Volumetric flow rate of 70 ml min^{-1} and agitation speed of 400 rpm. $N = 1.4$.

Figure 7.2 shows the different pulse input shapes and corresponding output curves measured at different flow rates for an impeller speed of 200 rpm. From the analysis of these experimental C-curves and corresponding D_{ax}/uL values in Figure 7.3, it was concluded that increasing impeller speed beyond 200 rpm had negligible effect on RTD performance. This suggests that short mixing times are already achieved at 200 rpm, whereby the salt tracer is quickly mixed with the bulk liquid in the MSMPR. This is observable from the input curves in Figure 7.1 and Figure 7.2 where a rapid rise in tracer concentration is followed by a gradual decay expected of a continuous stirred tank. Previous work by Choi et al. (2004) and Patwardhan (2001) has shown that vessel RTD performance increases with increasing impeller speed from 0 rpm until a constant value at ~100 rpm. Effective mixing is essential in the MSMPR to ensure that incoming feed solution is well-mixed with vessel contents for uniform distribution of temperature and supersaturation throughout the vessel volume.

Increasing volumetric flow rate was found to have little effect on the RTD performance of a single-stage MSMPR. For flow rates of 25, 50, and 70 ml min^{-1} ($\tau = 4$, 2, and 1.4 min respectively), D_{ax}/uL was in the range 0.86 – 1.24 ($N = 1.59$ – 1.48). Choi et al. (2004) showed that similar RTDs were obtained in an unbaffled 1.4-litre stirred tank regardless of

volumetric flowrate; thus, confirming impeller speed as the controlling parameter for vessel RTD performance. This implies that changing the mean residence time in an MSMPR would cause no significant change to the RTD of vessel contents. This outcome supports simulation results obtained by Su et al. (2017) for a continuously operated 500 ml MSMPR crystalliser, whereby doubling the mean residence time did not significantly change the RTD coefficient of variation (c.v. $= \sigma/\tau$). For the single-stage MSMPR system, D_{ax}/uL was determined as 1.07 $\pm$ 0.13, with N of 1.5 $\pm$ 0.05.

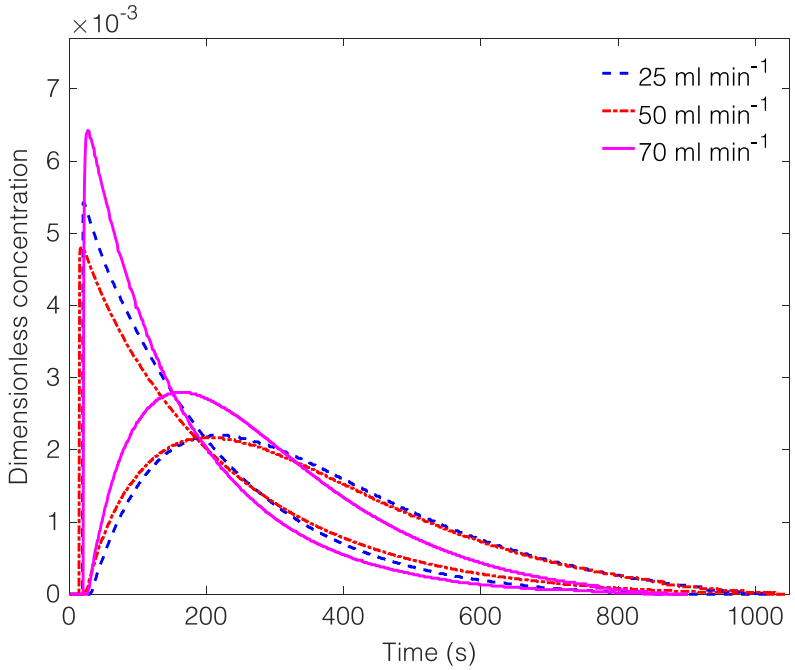

Figure 7.2 Normalised input and output curves measured for the single-stage MSMPR configuration at agitation speed of 200 rpm. Volumetric flow rates of 25 – 70 ml min^{-1}.

Adding a second stage significantly improved RTD performance by lowering D_{ax}/uL to 0.292 $\pm$ 0.04, with a corresponding N of 2.75 due to the feed/dissolution vessel operating at a higher volume of 250 ml. The improved RTD of the two-stage MSMPR is still far off from the performance of a tubular COBC such as the SPC mesoscale crystalliser[35,53] (see Table 7.1) which easily approximates to plug flow ($D_{ax}/uL = 0.002$; $N = 251$) at optimal oscillatory conditions and much lower mixing intensity, regardless of volumetric flow rate.

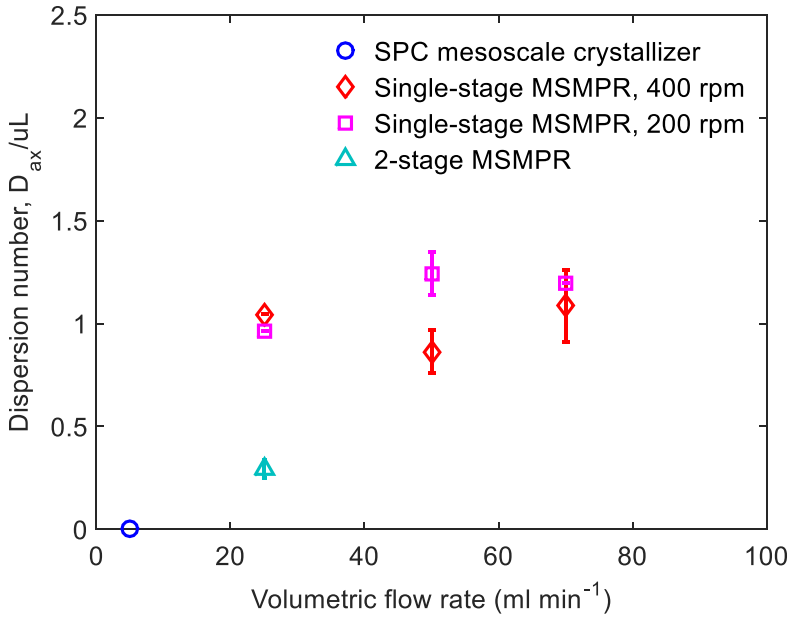

Figure 7.3 Effect of volumetric flow rate and impeller speed on RTD performance of the MSMPR system.

Table 7.1 Comparison of axial dispersion performance between the MSMPR crystalliser and SPC mesoscale crystalliser

Crystalliser	Stages/ length (m)	Flow rate (ml min^{-1})	Mixing intensity, N_{Re}/Re_o	τ_L (sec)	D_{ax}/uL (-)	D_{ax} (m^2 s^{-1})	Calculated tanks, N (-)
MSMPR	1	25	3364	40.1	0.966	8.5×10^{-3}	1.52
	1	25	6728	74.4	1.044	4.7×10^{-3}	1.48
	1	50	3364	22.7	1.243	1.7×10^{-2}	1.48
	1	50	6728	29.7	0.863	1.2×10^{-2}	1.59
	1	70	3364	23.2	1.197	1.6×10^{-2}	1.42
	1	70	6728	20.5	1.086	1.8×10^{-2}	1.47
	2	25	6728	193.3	0.292	1.1×10^{-3}	2.75
SPC mesoscale	9	5	371	-	2.0×10^{-3}	6.3×10^{-5}	251

This highlights the intrinsically broad RTDs of MSMPRs, indicating that broader product CSDs are to be expected from MSMPR crystallisers in comparison to tubular crystallisers. The outcome of the RTD study suggests that crystallisations performed in the single-stage MSMPR crystalliser at different mean residence times should essentially have the same material residence time distributions. Results also signify that operating in a two-stage MSMPR system could potentially decrease CSD span compared to a single-stage MSMPR crystalliser, while increasing total mean residence time for improved yield.

7.2.2 Just-suspended speed

With RTD performance of the MSMPR configurations now understood, good solid-liquid mixing in the MSMPR is necessary to ensure crystals experience similar RTD with the bulk solution. For the conditions specified in Table 7.2, N_{js} was computed as 554 rpm ± 20%. This corresponded to a total specific power input of 0.079 W kg^{-1}, and a vessel Reynolds number of 8310. A visual inspection of the start-up suspension found that an impeller speed of 500 rpm was sufficient for complete suspension of particles, and the suspension in the crystalliser appeared uniform (i.e. no axial settling or suspension gradients). The impeller speed was therefore maintained at this condition to minimise crystal attrition during crystallisation. To check for representative withdrawal at steady-state, the CSD of a sample obtained via intermittent withdrawal was compared with a sample taken from the bottom of MSMPR 2 at the end of the two-stage MSMPR crystallisation. The results are discussed in section 7.2.6.

Table 7.2 Specified conditions for calculating just-suspended speed, N_{js}

	Specification	Values
Vessel geometry	Base shape	DIN Torispherical
	Inner diameter (mm)	60
	Total height to tan (mm)	55
Impeller	Impeller type	3-bladed retreat curve impeller
	Tip diameter (mm)	30
	Clearance from base (mm)	10
	Impeller S number (-)	3.5
Mixing duty	Liquid volume (l)	0.1
	Liquid fill height (mm)	39
	Mass of solids (kg)	0.025‡
	Mass ratio of solid to liquid, X (%)	24.78
Physical properties	Liquid density, ρ_l (kg m^{-3})	1000
	Liquid dynamic viscosity (cP)	1.0
	Particle density, ρ_p (kg m^{-3})	1610
	Mean particle size (μm)	100
Performance at N_{js}	Specific power input (W kg^{-1})	0.079
	Vessel Reynolds number (-)	8310
	Tip speed (m s^{-1})	0.87

‡Solids mass based on GLY solution concentration at 40 °C.

7.2.3 Critical mean residence time

AspenONE® engineering suite was used in estimating C_p as 3823 J kg^{-1} K^{-1} for the 0.275 g/g GLY-water solution which had a density of 1090 kg m^{-3}. The UA for MSMPR 1 and 2 was estimated at 2.39 W K^{-1} using the Dynochem® UA utility. The critical mean residence time, $\tau_{critical,}$ was calculated as 9.06 min for a desired operating temperature of 20 °C and an

incoming feed temperature of 60 °C, with the MSMPR jacket temperature set to 0 °C. Table 7.3 summarises the specifications and results.

Table 7.3 Specified conditions for estimating UA

	Specification	Values
Vessel geometry	Liquid volume (l)	0.1
	Heat transfer area, A (m^2)	0.01
Process side	Impeller speed (rpm)	500
	Process heat transfer coefficient, h_i (W m^{-2} K^{-1})	3557
	Overall heat transfer coefficient, U (W m^{-2} K^{-1})	239
Wall and lining	Wall thickness (mm)	2.5
	Wall thermal conductivity (W m^{-1} K^{-1})	1.09
	Material of construction	Borosilicate
	Wall heat transfer coefficient, h_w (W m^{-2} K^{-1})	301
Jacket side	Heat transfer medium	SYLTHERM 8002
	Jacket type	Annular unbaffled
	Jacket heat transfer coefficient, h_o	1739

7.2.4 Single-stage unseeded MSMPR crystallisation

Table 7.4 summarises the operating conditions and results for Experiment 1 – 5 in the single-stage MSMPR crystalliser. In all experiments performed, α-GLY was consistently produced, as confirmed by offline Raman spectroscopy (Figure 7.4). Figure 7.5 shows the process time diagram for Experiment 1 which was operated with a mean residence time of 5 min. From the evolution of the FBRM statistics, four distinct phases were identified in the MSMPR crystalliser. In the start-up phase, MSMPR 1 was cooled to trigger spontaneous nucleation and create an initial batch suspension. Steadily decreasing total counts 1 – 1000 µm and counts 1 – 5 µm indicated a loss of crystal mass during the washout phase. This was driven primarily by the simultaneous withdrawal of start-up suspension and addition of feed solution to the crystalliser. In addition, the rapid addition of hot feed solution elevated the MSMPR temperature by ~10 °C, causing a decrease in supersaturation and further loss of crystals by dissolution. An accompanying increase in SWMCL indicated a predominantly bigger crystal population in MSMPR 1 from fines dissolution and crystal growth.

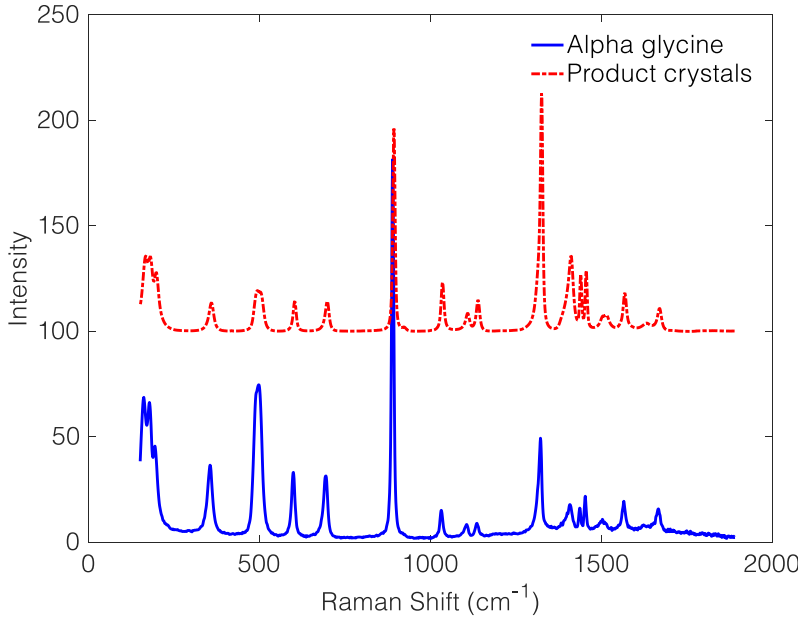

Figure 7.4 Offline Raman spectra for α-GLY and product crystals obtained.

A response phase was initiated at ~23 min when a low enough MSMPR temperature generated sufficient supersaturation to trigger secondary nucleation. The response phase signified a transition to a secondary nucleation-controlled crystallisation, as indicated by rising total counts and a decreasing mean chord length. Generally, the magnitude of a response phase depends on the maximum supersaturation generated in the MSMPR, which is dictated by the feed addition rate, heat removal rate of the MSMPR, and suspension density. In Experiment 1, a short mean residence time of 5 min allowed for rapid build-up of supersaturation, which caused faster nucleation rates and an observable response phase. For longer mean residence times in Experiment 2 and 3, the response phase was much less pronounced.

Unsurprisingly, MSMPR 1 did not attain the desired operating temperature of 20 °C following the addition of the hot feed solution, and instead the MSMPR temperature oscillated around ~27 °C (see Figure 7.5), causing fluctuations in local supersaturation. This was a result of the inadequate cooling capacity of the MSMPR for operation below $\tau_{critical}$ as earlier determined in section 7.2.3. Temperature profiles in Figure 7.6 demonstrate the inability of MSMPR 1 to achieve the setpoint even at a minimum jacket temperature of –4.5 °C. The oil bath was unable to cool beyond this temperature, and subsequently entered cooling and heating cycles. For a mean residence time of 5 min, attaining the desired operating temperature would require cooling the jacket to –42 °C, a temperature beyond the working range of silicone oil. The result of a higher MSMPR operating temperature, and insufficient time for crystal growth

was a heavily saturated steady-state suspension in MSMPR 1 with a poor yield of 33% (see Table 7.4).

Table 7.4 Summary of operating conditions and experimental results for single-stage MSMPR crystallisation

	Experiment				
	1	2	3	4	5
Mean residence time, τ (min)	5	10	15	20	10
Feed/dissolution vessel temperature (°C)	60	60	60	60	60
MSMPR 1 operating temperature (°C)	27	20	20	20	10
Pump flow rate (ml min^{-1})	20	10	9.33	5	10
Avg. operating volume (ml)	90	90	90	90	90
Mean residence times to steady-state, t/τ (-)	5	3.2	5	n/a	n/a
Feed concentration, C_f (g/g)	0.275	0.275	0.275	0.275	0.275
Exit from MSMPR 1, C_{ss}^1 (g/g)	0.2543	0.2225	0.2146	n/a	n/a
MSMPR 1 supersaturation, S (-)	1.206	1.234	1.190	n/a	n/a
Steady-state FBRM total counts (#/s)	2,741	3,334	1,645	n/a	n/a
Steady-state mean crystal size, $d_{4,3}$ (µm)	444 ± 18.5	768 ± 3.0	833 ± 5.5	n/a	n/a
Span (-)	3.33	1.59	1.39	n/a	n/a
Yield (%)	33	56	64	n/a	n/a

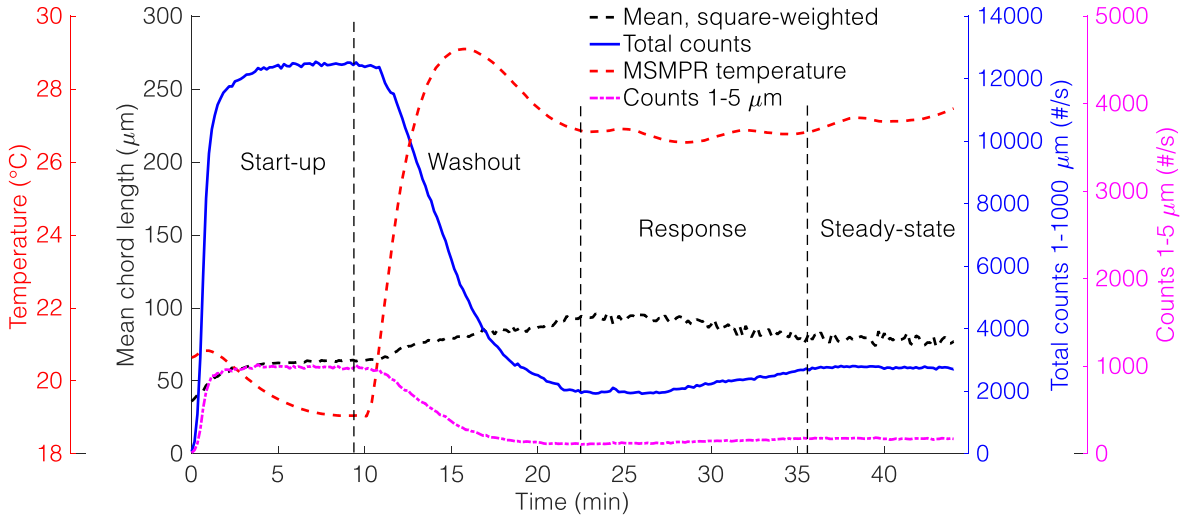

Figure 7.5 Process time diagram for Experiment 1 in the single-stage MSMPR crystalliser showing temperature, total counts, and square-weighted mean. $\tau = 5$ min.

Experiment 1 highlighted the heat transfer limitation imposed on the degree of supersaturation achievable in MSMPR 1, and therefore, the minimum obtainable product mean size. Previous work by Power et al. (2015) has shown the impact of energy balance constraints on minimum particle sizes attainable in MSMPR crystallisers. When compared to tubular crystallisers, stirred tank crystallisers have smaller surface area to volume (SAV) ratios, which essentially is the available heat transfer area per unit volume within the crystalliser. In this

instance, MSMPR 1 has an SAV of 100 m^{-1}, which is much smaller than the SAV of the SPC mesoscale crystalliser (1190 m^{-1}) (Onyemelukwe et al., 2018a). As a result, the excellent heat transfer performance of tubular crystallisers enables the attainment of high degrees of supersaturation during cooling crystallisations for faster nucleation rates. However, challenges with encrustation currently limit the use of primary and secondary nucleation for achieving small crystal mean sizes in these devices (McGlone et al., 2015; Brown et al., 2018).

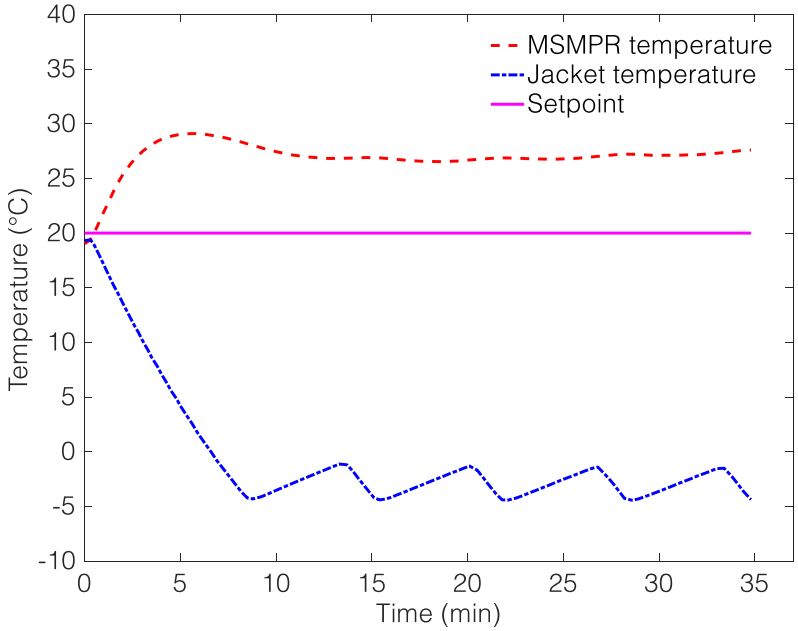

Figure 7.6 Temperature profiles in MSMPR 1 for Experiment 1.

Experiment 2 and 3 (Figure 7.7 and Figure 7.8) showed no detectable response phase as total counts 1 – 1000 µm steadily decreased and levelled off into a steady-state. The supersaturation generated by feed addition was consumed mainly by growth of crystals in the initial batch suspension. This was indicated by a steady rise in mean chord length throughout the washout phase. The presence of crystals in the 1 – 5 µm size range indicated that secondary nucleation necessary to sustain crystal mass was occurring on a much smaller magnitude. Both mean residence times ($\tau > \tau_{critical}$) permitted operation of MSMPR 1 at the desired temperature, and promoted crystal growth as indicated by steady-state mean crystal sizes ($d_{4,3}$) obtained (see Table 7.4). It follows therefore, that increasing mean residence time will lower supersaturation in the MSMPR crystalliser and cause less secondary nucleation than growth to occur; thereby giving rise to bigger crystals, improved yield, and a narrower CSD. It is evident from Figure 7.9, that as mean residence time was increased, a reduction in the fine end of the

steady-state distribution occurred, however no notable change in the coarse end of the CSD was observed. This is because as mean residence time increases, crystals on average spend more time in the crystalliser, and smaller crystals grow towards larger sizes, in this way a narrowing of the distribution occurs. It was also observed that longer mean residence times in MSMPR 1 produced a lower steady-state crystal population as indicated by total counts 1 – 1000 µm in Table 7.4. Experiment 1, however, had relatively lower total counts at steady-state than expected, due to operation at a much lower steady-state supersaturation than had been targeted.

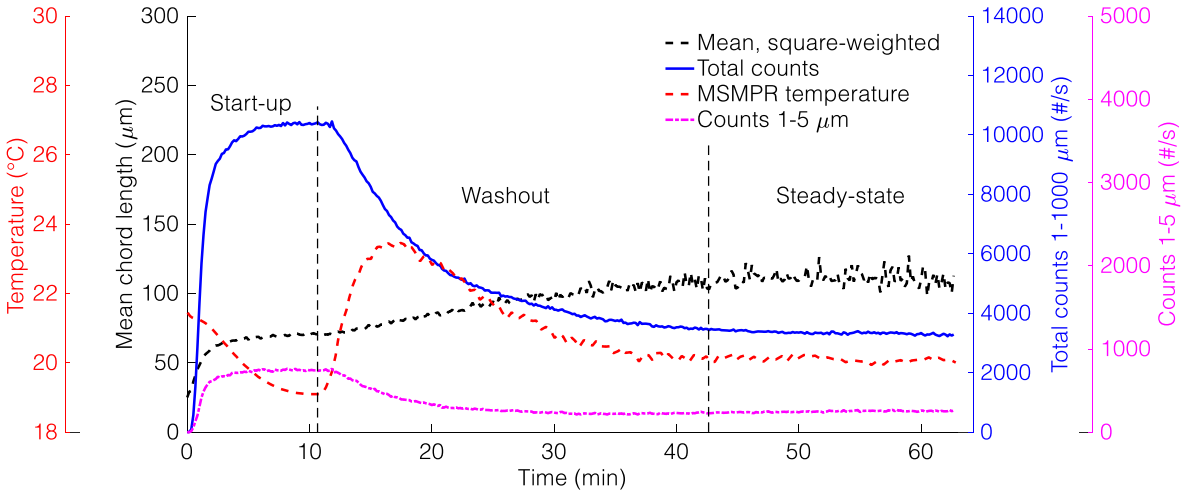

Figure 7.7 Process time diagram for Experiment 2 in the single-stage MSMPR crystalliser showing temperature, total counts, and square-weighted mean. $\tau = 10$ min.

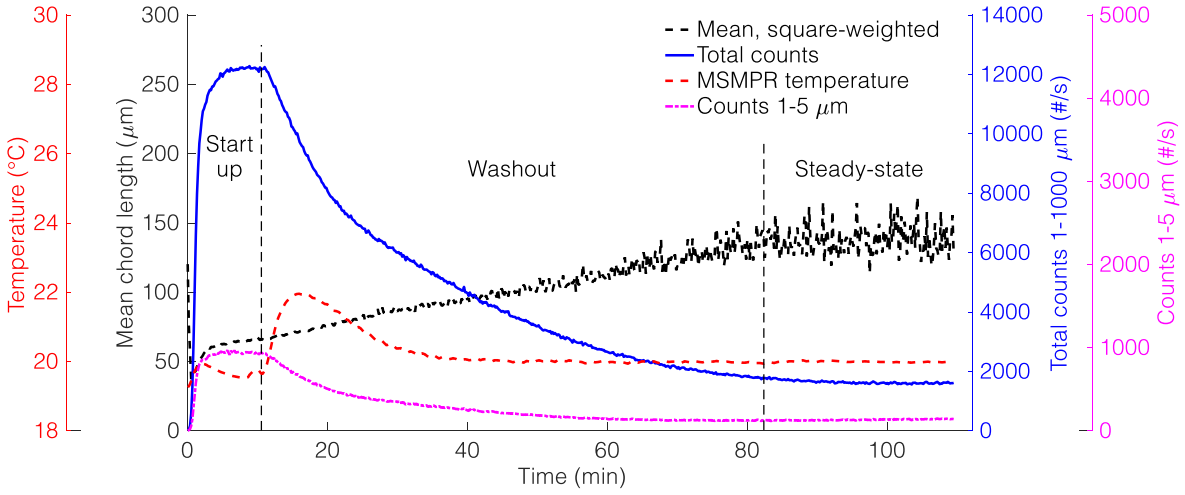

Figure 7.8 Process time diagram for Experiment 3 in the single-stage MSMPR crystalliser showing temperature, total counts, and square-weighted mean. $\tau = 15$ min.

Despite all three experiments having similar RTDs (for the same MSMPR), the steady-state product CSD from Experiment 1 was very different to Experiment 2 and 3. Strongly competing secondary nucleation in Experiment 1 created excessive fines and a bimodal distribution. The presence of fines and predominantly needle-shaped crystals are clearly visible in offline images of the isolated product (see Figure 7.10(a)). Doubling the mean residence time in Experiment 2 narrowed the span of the distribution and increased the mean size of the steady-state product. It can be said that Experiment 2 and 3 had similar steady-state CSDs due to weakly competing secondary nucleation in both experiments. The steady-state supersaturation of these two experiments are also not very different as seen in Figure 7.11. A marginal improvement to the product mean size, CSD span, and yield was however obtained in Experiment 3. Figure 7.10(b) and Figure 7.10(c) show the more regular prismatic shape of α-GLY obtained from the growth-dominated processes of Experiment 2 and 3 respectively. Extending the mean residence time to 20 min (Experiment 4) produced enormous crystals (see Figure 7.10(d)) which clogged the transfer line between MSMPR 1 and the feed/dissolution vessel. This indicated that larger tubing inner diameters are required for longer mean residence times to cope with fast-growing α-GLY crystals.

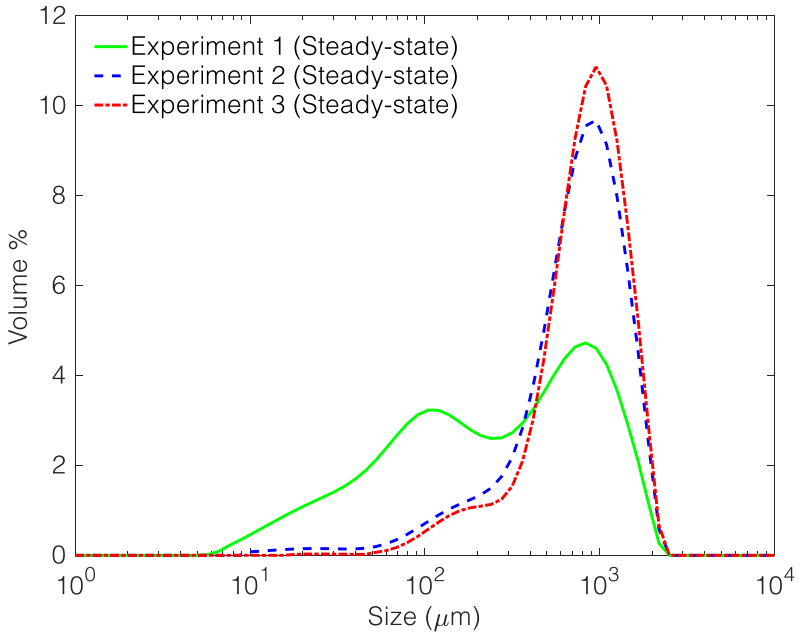

Figure 7.9 Steady-state α-GLY product CSDs obtained for Experiment 1, 2, and 3.

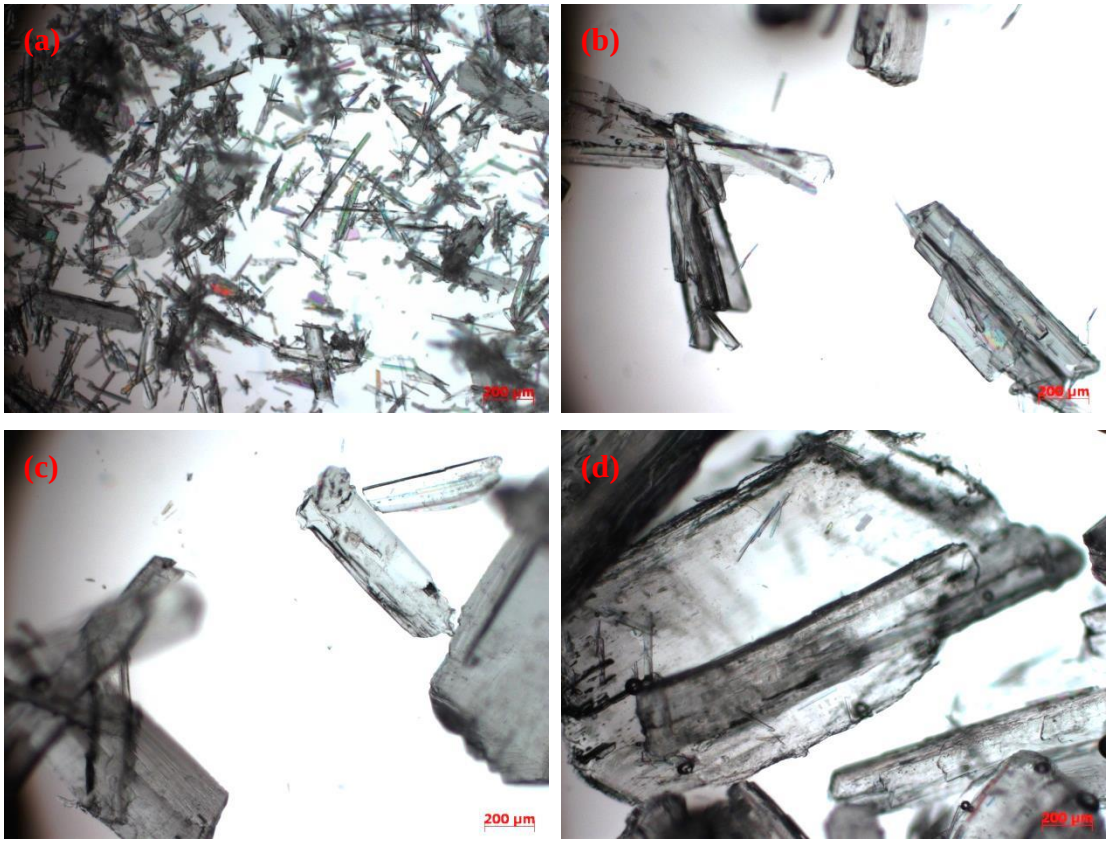

Figure 7.10 Offline microscope images of α-GLY product crystals from (a) Experiment 1 (at steady-state); (b) Experiment 2 (at steady-state); (c) Experiment 3 (at steady-state); (d) Experiment 4 (after blockage).

The results from Experiment 1 – 3 highlight the greater role of crystallisation mechanisms than RTD in shaping the final product CSD. The mean residence time does not change RTD, but it controls the rate of supersaturation generation and consumption in the crystalliser, which influences competing mechanisms. Since nucleation and growth rates are determined by available supersaturation, it is important to control supersaturation to promote one mechanism over the other, since the ratio of both mechanisms significantly affects product CSD. Minimising nucleation becomes necessary in this case since it creates substantial fines in the product. For the fast-growing α-GLY, Experiment 2 and 3 therefore suggest that extending the mean residence time in the MSMPR will promote growth over nucleation and give a better-quality product with improved yield.

The downside of prolonged mean residence times in a single-stage MSMPR is that high throughput times of a batch crystalliser will be approached without achieving the equivalent thermodynamic yield (i.e. recovered solute fraction), since the MSMPR operates at a fixed point (supersaturation) in the phase diagram.

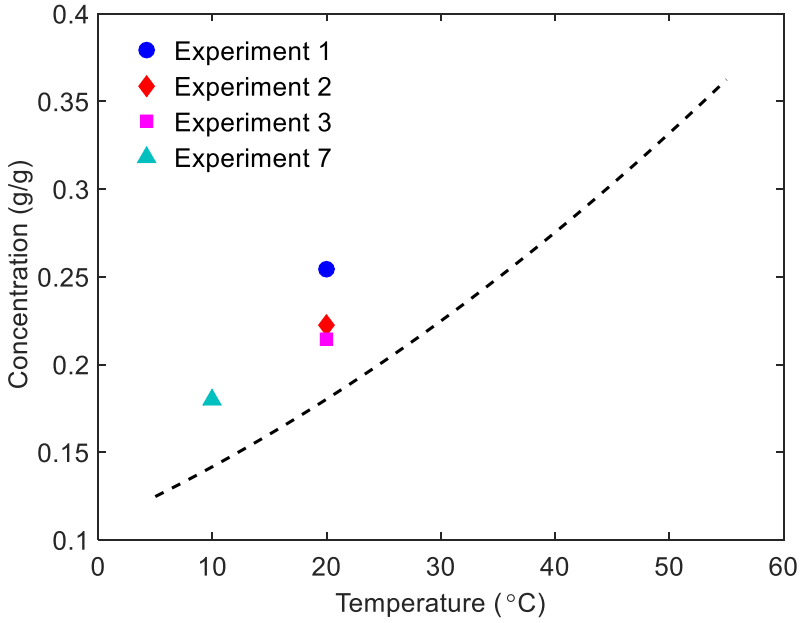

Figure 7.11 Steady-state concentrations for unseeded single-stage and two-stage MSMPR experiments. Black dashed line is the solubility curve.

To improve thermodynamic yield, operation of the single-stage MSMPR at a lower point in the phase diagram (MSMPR temperature of 10 °C) was attempted. This was however unsuccessful, as a high degree of supersaturation caused significant encrustation on the FBRM probe and crystalliser walls in Experiment 5. Therefore, the two-stage MSMPR crystalliser was explored.

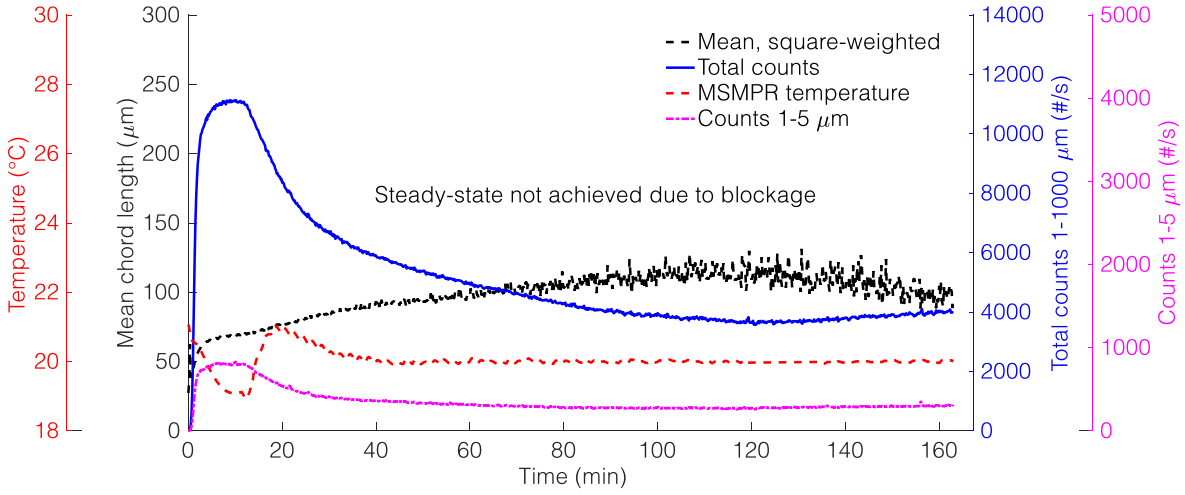

Figure 7.12 Process time diagram for Experiment 4 in the single-stage MSMPR crystalliser showing temperature, total counts, and square-weighted mean. $\tau = 20$ min.

7.2.5 Single-stage seeded MSMPR crystallisation

In Experiment 6 (Figure 7.13), the seeded cooling crystallisation showed a distinctive behaviour, where no washout is exhibited due to the absence of crystals in MSMPR 1 prior to start-up. The extent of crystal growth in MSMPR 1 was quantified using the normalised product size, L_p/L_s, which is the ratio of $d_{4,3}$ of the steady-state product (L_p) and $d_{4,3}$ of the starting seed material (L_s). Table 7.5 summarises the operating conditions and results from Experiment 6.

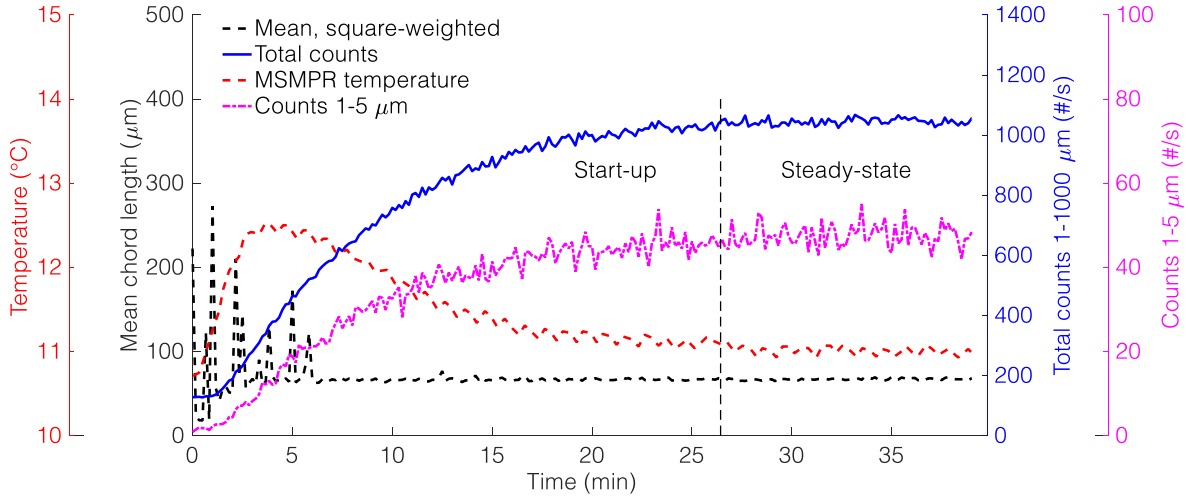

Figure 7.13 Process time diagram of Experiment 6 in the single-stage MSMPR crystalliser showing temperature, total counts, and square-weighted mean. $\tau = 10$ min.

Table 7.5 Summary of operating conditions and experimental results for Experiment 6

	Experiment 6
Mean residence time, τ (min)	10
Seed vessel temperature (°C)	19
MSMPR 1 operating temperature (°C)	11
Pump flow rate (ml min^{-1})	10
Avg. operating volume (ml)	90
Mean residence times to steady-state, t/τ (-)	3
Feed concentration, C_f (g/g)	0.180
Exit from MSMPR 1, C_{ss}^1 (g/g)	0.1697
MSMPR 1 supersaturation, S (-)	1.168
Steady-state FBRM total counts (#/s)	1112
Starting mean seed size, $d_{4,3}$ (μm)	48 ± 1.6
Starting seed span (-)	1.58
Steady-state mean crystal size, $d_{4,3}$ (μm)	185 ± 20.4
Normalised product size, L_p/L_s (-)	3.83
Span (-)	2.21
Yield (%)	21

A steady rise in total counts 1 – 1000 µm and counts 1 – 5 µm is observed as seed crystals flow in and suspension is removed intermittently from the crystalliser, until a steady-state is achieved after just 3 mean residence times. Operating within the metastable zone width (19 – 11 °C) ensured that the crystallisation process was growth-controlled and secondary nucleation was avoided. This is observed in the Figure 7.14, whereby the unimodality of milled α-GLY seed material was maintained in the right-shifted steady-state product distribution.

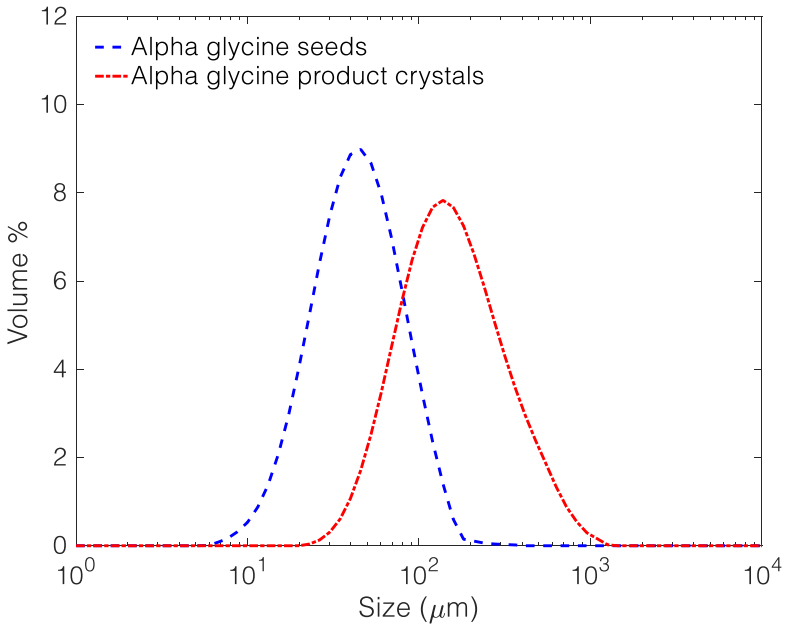

Figure 7.14 α-GLY seed and steady-state product CSDs obtained from Experiment 6.

Offline microscope images in Figure 7.15 showed no evidence secondary nucleation in the process, as there were no significant fines present in the steady-state product. The steady-state product crystals also showed no evidence of significant attrition, and this could be explained by the lower agitation speed and suspension density in MSMPR 1 compared to the unseeded crystallisation experiments. Despite the absence of secondary nucleation, the distribution of the steady-state product was widened. This can be seen in Table 7.5, where the span of the seed material and steady-state product is 1.58 and 2.21 respectively. The most obvious reason for this is the broad RTD of MSMPR 1 (see section 7.2.1), which means that crystals spend very different times in the crystalliser for the same τ. Also, in the backmixed crystalliser, local supersaturation distribution is poor (see section 2.5.1) and particles do not experience the same growth rates. Therefore, a broadening of the steady-state product distribution would occur. As observed in the unseeded crystallisation experiments, increasing the mean residence time in MSMPR 1 may help narrow the CSD of the steady-state product.

A direct comparison with seeded crystallisation in the SPC mesoscale crystalliser could not be made since the mean residence time, seed loadings, and temperature profiles were not the same. However, it is worth noting that for a τ of 10 min in MSMPR 1 and a seed loading of 10% w/w, L_p/L_s was 3.83 and yield was 21% (see Table 7.5). For a τ of 7.3 min and seed loading of 7% w/w in the SPC mesoscale crystalliser, L_p/L_s was 2.23 and yield was 70% (see Table 6.8 in Chapter 6). This is a striking difference in yield, especially since the single-stage MSMPR crystallisation was supposedly at a higher seed loading and τ. The explanation for this is that while the seed loading in the seed vessel was 10% w/w, the solids loading in MSMPR 1 was likely to be much lower than this value at steady-state operation. This means fewer crystals to consume available supersaturation and therefore lower yield (see section 6.2.9 of Chapter 6). Unfortunately, the mass of crystals in the steady-state slurry was not checked to confirm this. Comparing the width of seed and steady-state distributions, a greater difference in span was obtained in MSMPR 1 than in the SPC mesoscale crystalliser (see Table 6.8 and Table 7.5). This demonstrated the benefit of a tighter RTD for continuous crystallisation in the SPC mesoscale crystalliser.

Interestingly, despite Experiment 6 having a growth-dominated process, a larger steady-state mean size and yield were obtained in Experiment 2 (Table 7.4). This emphasised the combined effect of crystallisation mechanisms occurring in a process. In Experiment 2, competing secondary nucleation and growth would consume supersaturation at a faster rate than in Experiment 6, where growth was the only mechanism. Also, the product recycle operation in Experiment 2 allowed for further depletion of supersaturation across the MSMPR system, leading to much higher yields and bigger product crystals for the same τ.

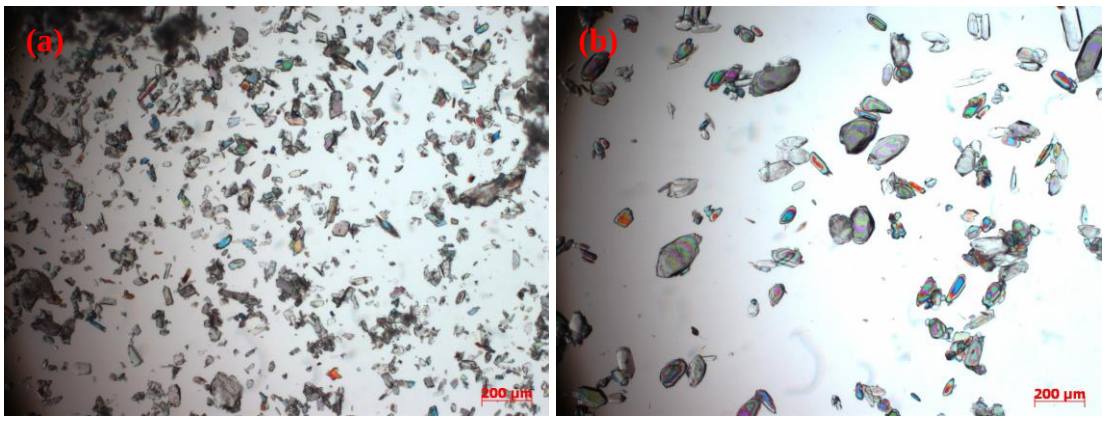

Figure 7.15 Offline microscope images of (a) α-GLY seed crystals and (b) α-GLY product crystals from Experiment 6.

7.2.6 Two-stage MSMPR crystallisation

In Experiment 7, the two-stage MSMPR crystalliser enabled continuous operation at a lower point in the phase diagram without fouling and encrustation issues encountered in Experiment 5 (see Figure 7.11). Table 7.6 summarises the operating conditions and results for Experiment 7. The process time diagram in Figure 7.16 shows a strong response phase in MSMPR 2 driven by significant supersaturation. Substantial secondary nucleation was evidenced by steadily increasing counts 1 – 5 µm which produced a high crystal number density (total counts) at steady-state. Figure 7.17 shows that the steady-state CSD from MSMPR 2 had a fraction of smaller crystals created by a secondary nucleation-dominated process. With a high suspension density, crystal-crystal and crystal-impeller collisions are promoted; and as glycine crystals approach larger sizes (~798 µm) (Su et al., 2017) the propensity for attrition increases. These combined mechanisms produced a smaller product mean size.

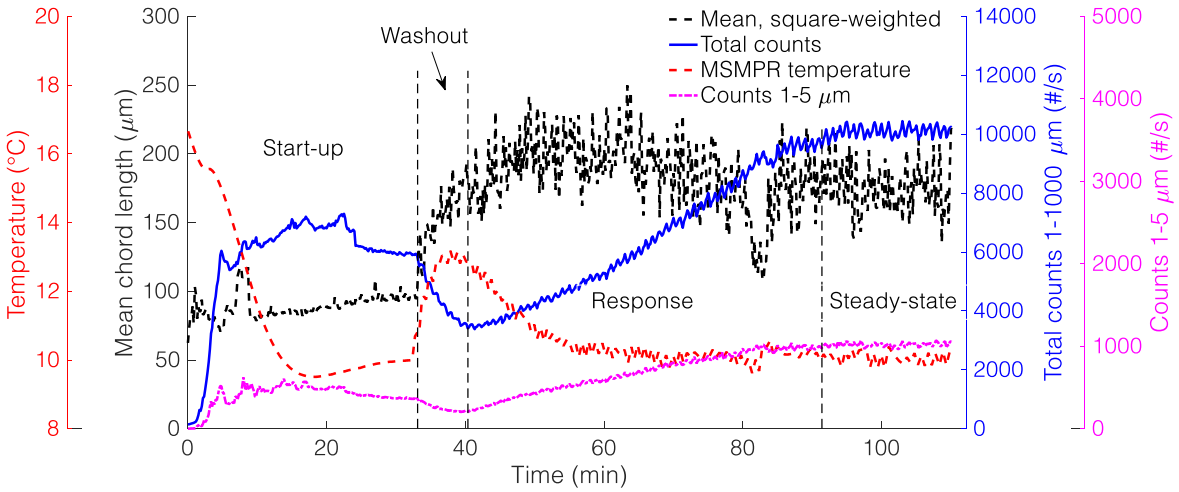

Figure 7.16 Process time diagram for Experiment 7 in the two-stage MSMPR system showing MSMPR 2 temperature, total counts, and square-weighted mean. $\tau = 10$ min.

Table 7.6 Summary of operating conditions and experimental results for two-stage MSMPR crystallisation

	Experiment 7		
	Feed	MSMPR 1	MSMPR 2
Mean residence time, τ (min)	25	10	10
Vessel operating temperature (°C)	60	20	10
Avg. operating volume (ml)	250	90	90
Feed concentration, C_f (g/g)	0.275	n/a	n/a
Exit from MSMPR, C_{ss}^i (g/g)	n/a	n/a	0.180
MSMPR supersaturation, S (-)	n/a	n/a	1.24
Steady-state FBRM total counts (#/s)	n/a	n/a	10,111
Steady-state mean crystal size, $d_{4,3}$ (µm)	n/a	766 ± 31.1	528 ± 3.6
Span (-)	n/a	1.58	2.37
Yield (%)	n/a	n/a	71

In contrast, the steady-state CSD from MSMPR 1 had a larger mean size and smaller span, indicating that crystal growth was dominant in the crystalliser. Offline microscope images in Figure 7.18(a) confirm the absence of significant fines in the isolated product from MSMPR 1.

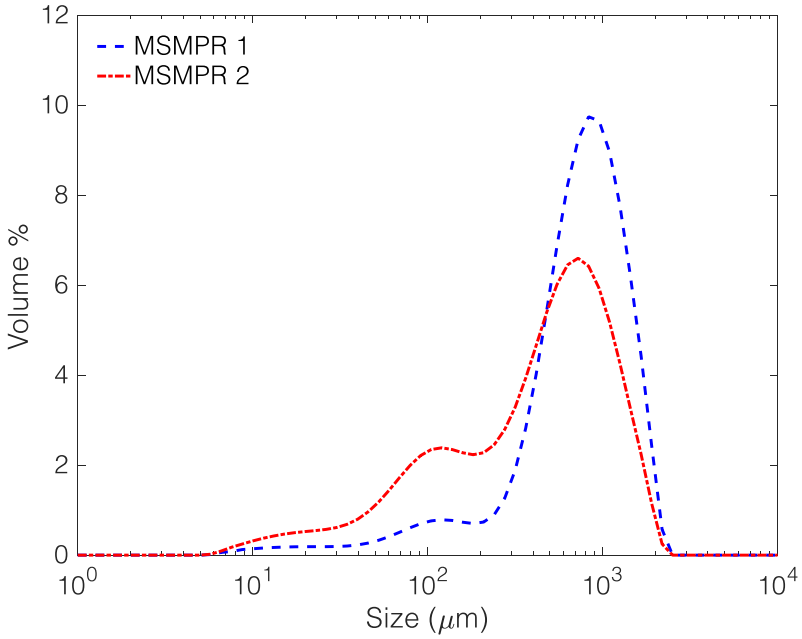

Figure 7.17 Steady-state α-GLY product CSDs obtained from MSMPR 1 and 2 in Experiment 7.

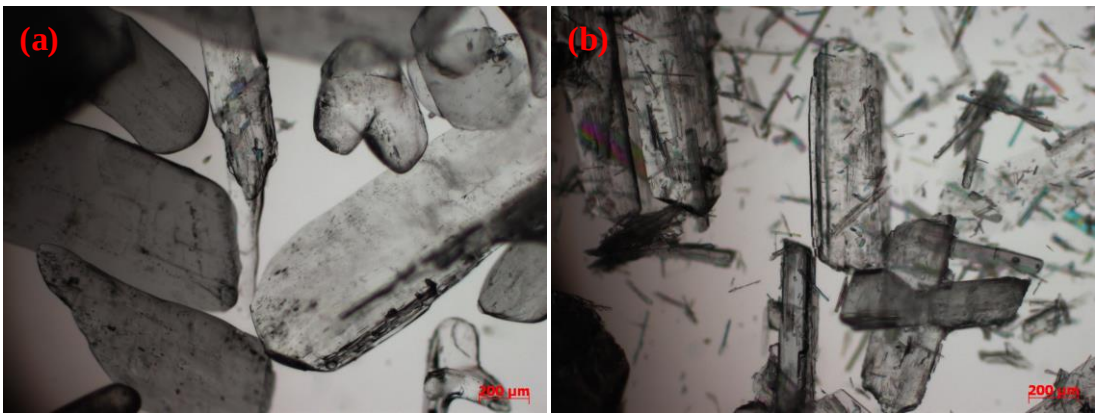

Figure 7.18 Microscope images of steady-state α-GLY product crystals from MSMPR 1 (a) and MSMPR 2 (b) in Experiment 7.

Figure 7.19 shows the similarity in steady-state CSDs from the single-stage MSMPR in Experiment 2 and MSMPR 1 in Experiment 7 for the same mean residence time and RTD. Fewer fines in MSMPR 1 suggests less secondary nucleation than in the single-stage MSMPR.

This is to be expected for a complete recycle operation, since an added crystallisation stage (MSMPR 2) would further decrease solution concentration in the feed/dissolution vessel, and consequently the supersaturation in MSMPR 1.

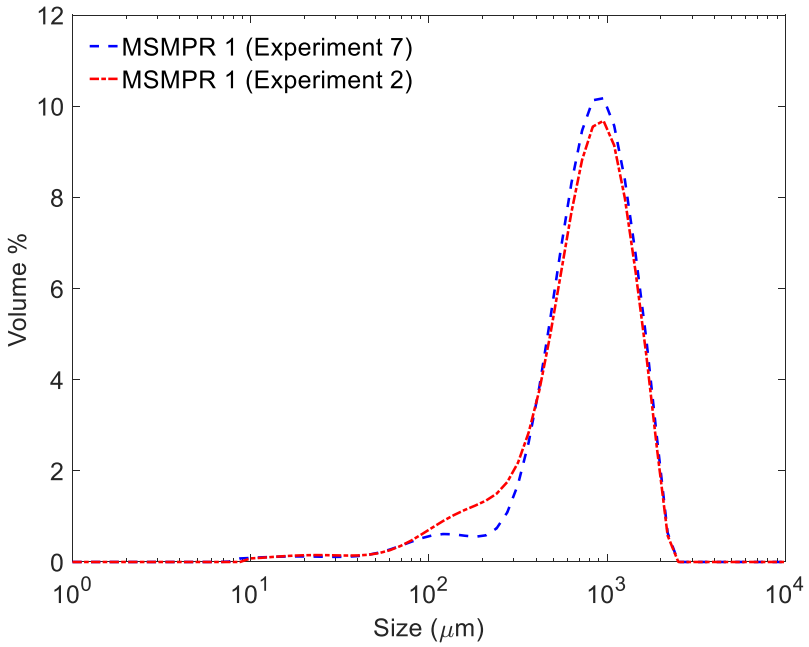

Figure 7.19 Comparison of steady-state α-GLY product CSDs from the single-stage MSMPR in Experiment 2 and MSMPR 1 in Experiment 7.

The two-stage cascade achieved a higher thermodynamic yield than could be attained in the single-stage MSMPR system, by overcoming practical limitations. However, despite its superior RTD performance, a broader product CSD was obtained due to a high degree of supersaturation in MSMPR 2. This stresses the importance of controlling supersaturation to avoid excessive nucleation, as the occurrence of nucleation will result in a wider distribution of residence times, and hence widen the steady-state CSD. Since supersaturation is determined by operating temperature and mean residence time, independent manipulation of these process variables in each MSMPR stage can achieve the desired objective. For the α-GLY system in this study, an optimal operating strategy may be identified based on the dominant crystallisation kinetics, whereby the total mean residence time is distributed between each stage in a bid to increase crystal mean size and narrow CSD, without compromising thermodynamic yield (i.e. maintaining MSMPR 2 at 10 °C). A good approach would be to drive moderate nucleation in the first stage to obtain sufficient surface area/suspension density and eliminate fines in the second stage through longer residence times that favour crystal growth. Controlling crystallisation mechanisms through decoupled operation is a key advantage of cascade design

which has been demonstrated in several cascade optimisation studies for systems with different crystallisation kinetics (Vetter et al., 2014; 2015; Power et al., 2015; Park et al., 2016).

Lastly, to check for representative withdrawal in the two-stage MSMPR crystallisation, a steady-state sample was isolated via rapid intermittent withdrawal and compared with a sample withdrawn from the bottom of MSMPR 2. From Figure 7.20, it was concluded that both CSDs are comparable; however, it appears that a slightly greater number of coarse crystals are present at the bottom of MSMPR 2 than in the isolated sample.

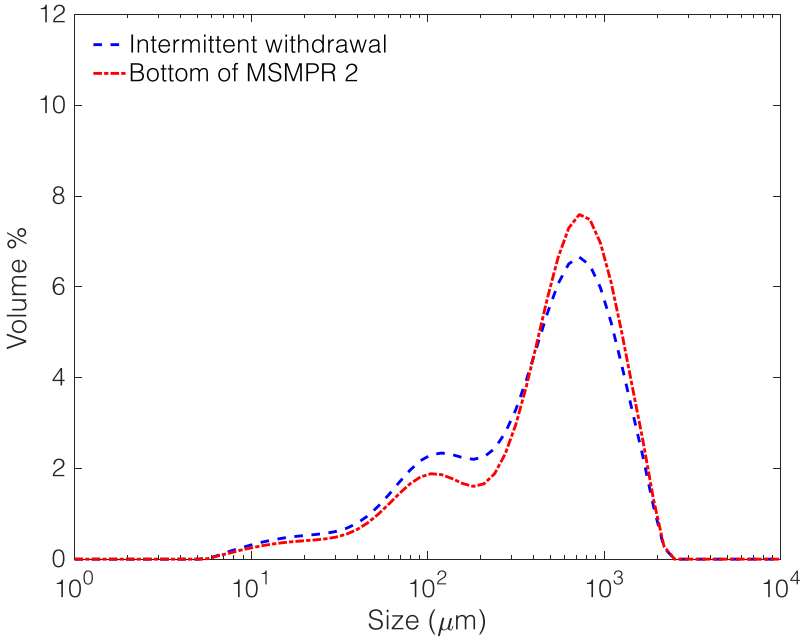

Figure 7.20 CSD comparison of steady-state samples taken by intermittent withdrawal and from the bottom of MSMPR 2.

This suggests that intermittent withdrawal may not be as efficient for suspensions containing coarse crystals. Yang et al. (2017) have observed similar behaviour using an intermittent pneumatic withdrawal method, whereby the mean particle size of the isolated sample was slightly smaller than in the crystalliser.

7.3 Conclusions

In this chapter, the continuous steady-state crystallisation of α-GLY in a single- and two-stage MSMPR crystalliser was made possible through the application of an intermittent vacuum-transfer technique. RTD characterisation confirmed that the material RTD in an MSMPR remains unchanged for different mean residence times. The mean residence time was

found to be an important design variable in crystallisation as it had a significant effect on the final product quality. Operating at longer mean residence times was shown to be an effective approach for obtaining narrower steady-state CSDs, despite the characteristic broad RTD of the single-stage MSMPR. Longer mean residence times also led to larger mean size and higher yield. The mean residence time however, had no discernible effect on the time required to achieve steady-state operation in the MSMPR crystalliser. Cooling crystallisation experiments revealed the greater influence of secondary nucleation and growth mechanisms than RTD in determining steady-state product CSD. Specifically, secondary nucleation broadened steady-state CSD regardless of RTD performance; while growth-dominated processes improved product quality by narrowing CSD, increasing crystal mean size, and improving crystal shape.

The benefit of extending the number of crystallisation stages was demonstrated with the two-stage MSMPR cascade, which enabled successful operation at a lower crystalliser temperature than possible in the single-stage MSMPR system. Although the addition of a second stage achieved a better RTD and thermodynamic yield than feasible in the single-stage MSMPR system, a poorer product quality was obtained. This emphasizes the importance of balancing growth and nucleation by carefully controlling supersaturation in the multi-stage MSMPR, and that control of supersaturation is key to improving CSD in an MSMPR cascade. CSD control is much easier in tubular crystallisers like the SPC mesoscale crystalliser due to tighter control of supersaturation resulting from its superior RTD profiles and heat transfer performance, as demonstrated in previous chapters of this thesis. To benefit from improved RTDs provided by multistage MSMPR crystallisers, an optimum operating strategy must be identified that appropriately controls crystallisation mechanisms in each MSMPR stage. The flexibility provided by extending the number of stages can allow for the manipulation of key design variables to achieve desired objectives.

On the other hand, better control of product CSD was demonstrated through single-stage seeded continuous cooling crystallisation. The ability to control final product CSD through tailored starting material and operation within the MSZW came with a heavy compromise on yield. Extending the mean residence time or increasing seed loading are potential ways to improve the yield of a continuously seeded MSMPR crystallisation process.

Chapter 8 Conclusions and recommendations

8.1 Main conclusions

In this thesis, two approaches to continuous crystallisation, namely the SPC mesoscale crystalliser and MSMPR crystalliser were investigated. The main aim of the work presented was to investigate the cooling crystallisation of a model compound in both crystallisation platforms to demonstrate the potential to transform industrial practice. This was achieved in both platforms for the GLY-water system through the application of in-line PAT tools, temperature monitoring, and offline solid-state analytical techniques for process monitoring, steady-state determination, and product attributes characterisation. In the SPC mesoscale crystalliser, the successful integration and application of a 5.5 mm I.D. Raman immersion probe, using specially designed accessories and a multivariate calibration for solution phase concentration enabled real-time monitoring of seeded continuous cooling crystallisations. In the single- and two-stage MSMPR crystalliser, a suitably sized S400 FBRM probe was utilised to detect crystallisation mechanisms including primary and secondary nucleation, growth, and dissolution during unseeded and seeded cooling crystallisation studies. The FBRM total counts statistic was used as a qualitative indicator of steady-state operation for all processes monitored. However, the mean chord length statistic was an unreliable indicator of true crystal size, as real-time measurements did not correspond with offline imaging and laser diffraction data. The data generated in process time diagrams demonstrated the immense value of PAT for increased mechanistic and process understanding of continuous crystallisation across both platforms.

A key objective of this research was to assess the suitability of the SPC mesoscale crystalliser for continuous crystallisation processes. By developing a novel dual backlit imaging technique, a more reliable and accurate estimation of the axial dispersion performance was possible. Homogeneous tracer measurements confirmed that the SPC mesoscale crystalliser is especially effective for finely controlling and obtaining narrow RTD profiles through appropriate combinations of oscillation amplitude, frequency, and net flow. Results highlighted a major difference in oscillatory flow behaviour between the SPC mesoscale crystalliser and conventional scale COBCs, in that a combination of smaller oscillatory amplitudes ($x_0 = 0.5 – 1.0$ mm) and higher frequencies ($f = 6 – 12$ Hz) approximates to plug flow behaviour in the SPC mesoscale crystalliser. The linear geometric scaling ability of the

SPC mesoscale crystalliser means that hydrodynamic conditions can be replicated at conventional and pilot scales by simply identifying appropriate combinations of oscillatory amplitude and frequency, regardless of net flow. Heterogeneous tracer measurements using polystyrene particles indicated that solids flowing in the SPC mesoscale crystalliser are more likely to experience significantly higher dispersion than the liquid phase at $Re_o < 93$, and solids do not experience the exact degree of dispersion as the liquid phase even at near plug flow conditions. The characterisation based on polystyrene particles identified an optimum range of Re_o between 93 – 185 suitable for performing solid-liquid plug flow crystallisation. The second aspect of equipment capability assessment focused on the heat transfer performance of the SPC mesoscale crystalliser. Experimental measurements combined with an estimability analysis confirmed that the SPC mesoscale crystalliser achieves its highest rates of heat transfer at plug flow conditions. An empirical correlation was developed for estimating the tube-side Nusselt number in the SPC mesoscale crystalliser. This correlation can be incorporated into heat balance equations to accurately predict spatial temperature profiles in the SPC mesoscale crystalliser for continuous cooling crystallisation. The information from RTD and heat transfer characterisation established the SPC mesoscale crystalliser as a platform capable of providing a highly reliable mixing environment and tight control of local supersaturation for cooling crystallisation processes.

Improved micro-mixing and heat transfer was evidenced by narrower MSZWs observed for GLY in the batch SPC mesoscale crystalliser at much lower specific power inputs, compared to the batch STC. However, despite having superior mixing and heat transfer performance, the SPC mesoscale crystalliser was unable to handle unseeded continuous cooling crystallisations where primary and secondary nucleation were the dominant mechanisms. Major problems of encrustation caused by high levels of supersaturation, and adhesion of primary nuclei/crystals to constriction surfaces prevented the continuous operation of the SPC mesoscale crystalliser. These challenges were successfully mitigated through continuous seeding, whereby low supersaturation levels were maintained within the metastable zone in the crystalliser.

A systematic study on the GLY-water system in the SPC mesoscale crystalliser identified four operating strategies for producing crystal product with desired attributes. With regards to mixing conditions, operating at near plug flow conditions was shown to be essential for achieving higher heat and mass transfer rates. This ensured maximum possible crystal growth rates were attained during crystallisation to obtain larger crystals in the GLY product. With crystal growth rate being a limiting kinetic factor to achieving larger crystal sizes, increasing

the mean residence time in the SPC mesoscale crystalliser by lowering the mass flow rate permitted further growth of seeds. The result was a bigger GLY product and higher yield, at a cost of broader CSD. Since a broader product CSD is likely to cause filtration and drying delays, extending the SPC mesoscale crystalliser to reasonably acceptable lengths would retain a narrow CSD in the final product, so far supersaturation is well distributed via an optimised temperature profile. In addition to increasing the mean residence time, continuously seeding the crystalliser with small-sized seeds was found to produce bigger-sized product; however, balancing the seed surface area was key to achieving an acceptable product size and satisfactory yield. A maximum seed loading of 12% w/w was found to give the smallest product size, with a marginal improvement in yield over 7% w/w seed loading. Operating at a seed loading beyond 12% w/w would be unproductive, and likely to cause operational challenges for the crystalliser due to excessive solids dampening oscillations. Lastly, and most importantly, continuously seeding with the right polymorph (the fast growing α-GLY in this case) ensured that the crystallisation process benefited from the above-mentioned operating strategies, and that desired product attributes were consistently obtained.

The implementation of an intermittent slurry withdrawal method and a complete recycle operation enabled the successful operation of two configurations of the MSMPR crystalliser for prolonged periods with minimal material waste. This was a key research objective which permitted systematic investigations to be conducted in both single- and two-stage MSMPR configurations. Homogeneous tracer experiments demonstrated the contrasting RTD profiles offered by the MSMPR crystalliser and the SPC mesoscale crystalliser. Results particularly highlighted the inherently broad RTD exhibited by the single-stage MSMPR crystalliser, whereby changing volumetric flow rate and impeller speed had no influence on mixing performance. Unseeded cooling crystallisations in the single-stage MSMPR crystalliser highlighted the mean residence time as an important variable for controlling crystallisation mechanisms, with longer mean residence times promoting growth-dominated processes, and mean residence times significantly shorter than $\tau_{critical}$ causing nucleation-dominated processes. Longer mean residence times were found to narrow the CSD and yield of the steady-state product; however, there was no specific effect of mean residence time on the time to attain steady-state operation. The importance of $\tau_{critical}$ as an operational constraint was also emphasised by undesired steady-state conditions and poor product quality obtained when operating below this constraint. Finally, the advantage of MSMPR cascade operation was demonstrated by operating at a lower MSMPR stage temperature and achieving a higher overall

yield than was feasible in a single-stage MSMPR crystalliser. The ability to decouple crystallisation mechanisms between MSMPR stages was demonstrated by promoting growth in the 1st stage and secondary nucleation/attrition in the 2nd stage. Interestingly, despite its improved RTD performance, the final product from the two-stage MSMPR crystalliser was of poorer quality than the single-stage MSMPR crystalliser, because of a poor control of supersaturation between the MSMPR stages. Results therefore indicated that the two-stage MSMPR operation has the potential to improve the product CSD of a single-stage MSMPR if a better control of supersaturation is achieved across the system. The increased degree of freedom in manipulating operating variables in the two-stage MSMPR could allow identification of an optimal supersaturation trajectory for obtaining a desired product and process quality.

8.2 Recommendations

A framework for monitoring continuous cooling crystallisation processes was established using a minimal number of PAT tools namely an FBRM probe and Raman immersion probe. While these were adequate for guiding process development and providing process understanding, a suite of PAT tools would provide rich data in real-time for improved process understanding of solid and solution phase phenomena. In GLY cooling crystallisation for instance, integrating FBRM and/or Raman probes at different locations in the SPC mesoscale crystalliser would help monitor the evolution of CLD and solution concentration along the crystalliser. The same information may be gained in an MSMPR crystalliser system, by distributing FBRM and/or Raman probes between MSMPR stages. This would be beneficial for understanding the supersaturation trajectory in the crystalliser and how it influences primary and secondary nucleation, growth, and agglomeration mechanisms that occur during the crystallisation process. Depending on the model system, multiple *in situ* probes (i.e. Raman, ATR-UV/Vis, FBRM, PVM, FTIR) can be combined into a PAT array which makes use of multivariate methods (PLSR, PCR), and information systems tools such as the crystallisation process informatics system (CryPRINS) to provide an automated intelligent decision support (IDS) framework. An IDS system would aid the early detection of process disturbances i.e. encrustation, and temperature or flow rate fluctuations, and help in establishing appropriate control strategies to mitigate disturbances that could potentially cause deviations from steady-state operation. Possible hindrances to the implementation of a PAT array could be size

constraints of commercially available PAT probes, and the ease of integration into the crystallisation platform. In this work, integration of more than one PAT probe in each MSMPR stage was not possible due to vessel diameters and limited ports on the vessel lid. Larger diameter vessels (>DN-60) would easily accommodate more PAT probes. In the case of the SPC mesoscale crystalliser, a G400 FBRM probe (9.5 mm I.D.) was integrated in addition to a Raman immersion probe, however significant fluctuations in FBRM particle counts were encountered, and this prevented reliance on its data for steady-state characterisation. This suggests that the FBRM probe positioning is suboptimal, or it is simply not appropriate for the platform. An S400 FBRM probe with a diameter (8 mm I.D.) closer to that of the SPC mesoscale crystalliser would cause less disruption of the hydrodynamic environment and can be easily integrated into different locations of the crystalliser using modified U-shaped glass bends.

This work revealed the inability of the SPC mesoscale crystalliser to handle unseeded cooling crystallisations due to the adhesion of nuclei/crystals on constriction surfaces and occurrence of encrustation on crystalliser glass walls. These problems are mainly caused by the hydrophilic nature and large surface area to volume of the glass SPC meso-tube and can be addressed by investigating materials of construction with surface properties (i.e. wettability, friction, lubrication, and adhesion) that reduce the tendency for crystal adhesion and encrustation. Polymeric materials such as fluorinated ethylene polymer (FEP), polyethylene (PE), polypropylene (PP), perfluoroalkoxy (PFA), polytetrafluoroethylene (PTFE) have been shown to have high contact angles (108° – 113°) (Yasuda et al., 1994; Yuan and Lee, 2013), indicating that the surfaces are hydrophobic, non-stick with low surface free energy. These materials are chemically inert and medically approved and could be used to develop a polymeric SPC mesoscale crystalliser that is less prone to encrustation and fouling. An alternative approach to encrustation mitigation could be treatment of the glass SPC meso-tube with inert polymer-based coatings such as (3-aminopropyl)triethoxysilane (APTES), 2-bromoisobutyryl bromide (BIBB) and hexamethyldisilazane (HMDS) which reduce the surface free energy and lower the adhesive strength of the glass surface. With regards to better control of spatial supersaturation, the spatially approximated cubic profile implemented in this work has shown that a closely mimicked cubic temperature profile can be achieved by discretizing the SPC mesoscale crystalliser into an optimum number of independent temperature-controlled segments. This can provide substantial improvements to the final CSD over a stepped linear profile and avoid excessive encrustation from sharp temperature drops. In closely approximating the cubic profile, consideration must be given to improving the energy

efficiency of the process. This can be achieved by using alternative temperature control devices such as Peltier heat pumps to minimise energy consumption and platform footprint. In this work, the large volume of cooling fluid (3.2 L) in each of the Huber Ministat 230 circulators means that heating or cooling the process fluid in each temperature segment to a desired temperature is heavily energy and time consuming. With Peltier heat pumps, the process fluid in each segment can be rapidly heated or cooled, with less energy consumption. This can enable the application of temperature cycling strategies to mitigate encrustation. Furthermore, the current design of the SPC mesoscale crystalliser can be improved by incorporating jacketed U-shaped glass bends. These would help improve supersaturation control and minimise blockages.

Solid phase RTD experiments were performed in this work using spherical polystyrene particles which had a small density difference with the bulk fluid. While these particles provided good insight into the solids handling capability of the SPC mesoscale crystalliser, their flow behaviour would be less representative of denser crystal suspensions with varying morphologies. Therefore, in future crystallisation process development, it would be necessary to perform solid RTD characterisation studies on the model compound or API of interest to capture the true flow behaviour of the crystals. This would identify the optimum oscillatory conditions for solid-liquid plug flow crystallisation and allow accurate determination of the solid phase dispersion coefficient for use in population balance models.

From the MSZW measurements performed, it was concluded that faster cooling rates narrowed the MSZW in the batch SPC mesoscale crystalliser. This is a surprising contrast to literature findings for conventional scale OBCs and STCs, in which faster rates of supersaturation generation (either by cooling or anti-solvent addition rate) have resulted in wider MSZWs (Fujiwara et al., 2002; Liang et al., 2004; Ni and Liao, 2008; 2010; Brown and Ni, 2011). Further investigations would therefore be necessary to identify the underlying mechanism responsible for this profound difference in the batch SPC mesoscale crystalliser.

The operating strategy for the MSMPR crystalliser and SPC mesoscale crystalliser could be optimised for specific objectives using a combination of rigorous *in silico* modelling and experimentation. The main goal would be to optimize the product crystal attributes obtained by manipulating supersaturation with respect to length in the SPC mesoscale crystalliser, and with respect to stage in the MSMPR crystalliser. This can be facilitated by building flow sheet simulations in commercial software packages like gCRYSTAL® (Process Systems Enterprise Ltd.) (Su et al., 2015), or first principle process systems models in mathematical modelling software like MATLAB® (Ridder et al., 2014), which use spatially distributed mass, heat, and

population balances. The coupling of hydrodynamic and heat transfer parameters determined in this work with dynamic or steady-state population balance models could aid the rapid identification of optimum process performance settings with few experiments required to validate model predictions. Prior to *in silico* optimisation, a rigorous sequential parameter estimation (Perez-Calvo et al., 2016) may be performed to accurately determine kinetic parameters of the crystallisation of the model compound or API. This would involve carefully designed isothermal experiments that facilitate the decoupling of the different crystallization phenomena namely primary and secondary nucleation, growth, agglomeration, and attrition, and the sequential estimation of kinetics thereof. Once kinetic parameters are obtained, representative models of the crystallisation process in the SPC mesoscale crystalliser and MSMPR crystalliser can be built for optimisation studies.

The two-stage MSMPR cascade has demonstrated the potential of MSMPR cascades to give better yields and decouple crystallisation mechanisms. A greater number of MSMPR stages, which offer an improved RTD, could be systematically investigated *in silico* and experimentally to gain better control of supersaturation for improved product quality. More importantly, a comparative study of the process performance of multiple MSMPR configurations against the SPC mesoscale crystalliser would provide invaluable insight into the capabilities of both platforms for developing robust continuous crystallisation processes.

Investigative efforts in this work on the GLY-water system have demonstrated that the SPC mesoscale crystalliser is a promising platform for developing seeded continuous cooling crystallisation processes. However, to establish its robustness and capability for handling different crystallisation behaviours, more investigations would need to be performed on a wider range of model systems exhibiting varying impurity profiles, solubilities, MSZWs, crystallisation kinetics, and physicochemical molecular properties. This will help build a much-needed database of demonstrated evidence where the SPC mesoscale crystalliser has delivered superior process performance and attributes control compared to equivalent batch processes for a wider range of APIs and model compounds.

The process development carried out in this research had no scale-up work involved. The hydrodynamics in the batch SPC mesoscale crystalliser was replicated in the continuous SPC mesoscale crystalliser, and the MSZW from the batch environment was easily transferred into the final continuous platform for crystallisation. This offers great potential for significantly reducing process development times for model compounds and APIs by eliminating complex scale-up steps encountered in batch crystallisation process development. An added benefit of the SPC mesoscale crystalliser is that the components can easily be manufactured at low cost.

This is convenient for replacing damaged glassware and parts, and particularly, as demonstrated in this work, for easily modifying the SPC mesoscale crystalliser to allow the integration of suitable PAT tools. With a polymeric SPC mesoscale crystalliser, the low cost of construction materials would allow meso-tubes to be disposable and provide a "plug-and-play" operation approach. The small volumes of material used for systematic investigations contributed to minimizing the cost of materials and waste generated; this would be very attractive for late stage process development in pharmaceutical industrial applications. The SPC design therefore holds the potential for use as a production platform for small-volume biopharmaceutical drugs (<10 kg/year) which have niche markets or small patient populations. Its minimal footprint would also allow high-process mobility and portability, either within the same facility or between different manufacturing sites, which can be strategically distributed to serve local markets. Furthermore, numbering up with parallel units could allow for rapid capacity adjustments to produce other niche drugs. It is a very important platform which deserves further investigation.

References

Aamir, E., Nagy, Z. K., Rielly, C. D., 2010. Optimal seed recipe design for crystal size distribution control for batch cooling crystallisation processes, Chem. Eng. Sci., 65, 3602 – 3614.

Acevedo, D., Kamaraju, V. K., Glennon, B., Nagy, Z. K., 2017. Modeling and characterization of an in situ wet mill operation, Org. Proc. Res. Dev., 21(7), 1069–1079. doi: 10.1021/acs.oprd.7b00192.

Adamo, A., Beingessner, R. L., Behnam, M., Chen, J., Jamison, T. F., Jensen, K. F., Monbaliu, J.-C. M., Myerson, A. S., Revalor, E. M., Snead, D. R., Stelzer, T., Weeranoppanant, N., Wong, S. Y., Zhang, P., 2016. On-demand continuous-flow production of pharmaceuticals in a compact, reconfigurable system, Science, 352(6281), 61–67. doi: 10.1126/science.aaf1337.

Adams, M.J., 2004. Chemometrics in Analytical Spectroscopy, 2nd edition, Royal Society of Chemistry.

Agimelen, O. S., Hamilton, P., Haley, I., Nordon, A., Vasile, M., Sefcik, J., Mulholland, A. J., 2015. Estimation of particle size distribution and aspect ratio of non-spherical particles from chord length distribution, Chem. Eng. Sci., Elsevier, 123, 629–640. doi: 10.1016/j.ces.2014.11.014.

Agimelen, O. S., Hamilton, P., Haley, I., Nordon, A., Vasile, M., Sefcik, J., Mulholland, A.J., 2015. Estimation of particle size distribution and aspect ratio of non-spherical particles from chord length distribution, Chem. Eng. Sci., 123, 629 – 640. https://doi.org/10.1016/j.ces.2014.11.014.

Agimelen, O. S., Mulholland, J., Sefcik, J., 2017. Modelling of artefacts in estimations of particle size of needle-like particles from laser diffraction measurements, Chem. Eng. Sci., 158, 445 – 452.

Agnew, L. R., McGlone, T., Wheatcroft, H. P., Robertson, A., Parsons, A. R., Wilson, C. C., 2017. Continuous crystallisation of paracetamol (acetaminophen) form II: Selective access to a metastable solid form, Cryst. Growth Des., 17(5), 2418–2427. doi: 10.1021/acs.cgd.6b01831.

Ahmed, S. M. R., Phan, A. N., Harvey, A. P., 2018. Mass transfer enhancement as a function of oscillatory baffled reactor design, Chemical Engineering and Processing - Process Intensification, Elsevier, 130(May), 229–239. doi: 10.1016/j.cep.2018.06.016.

Aksu, B., De Beer, T., Folestad, S., Ketolainen, J., Lindén, H., Lopes, J. A., De Matas, M., Oostra, W., Rantanen, J., Weimer, M., 2012. Strategic funding priorities in the pharmaceutical sciences allied to quality by design (QbD) and process analytical technology (PAT), Eur. J. Pharm. Sci., Elsevier B.V., 47(2), 402–405. doi: 10.1016/j.ejps.2012.06.009.

Allison, G., Cain, Y. T., Cooney, C., Garcia, T., Bizjak, T. G., Holte, O., Jagota, N., Komas, B., Korakianiti, E., Kourti, D., Madurawe, R., Morefield, E., Montgomery, F., Nasr, M., Randolph, W., Robert, J. L., Rudd, D., Zezza, D., 2015. Regulatory and quality considerations for continuous manufacturing May 20-21, 2014 continuous manufacturing symposium, J. Pharm. Sci., 104(3), 803–812. doi: 10.1002/jps.24324.

Al-Rashed, M., Wójcik, J., Plewik, R., Synowiec, P., Kuś, A., 2013. Multiphase CFD modeling: Fluid dynamics aspects in scale-up of a fluidized-bed crystallizer, Chemical Engineering and Processing: Process Intensification, 63, 7–15. doi: 10.1016/j.cep.2012.11.001.

Alvarez, A. J., Singh, A., Myerson, A. S., 2011. Crystallisation of cyclosporine in a multi-stage continuous MSMPR crystalliser, Cryst. Growth Des., 11, 4392 – 4400.

Amara, N., Ratsimba, B., Wilhelm, A., Delmas, H., 2004. Growth rate of potash alum crystals: Comparison of silent and ultrasonic conditions, Ultrason. Sonochem., 11, 17 – 21.

Anderson, N.G., 2012. Practical process research and development: A guide for organic chemists. Academic Press.

Ayranci, I., Kresta, S. M., 2011. Design rules for suspending concentrated mixtures of solids in stirred tanks. Chem. Eng. Res. Des., 89, 1961 – 1971. https://doi.org/10.1016/j.cherd.2011.01.008.

Ayranci, I., Kresta, S. M., 2014. Critical analysis of Zwietering correlation for solids suspension in stirred tanks, Chem. Eng. Res. Des., 92, 413 – 422. https://doi.org/10.1016/j.cherd.2013.09.005.

Badman, C., Trout, B. L., 2015. Achieving continuous manufacturing May 20-21, 2014 continuous manufacturing symposium, J. Pharm. Sci., 104(3), 779–780. doi: 10.1002/jps.24246.

Baird, M.H.I., Stonestreet, P., 1995. Energy dissipation in oscillatory flow within a baffled tube, Trans. IChem. E. 73 (A), 503–511.

Bakar, M.R.A., Nagy, Z.K., Rielly, C.D., 2009. Seeded batch cooling crystallisation with temperature cycling for the control of size uniformity and polymorphic purity of sulfathiazole crystals, Org. Process Res. Dev., 13 (6), 1343-1356.

Bakar, M.R.A., Nagy, Z.K., Rielly, C.D., Dann, S.E., 2011. Investigation of the riddle of sulfathiazole polymorphism, Int. J. Pharm., 414, 86 – 103.

Bakar, M.R.A., Nagy, Z.K., Saleemi, A.N., Rielly, C.D., 2008. Impact of direct nucleation control on crystal size distribution in pharmaceutical crystallisation process, Cryst. Growth Des., 9(3), 1378-1384.

Bakar, M.R.H.A., 2010. Process Analytical technology based approaches for the monitoring and control of size and polymorphic form in pharmaceutical crystallisation processes, Loughborough University.

Bakeev, K.A., 2010. Process Analytical Technology, Blackwell.

Baldyga, J., Bourne, J.R., 1986. Principles of micromixing, In *Encyclopaedia of fluid mechanics*, 145, Gulf Publishing, Houston.

Baldyga, J., Bourne, J.R., Zimmermann, B., 1994. Investigation of mixing in jet reactors using fast competitive-consecutive reactions, Chem. Eng. Sci. 44, 1937.

Banerjee, S., Briesen, H., 2009. Molecular dynamics simulations of glycine crystal-solution interface, J. Chem. Phys., 131, 184705.

Barrett, P., Glennon, B., 1999. In-line FBRM monitoring of particle size in dilute agitated suspensions. Part. Part. Syst. Charact. 16, 207–211.

Barrett, P., Glennon, B., 2002. Characterizing the metastable zone width and solubility curve using lasentec FBRM and PVM. Trans iChem, 80, 799 – 805.

Barthe, S. C., Grover, M. A., Rousseau, R. W., 2008. Observation of polymorphic change through analysis of FBRM data: Transformation of paracetamol from form II to form I, Cryst. Growth Des., 8(9), 3316–3322. doi: 10.1021/cg800232x.

Bauer, H. H., Fischer, M., 2000. Product life cycle patterns for pharmaceuticals and their impact on R&D profitability of late mover products, International Business Review, 9 (6), 703–725.

Baxendale, I. R., Braatz, R. D., Hodnett, B. K., Jensen, K. F., Johnson, M. D., Sharratt, P., Sherlock, J. P., Florence, A. J., 2015. Achieving continuous manufacturing: Technologies and approaches for synthesis, workup, and isolation of drug substance May 20-21, 2014 continuous manufacturing symposium, J. Pharm. Sci. doi: 10.1002/jps.24252.

Bellhouse, B., Bellhouse, F., Curl, C., Macmillan, T., Gunning, A., Spratt, E., MacMurray, S., Nelems, J., 1973. A high efficiency membrane oxygenator and pulsatile pumping system, and its application to animal trials, Trans. Am. Soc. Artif. Inter. Organs 19, 72 – 79.

Benyahia, B, Lakerveld, R, Barton, P.I., 2012. A plant-wide dynamic model of a continuous pharmaceutical process, Ind. Eng. Chem. Res., 51(47), 15393-15412, ISSN: 0888-5885.

Benyahia, B., 2010. Modélisation, expérimentation et optimisation multicritère d'un procédé de copolymérisation en émulsion en présence d'un agent de transfert de chaîne, Ph.D. Thesis, National Polytechnic Institute of Lorraine, Nancy-University, France.

Benyahia, B., Latifi, M.A., Fonteix, C., Pla, F., 2013. Emulsion copolymerization of styrene and butyl acrylate in the presence of a chain transfer agent. Part 2: Parameters estimability and confidence regions, Chem. Eng. Sci 90, 110 – 118.

Betz, G., Junker-Bürgin, P., Leuenberger, H., 2003. Batch and continuous Processing in the production of pharmaceutical granules, Pharm Dev Technol., 8(3), 289-97

Bhat, M. N., Dharmaprakash, S. M., 2002. Growth of nonlinear optical γ-glycine crystals, J. Cryst. Growth., 236, 376 – 380.

Binev, D., Seidel-Morgenstern, A., Lorenz, H., 2016. Continuous separation of isomers in fluidized bed crystallizers, Cryst. Growth Des., 16(3), 1409–1419. doi: 10.1021/acs.cgd.5b01513.

Biscans, B., 2011. Industrial crystallisation - challenges and scientific issues. 18th Internation Symposium on Industrial Crystallisation, http://www.aidic.it/isic18/webpapers/309Biscans.pdf (Accessed 27/09/2013).

Bischoff, K.N., Levenspiel, O., 1962. Fluid dispersion-generalization and comparison of mathematical models – I. Generalization of models, Chem. Eng. Sci., 17, 245 – 255.

Blagden, N., de Matas, M., Gavan, P.T., York, P., 2007. Crystal engineering of active pharmaceutical ingredients to improve solubility and dissolution rates, Advanced Drug Delivery Reviews, 59, 617–630.

Blais, B., Bertrand, O., Fradette, L., Bertrand, F., 2017. CFD-DEM simulations of early turbulent solid–liquid mixing: prediction of suspension curve and just-suspended speed, Chem. Eng. Res. Des., 123, 388 – 406. https://doi.org/10.1016/j.cherd.2017.05.021.

Booth, R., 1999. The global supply chain, FT Healthcare Management Report, London: Financial Times Business Ltd.

Braatz, R.D., 2002. Advanced control of crystallisation processes, Annual Reviews in Control, 26, 87–99.

Brereton, R.G., 2003. Chemometrics data analysis for the laboratory and chemical plant, Wiley.

Briggs, N. E. B., Schacht, U., Raval, V., McGlone, T., Sefcik, J., Florence, A.J., 2015. Seeded crystallisation of β-*L*-glutamic acid in a continuous oscillatory baffled crystallizer. Org. Process Res. Dev., 19, 1903 – 1911. https://doi.org/10.1021/acs.oprd.5b00206.

Brown, C. J., Ni, X. W., 2011. Evaluation of growth kinetics of antisolvent crystallisation of paracetamol in an oscillatory baffled crystallizer utilizing video imaging, Cryst. Growth Des., 11(9), 3994–4000. doi: 10.1021/cg200560b.

Brown, C. J. et al., 2018. Enabling precision manufacturing of active pharmaceutical ingredients: workflow for seeded cooling continuous crystallisations, Molecular Systems Design & Engineering, Royal Society of Chemistry. doi: 10.1039/C7ME00096K.

Brown, C. J., Adelakun, J. A., Ni., X., 2015. Characterization and modelling of antisolvent crystallisation of salicylic acid in a continuous oscillatory baffled crystalliser, Chem. Eng. Proc., 97, 180 – 186.

Brown, C., 2013. Scientific understanding of seeding in continuous oscillatory baffled crystalliser. Report for the Centre for Oscillatory Baffled Reactor Advancement (COBRA).

Brown, C.J., Ni, X., 2012. Determination of metastable zone width, mean particle size and detectable number density using video imaging in an oscillatory baffled crystalliser, CrystEngComm. 14 (8), 2944 – 2949.

Brunold, C.R., Hunns, J.C.B., Mackley, M.R., Thompson, J.W., 1989. Experimental-observations on flow patterns and energy-losses for oscillatory flow in ducts containing sharp edges, Chem. Eng. Sci., 44, 1227–1244.

Buchholz, S., 2010. Future manufacturing approaches in the chemical and pharmaceutical industry. Chemical Engineering and Processing: Process Intensification, 49 (10), Elsevier B.V, 993–995.

Byrn, S., Futran, M., Thomas, H., Jayjock, E., Maron, N., Meyer, R. F., Myerson, A. S., Thien, M. P., Trout, B. L., 2015. Achieving continuous manufacturing for final dosage formation: Challenges and how to meet them May 20-21, 2014 continuous manufacturing symposium, J. Pharm. Sci., 104(3), 792–802. doi: 10.1002/jps.24247.

Caillet, A., Puel, F., Fevotte, G., 2006. In-line monitoring of partial and overall solid concentration during solvent-mediated phase transition using Raman spectroscopy, Int. J. Pharm., 307(2): 201–208.

Calabrese, G. S., Pissavini, S., 2011. From batch to continuous flow processing in chemicals manufacturing, AIChE J., 57 (4), 828–834.

Callahan, C.J., Ni, X., 2012. Probing into nucleation mechanisms of cooling crystallisation of sodium chlorate in a stirred tank crystalliser and an oscillatory baffled crystalliser, Cryst. Growth. Des., 12, 2525 – 2532.

Cano. H., Gabas, N., Canselier, J.P., 2001, Experimental study on the ibuprofen crystal growth morphology in solution, J. Cryst. Growth, 224, 335–341.

Castro, F., Ferreira, A., Rocha, F., Vicente, A., Teixeira, J. A., 2013. Continuous-flow precipitation of hydroxyapatite at 37 °C in a meso oscillatory flow reactor, Ind. Eng. Chem. Res., 52, 9816 – 9821.

Castro, F., Ferreira, A., Rocha, F., Vicente, A., Teixeira, J. A., 2013. Precipitation of hydroxyapatite at 37 °C in a meso oscillatory flow reactor operated in batch at constant power density, AIChE J., 59 (12), 4483 – 4493.

Castro, F., Ferreira, A., Teixeira, J. A., Rocha, F., 2016. Protein crystallisation as a process step in a novel meso oscillatory flow reactor: study of lysozyme phase behavior, Cryst. Growth Des., 16(7), 3748–3755. doi: 10.1180/minmag.1997.061.404.09.

Castro, F., Ferreira, A., Teixeira, J. A., Rocha, F., 2018. Influence of mixing intensity on lysozyme crystallisation in a meso oscillatory flow reactor, Cryst. Growth Des., doi: 10.1021/acs.cgd.8b00721.

Chavan, R. B., Thipparaboina, R., Yadav, B., Shastri, N. R., 2018. Continuous manufacturing of co-crystals: challenges and prospects, Drug Delivery and Translational Research, Drug Delivery and Translational Research, (May 2015), 1–14. doi: 10.1007/s13346-018-0479-7.

Chen, J., Sarma, B., Evans, J. M. B., Myerson, A. S., 2011. Pharmaceutical crystallisation, Cryst. Growth Des., 11 (4):887 – 95.

Chen, Z.P., Fevotte, G., Caillet, A., Littlejohn, D., Morris, J., 2008. Advanced calibration strategy for in situ quantitative monitoring of phase transition processes in suspensions using FT-Raman spectroscopy, Analytical Chemistry 80, 6658–6665.

Chew, C. M., Ristic, R. I., Dennehy, R. D., De Yoreo, J. J., 2004. Crystallisation of paracetamol under oscillatory flow mixing conditions, Cryst. Grow. Des., 4, 1045 – 1052.

Chianese, A., Berardino, F.D., Jones, A.G., 1993. On the effect of secondary nucleation on the crystal size distribution from a seeded batch crystalliser, Chem. Eng. Sci., 48(3), 551 – 560.

Choi, B. S., Wan, B., Philyaw, S., Dhanasekharan, K., Ring, T.A., 2004. Residence time distributions in a stirred tank: comparison of CFD predictions with experiment, Ind. Eng. Chem. Res., 43, 6548 – 6556. https://doi.org/10.1021/ie0308240.

Chow, A.H.L., Chow, P.K.K, Zhongshan, W., grant, D.J.W., 1985. Modification of acetaminophen crystals: influence of growth in aqueous solutions containing p-acetoxyacetanilide on crystal properties, Int. J. Pharm., 24, 239 – 258.

Cui, Y., O'Mahony, M., Jaramillo, J. J., Stelzer, T., Myerson, A. S., 2016. Custom-built miniature continuous crystallisation system with pressure-driven suspension transfer, Org. Proc. Res. Dev., 20(7), 1276–1282. doi: 10.1021/acs.oprd.6b00113.

De Beer, T., Burggraeve, A., Fonteyne, M., Saerens, L., Remon, J. P., Vervaet, C., 2011. Near Infrared and Raman spectroscopy for the in- process monitoring of pharmaceutical production processes, Int. J. Pharm. 2011, 417, 32−47.

Diab, S., Gerogiorgis, I., 2017. Technoeconomic evaluation of multiple mixed suspension-mixed product removal (MSMPR) crystalliser configurations for continuous cyclosporine crystallisation, Org. Process Res. Dev., 21, 1571 – 1587.

Dickens, A., Mackley, M., Williams, H., 1989. Experimental residence time distribution measurements for unsteady flow in baffled tubes, Chem. Eng. Sci. 44, 1471 – 1479.

Donovan, J.G., 2003. Fracture toughness-based models for the prediction of power consumption, product size, and capacity of jaw crushers. PhD Thesis, Virginia Polytechnic Institute and State University, Blacksburg, Virginia.

Eder, R. J. P., Radl, S., Schmitt, E., Innerhofer, S., Maier, M., Gruber-Woelfler, H., Khinast, J.G., 2010. Continuously seeded, continuously operated tubular crystallizer for the production of active pharmaceutical ingredients, Cryst. Growth Des., 10, 2247 – 2257. https://doi.org/10.1021/cg9015788.

Eder, R. J. P., Schmitt, E. K., Grill, J., Radl, S., Gruber-Woelfler, H., Khinast, J. G., 2011. Seed loading effects on the mean crystal size of acetylsalicylic acid in a continuous-flow crystallisation device, Crystal Research and Technology, 46(3), 227–237. doi: 10.1002/crat.201000634.

Eder, R. J. P., Schmitt, E.K., Grill, J., Radl, S., Gruber-Woelfler, H., Khinast, J.G., 2011. Seed loading effects on the mean crystal size of acetylsalicylic acid in a continuous-flow crystallisation device, Cryst. Res. Technol., 46, 227 – 237. https://doi.org/10.1002/crat.201000634.

Eder, R.J.P., Schrank, S., Besenhard, M.O., Roblegg, E., Gruber-Woelfler, H., Khinast, J.G., Continuous sonocrystallisation of acetylsalicylic acid (ASA): Control of crystal size, Cryst. Growth Des., 12 (2012) 4733–4738.

Ejim, L. N., Yerdelen, S., McGlone, T., Onyemelukwe, I., Johnston, B., Florence, A. J., Reis, N. M., 2017. A factorial approach to understanding the effect of inner geometry of baffled mesoscale tubes on solids suspension and axial dispersion in continuous, oscillatory liquid-solid plug flows, Chem. Eng. J., 308, 669 – 682.

Esmonde-White, K. A., Cuellar, M., Uerpmann, C., Lenain, B., Lewis, I. R., 2017. Raman spectroscopy as a process analytical technology for pharmaceutical manufacturing and bioprocessing, Analytical and Bioanalytical Chemistry, 409(3), 637–649. doi: 10.1007/s00216-016-9824-1.

Muller, F. L., Fielding, M., Black, S., 2009. A practical approach for using solubility to design cooling crystallisations, Org. Process Res. Dev., 2009, 13, 1315–1321.

Ferguson, S., Morris, G., Hao, H., Barrett, M., Glennon, B., 2012. In situ monitoring and characterization of plug flow crystallizers, Chem. Eng. Sci., 77, 105 – 111. https://doi.org/10.1016/j.ces.2012.02.013.

Ferguson, S., Morris, G., Hao, H., Barret, M., Glennon, B., 2013. Characterization of the anti-solvent batch, plug flow and MSMPR crystallisation of benzoic acid, Chem. Eng. Sci., 104, 44 – 54. https://doi.org/10.1016/j.ces.2013.09.006.

Ferguson, S., Ortner, F., Quon, J., Peeva, L., Livingston, A., Trout, B. L., Myerson, A. S., 2014. Use of continuous MSMPR crystallisation with integrated nanofiltration membrane recycle for enhanced yield and purity in API crystallisation, Cryst. Growth Des., 14(2), 617–627. doi: 10.1021/cg401491y.

Ferreira, A., Adesite, P. O., Teixeira, J. A., Rocha, F., 2017. Effect of solids on O_2 mass transfer in an oscillatory flow reactor provided with smooth periodic constrictions, Chem. Eng. Sci., Elsevier Ltd, 170, 400–409. doi: 10.1016/j.ces.2016.12.067.

Ferreira, A., Teixeira, J. A., Rocha, F., 2015. O_2 mass transfer in an oscillatory flow reactor provided with smooth periodic constrictions. Individual characterization of k_L and a, Chem. Eng. J., 262, 499 – 508.

Févotte, G., 2007. In situ Raman spectroscopy for in-line control of pharmaceutical crystallisation and solids elaboration processes: A review, Chem. Eng. Res. Des., 85(7), 906–920. doi: 10.1205/cherd06229.

Finnie, S.D., Ristic, R. I., Sherwood, J.N., Zikic, A.M., 1999. Morphological and growth rate distributions of small self-nucleated paracetamol crystals grown from pure aqueous solutions, J. Cryst. Growth, 207, 308 – 318.

Fitch, A. W., Jian, H., Ni, X., 2005. An investigation of the effect of viscosity on mixing in an oscillatory baffled column using digital particle image velocimetry and computational fluid dynamics simulation. Chem. Eng. J., 112 (1-3), 197–210.

Fitch, A.W., Ni, X., 2003. On the determination of axial dispersion coefficient in a batch oscillatory baffled column using laser induced fluorescence, Chem. Eng. J., 92, 243 – 253.

Fogler, H. S., 1999. Elements of chemical reaction engineering, 3rd ed., Prentice Hall: Upper Saddle River, NJ.

Froment, G.F., Bischoff, K.B., 1990. Chemical reactor analysis and design, John Wiley & Sons, New York.

Fujiwara, M., Chow, P. S., Ma, D. L., Braatz, R. D., 2002. Paracetamol crystallisation using laser backscattering and ATR-FTIR spectroscopy: Metastability, agglomeration, and control, Cryst. Growth Des., 2 (5), 363 – 370.

Fujiwara, M., Nagy, Z.K., et al., 2004. First-principles and direct design approaches for the control of pharmaceutical crystallisation, Journal of Process Control, 15, 493 – 509.

Galan, K., Eicke, M. J., Elsner, M. P., Lorenz, H., Seidel-Morgenstern, A., 2015. Continuous preferential crystallisation of chiral molecules in single and coupled mixed-suspension mixed-product-removal crystallisers, Cryst. Growth Des., 15, 1808 – 1818.

Gao, S., Ni, X., Cumming, R.H., Greated, C.A., Norman, P., 1998. Experimental investigation of bentonite flocculation in a batch oscillatory baffled column, Separ Sci Technol., 33: 2143–2157.

Gao, Z., Rohani, S., Gong, J., Wang, J., 2017. Recent developments in the crystallisation process: Toward the pharmaceutical industry, Engineering, Elsevier LTD on behalf of Chinese Academy of Engineering and Higher Education Press Limited Company, 3(3), 343–353. doi: 10.1016/J.ENG.2017.03.022.

Gao, Z., Wu, Y., Gong, J., Wang, J., Rohani, S., 2018. Continuous Crystallisation of α-Form *L*-Glutamic Acid in an MSMPR-Tubular Crystallizer System. J. Cryst. Growth. https://doi.org/10.1016/j.jcrysgro.2018.07.007**.**

Garekani, H.A., Sadeghi, F., Badiee, A., Mostafa, S.A., Rajabi-Siahboomi, A.R., 2001. Crystal habit modifications of ibuprofen and their physicomechanical characteristics, Drug Dev. Ind. Pharm., 27, 803-809.

Garside, J., Mersmann, A., Nyvlt, J., 2002. Measurement of crystal growth and nucleation rates, 2nd ed., Institution of Chemical Engineers: Rugby, U.K.

Gates, L.E., Morton, J.R., and Fondy, P.L., 1976. Selecting agitator systems to suspend solids in liquids, Chem. Eng. 83, 144-150.

Gerstlauer, A., Motz, S., Mitrović, A., Gilles, E. D., 2002. Development, analysis and validation of population models for continuous and batch crystallizers, Chem. Eng. Sci., 57(20), 4311–4327. doi: 10.1016/S0009-2509(02)00348-2.

Gibbs, J.W., 1961. The scientific papers of J. W. Gibbs. Dover, New York.

Girolami M.W., Rousseau R.W., 1985. Size-dependent crystal growth – A manifestation of growth rate dispersion in the potassium alum water system. AIChE J., 31(11):1821–1828.

Glennon, B., Macloughlin, P.F., Malone, D.M., 1988. Mixing and dispersion studies in an air-lift reactor, Proc 2nd Intl. Conf. on Bioreactor Fluid Dynamics, (BHRA Fluid Engineering, Cambridge, England) Paper H3, 415 – 429.

Gordon, R.E., Amin, S.I., 1984, Crystallisation of Ibuprofen, US patent 4476248.

Grabowski, H., 1997. The effect of pharmacoeconomics on company research and development decisions, Pharmacoeconomics, 11, 389–397.

Grant, D.J.W., 1999. Theory and origin of polymorphism, in: Brittain, H.G. (Ed.), *Polymorphism in pharmaceutical solids*, 95, Marcel Dekker, New York, 1–33.

Green, D., 2002. Crystallizer mixing: Understanding and modelling crystallizer mixing and suspension flow in *Handbook of Industrial Crystallisation*, 2nd ed., Butterworth-Heinemann, Boston.

Griffin, D. W., Mellichamp, D. A., Doherty, M. F., 2010. Reducing the mean size of API crystals by continuous manufacturing with product classification and recycle, Chem. Eng. Sci., Elsevier, 65(21), 5770–5780. doi: 10.1016/j.ces.2010.05.026.

Griffin, D. W., Mellichamp, D. A., Doherty, M. F., 2010. Reducing the mean size of api crystals by continuous manufacturing with product classification and recycle, Chem. Eng. Sci., 65, 5770 – 5780. https://doi.org/10.1016/j.ces.2010.05.026.

Gron, H., Mougin, P., Thomas, A., White, G., Wilkinson, D., 2003. Dynamic in-process examination of particle size and crystallographic form under defined conditions of reactant supersaturation as associated with the batch crystallisation of monosodium glutamate from aqueous solution, Ind. Eng. Chem. Res., 42, 4888–4898.

Guo, H., Ali, H. M., Hassanzadeh, A., 2016. Simulation study of flat-sheet air gap membrane distillation modules coupled with an evaporative crystallizer for zero liquid discharge water desalination, Applied Thermal Engineering. Elsevier Ltd, 108, 486–501. doi: 10.1016/j.applthermaleng.2016.07.131.

Guo, Z., Zhang, M., Li, H., Wang, J., Kougoulos, E., 2005. Effect of ultrasound on anti-solvent crystallisation process, J. Cryst. Growth, 273, 555 – 563.

Harrington, T., 2013. Continuous manufacturing: Barriers and enablers. Centre for Continuous Manufacturing and Crystallisation, University of Cambridge.

Harvey, A., Mackley, M., Reis, N., Teixeira, J., Vicente, A., 2003. The fluid mechanics relating to a novel oscillatory flow micro reactor, in: 4th European Congress of Chemical Engineering, Granada, 0-6.4-004.

Harvey, A., Mackley, M., Seliger, T., 2003. Process intensification of biodiesel production using a continuous oscillatory flow reactor, J. Chem. Technol. Biotechnol., 78:338–341.

Harvey, A., Mackley, M., Stonestreet, P., 2001. Operation and optimisation of an oscillatory flow continuous reactor, Ind. Eng. Chem. Res. 40, 5371 – 5377.

Hausen, H., 1959. Neue Gleichungen fur die Warmeubeitragung bei freier oder erzwungener stromung. Allg. Waermetech., 9, 75 – 79.

Hausman, D.S., Cambron, R.T., Sakr, A., 2005. Application of on-line Raman spectroscopy for characterizing relationships between drug hydration state and tablet physical stability, Int. J. Pharm., 299 (1-2), 19-33.

Himmelblau, M.D., 1970. Process analysis by statistical methods, John Wiley & Sons, Inc. New York.

Hishamuddin, E., Stapley, A. G. F., Nagy, Z. K., 2011. Application of laser backscattering for monitoring of palm oil crystallisation from melt, J. Cryst. Growth, 335 (1), 172–180.

Hörter, D., Dressman, J.B., 2001. Influence of physicochemical properties on dissolution of drugs in the gastrointestinal tract, Advanced Drug Delivery Reviews, 46, 75–87.

Hou, G., Power, G., Barrett, M., Glennon, B., Morris, G., Zhao, Y., 2014. Development and characterization of a single stage mixed-suspension, mixed-product-removal crystallisation process with a novel transfer unit, Cryst. Growth Des., 14(4), 1782–1793. doi: 10.1021/cg401904a.

Hou, G., Power, G., Barrett, M., Glennon, B., Morris, G., Zhao, Y., 2014. Development and characterization of a multi-stage continuous cooling crystallisation process using in-line process analytical technology, Growth Des., 14, 1782 – 1793.

Howes, T., Mackley, M., Roberts, E., 1991. The simulation of chaotic mixing and dispersion for periodic flows in baffled channels, Chem. Eng. Sci., 46, 1669–1677.

Howes, T., Mackley, M.R., Roberts, E.P.L., 1991. The simulation of chaotic mixing and dispersion for periodic flows in baffled channels, Chem. Eng. Sci., 46, 1669–1677.

Hu, Y., Liang, J.K., Myerson, A.S., Taylor, L.S., 2005. Crystallisation monitoring by Raman spectroscopy: Simultaneous measurement of de-supersaturation profile and polymorphic form in flufenamic acid systems, Ind. Eng. Chem. Res., 44 (5), 1233 - 1240.

Hu, Y., Wikström, H., Byrn, S.R., Taylor, L.S., 2006. Effect of particle size on polymorphic quantitation by Raman spectroscopy, Applied Spectroscopy, 9 (60), 977–984.

Hu, Y., Wikström, H., Byrn, S.R., Taylor, L.S., 2007. Estimation of the transition temperature for an enantiotropic polymorphic system from the transformation kinetics monitored using Raman spectroscopy, Journal of Pharmaceutical and Biomedical Analysis, 45 (4), 546–551.

Huang, J., Romero-Torres, S., Moshgbar, M., 2010. Practical considerations in data pre-treatment for NIR and Raman spectroscopy, American Pharmaceutical Review, 13 (6).

Iitaka, Y., 1958. The crystal structure of γ-glycine, Acta Crystallogr., 11. 225 – 226.

Iitaka, Y., 1960. The crystal structure of β-glycine, Acta Crystallogr., 13, 35.

Zaccaro, J., Matic, J., Myerson, A.S., Garetz, B.A., 2001. nonphotochemical, laser-induced nucleation of supersaturated aqueous glycine produces unexpected γ-polymorph, Cryst. Growth Des., 1, 5 – 8.

Jian, H., Ni, X., 2005. A numerical study on the scale-up behaviour in oscillatory baffled columns, Chem. Eng. Res. Des., 83(10), 1163–1170. doi: 10.1205/cherd.03312.

Jiang, K., Zhou, K., Yang, Y., Du, H., 2013. A pilot-scale study of cryolite precipitation from high fluoride-containing wastewater in a reaction-separation integrated reactor, Journal of Environmental Sciences (China), 25(7), 1331–1337. doi: 10.1016/S1001-0742(12)60204-6.

Jimeno, G., Lee, Y. C., Ni, X.-W., 2018. On the evaluation of power density models for oscillatory baffled reactors using CFD, Chemical Engineering and Processing - Process Intensification, 134(May), 153–162. doi: 10.1016/J.CEP.2018.11.002.

Jinno, J., Kamada, N., Miyake, M., Yamada, K., Mukai, T., Odomi, M., Toguchi, H., Liversidge, G., Higaki, K., Kimura, T., 2006. Effect of particle size reduction on dissolution and oral absorption of a poorly water-soluble drug, cilostazol, in beagle dogs, Journal of Controlled Release, 111, 56 – 64.

Johnson, M. D., May, S. A., Calvin, J. R., Remacle, J., Stout, J.R., Diseroad, W. D., Zaborenko, N., Haeberle, B. D., Sun, W., Miller, M. T., Brennan, J., 2012. Development and scale-up of a continuous, high-pressure, asymmetric hydrogenation reaction, workup, and isolation, Org. Process Res. Dev. 2012, 5, 1017−1038.

Jones, A.G., 2002. *Crystallisation process systems*, 1st ed., Butterworth-Heinemann, Oxford.

Jones, A.G., Bud, J., Mullin, J.W., 1987. Batch crystallisation and solid-liquid separation of potassium sulphate, Chem. Eng. Sci., 42(4), 619-629.

Jozwiakowski, M.J., Nguyen, N-A T., Sisco, J.M., Spancake, C.W., 1996. Solubility behaviour of lamivudine crystal forms in recrystallisation solvents, J. Pharm. Sci., 85, 193 – 199.

Srinivasan, K., Arumugam, J., 2007. Growth of non-linear optical γ-glycine single crystals and their characterization, Opt. Mater. 30, 40 – 43.

Kacker, R., Regensburg, S. I., Kramer, H. J. M., 2017. Residence time distribution of dispersed liquid and solid phase in a continuous oscillatory flow baffled crystalliser, Chem. Eng. J., 317, 413–423. doi: 10.1016/j.cej.2017.02.007.

Karr, A., 1959. Performance of a reciprocating-plate extraction column, AIChE J., 446 – 452.

Kawabata, Y., Wada,K., et al., 2011, Formulation design for poorly water-soluble drugs based on biopharmaceutics classification system: Basic approaches and practical applications, Int. J. Pharm., 420, 1–10.

Kim, J. M., Chang, S. M., Chang, J. H., Kim, W. S., 2011. Agglomeration of nickel/cobalt/manganese hydroxide crystals in Couette-Taylor crystallizer, colloids and surfaces A: Physicochemical and engineering aspects. Elsevier B.V., 384(1–3), 31–39. doi: 10.1016/j.colsurfa.2011.03.016.

Kim, K., Mersmann, A., 2001. Estimation of metastable zone width in different nucleation processes, Chem. Eng. Sci., 56(7), 2315 – 2324.

Kim, S., Wei, C., Kiang, S., 2003. Crystallisation process development of an active pharmaceutical ingredient and particle engineering via the use of ultrasonics and temperature cycling, Org. Process Res. Dev. 7, 997–1001.

Kneule, F., 1956. Die Prüfung von Rührern durch Löslichkeitsbestimmung. Chemie Ingenieur Technik, 28, 221 – 225. https://doi.org/10.1002/cite.330280316.

Kobayashi, R., Fujimaki, Y., Ukita, T., Hiyama, Y., 2006. Monitoring of solvent-mediated polymorphic transitions using in situ analysis tools, Org Process Res Dev, 10(6): 1219–1226.

Kolbach-Mandel, A. M., Kleinman, J. G., Wesson, J. A., 2015. Exploring calcium oxalate crystallisation: A constant composition approach, Urolithiasis. Springer Berlin Heidelberg, 43(5), 397–409. doi: 10.1007/s00240-015-0781-5.

Konstantinov, K. B., Cooney, C. L., 2015. White paper on continuous bioprocessing May 20-21, 2014 continuous manufacturing symposium, J. Pharm. Sci., 104(3), 813–820. doi: 10.1002/jps.24268.

Kougoulos, E., Jones, A. G., Wood-Kaczmar, M. W., 2005. Estimation of crystallisation kinetics for an organic fine chemical using a modified continuous cooling mixed suspension mixed product removal (MSMPR) crystalliser, J. Cryst. Growth, 273 (3-4), 520–528.

Kougoulos, E., Jones, A. G., Jennings, K. H., Wood-Kaczmar, M. W., 2005. Use of focused beam reflectance measurement (FBRM) and process video imaging (PVI) in a modified mixed suspension mixed product removal (MSMPR) cooling crystalliser, J. Cryst. Growth, 273 (3-4), 529–534.

Kougoulos, E., Jones, A. G., Wood-Kaczmar, M. W., 2006. Process modelling tools for continuous and batch organic crystallisation processes including application to scale-up, Org. Process Res. Dev., 10 (4), 739 – 750.

Kralj D, Brečević L, Kontrec J., 1997. Vaterite growth and dissolution in aqueous solu- tion III. Kinetics of transformation. J. Cryst. Growth., 177(3–4):248–57.

Krstulovic, A. M., Lee, C. R., 1997. Defining drug purity through chromatographic and related methods: Current status and perspectives, Journal of Chromatography B: Biomedical Applications, 689(1), 137–153. doi: 10.1016/S0378-4347(96)00439-2.

Kumar, S., Rai, A. K., Singh, V. B., Rai, S. B., 2005. Vibrational spectrum of glycine molecule, Spectrochimica Acta - Part A: Molecular and Biomolecular Spectroscopy, 61(11–12), 2741–2746. doi: 10.1016/j.saa.2004.09.029.

Lai, T. C., Cornevin, J., Ferguson, S., Li, N., Trout, B. L., Myerson, A. S., 2015. Control of polymorphism in continuous crystallisation via mixed suspension mixed product removal systems cascade design, Cryst. Growth Des., 15(7), 3374–3382. doi: 10.1021/acs.cgd.5b00466.

Lakerveld, R., Benyahia, B., Heider, P. L., Zhang, H., Wolfe, A., Testa, C. J., Ogden, S., Hersey, D. R., Mascia, S., Evans, J. M. B., Braatz, R. D., Barton, P. I., 2015. The application of an automated control strategy for an integrated continuous pharmaceutical pilot plant, Org. Process Res. Dev., 19, 1088 – 1100.

Lakerveld, R., Van Krochten, J. J. H., Kramer, H. J. M., 2014. An air-lift crystalliser can suppress secondary nucleation at a higher supersaturation compared to a stirred crystalliser, Cryst. Growth Des., 14(7), 3264–3275. doi: 10.1021/cg500090g.

Langan, P., Mason, S.A., Myles, D., Schoenborn, B.P., 2002. Structural characterization of crystals of alpha-glycine during anomalous electrical behaviour, Acta Crystallogr B., 58, 728 – 733.

Lawton, S., Steele, G., Shering, P., Zhao, L., Laird, I., Ni, X.-W., 2009. Continuous crystallisation of pharmaceuticals using a continuous oscillatory baffled crystalliser, Org. Process Res. & Dev., 13 (6), 1357–1363.

Lee, I., Variankaval, N., Lindemann, C., Starbuck, C., 2004. Rotor-stator milling of APIs – empirical scale-up parameters and theoretical relationships between the morphology and breakage of crystals, Am. Pharmaceut. Rev. 7, 120–123.

Lee, S., Choi, A., Kim, W. S., Myerson, A. S., 2011. Phase transformation of sulfamerazine using a Taylor vortex', Cryst. Growth Des., 11(11), 5019–5029. doi: 10.1021/cg200925v.

Levenspiel, O., 1999. *Chemical reaction Engineering*, 3rd Ed. John Wiley & Sons, London.

Levenspiel, O., Smith, W.K., 1957. Notes on the diffusion-type for the longitudinal mixing of fluids in flow, Chem. Eng. Sci. 6, 227 – 233.

Li, J., Trout, B. L., Myerson, A. S., 2016. Multi-stage continuous mixed-suspension, mixed-product (MSMPR) crystallisation with solids recycle, Org. Process Res. Dev., 20, 510 – 516. doi: 10.1021/acs.oprd.5b00306.

Li, J., Tsai-ta, C., Trout, B. L., Myeson, A. S., 2017. Continuous crystallisation of cyclosporine: Effect of operating conditions on yield and purity, Cryst. Growth Des., 17, 1000 – 1007.

Li, Y.-E. Control of polymorphism of an active pharmaceutical ingredient during manufacture, Paper 107, Annual Meeting AIChE, Indianapolis, IN, November 3-8, 2002.

Liang, J.K., 2002. Process scale dependence of batch crystallisation of L-glutamic acid from aqueous solution in relation to reactor internals reactant mixing and process conditions, Heriot-Watt University, Edinburgh.

Liang, J.K., Wikinson, D., Ford, L.J., Roberts, K.J., Wood, W.M.L., 2004. An examination into the effect of stirrer material and agitation rate on the nucleation of L-glutamic acid batch crystallised from supersaturated aqueous solutions, Cryst. Growth Des., 4(5), 1039 – 1044.

Liang, K., White, G., Wilkinson, D., 2004. Examination of the process scale dependence of L-glutamic acid batch crystallized from supersaturated aqueous solution in relation to reactor hydrodynamics, Ind. Eng. Chem. Res., 43 (5), 1227 – 1234.

Lindenberg, C., Krattli, M., Cornel, J., Mazotti, M. 2009. Design and optimisation of a combined cooling/antisolvent crystallisation, Cryst. Growth Des 9, 1124 – 1136.

Liu, W.J., Ma, C.Y., Liu, J.J., Zhang, Y., Wang, X.Z., 2016. Continuous reactive crystallisation of pharmaceuticals using impinging jet mixers, AIChE J., 63(3), 967 – 974.

Llinàs A, Goodman JM., 2008. Polymorph control: Past, present and future, Drug Discov. Today,13(5–6):198–210.

Loï Mi Lung-Somarriba, B., 2003. Study of the mechanisms involved in the crystallisation of glycine: control of particle size distribution and scaling, Ph.D. Thesis, Pierre & Marie Curie university, Paris, France.

Loï Mi Lung-Somarriba, B., Moscosa-Santillan, M., Porte, C., Delacroix, A., 2004. Effect of seeded surface area on crystal size distribution in glycine batch cooling crystallisation: A seeding methodology, J. Crys. Growth, 270, 624 – 632.

Mackay, M.E., Mackley, M.R., Wang, Y., 1991. Oscillatory flow within tubes containing wall or central baffles, Transactions of the Institutions of Chemical Engineers, Chem. Eng. Res. Des., 69A, 506 – 513.

Mackley, M., Stonestreet, P., 1995. Heat transfer and associated energy dissipation for oscillatory flow in baffled tubes, Chem. Eng. Sci. 50, 2211 – 2224.

Mackley, M., Tweddle, G.M., Wyatt, I.D., 1990. Experimental heat transfer measurements for pulsatile flow in baffled tubes, Chem. Eng. Sci. 45, 1237 – 1242.

Mackley, M.R., Ni, X., 1991. Mixing and dispersion in a baffled tube for steady laminar and pulsatile flow, Chem. Eng. Sci., 46, 3139 – 3151.

Mackley, M.R., Ni, X., 1993. Experimental fluid dispersion measurements in periodic baffled tube arrays, Chem. Eng. Sci., 48: 3293–3305.

Mahajan, A., and Kirwan, D.J., 1996. Micromixing effects in two impinging jets precipitator, AIChE J., 42, 1801-1814.

Majumder, A., Nagy, Z. K., 2013. Fines removal in a continuous plug flow crystalliser by optimal spatial temperature profiles with controlled dissolution, AIChE J., 59 (12), 4582 – 4594.

Majumder, A., Nagy, Z. K., 2015. Dynamic modeling of encrust formation and mitigation strategy in a continuous plug flow crystalliser, Cryst. Growth Des., 15(3), 1129–1140. doi: 10.1021/cg501431c.

Maleky, F., Marangoni, A., 2011. Thermal and mechanical properties of Cocoa butter crystallized under an external laminar shear field, Cryst. Growth Des., 11(6), 2429–2437. doi: 10.1021/cg200202u.

Maleky, F., Smith, A. K., Marangoni, A., 2011. Laminar shear effects on crystalline alignments and nanostructure of a triacylglycerol crystal network, Cryst. Growth Des., 11(6), 2335–2345. doi: 10.1021/cg200014w.

Manninen, M., Gorshkova, E., Immonen, K., Ni, X.-W., 2013. Evaluation of axial dispersion and mixing performance in oscillatory baffled reactors using CFD, Journal of Chemical Technology & Biotechnology, 88 (4), 553–562.

Marchal, P., David, R., Klein, J.P., Villermeux, J., 1988. Crystallisation and precipitation engineering I: An efficient method for solving population balance on crystallisation with agglomeration, Chem. Eng. Sci., 43, 59–67.

Marre, S., Jensen, K. F., 2010, Synthesis of micro and nanostructures in microfluidic systems, Chemical Society Reviews, 39(3), 1183–1202. doi: 10.1039/b821324k.

Marsh, R. E., 1958. A refinement of the crystal structure of glycine, Acta Crystallog., 11, 654 – 663.

Mascia, S., Heider, P. L., Zhang, H., Lakerveld, R., Benyahia, B., Barton, P. I., Braatz, R. D., Cooney, C. L., Evans, J. M. B., Jamison, T. F., Jensen, K. F., Myerson, A. S., Trout, B. L., 2013. End-to-end continuous manufacturing of pharmaceuticals: Integrated synthesis, purification, and final dosage formation, Angew Chem. Int. Ed., 52, 12359 – 12363.

Matero, S., Berg, F. van D., Poutiainen, S., Rantanen, J., Pajander, J., 2013, Towards better process understanding: Chemometrics and multivariate measurements in manufacturing of solid dosage forms, J. Pharm. Sci., 102 (5), 1385–1403.

Matsumoto, M., Wada, Y., Oonaka, A., Onoe, K., 2013. Polymorph control of glycine by antisolvent crystallisation using nitrogen minute-bubbles, J. Cryst. Growth, 373, 73 – 77, doi: 10.1016/j.jcrysgro.2012.11.022.

Mayra, Q. P., Kim, W. S., 2015. Agglomeration of Ni-rich hydroxide in reaction crystallisation: Effect of Taylor Vortex dimension and intensity, Cryst. Growth Des., 15(4), 1726–1734. doi: 10.1021/cg501727v.

Mazubert, A., Fletcher, D. F., Poux, M., Aubin, J., 2016. Hydrodynamics and mixing in continuous oscillatory flow reactors—Part I: Effect of baffle geometry, Chemical Engineering and Processing: Process Intensification, 108, 78–92. doi: 10.1016/j.cep.2016.07.015.

Mazzanti, G., Li, M., Marangoni, A. G., Idziak, S. H. J., 2011. Effects of shear rate variation on the nanostructure of crystallizing triglycerides, Cryst. Growth Des., 11(10), 4544–4550. doi: 10.1021/cg200786k.

McCabe, W.L., Smith, J.C., Harriott, P., 2005. *Unit operations in chemical engineering*, McGraw Hill, 7th Edition, New York.

McDonough, J.R., Phan, A.N., Harvey, A.P., 2015. Rapid process development using oscillatory baffled mesoreactors – A state-of-the-art review, Chem. Eng. J. 265, 110 – 121.

McGlone, T., Briggs, N.E.B., Clark, C.A., Brown, C.J., Sefcik, J., Florence, A.J., 2015. Oscillatory Flow Reactors (OFRs) for Continuous Manufacturing and Crystallisation. Org. Process Res. Dev., 19, 1186–1202. https://doi.org/10.1021/acs.oprd.5b00225.

McKenzie, P., Kiang, S., Tom, J., Rubin, A.E., Futran, M., Can pharmaceutical process development become high tech? AIChE J., 52, 3990-3994.

McLachlan, H., Ni, X., 2016. On the effect of added impurity on crystal purity of urea in an oscillatory baffled crystalliser and a stirred tank crystalliser, J. Cryst. Growth, 442, 81-88.

McWilliams, J. C., Allian, A.D., Opalka, S.M., May, S.A., Journet, M., Braden, T.M. The evolving state of continuous processing in pharmaceutical api manufacturing: A survey of pharmaceutical companies and contract manufacturing organizations, Org. Process Res. Dev, 22, 1143 – 1166. https://doi.org/10.1021/acs.oprd.8b00160.

Meckelenburgh, J.C., Hartland, S., 1975, *The theory of backmixing*, Wiley, London.

Mersmann, A., 2001. *Crystallisation technology handbook*, Marcel Dekker Incorporated, Garching, Germany.

Mesbah, A., Kramer, H.J.M., Huesman, A.E.M., van de Hof, P.M.J., 2009. A control oriented study on the numerical solution of the population balance equation for crystallisation process, Chem. Eng. Sci., 64, 4262 – 4277.

Middis, J., Paul, S. T., Müller-Steinhagen, H. M., 1998. Reduction of heat transfer fouling by the addition of wood pulp fibers, Heat Transfer Eng., 19, 36.

Mohd-Rasdi, F., Phan, A., Harvey, A., 2012. Rapid determination of the reaction kinetics of an n-butylbenzaldimine synthesis using a novel mesoscale oscillatory baffled reactor, Procedia Eng., 42, 1527 – 1539.

Morris, G., Power, G., Ferguson, S., Barrett, M., Hou, G., Glennon, B., 2015. Estimation of nucleation and growth kinetics of benzoic acid by population balance modelling of a continuous cooling mixed suspension, mixed product removal crystalliser, Org. Process Res. Dev., 19, 1891 – 1902.

Mosharraf, M., Nystrom, C., 1998. The effect of dry mixing on the apparent solubility of some sparingly soluble drugs, PharmSci 1:S268.

Mullin, J. W., 2001. *Crystallisation*, 4th Edition, Oxford: Butterworth-Heinemann.

Mullin, J.W., Sohnel, O., 1977. Expressions of supersaturation in crystallisation studies, Chem. Eng. Sci., 32, 683 – 686.

Mydlarz, J., Briedis, D., 1992. Growth rate dispersion vs size-dependent growth rate for MSMPR crystalliser data, Computers and Chemical Engineering, 16(9), 917–922. doi: 10.1016/0098-1354(92)80042-8.

Mydlarz, J., Jones, A.G., 1994. An assessment of MSMPR crystallisation kinetics data for systems modelled by size-dependent crystal growth rate functions, Chem. Eng. J., 55, 69-80.

Myerson, A. S., 2002. *Handbook of Industrial Crystallisation*, 2nd ed., Butterworth-Heinemann, Boston.

Nagy, Z. K., 2009. Model based robust control approach for batch crystallisation product design, Computers and Chemical Engineering, 33, 1685 – 1691.

Nagy, Z. K., Févotte, G., Kramer, H., Simon, L. L., 2013. Recent advances in the monitoring, modelling and control of crystallisation systems, Chem. Eng. Res. Des., 91 (10), 1903-1922

Nagy, Z.K., Baker, M., Pedge N., Steele, G., 2008. Supersaturation and direct nucleation control of an industrial pharmaceutical crystallisation using a crystallisation process informatics system, AstraZeneca, Charnwood, UK.

Nagy, Z.K., Fujiwara, M., Woo, X.Y., Braatz, R.D., 2008. Determination of the kinetic parameters for the crystallisation of paracetamol from water using metastable zone width experiments, Ind. Eng. Chem. Res. 47, 1245 – 1252.

Bhat, M.N., Dharmaprakash, S.M., 2002. Growth of nonlinear optical γ-glycine crystals, J. Cryst. Growth, 236, 376 – 380.

Narducci, O., Jones, A. G., Kougoulos, E., 2011. Continuous crystallisation of adipic acid with ultrasound, Chem. Eng. Sci., 66, 1069 – 1076.

Narducci, O., Jones, A. G., Kougoulos, E., 2011. Crystal product engineering in the seeded cooling crystallisation of adipic acid from aqueous solution, Org. Process Res. Dev., 15, 974 – 980.

Nauman, E., 2002. *Chemical reactor design, optimization, and scaleup*, McGraw-Hill Professional: New York, 600-605.

Nepveux, K., Sherlock, J. P., Futran, M., Thien, M., Krumme, M., 2015. How development and manufacturing will need to be structured-heads of development/manufacturing May 20-21, 2014 continuous manufacturing symposium, J. Pharm. Sci., 104(3), 850–864. doi: 10.1002/jps.24286.

Nere, N.K., Ramkrishna, D., Parker, B.E., Bell III, W.V., Mohan, P., 2007. Transformation of the chord-length distributions to size distributions for nonspherical particles with orientation bias, Ind. Eng. Chem. Res. 46, 3041–3047.

Ni, X., Gough, P., 1997. On the discussion of the dimensionless groups governing oscillatory flow in a baffled tube, Chem. Eng. Sci. 52, 3209–3212.

Ni, X., Liao, A., 2010. Effects of mixing, seeding, material of baffles and final temperature on solution crystallisation of L-glutamic acid in an oscillatory baffled crystallizer, Chem. Eng. J., 156(1), 226–233. doi: 10.1016/j.cej.2009.10.045.

Ni, X., Mackley, M. R., 1991. On the discussion of the dimensionless groups governing oscillatory flow in a baffled tube, Chem. Eng. Sci., 46 (12), 3139–3151.

Ni, X., Mackley, M. R., 1993, Chemical reaction in batch pulsatile flow and stirred tank reactors, Chem. Eng. J., 52: 107-114.

Ni, X., Brogan, G., Struthers, A., Bennett, D. C., Wilson, S. F., 1998. A systematic study of the effect of geometrical parameters on mixing time in oscillatory baffled columns, Chem. Eng. Res. Des., 76 (5), 635–642.

Ni, X., Brown, C., 2012. Evaluating crystal growth of antisolvent crystallisation of paracetamol in an oscillatory baffled crystalliser with video imaging, Paper presented at 2012 Annual Conference of the British Association for Crystal Growth, Glasgow, United Kingdom, 17/06/12 - 20/06/12.

Ni, X., Gao, S., 1996. Scale-up correlation for mass transfer coefficients in pulsed baffled reactors, Chem. Eng. J. 63 (3), 157–166.

Ni, X., Gao, S., Cumming, R.H., Pritchard, D.W., 1995. A comparative study of mass transfer in yeast for a batch pulsed baffled bioreactor and a stirred tank fermenter, Chem. Eng. Sci., 50, 13, 2127-2136.

Ni, X., Gao, S., Pritchard, D.W., 1995. A study of mass transfer in yeast in a pulse baffled bioreactor, Biotechnol. Bioeng., 45 (1995) 165–175.

Ni, X., Jian, H., Fitch, A., 2002. Computational fluid dynamic modelling of flow patterns in an oscillatory baffled column, Chem. Eng. Sci. 57, 2849 – 2862.

Ni, X., Liao, A., 2008. Effects of cooling rate and solution concentration on the solution crystallisation of L-glutamic acid in an oscillatory baffled crystalliser. Cryst. Growth Des., 8 (8), 2875 – 2881.

Ni, X., Mackley, M. R., Harvey, A. P., Stonestreet, P., Baird, M. H. I., Rao, N. V. R., 2003. Mixing through oscillations and pulsations—A guide to achieving process enhancements in the chemical and process industries. Chem. Eng. Res. Des., 81 (3), 373–383.

Ni, X., Valentine, A., Liao, A., Sermage, S. B. C., Thomson, G. B., Roberts, K. J., 2004. On the crystal polymorphic forms of L-glutamic acid following temperature programmed crystallisation in a batch oscillatory baffled crystalliser. Cryst. Growth Des., 4 (6), 1129 – 1135.

Nienow, A.W., 1997. The mixer as a reactor: Liquid/solid systems. In *Mixing in the process industries*, Nienow, A.W., Edwards, M.F., Harnby, N., Eds., 2nd ed., Butterworth-Heinemann, 349 – 411, https://doi.org/10.1016/B978-0-7506-3760-2.X5020-3.

Nienow, A.W., Edwards, M.F., Harnby, N., 1997. *Mixing in the process industries*, 2nd ed., Butterworth-Heinemann. https://doi.org/10.1016/B978-0-7506-3760-2.X5020-3.

Nii, S., Takayanagi, S., 2014. Growth and size control in anti-solvent crystallisation of glycine with high frequency ultrasound, Ultrasonics Sonochemistry, 21(3), 1182–1186. doi: 10.1016/j.ultsonch.2013.11.009.

Nývlt, J., 1968. Kinetics of nucleation in solutions, J. Cryst. Growth, 3, 377 – 383.

Nývlt, J., Söhnel, O., Matachová, M., Broul, M., 1985. *The kinetics of industrial crystallisation*, New York: Elsevier.

Broul, M., Nývlt, J., 1979. Crystallisation using recycle of mother liquor, Int. Chem. Eng., 19(3), 547–552.

O'Grady, D., Barrett, M., Casey, E., Glennon, B., 2007. The effect of mixing on the metastable zone width and nucleation kinetics in the anti-solvent crystallisation of benzoic acid, Chem. Eng. Res. Des., 85(7 A), 945–952. doi: 10.1205/cherd06207.

O'Sullivan, B., Barrett, P., Hsiao, G., Carr, A., Glennon, B., 2003. In situ monitoring of polymorphic transitions, Org. Process Res. Dev., 7(6): 977–982.

Obradovic, B., Dudukovic, A., Vunjak-Novakovic, G., 1997. Response data analysis of a three phase airlift reactor, Trans IChemE. 75, Part A, 473 – 479.

Onyemelukwe, I. I., Parsons, A. R., Wheatcroft, H. P., Robertson, A., Nagy, Z. K., Rielly, C. D., 2018. The role of residence time distribution in the continuous steady-state MSMPR crystallisation of glycine, Cryst. Growth Des., doi: 10.1021/acs.cgd.8b00853.

Onyemelukwe, I.I., Benyahia, B., Reis, N.M., Nagy, Z.K., Rielly, C.D., 2018. The heat transfer characteristics of a mesoscale continuous oscillatory flow crystallizer with smooth periodic constrictions, Int. J. Heat Mass Transfer, 123, 1109 – 1119. https://doi.org/10.1016/j.ijheatmasstransfer.2018.03.015.

Page, T., Dubina, H., Fillipi, G., Guidat, R., Patnaik, S., Poechlauer, P., Shering, P., Guinn, M., Mcdonnell, P., Johnston, C., 2015. Equipment and analytical companies meeting continuous challenges May 20-21, 2014 continuous manufacturing symposium, J. Pharm. Sci., 104(3), 821–831. doi: 10.1002/jps.24282.

Palma, M., Giudici, R., 2003. Analysis of axial dispersion in an oscillatory-flow continuous reactor, Chem. Eng. J., 94 (3), 189 – 198.

Park, K., Evans, J. M. B., Myerson, A. S., 2003. Determination of solubility of polymorphs using differential scanning calorimetry, Cryst. Growth Des., 3 (6), 991 – 995. doi: 10.1021/cg0340502.

Park, K., Kim, D. Y., Yang, D. R., 2016. Operating strategy for continuous multistage mixed suspension and mixed product removal (MSMPR) crystallisation processes depending on crystallisation kinetic parameters, Ind. Eng. Chem. Res., 55, 7142 – 7153. https://doi.org/10.1021/acs.iecr.6b01386.

Patwardhan, A. W., 2001. Prediction of residence time distribution of stirred reactors. Industrial and Engineering Chemistry Research, 40, 5686 – 5695. https://doi.org/10.1021/ie0103198.

Peña, R., Nagy, Z. K., 2015. Process intensification through continuous spherical crystallisation using a two-stage mixed suspension mixed product removal (MSMPR) system, Cryst. Growth Des., 15, 4225 – 4236.

Peña, R., Oliva, J. A., Burcham, C. L., Jarmer, D. J., Nagy, Z. K., 2017. Process intensification through continuous spherical crystallisation using an oscillatory flow baffled crystalliser, Cryst. Growth Des., 17(9), 4776–4784. doi: 10.1021/acs.cgd.7b00731.

Pereira, N. E., Ni, X., 2001. Droplet size distribution in a continuous oscillatory baffled reactor, 56, 735–739.

Perez-Calvo, J.-F., Kadam, S. S., Kramer, H. J. M., 2016. Determination of kinetics in batch cooling crystallisation processes—A sequential parameter estimation approach, AIChE J., 7, 3992–4012. doi: 10.1002/aic.

Perry, R.H., 1997. *Perry's chemical engineer's handbook*, 2nd ed. New York: McGraw Hill.

Phan, A. N., Harvey, A. P., Eze, V., 2012. Rapid production of biodiesel in mesoscale oscillatory baffled reactors, Chem. Eng. Tech., 35(7), 1214–1220. doi: 10.1002/ceat.201200031.

Phan, A. N., Harvey, A. P., 2010. Development and evaluation of novel designs of continuous mesoscale oscillatory baffled reactors, Chem. Eng. J., 159, 212 – 219.

Phan, A. N., Harvey, A. P., Lavender, J., 2011. Characterisation of fluid mixing in novel designs of mesoscale oscillatory baffled reactors operating at low flow rates (0.3 – 0.6 ml/min), Chem. Eng. Proc., 50, 245 – 263.

Phan, A., Harvey, A., 2012. Characterisation of mesoscale oscillatory helical baffled reactor – experimental approach, Chem. Eng. J., 180, 229 – 236.

Phan, A., Harvey, A., 2013. Flow reactors for multiphase reactions: From meso-scale to conventional scale, in: 9th European Congress of Chemical Engineering, The Hague, Netherlands.

Phan, A., Harvey, A., Rawcliffe, M., 2011. Continuous screening of base-catalysed biodiesel production using new designs of mesoscale oscillatory baffled reactor, Fuel Process. Technol. 92, 1560 – 1567.

Plumb, K., 2005. Continuous processing in the pharmaceutical industry: Changing the mindset, Chem. Eng. Res. Des., 83(6 A), 730–738. doi: 10.1205/cherd.04359.

Poechlauer, P., Manley, J., Broxterman, R., Gregertsen, B., Ridemark, M., 2012. Continuous processing in the manufacture of active pharmaceutical ingredients and finished dosage forms: An industry perspective, Org. Process Res. Dev., 16 (10), 1586–1590.

Porru, M., Özkan, L., 2018. Control of a two-stage mixed suspension mixed product removal crystallizer, IFAC PapersOnLine, 51-18, 898 – 903. https://doi.org/10.1016/j/ifacol.2018.09.231.

Powell, K. A., Saleemi, A. N., Rielly, C. D., Nagy, Z. K., 2015. Periodic steady-state flow crystallisation of a pharmaceutical drug using MSMPR operation, Chemical Engineering and Processing, 97, 195 – 212.

Powell, K.A., Saleemi, A. N., Nagy, Z. K., Rielly, C. D., 2016. Continuous crystallisation of paracetamol in the presence of an additive using an integrated PAT array and multivariate methods, Org. Process Res. Dev., 20 (3), 626–636.

Power, G., Hou, G., Kamaraju, V. K., Morris, G., Zhao, Y., Glennon, B., 2015. Design and optimisation of a multi-stage continuous cooling mixed suspension, mixed product removal crystalliser, Chem. Eng. Sci., 133: 125 – 39.

Qu, H., Kohonen, J., Louhi-Kultanen, M., Reinikainen, S.P., Kallas, J., 2008. Spectroscopic monitoring of carbamazepine crystallisation and phase transformation in ethanol–water solution, Industrial and Engineering Chemistry Research 47, 6991–6998.

Quon, J. L., Zhang, H., Alvarez, A., Evans, J., Myerson, A. S., Trout, B. L., 2012. Continuous crystallisation of aliskiren hemifumarate, Cryst. Growth Des., 12 (6), 3036–3044.

Marsh, R.E., 1958. A refinement of the crystal structure of glycine, Journal of Acta Crystallographica, 11, 654.

Rabesiaka, M., Sghaier, M., Fraisse, B., Porte, C., Havet, J. L., Dichi, E., 2010. Preparation of glycine polymorphs crystallized in water and physicochemical characterizations, J. Cryst. Growth, Elsevier, 312(11), 1860–1865. doi: 10.1016/j.jcrysgro.2010.03.011.

Rajalahti, T., Kvalheim, O. M., 2011. Multivariate data analysis in pharmaceutics: A tutorial review, Int. J. Pharm. 2011, 417, 280.

Randolph, A., Larson, M., 1971. *Theory of particulate processes: analysis and techniques of continuous crystallisation*, Academic Press: New York, https://doi.org/10.1016/B978-0-12-579650-7.X5001-5.

Randolph, A.D., Deepak, C., Iskander, M. 1968. On the narrowing of particle-size distributions in staged vessels with classified product removal, AIChE J., 14, 827 – 830. https://doi.org/10.1002/aic.690140532.

Rasenack, N., Muller, B., 2002. Crystal habit and tableting behaviour, Int. J. Pharm., 244, 45– 57.

Reay, D., Ramshaw, C., Harvey, A., 2008. Process intensification: Engineering for efficiency, sustainability and flexibility, Amsterdam: Butterworth-Heinemann.

Reis, N., Goncalves, C., Vicente, A., Teixeira, J., 2006. Proof-of-concept of a novel micro-bioreactor for fast development of industrial bioprocesses, Biotechnol. Bioeng. 95, 744–753.

Reis, N., Goncalves, C., Aguedo, M., Gomes, N., Teixeira, J., Vicente, A., 2006. Application of a novel oscillatory flow micro-bioreactor to the production of γ-decalactone in a two-immiscible liquid phase medium, Biotechnol. Lett., 28, 485– 490.

Reis, N., Goncalves, C., Vicente, A., Teixeira, J., 2006. Proof-of-concept of a novel microbioreactor for fast development of industrial bioprocesses, Biotechnol. Bioeng., 95, 744–753.

Reis, N., Harvey, A., Mackley, M., Vicente, A., Teixeira, J., 2005. Fluid mechanics and design aspects of a novel oscillatory flow screening mesoreactor, Trans. IChemE, 83, 357 – 371.

Reis, N., Mena, P., Vicente, A., Teixeira, J., Rocha, F., 2007. The intensification of gas-liquid flows with a periodic, constricted oscillatory meso-tube, Chem. Eng. Sci., 62, 7454 – 7462.

Reis, N., Pereira, R., Vicente, A., Teixeira, J., 2008. Enhanced gas-liquid mass transfer of an oscillatory constricted-tubular reactor, Ind. Eng. Chem. Res., 47, 7190 – 7201.

Reis, N., Vicente, A. A., Teixeira, J. A., 2010. Liquid backmixing in oscillatory flow through a periodically constricted meso-tube, Chem. Eng., Processing, 49, 793 – 803.

Reis, N., Vicente, A.A., Teixeira, J.A., Mackley, M.R., 2004. Residence times and mixing of a novel continuous oscillatory flow screening reactor, Chem. Eng. Sci. 59, 4967 – 4974.

Ricardo, C., Xiongwei, N., 2009. Evaluation and establishment of a cleaning protocol for the production of vanisal sodium and aspirin using a continuous oscillatory baffled reactor, Org. Proc. Res. Dev., 13(6), 1080–1087. doi: 10.1021/op900120h.

Ridder, B.J., Majumder, A., Nagy, Z.K., 2014. Population balance model-based multiobjective optimisation of a multisegment multiaddition (MSMA) continuous plug-flow antisolvent crystalliser, Ind. Eng. Chem. Res., 53(1), 4387 – 4397.

Rieger, F., and Difl, P., 1982. Suspension of solid particles in agitated vessels, In Proceedings of the 4th European Conference on Mixing, BHRA Fluid Engineering, Cranfield, UK.

Rielly, C. D., Habib, M., Sherlock, J. P., 2007. Flow and mixing characteristics of a retreat curve impeller in a conical-based vessel, Chem. Eng. Res. Des., 85, 953 – 962. https://doi.org/10.1205/cherd07002.

Rielly, C. D., Marquis, A. J., 2001. A particle's eye view of crystalliser fluid mechanics, Chem. Eng. Sci., 56(7), 2475–2493. doi: 10.1016/S0009-2509(00)00457-7.

Rielly, C.D., 2013. Fluid dynamics in batch and continuous crystallisation, Doctoral Training Centre in Continuous Manufacturing and Crystallisation.

Ristić, R. I., 2007. Oscillatory mixing for crystallisation of high crystal perfection pharmaceuticals, Chem. Eng. Res. Des., 85 (7), 937–944.

Ristić, R. I., Sherwood, J. N., Wojciechowski, K., 1988. Assessment of the strain in small sodium chlorate crystals and its relation to growth rate dispersion, J. Cryst. Growth, 91, 163 – 168.

Roberge, D. M., Ducry, L., Bieler, N., Cretton, P., Zimmermann, B., 2005. Microreactor technology: A revolution for the fine chemical and pharmaceutical industries, Chem. Eng. Tech., 28 (3), 318–323.

Rossi, D., Jamshidi, R., Saffari, N., Kuhn, S., Gavriilidis, A., Mazzei, L., 2015. Continuous-flow sonocrystallisation in droplet-based microfluidics, Cryst. Growth Des., 15(11), 5519–5529. doi: 10.1021/acs.cgd.5b01153.

Rougeot, C., Hein, J. E., 2015. Application of continuous preferential crystallisation to efficiently access enantiopure chemicals, Org. Proc. Res. Dev., 19(12), 1809–1819. doi: 10.1021/acs.oprd.5b00141.

Saleemi, A. N., Rielly, C. D., Nagy, Z. K., 2012. Comparative investigation of supersaturation and automated direct nucleation control of crystal size distributions using ATR-UV/Vis spectroscopy and FBRM, Cryst. Growth Des., 12, ACS Publications, 1792–1807.

Saleemi, A., Onyemelukwe, I. I., Nagy, Z., 2013. Effects of a structurally related substance on the crystallisation of paracetamol, Frontiers of Chemical Science and Engineering, 7(1). doi: 10.1007/s11705-013-1308-7.

Saleemi, A.S., 2011. Strategic feedback control of pharmaceutical crystallisation systems, PhD Thesis.

Sang-Il Kwon, J., Nayhouse, M., Orkoulas, G., Christofides, P. D., 2014. Crystal shape and size control using a plug flow crystallisation configuration, Chem. Eng. Sci., 119, 30–39. doi: 10.1016/j.ces.2014.07.058.

Sangwal, K., 2009. A novel self-consistent Nyvlt-like equation for metastable zone width determined by the polythermal method, Cryst. Res. Tech., 44(3), 231 – 247. doi: 10.1002/crat.200800501

Sangwal, K., 2009. Effect of impurities on the metastable zone width of solute-solvent systems, J. Cryst. Growth, 311, 4050–4061.

Sayan, P., Sargut, S.T., Kiran, B., 2011. Effect of ultrasonic irradiation on crystallisation kinetics of potassium dihydrogen phosphate, Ultrason. Sonochem., 18, 795 – 800.

Schaber, S. D., Gerogiorgis, D. I., Ramachandran, R., Evans, J. M. B., Barton, P. I., Trout, B. L., 2011. Economic analysis of integrated continuous and batch pharmaceutical manufacturing: A case study, Industrial and Engineering Chemistry Research, 50(17), 10083–10092. doi: 10.1021/ie2006752.

Schiewe, J. & Zierenberg, B., 2003. Process and apparatus for producing inhalable medicaments, US patent application 10/125,044. 2003.

Schmidt, B., Patel, J., Ricard, F. X., Brechtelsbauer, C. M., Lewis, N., 2004. Application of process modelling tools in the scale-up of pharmaceutical crystallisation processes, Org. Proc. Res. Dev., 8(6), 998–1008. doi: 10.1021/op040013n.

Schwartz, A., Myerson, A., 2001. Solutions and solution properties, In: A. Myerson, ed., *Handbook of industrial crystallisation*, 2nd ed. New York: Elsevier Science and Technology Books, 1-31.

Sermage, S., 2002. Crystallisation of L-glutamic acid in an oscillatory baffled crystalliser, M. Philos. Thesis, Heriot-Watt University, Edinburgh, UK.

Shah, N., 2004. Pharmaceutical supply chains: Key issues and strategies for optimisation, Computers & Chemical Engineering, 28 (6-7), 929–941.

Shamlou, P.A., and Koutsakos, E., 1989. Solids suspension and distribution in liquids under turbulent agitation, Chem. Eng. Sci., 44(3), 529-542.

Shankland, N., Florence, A.J., Cox, P.J., Sheen, D.B., Love, S.W., Stewart, N.S., Wilson, C.C., 1996. Crystal morphology of ibuprofen predicted from single-crystal pulsed neutron diffraction data, Chem. Commun., 855–856.

Shiau, L. D., Berglund, K. A., 1987. Growth kinetics of fructose crystals formed by contact nucleation, Ind. Eng. Chem. Res., 26, 2515–2521.

Siddique, H., Brown, C. J., Houson, I., Florence, A. J., 2015. Establishment of a continuous sonocrystallisation process for lactose in an oscillatory baffled crystalliser, Org. Process Res. Dev., 19, 1871 – 1881.

Sieder, E.N., Tate, G.E., 1936. Heat transfer and pressure drop of liquids in tubes, Ind. Eng. Chem. 28 (12), 1429 – 1435.

Siemens, 2013. Continuous manufacturing, http://www.industry.siemens.com/verticals/global/en/pharma-industries/continuous-manufacturing/pages/continuous-production-becomes-reality.aspx (accessed, July 30, 2018).

Simakin, A., Bindeman, I., 2008. Evolution of crystal sizes in the series of dissolution and precipitation events in open magma systems, Journal of Volcanology and Geothermal Research, 177(4), 997 – 1010.

Simon, L. L., Pataki, H., Marosi, G., Meemken, F., Hungerbühler, K., Baiker, A., Tummala, S., Glennon, B., Kuentz, M., Steele, G., Kramer, H. J. M., Rydzak, J. W., Chen, Z., Morris, J., Kjell, F., Singh, R., Gani, R., Gernaey, K. V., Louhi-Kultanen, M., Oreilly, J., Sandler, N., Antikainen, O., Yliruusi, J., Frohberg, P., Ulrich, J., Braatz, R. D., Leyssens, T., Von Stosch, M., Oliveira, R., Tan, R. B. H., Wu, H., Khan, M., Ogrady, D., Pandey, A., Westra, R., Delle-Case, E., Pape, D., Angelosante, D., Maret, Y., Steiger, O., Lenner, M., Abbou-Oucherif, K., Nagy, Z. K., Litster, J. D., Kamaraju, V. K., Chiu, M. 2015. Assessment of recent process analytical technology (PAT) trends: A multiauthor review, Org. Proc. Res. Dev., doi: 10.1021/op500261y.

Simone, E., Saleemi, A. N., Nagy, Z. K., 2014. Application of quantitative Raman spectroscopy for the monitoring of polymorphic transformation in crystallisation processes using a good calibration practice procedure, Chem. Eng. Res. Des., Institution of Chemical Engineers, 92(4), 594–611. doi: 10.1016/j.cherd.2013.11.004.

Smith, G.W., Tavlarides, L.L., Placek, J., 1990. Turbulent flow in stirred tanks: Scale-up computations for vessel hydrodynamics, Chem. Eng. Commun. 93, 49–73.

Smith, K. B., Mackley, M. R., 2006. An experimental investigation into the scale-up of oscillatory flow mixing in baffled tubes, Chem. Eng. Res. Des., 84(A11), 1001–1011. doi: 10.1205/cherd.05054.

Smith, K.B., 1999. The scale-up of oscillatory flow mixing, PhD thesis, University of Cambridge.

Smith, R., 2005. *Chemical process design and integration*, John Wiley and Sons limited, West Sussex, UK.

Smoluchowski, M.V., 1916. Versuch einer mathematischen Theorieder Koagulationskinetik kolloider Losungen, Zeitschrift f. physik.Chemie. 92, 129-168.

Snider, D. A., Addicks, W., Owens, W., 2003. Polymorphism in generic drug product development, Advanced Drug Delivery Reviews, 56, 391–395.

Soare, A., Pérez Escobar, S. A., Stankiewicz, A. I., Rodriguez Pascual, M., Kramer, H. J. M., 2013. 2-D flow and temperature measurements in a multiphase airlift crystallizer, Industrial and Engineering Chemistry Research, 52(34), 12212–12222. doi: 10.1021/ie4006723.

Sobey, I., 1980. On flow through furrowed channels. Part 1. Calculate flow patterns, J. Fluid Mech. 96, 1 – 26.

Sohnel, O., Nývlt, J., 1975. Evaluation of experimental data on width of metastable region in aqueous solutions, Collection of Czechoslavak Chemical Communications, 40, 511.

Solano, J.P., Herrero, R., Espín, S., Phan, A.N., Harvey, A.P., 2012. Numerical study of the flow pattern and heat transfer enhancement in oscillatory baffled reactors with helical coil inserts, Chem. Eng. Res. Des., 90, 732 – 742.

Srai, J. S., Badman, C., Krumme, M., Futran, M., Johnston, C., 2015. Future supply chains enabled by continuous processing opportunities and challenges May 20-21, 2014 continuous manufacturing symposium, J. Pharm. Sci., 104(3), 840–849. doi: 10.1002/jps.24343.

Srinivasan, K., 2008. Crystal growth of α and γ glycine polymorphs and their polymorphic phase transformations, J. Cryst. Growth. 311, 156 – 162. doi: 10.1016/j.jcrysgro.2008.10.084.

Srinivasan, K., Arumugam, J., 2007. Growth of non-linear γ-glycine single crystals and their characterization, J. Opt. Mater, 30, 40 – 43.

Steendam, R. R. E., Keshavarz, L., Blijlevens, M. A. R., De Souza, B., Croker, D. M., Frawley, P. J., 2018. Effects of scale-up on the mechanism and kinetics of crystal nucleation, Cryst. Growth Des., 18(9), 5547–5555. doi: 10.1021/acs.cgd.8b00857.

Stephanoff, K., Sobey, I., Bellhouse, B., 1980. On flow through furrowed channels. Part 2. Observed flow patterns, J. Fluid Mech. 96, 27 – 32.

Stephens, G.G., Mackley, M.R., 2002. Heat transfer performance for batch oscillatory flow mixing, Exp. Therm. Fluid Sci., 25, 583 – 594.

Stonestreet, P., van der Veeken, P.M.J., 1999. The effects of oscillatory flow and bulk flow components on the residence time distribution in baffled tube reactors. Trans IChemE, Part A, Chem. Eng., Res. Des., 77, 671 – 684.

Su, Q., Benyahia, B., Nagy, Z. K., Rielly, C. D., 2015. Mathematical modelling, design, and optimisation of a multi-segment multi-addition plug flow crystalliser for antisolvent crystallisations, Org. Process Res. Dev., 19, 1859 – 1870.

Su, Q., Rielly, C.D., Powell, K.A., Nagy, Z.K., 2017. Mathematical modelling and experimental validation of a novel periodic flow crystallisation using MSMPR crystallizers, AIChE J., 63, 1313 – 1327. https://doi.org/10.1002/aic.15510.

Sun, M., Tang, W., Du, S., Zhang, Y., Fu, X., Gong, J., 2018. Understanding the roles of oiling-out on crystallisation of β-alanine: unusual behavior in metastable zone width and surface nucleation during growth stage, Cryst. Growth Des., 18(11), 6885–6890. doi: 10.1021/acs.cgd.8b01096.

Sun, Y. Z., Song, X. F., Jin, M. M., Jin, W., Yu, J. G., 2013. Gas-liquid reactive crystallisation of lithium carbonate by a falling film column, Industrial and Engineering Chemistry Research, 52(49), 17598–17606. doi: 10.1021/ie402698v.

Takiyama, H., Matsuoka, M., 2001. Design of seed crystal specifications for start-up operation of a continuous MSMPR crystallizer, Powder Tech., 121(1), 99–105. doi: 10.1016/S0032-5910(01)00381-3.

Tavare, N., Garside, J., Larson, M., 1986. Crystal size distribution from a cascade of MSMPR crystallizers with magma recycle, Chem. Eng. Commun., 47, 185 – 199. https://doi.org/10.1080/00986448608911763.

Taylor, G.I., 1954. The dispersion of matter in turbulent flow through a pipe, Proc. Roy. Soc., 225A, 446 – 468.

Ter Horst, J. H., Bedeaux, D., Kjelstrup, S., 2011. The role of temperature in nucleation processes, Journal of Chemical Physics, 134(5). doi: 10.1063/1.3544689.

Thoenes, D., 1994. Chemical reactor development: From laboratory synthesis to industrial production, Springer, 347–354.

Tung, H. H., Paul, E. L., 2009. *Crystallisation of organic compounds: An industrial perspective*, 1st ed., John Wiley & Sons, New Jersey.

US Food and Drug Administration, 2004. Guidance for industry PAT – A framework for innovative pharmaceutical development, manufacturing, and quality assurance; FDA: Rockville, MD, 16.

US Food and Drug Administration, 2004. Pharmaceutical cGMPs for the 21st century−A risk-based approach, Final Report, http://www.fda.gov/downloads/ Drugs/DevelopmentApprovalProcess/Manufacturing/ QuestionsandAnswersonCurrentGoodManufacturingPracticescGMPforDrugs/UCM176374.pdf (accessed Dec 15, 2018).

US Food and Drug Administration, 2007. Guidance for industry ANDA: Pharmaceutical solid polymorphism – Chemistry, manufacturing, and controls information; FDA: Rockville, MD.

Van Dijck, W., 1934. Process and apparatus for intimately contacting fluids, US Patent 2,011,186.

Vankeirsbilck, T., Vercauteren, A., Baeyens, W., Van der Weken, G., Verpoort, F., Vergote, G., Remon, J.P., 2002. Applications of Raman spectroscopy in pharmaceutical analysis, Trac trends in analytical chemistry, 21 (12), 869–877.

Variankaval, N., Cote, A.S., Doherty, M.F., 2008. From form to function: Crystallisation of active pharmaceutical ingredients, AIChE J., 54, 1682–1688.

Verlaan, P., Van Eijs, A.M.M., Tramper, J., Van't Riet K., Luyban, K., 1989. Estimation of axial dispersion in individual sections of an airlift-loop reactor, Chem. Eng. Sci., 44, 1139 – 1146.

Vetter, T., Burcham, C. L., Doherty, M. F., 2015. Designing robust crystallisation processes in the presence of parameter uncertainty using attainable regions. Ind. Eng. Chem. Res., 54, 10350 – 10363. https://doi.org/10.1021/acs.iecr.5b00693.

Vetter, T., Burcham, C.L., Doherty, M.F., 2014. Regions of attainable particle sizes in continuous and batch crystallisation processes, Chem. Eng. Sci., 106, 167 – 180.

Volmer, M., 1939. *Kinetic der Phasenbildung*, T. Steinkopff, Leipzig.

Wadnerkar, D., Utikar, R.P., Tade, M.O., Pareek, V.K., 2012. CFD simulation of solid-liquid stirred tanks, Adv. Powder Tech., 23, 445 – 453. https://doi.org/10.1016/j.apt.2012.03.007.

Walter, E., Pronzato, L., 1994. *Identification of parametric models from experimental data*, Berlin: Springer.

Wang, J., Li, F., Lakerveld, R., 2018. Process intensification for pharmaceutical crystallisation, Chemical Engineering and Processing - Process Intensification, 127, 111–126. doi: 10.1016/j.cep.2018.03.018.

Wang, T., Lu, H., Wang, J., Xiao, Y., Zhou, Y., Bao, Y., Hao, H., 2017. Recent progress of continuous crystallisation, Journal of Industrial and Engineering Chemistry, The Korean Society of Industrial and Engineering Chemistry, 54, 14–29. doi: 10.1016/j.jiec.2017.06.009.

Wei, H.Y., and Garside, J., 1997. Application of CFD modeling to precipitation systems, TransIChemE., 75(A), 217-227.

Westhoff G, Kramer H, Jansens P, Grievink J., 2004. Design of a multi- functional crystallizer for research purposes, Chem. Eng. Res. Des., 82(7), 865–80. https://doi.org/10.1205/0263876041596670.

Wibowo, C., Chang, W.-C., Ng, K.M., 2001. Design of integrated crystallisation systems, AIChE J., 47(11), 2474 – 2492.

Wilkes, J.O., 2006. *Fluid mechanics for chemical engineers*, 2nd ed., Prentice Hall, Massachusetts.

Wong, S. Y., Tatusko, A. P., Trout, B. L., Myerson, A. S., 2012. Development of continuous crystallisation processes using a single-stage mixed suspension mixed product removal crystalliser with recycle, Cryst. Growth Des., 12 (11), 5701–5707.

Woo, X.Y., Nagy, Z.K., Tan, R.B.H., Braatz, R.D., 2009. Adaptive concentration control of cooling and antisolvent crystallisation with laser backscattering measurement, Cryst. Growth Des., 9(1), 182 – 191.

Xie, L., Rielly, C.D., Eagles, W., Özcan-Tas kin, G., 2007. Dispersion of nano-particle clusters using mixed flow and high shear impellers in stirred tanks, Chem. Eng. Res. Des., 85 (A5), 676–684.

Yang, X., Acevedo, D., Mohammad, A., Pavurala, N., Wu, H., Brayton, A. L., Shaw, R. A., Goldman, M. J., He, F., Li, S., Fisher, R. J., O'Connor, T. F., Cruz, C. N., 2017. Risk considerations on developing a continuous crystallisation system for carbamazepine, Org. Proc. Res. Dev., 21(7), 1021–1033. doi: 10.1021/acs.oprd.7b00130.

Yang, Y., Nagy, Z.K., 2014. Model-based systematic design and analysis approach for unseeded combined cooling and antisolvent crystallisation (CCAC) systems, Cryst. Growth Des., 14, 687 – 698. https://doi.org/10.1021/cg401562t.

Yang, Y., Nagy, Z. K., 2015. Advanced control approaches for combined cooling/antisolvent crystallisation in continuous mixed suspension mixed product removal cascade crystallisers, Chem. Eng. Sci., 127, 362 – 373

Yang, Y., Song, L., Nagy, Z. K., 2015. Automated direct nucleation control in continuous mixed suspension mixed product removal cooling crystallisation, Cryst. Growth Des., 15(12), 5839–5848. doi: 10.1021/acs.cgd.5b01219.

Yang, Y., Song, L., Gao, T., Nagy, Z. K., 2015. Integrated upstream and downstream application of wet milling with continuous mixed suspension mixed product removal crystallisation, Cryst. Growth Des., 15 (12): 5879 – 85.

Yang, Y., Song, L., Zhang, Y., Nagy, Z. K., 2016. Application of wet milling-based automated direct nucleation control in continuous cooling crystallisation processes, Industrial and Engineering Chemistry Research, 55(17), 4987–4996. doi: 10.1021/acs.iecr.5b04956.

Yao, K.Z., Shaw, B.M., Kou, B., McAuley, K.B., Bacon, D.W., 2003. Modeling ethylene/butene copolymerization with multi-site catalysts: Parameter estimability and experimental design, Poly. React. Eng., 11, 563 – 588.

Yasuda, T., Okuno, T., Yasuda, H., 1994. Contact angle of water on polymer surfaces, Langmuir 10, 2435–2439.

Yazdanpanah, N., Langrish, T. A. G., 2011. Crystallisation and drying of milk powder in a multiple-stage fluidized bed dryer, Drying Technology, 29(9), 1046–1057. doi: 10.1080/07373937.2011.561461.

Yuan, Y., Lee, T.R., 2013. Contact angle and wetting properties, Springer Ser. Surf. Sci., 51, 3–34.

Zaccaro, J., Matic, J., Myerson, A. S., Garetz, B. A., 2001. Nonphotochemical, laser-induced nucleation of supersaturated aqueous glycine produces unexpected γ-polymorph, Cryst. Growth Des., 1 (1), 5 – 8.

Zarkadas Dimitrios M., Sirkar Kamalesh K., 2006. Cooling crystallisation of paracetamol in hollow fiber devices, Ind. Eng. Chem. Res., 46, 10, 2928-2935.

Zettler, H. U., Wei, M., Zhao, Q., 2005. Müller-Steinhagen, H. Heat Transfer Eng., 26,3.

Zhang, D., Xu, S., Du, S., Wang, J., Gong, J., 2017. Progress of pharmaceutical continuous crystallisation, Engineering, 3, 354 – 364.

Zhang, H. L., Han, S. J., 1996. Viscosity and density of water+sodium chloride+potassium chloride solutions at 298.15 K, Journal of Chemical and Engineering Data, 41(3), 516–520. doi: 10.1021/je9501402.

Zhang, H., Lakerveld, R., Heider, P. L., Tao, M., Su, M., Testa, C. J., Dantonio, A. N., Barton, P. I., Braatz, R. D., Trout, B. L., Myerson, A. S., Jensen, K. F., Evans, J. M. B., 2014. Application of continuous crystallisation in an integrated continuous pharmaceutical pilot plant, Cryst. Growth Des., 14(5), 2148–2157. doi: 10.1021/cg401571h.

Zhang, H., Quon, J., Alvarez, A. J., Evans, J., Myerson, A. S., Trout, B., 2012. Development of continuous anti-solvent/cooling crystallisation process using cascaded mixed suspension, mixed product removal crystallisers, Org. Process Res. Dev., 16 (5), 915–924.

Zhao, L., Raval, V., Briggs, N. E. B., Bhardwaj, R. M., McGlone, T., Oswald, I. D. H., Florence, A. J., 2014. From discovery to scale-up: α-lipoic acid: nicotinamide co-crystals in a continuous oscillatory baffled crystalliser, Cryst. Eng. Comm., 16, 5743 – 5934.

Zheng, M., Mackley, M., 2008. The axial dispersion performance of an oscillatory flow meso-reactor with relevance to continuous flow operation, Chem. Eng. Sci., 63, 1788 – 1799.

Zheng, M., Skelton, R. L., Mackley, M. R., 2007. Biodiesel reaction screening using oscillatory flow meso reactors, Journal of Process Safety and Environmental Protection, 85, 365 – 371.

Zhu, G., Zhu, X., Fan, Q., Wan, X., 2011. Raman spectra of amino acids and their aqueous solutions, Spectrochimica Acta - Part A: Molecular and Biomolecular Spectroscopy, 78(3), 1187–1195. doi: 10.1016/j.saa.2010.12.079.

Zwietering, T. N., 1958. Suspending of solid particles in liquid by agitators, Chem. Eng. Sci., 8, 244 – 253.

Appendix A

A-1 MATLAB® script for image analysis and calculation of axial dispersion coefficient

```
close all
clear all
clc

%import CamA images from windows folder. Read image 1.jpg through m.jpg
sequentially. Files are in the "myFolder" directory.
 myFolder1 = 'C:\' %specify folder 1 path on local drive
 myFolder2 = 'C:\' %specify folder 2 path on local drive
 n = m;            %m is the number digit of last file

%create time stamp for images
 t_int = 1.12;                %specify interval for image capture (s)
 t = 0:t_int:t_int*(n-1);     %time stamp for all images
 t = t';                      %transpose vector dimensions

%create zero vector to receive output from for-loop
 intA = zeros(n);
 intB = zeros(n);

 for k = 1:n
   jpgFilename1 = sprintf('CamA%d.jpg',k);
   fullFileName1 = fullfile(myFolder1,jpgFilename1);
   imgarray1 = imread(fullFileName1);
   Icrop1 = imcrop(imgarray1,[75,200,250,110]);  %crop to ROI
   gmap1 = rgb2gray(Icrop1);   %convert to grayscale

   figure(1) %show CamA images
   imshow(gmap1)

   jpgFilename2 = sprintf('CamB%d.jpg', k);
   fullFileName2 = fullfile(myFolder2, jpgFilename2);
   imgarray2 = imread(fullFileName2);
   Icrop2 = imcrop(imgarray2,[150,165,230,110]); %crop to ROI
   gmap2 = rgb2gray(Icrop2);   %convert to grayscale
   %gmap2 = rgb2gray(imgarray2);

   figure(2) %show CamB images
   imshow(gmap2)

   %calculate mean gray level (average intensity of grayscale image)
   meangraylevel1 = mean(mean(gmap1));
   intA(k) = meangraylevel1;

   meangraylevel2 = mean(mean(gmap2));
   intB(k) = meangraylevel2;

 end


%generate and plot absorbance-time curve
 Max_intA = max(intA(:,1))
 p1 = -log(intA(:,1)./Max_intA);
```

```
 Max_intB = max(intB(:,1));
 p2 = -log(intB(:,1)./Max_intB);

 figure(3)
 clf;
 h1 = plot(t,p1,'b-');
 hold on
 h2 = plot(t,p2,'r-');
 xlabel ('Time (s)','fontsize',16,'fontweight','bold');
 ylabel ('Absorbance','fontsize',16,'fontweight','bold');
 set(gca,'fontSize',16,'fontweight','bold');
 set([h1,h2],'linewidth',2);

%RTD experiment parameters
 ni = 10;                % First ni points
 nf = 10;                % Last nf points
 expt = 2;               % 1 for step input and 2 for pulse input

 ID  = 5/1000;           %tube diameter (m)
 nL = 3;                 %multiplier for test section
 q = 2/1000000/60;       %volumetric flowrate (m3/s)
 L = 897.4*nL/1000;      %length of test section (m)
 rho = 998.17;           %density of bulk fluid (kg/m3)
 m = q*rho;              %mass flow rate (kg/s)
 CSA = (pi*ID^2)/4;      %tube cross-sectional area (m2)

%normalise and plot absorbance data
 pn1 = normalise(t,p1,expt,ni,nf);
 pn2 = normalise(t,p2,expt,ni,nf);

 figure(4)
 clf;
 h1 = plot(t,pn1,'b-');
 hold on
 h2 = plot(t,pn2,'r-');
 xlabel('Time (s)','fontsize',16,'fontweight','bold');
 ylabel('Dimensionless conc.','fontsize',16,'fontweight','bold');
 ylim([0 max(pn1)+0.0005]);
 set(gca,'fontSize', 16,'fontweight','bold');
 set([h1,h2],'linewidth',2);

%calculate mean residence time
 t1 = trapz(t,t.*pn1);
 t2 = trapz(t,t.*pn2);

%calculate variance and DUL
 var1 = trapz(t,(t-t1).^2.*pn1);
 var2 = trapz(t,(t-t2).^2.*pn2);
 DUL = (var2-var1)/(t2-t1)^2/2;

%calculate cross-correlation function between input and output
 figure(5)
 [r,lags]=xcorr(p2,p1,'coeff');
 plot(lags,r);
 grid on
 time_delay = lags(find(r>=max(r)))
 xlabel ('Delay Time/s');
 ylabel ('Cross-correlation function');

 tau = t2-t1;   %experimental mean residence time
```

```
 %x0= [x];   %could use as initial guess
 x0 = [DUL,tau];   %experimental DUL and tau as initial guess
 f = @(x)objfun(x,t,pn1,pn2);
 options     =     optimset('GradObj','off','TolCon',1e-20,'TolFun',1e-
 20,'TolX',1e-20,'Display','iter','MaxIter',200,'Diagnostics','on');
 [x, fval] = fminunc(f,x0,options);  %fitting for optimised DUL, tau

%display results of fitting
 disp('fval: ')
 disp(fval);
 disp('Optimised DUL, tau: ')
 disp(x);
 disp('Time Delay (Seconds): ')
 disp(time_delay)

%Fourier convolution to obtain model response (predicted output)
 response = model(t,x(1),x(2));
 l = length(t);
 NFFT = 2^nextpow2(l); %Next power of 2 from length of t

 f1 = fft(pn1,NFFT);     %fast fourier transform
 f2 = fft(response,NFFT);
 pn2pred = ifft(f1.*f2); %inverse fast fourier transform

 figure(6)
 clf
 plot(t,response)

 figure(4)
 h3 = plot(t,pn2pred(1:length(t)),'-g');
 ylim ([0 max(pn1)+0.0005]);
 legend('Input','Output','Predicted Response');
 legend('boxoff')
 set([h3],'linewidth',2);
 pbaspect([1.3 1 1]);

%calculate axial dispersion coefficient
 u = L/tau;  %superficial velocity (m/s)
 D = u*L*x(1);

 disp(Superficial velocity: ')
 disp(u)
 disp('Optimised Dispersion coefficient: ')
 disp(D)

%calculate number of tanks-in-series, N
 N = 1/(2*x(1))+1;
 disp('Number of tanks in series, N: ')
 disp(N)
```

A-2 MATLAB® function for the calculation of the outside heat transfer area of the inner tube

```
function Main

 clc
 clear all

 Lconstr = 0:0.1:4;      %constriction surface length (mm);
 Lstra = 9;              %straight surface length (mm)
 LRconstr = (-0.28.*Lconstr.^2+1.12*Lconstr);    %lower radius (mm)
 URconstr = 7+(0.28.*Lconstr.^2-1.12*Lconstr);   %upper radius (mm)

 D = URconstr-LRconstr;  %diameter for the constriction (mm)

 figure(1)
 plot(Lconstr, LRconstr)
 hold on
 plot(Lconstr, URconstr)
 hold on
 xlabel('Constriction length (mm)')
 ylabel('Outer radius (mm)')

 Aconstr = pi*trapz(D,Lconstr)*1e-6; %constr surface area, Ac (m2)
 disp(Aconstr)
 Astra = pi*7*Lstra*1e-6;      %Straight surface area, As (m2)
 disp(Astra)
 TotalS=51*(Aconstr+Astra);    %outside heat transfer area, A (m2)

 fprintf('\t Total surface area: %8.5f m2 \n', TotalS)

return
```

A-3 MATLAB® script for PLS calibration model

```
clc;
clear;
load StepwiseVariables20 in1   %Stepwise regressed data of most
optimal spectra for predicting response
tic

%%%%%%%%%%%%%%%%%%%%%%%%%%%%%%%%%%%%%%%%%%%%%%%%%%%%%%%%%%%%%%%%%%%%%%%%%%%%%%%

%Input parameters
 nfactPLS = 5;        % Change number of PLS components
 nfactPCR = 5;        % Change number of PCR components
 k = 10;              % k-fold cross validation (CV)
 width = 11;          % Set value for width for savgol smoothing
 order = 3;           % Set polynomial order for savgol smoothing
 deriv = 1;           % Set value for derivative for savgol smoothing


%%%%%%%%%%%%%%%%%%%%%%%%%%%%%%%%%%%%%%%%%%%%%%%%%%%%%%%%%%%%%%%%%%%%%%%%%%%%%%%


%Load data from Excel sheet
```

```
 data=xlsread('December_Raman_Calibration_Meso.xlsx','All_Spectra2');

%Reads data from Excel sheet
 X = data(2:274,in1);            % Select spectral & temperature data.
 'in' file located in StepwiseVariable# file
 y = data(2:274,3328);           % Select concentration values for
 model training data
 [n,p]=size(X);                  % Gives size of the temperature and
 spectral data matrix

%Data pre-processing
 meanX = mean(X);                  % Calculates mean of the array
 [X] = msc(X,meanX);             % Scatter correction by performing
 centring on the array around the mean reference spectra
 %[X] = savgol(X,width,order,deriv);         % Smoothing of the
 corrected spectra. Set values for (width,order,deriv)above
 [X_Scaled,mx,stdx]= autoscale(X,[],[]);     % Autoscale X axis
 [y_Scaled,my,stdy]= autoscale(y,[],[]);     % Autoscale Y axis

%%%%%%%%%%%%%%%%%%%%%%%%%%%%%%%%%%%%%%%%%%%%%%%%%%%%%%%%%%%%%%%%%%%%%%%%%%%

%PLS model

 [Xloadings,Yloadings,Xscores,Yscores,betaPLS,PLSPctVar,PLSmsep,stats]
 = plsregress(X_Scaled,y_Scaled,nfactPLS,'CV',k); % Performs PLS
 regression with factors

 figure (1), plot(1:nfactPLS,cumsum(100*PLSPctVar(2,:)),'-bo');
 xlabel('Number of PLS components');
 ylabel('Percent Variance Explained in Y'); % The plot shows how much
 variance in vector Y is explained by each PLS component
 yfitPLS = [ones(n,1) X_Scaled]*betaPLS.*stdy + my; % Calculates
 concentraion of the training data with the developed model
% yval = [ones(n,1) X_Scaled]*betaPLS3;
 pbaspect([1.3 1 1]);


%%%%%%%%%%%%%%%%%%%%%%%%%%%%%%%%%%%%%%%%%%%%%%%%%%%%%%%%%%%%%%%%%%%%%%%%%%%

% PCR Model

 [PCALoadings,PCAScores,PCAVar] = princomp(X_Scaled); %Builds PCR
 model
 betaPCR = regress(y-mean(y), PCAScores(:,1:nfactPCR)); %Change
 nfactPCR above to change no. of factors
 betaPCR = PCALoadings(:,1:nfactPCR)*betaPCR; % *stdy + my; % This
 should be same as in previous line
 betaPCR = [mean(y) - mean(X_Scaled)*betaPCR; betaPCR];
 yfitPCR = [ones(n,1) X_Scaled]*betaPCR;

 figure (2),
 plot(100*cumsum(PCAVar(1:nfactPCR))/sum(PCAVar(1:nfactPCR)),'r-^');
 xlabel('Number of PCR components');
 ylabel('Percent Variance Explained in Y');
 pbaspect([1.3 1 1]);

 PCRmsep = sum(crossval(@pcrsse,X,y,'KFold',10),1)/n; %Error between
 the actual and predicted concentration


%save MainModel betaPLS meanX mx stdx my stdy
```

```
%%%%%%%%%%%%%%%%%%%%%%%%%%%%%%%%%%%%%%%%%%%%%%%%%%%%%%%%%%%%%%%%%%%%%%%%%%%%

%PRESS Plot

 % figure (3), plot(0:10,PLSmsep(2,:),'b-o',0:15,PCRmsep,'r-^');
 % xlabel('Number of components');
 % ylabel('Estimated Mean Squared Prediction Error');
 % legend({'PLSR' 'PCR'},'location','NE');

%%%%%%%%%%%%%%%%%%%%%%%%%%%%%%%%%%%%%%%%%%%%%%%%%%%%%%%%%%%%%%%%%%%%%%%%%%%%

%Principal Component Analysis

 figure (4)
 pcclusters = clusterdata(PCAScores(:,1:10),7);
 gscatter(PCAScores(:,3),PCAScores(:,4),pcclusters); % For generating
 Scores scatter plot.
 pbaspect([1.3 1 1]);
 xlabel('PC2');
 ylabel('PC3');

%%%%%%%%%%%%%%%%%%%%%%%%%%%%%%%%%%%%%%%%%%%%%%%%%%%%%%%%%%%%%%%%%%%%%%%%%%%%

 figure (5), plot(y,yfitPLS,'bo');
 xlabel('Observed Response');
 ylabel('Fitted Response');
 legend({'PLSR with 5 Components'},  ...
    'location','NW');
 pbaspect([1.3 1 1]);

%%%%%%%%%%%%%%%%%%%%%%%%%%%%%%%%%%%%%%%%%%%%%%%%%%%%%%%%%%%%%%%%%%%%%%%%%%%%

 figure (6), plot(y,yfitPCR,'r^');
 xlabel('Observed Response');
 ylabel('Fitted Response');
 legend({'PCR with 5 Components'},  ...
    'location','NW');

%%%%%%%%%%%%%%%%%%%%%%%%%%%%%%%%%%%%%%%%%%%%%%%%%%%%%%%%%%%%%%%%%%%%%%%%%%%%

%Error calculation PCR/PLS

 TSS = sum((y-mean(y)).^2);
 RSS_PLS = sum((y-yfitPLS).^2);
 rsquaredPLS = 1 - RSS_PLS/TSS
 RSS_PCR = sum((y-yfitPCR).^2);
 rsquaredPCR = 1 - RSS_PCR/TSS

%%%%%%%%%%%%%%%%%%%%%%%%%%%%%%%%%%%%%%%%%%%%%%%%%%%%%%%%%%%%%%%%%%%%%%%%%%%%

%Validation

 data=xlsread('December_Raman_Calibration_Meso.xlsx','All_Spectra2');
 X2 = data(275:314,in1); % Test/Validataion data
 y2 = data(275:314,3328); % Concentration values for model test data


 [X2] = msc(X2,meanX);
 %[X2] = savgol(X2,width,order,deriv);
```

```
 %[n,p]=size(X2); % Gives size of the temperature and spectral data
 matrix
 [X2_Scaled]=autoscale(X2,mx,stdx);

 yvalPLS = [ones(size(X2,1),1) X2_Scaled]*betaPLS.*stdy+my;
 yvalPCR = [ones(size(X2,1),1) X2]*betaPCR; % *stdy+my;

 figure (7), plot(y2,yvalPLS,'bo',y,yfitPLS,'r^');
 hold on
 plot (linspace(0.15,0.30,10),linspace(0.15,0.30,10))
 xlabel('Observed Response');
 ylabel('Fitted Response');
 legend({'Validation standards', 'Calibration standards'},  ...
 'location','NW');
 pbaspect([1.3 1 1]);

 figure (8), plot(y2,yvalPCR,'bo',y,yfitPCR,'r^');
 xlabel('Observed Response');
 ylabel('Fitted Response');
 legend({'PCR with 5 Components'},  ...
 'location','NW');
 pbaspect([1.3 1 1]);

%Error calculation PCR/PLS

 TSS = sum((y2-mean(y)).^2);
 RSS_PLS = sum((y2-yvalPLS).^2);
 rsquaredPLS = (1 - RSS_PLS/TSS);
 RSS_PCR = sum((y2-yvalPCR).^2);
 rsquaredPCR = (1 - RSS_PCR/TSS);

%Root mean squared error of prediction

 PLSrmsep = sqrt(sum((y2-yvalPLS).^2)/40) %RMSEP for PLS model (Change
 this to sample size of validation set)
 PCRrmsep = sqrt(sum((y2-yvalPCR).^2)/40) %RMSEP for PCR model

%Residual calculation
 Res = [(yvalPLS-y2)./y2; (yfitPLS-y)./y];
 figure(9)
 plot([y2;y],res*100,'o'),hold on
 plot([y2;y],res*0),hold off
 xlabel('Actual concentration'), ylabel('% Error')
 pbaspect([1.3 1 1]);

%%%%%%%%%%%%%%%%%%%%%%%%%%%%%%%%%%%%%%%%%%%%%%%%%%%%%%%%%%%%%%%%%%%%%%%%%%%%

%Prediction

 data = xlsread('2ndNovember_2mm2Hz_10percent_7minsRT.xlsx','Sheet1');
 in1(end) = 3326;
 X3 = data(2:198,in1); % Test/Validation data

 %[X3] = msc(X3,mean(X));
 %[X3] = savgol(X3,7,3,1);
 %col2 = size(X3,2);
 %mx2 = mean(X3,2);
 %stdx2 = std(X3,0,2);
 X3_Scaled = autoscale(X3,mx,stdx);
```

```
 ypredPLS = [ones(size(X3_Scaled,1),1) X3_Scaled]*betaPLS.*stdy+my;
 ypredPCR = [ones(size(X3,1),1) X3]*betaPCR;

toc
```

A-4 Analytical solution of the heat balance ODEs

Process fluid

$$\frac{dT_1}{dx} = \frac{(T_2 - T_1)}{X_1} \tag{1}$$

where $X_1 = \frac{\dot{m}_1 C_{p1}}{A_{L1} U_{21}}$

Cooling fluid

$$\frac{dT_2}{dx} = \frac{(T_1 - T_2)}{X_{21}} \tag{2}$$

where $X_{21} = -\frac{\dot{m}_2 C_{p2}}{A_{L1} U_{21}}$

Combination into a single ODE

From Equation (1)

$$T_2 = X_1 \frac{dT_1}{dx} + T_1 \tag{3}$$

Substituting in Equation (2) and collecting terms

$$X_1 X_{21} \frac{d^2 T_1}{dx^2} + (X_{21} + X_1) \frac{dT_1}{dx} = 0 \tag{4}$$

Rewriting by defining new variables a, b

$$a \frac{d^2 T_1}{dx^2} + b \frac{dT_1}{dx} = 0 \tag{5}$$

where $a = X_1 X_{21}$, $b = X_{21} + X_1$

Solution of the ODE

Solving Equation (4) subject to the initial condition that $T_1 = T_{1in}$ at $x = 0$ gives

$$T_1 = -C_2 + T_{1in} + C_2 \exp(B_2 x) \tag{6}$$

where C_2 is the integration constant and $B_2 = -\frac{b}{a}$

Substituting equation (6) back into Equation (3) gives

$$T_2 = -C_2 + T_{1in}\, C_2(X_1 B_2 + 1) \exp(B_2 x) \tag{7}$$

Application of the boundary conditions

For $T_2 = T_{2in}$ at $x = L_1$ Equation (7) becomes

$$T_{2in} = T_{1in} + C_2((X_1 B_2 + 1) \exp(B_2 L_1) - 1) \tag{8}$$

Rewriting Equation (8) in terms of simpler variables

$$F = E C_2 \tag{9}$$

Where $E = (X_1 B_2 + 1) \exp(B_2 L_1) - 1$, $F = T_{2in} - T_{1in}$

The solution to Equation (9) is

$$C_2 = \frac{F}{E} \tag{10}$$

Solution parameters

$X_1, X_{21}, a, b, B_2, C_2, E, F$

A-5 Liquid phase axial dispersion coefficients from conductivity measurements

Flow rate (ml min^{-1})	f (Hz)	Re_o	τ (s)	D_{ax}/uL	u (m s^{-1})	D_{ax} (m^2 s^{-1})	N
5	2	31	446.7	3.68×10^{-2}	5.50×10^{-3}	5.49×10^{-4}	15
			437.2	3.86×10^{-2}	5.70×10^{-3}	5.94×10^{-4}	14
	4	62	441.6	4.43×10^{-2}	5.60×10^{-3}	6.66×10^{-4}	12
	6	93	454.9	3.14×10^{-3}	5.60×10^{-3}	4.72×10^{-4}	17
	8	123	460.1	2.48×10^{-2}	5.60×10^{-3}	3.72×10^{-4}	21
	10	154	466.4	1.69×10^{-3}	5.60×10^{-3}	2.55×10^{-4}	31
	12	185	479.2	1.08×10^{-3}	5.60×10^{-3}	1.64×10^{-4}	47

A-6 Liquid and solid phase axial dispersion coefficients from dye tracer measurements

A-6.1 Liquid phase axial dispersion coefficients for $x_0 = 0.5$ mm

Flow rate (ml min^{-1})	f (Hz)	Re_o	τ (s)	D_{ax}/uL	u (m s^{-1})	D_{ax} (m^2 s^{-1})	N
5	2	31	433.7	1.76×10^{-2}	5.90×10^{-3}	2.82×10^{-4}	29
			445.7	1.73×10^{-2}	5.80×10^{-3}	2.71×10^{-4}	30
			442.5	1.73×10^{-2}	6.00×10^{-3}	2.77×10^{-4}	30
			423.2	2.02×10^{-2}	6.10×10^{-3}	3.30×10^{-4}	26
	4	62	436.6	1.26×10^{-2}	6.00×10^{-3}	2.04×10^{-4}	41
			429.8	2.15×10^{-2}	5.90×10^{-3}	3.44×10^{-4}	25
	6	93	445.2	8.60×10^{-3}	5.90×10^{-3}	1.37×10^{-4}	59
			430.6	8.70×10^{-3}	6.10×10^{-3}	1.44×10^{-4}	58
	8	123	438.9	1.27×10^{-2}	6.00×10^{-3}	2.03×10^{-4}	40
			441.1	6.10×10^{-3}	6.00×10^{-3}	9.78×10^{-4}	84
			453.0	5.30×10^{-3}	5.80×10^{-3}	8.39×10^{-5}	95
	10	154	480.6	6.80×10^{-3}	5.50×10^{-3}	1.01×10^{-4}	75
			431.7	5.40×10^{-3}	6.10×10^{-3}	8.91×10^{-5}	93
			449.4	6.40×10^{-3}	5.90×10^{-3}	1.02×10^{-4}	79
			454.8	3.90×10^{-3}	5.90×10^{-3}	6.10×10^{-5}	130
	12	185	448.9	3.70×10^{-3}	5.90×10^{-3}	5.93×10^{-5}	136
			442.4	5.50×10^{-3}	6.00×10^{-3}	8.92×10^{-5}	92
			446.1	5.40×10^{-3}	5.90×10^{-3}	8.66×10^{-5}	93
2	2	31	1475.0	3.73×10^{-2}	2.60×10^{-3}	2.61×10^{-4}	14
			930.5	1.58×10^{-2}	2.90×10^{-3}	1.23×10^{-4}	33
			933.5	3.87×10^{-2}	2.90×10^{-3}	3.02×10^{-4}	14
	4	62	986.6	2.52×10^{-2}	2.70×10^{-3}	1.83×10^{-4}	21
			958.3	2.37×10^{-2}	2.80×10^{-3}	1.79×10^{-4}	22
	6	93	969.4	1.48×10^{-2}	2.80×10^{-3}	1.12×10^{-4}	35
			986.7	1.90×10^{-2}	2.70×10^{-3}	1.38×10^{-4}	27
	8	123	1044	1.91×10^{-2}	2.70×10^{-3}	1.39×10^{-4}	27
			982.2	1.56×10^{-2}	2.80×10^{-3}	1.18×10^{-4}	33
	10	154	997.3	1.16×10^{-2}	2.70×10^{-3}	8.43×10^{-5}	44
			974.6	8.20×10^{-2}	2.80×10^{-3}	6.18×10^{-5}	62
	12	185	1021	5.10×10^{-3}	2.60×10^{-3}	3.57×10^{-5}	99
			1047	1.71×10^{-2}	2.60×10^{-3}	1.20×10^{-4}	30

A-6.2 Liquid phase axial dispersion coefficients for $x_0 = 1.0$ mm

Flow rate (ml min^{-1})	f (Hz)	Re_o	τ (s)	D_{ax}/uL	u (m s^{-1})	D_{ax} (m^2 s^{-1})	N
5	2	62	451.9	3.03×10^{-2}	5.90×10^{-3}	4.81×10^{-4}	18
			453.1	2.35×10^{-2}	5.90×10^{-3}	3.73×10^{-4}	22
	4	123	449.1	2.77×10^{-2}	6.00×10^{-3}	4.47×10^{-4}	19
			454.7	2.19×10^{-2}	5.90×10^{-3}	3.48×10^{-4}	24
	6	185	430.4	2.29×10^{-2}	5.90×10^{-3}	3.64×10^{-4}	23
			436.6	1.81×10^{-2}	5.90×10^{-3}	2.88×10^{-4}	29
	8	247	429.4	1.93×10^{-2}	6.30×10^{-3}	3.27×10^{-4}	27
			435.1	1.67×10^{-2}	6.20×10^{-3}	2.79×10^{-4}	31
	10	308	437.4	1.34×10^{-2}	6.00×10^{-3}	2.16×10^{-4}	38
			435.0	1.36×10^{-2}	6.20×10^{-3}	2.27×10^{-4}	38
	12	370	443.2	1.05×10^{-2}	5.90×10^{-3}	1.67×10^{-4}	49
			433.6	1.01×10^{-2}	6.00×10^{-3}	1.63×10^{-4}	51

A-6.3 Liquid phase axial dispersion coefficients for $x_0 = 2.0$ mm

Flow rate (ml min^{-1})	f (Hz)	Re_o	τ (s)	D_{ax}/uL	u (m s^{-1})	D_{ax} (m^2 s^{-1})	N
5	2	123	413.0	4.10×10^{-2}	5.60×10^{-3}	6.19×10^{-4}	14
			431.2	3.55×10^{-2}	6.20×10^{-3}	5.93×10^{-4}	15
	4	247	430.6	2.99×10^{-2}	5.60×10^{-3}	4.51×10^{-4}	18
			440.7	3.30×10^{-2}	6.10×10^{-3}	5.42×10^{-4}	16
	6	370	438.6	2.36×10^{-2}	5.70×10^{-3}	3.62×10^{-4}	22
			432.3	2.12×10^{-2}	6.20×10^{-3}	3.54×10^{-4}	25
	8	493	437.3	1.79×10^{-2}	5.80×10^{-3}	2.80×10^{-4}	29
			438.1	1.78×10^{-2}	6.10×10^{-3}	2.92×10^{-4}	29
	10	617	441.3	1.11×10^{-2}	6.00×10^{-3}	1.79×10^{-4}	46
			445.7	1.31×10^{-2}	6.00×10^{-3}	2.12×10^{-4}	39
	12	740	454.7	7.90×10^{-2}	5.90×10^{-3}	1.25×10^{-4}	64
			450.0	1.25×10^{-2}	6.00×10^{-3}	2.02×10^{-4}	41

A-6.4 Solid phase axial dispersion coefficients for $x_0 = 0.5$ mm

Flow rate (ml min^{-1})	f (Hz)	Re_o	τ (s)	D_{ax}/uL	u (m s^{-1})	D_{ax} (m^2 s^{-1})	N
5	2	31	429.5	2.11×10^{-2}	6.30×10^{-3}	3.58×10^{-4}	25
			538.7	3.20×10^{-2}	4.90×10^{-3}	4.22×10^{-4}	17
	4	62	444.3	1.81×10^{-2}	6.10×10^{-3}	2.97×10^{-4}	29
			476.6	2.56×10^{-2}	5.70×10^{-3}	3.93×10^{-4}	21
	6	93	457.3	1.42×10^{-2}	5.90×10^{-3}	2.26×10^{-4}	36
			430.6	1.05×10^{-2}	6.30×10^{-3}	1.78×10^{-4}	49
	8	123	437.2	9.30×10^{-3}	6.30×10^{-3}	1.58×10^{-4}	55
			460.9	1.38×10^{-2}	5.90×10^{-3}	2.19×10^{-4}	37
	10	154	401.3	8.60×10^{-3}	6.90×10^{-3}	1.60×10^{-4}	59
			459.3	1.14×10^{-2}	5.90×10^{-3}	1.81×10^{-4}	45
	12	185	406.4	5.90×10^{-3}	6.70×10^{-3}	1.06×10^{-4}	86
			475.3	7.00×10^{-3}	5.70×10^{-3}	1.07×10^{-4}	72

A-7 Temperature readings for heat transfer experiments

A-7.1 Steady flow in the plain and SPC meso-tube

meso-tube	Flow rate (ml min^{-1})	Re_n	f (Hz)	x_0 (m)	Re_o	$T_{1_{in}}$ (°C)	$T_{1_{out}}$ (°C)	T_w (°C)
Plain	2	10.79	0	0	0	55.56	5.33	3.80
		10.79	0	0	0	55.58	5.24	3.81
	4	21.59	0	0	0	55.71	4.72	3.79
		21.59	0	0	0	55.78	4.79	3.79
	6	32.38	0	0	0	55.03	4.59	3.33
		32.38	0	0	0	55.96	4.54	3.83
	8	43.18	0	0	0	55.53	4.48	3.73
		43.18	0	0	0	55.55	4.49	3.78
	10	53.97	0	0	0	55.43	4.59	3.57
		53.97	0	0	0	55.40	4.54	3.59
SPC	2	10.79	0	0	0	35.51	6.45	3.72
	4	21.59	0	0	0	55.49	4.47	3.75
	6	32.38	0	0	0	56.04	4.37	3.67
	8	43.18	0	0	0	55.68	4.35	3.81
	10	53.97	0	0	0	55.95	4.75	3.81

All temperatures were averaged over 1 min measurements at steady-state.

A-7.2 Unsteady flow in the SPC meso-tube with varying amplitude

Flow rate (ml min^{-1})	Re_n	f (Hz)	x_0 (m)	Re_o	$T_{1_{in}}$ (°C)	$T_{1_{out}}$ (°C)	T_w (°C)
8	43.18	2	0.5	39	55.62	4.57	4.07
	43.18	4	0.5	79	55.63	4.52	4.03
	43.18	6	0.5	118	55.41	4.49	4.03
	43.18	8	0.5	157	55.72	4.54	4.05
	43.18	10	0.5	197	55.98	4.40	3.86
8	43.18	2	1	79	55.04	4.53	3.95
	43.18	4	1	157	55.37	4.34	3.90
	43.18	6	1	236	55.84	4.35	3.93
	43.18	8	1	315	55.12	4.37	3.95
	43.18	10	1	393	55.09	4.39	3.94
8	43.18	2	1.5	118	55.12	4.66	3.95
	43.18	4	1.5	236	55.84	4.40	3.93
	43.18	6	1.5	354	55.58	4.36	3.92
	43.18	8	1.5	472	55.33	4.42	3.95
	43.18	10	1.5	590	55.33	4.47	3.92
8	43.18	2	2	157	54.84	4.79	3.93
	43.18	4	2	315	55.59	4.48	3.93
	43.18	6	2	472	55.62	4.48	3.96
	43.18	8	2	629	55.70	4.48	3.93
	43.18	10	2	786	55.34	4.49	3.94

All temperatures were averaged over 1 min measurements at steady-state

A-7.3 Unsteady flow in the SPC meso-tube with fixed amplitude

Flow rate (ml min^{-1})	Re_n	f (Hz)	x_0 (m)	Re_o	$T_{1_{in}}$ (°C)	$T_{1_{out}}$ (°C)	T_w (°C)
2	10.79	2	0.5	39	34.74	4.65	2.80
4	21.59	2	0.5	39	55.18	4.18	3.72
6	32.38	2	0.5	39	55.68	4.15	3.78
8	43.18	2	0.5	39	55.56	4.21	3.79
10	53.97	2	0.5	39	55.80	4.32	3.62
2	10.79	4	0.5	79	35.65	4.42	3.41
4	21.59	4	0.5	79	55.52	4.28	3.86
4	21.59	4	0.5	79	55.48	4.28	3.91
6	32.38	4	0.5	79	56.04	4.12	3.78
8	43.18	4	0.5	79	55.93	4.22	3.79
8	43.18	4	0.5	79	55.97	4.19	3.96
10	53.97	4	0.5	79	55.51	4.19	3.75
2	10.79	6	0.5	118	35.64	4.43	3.65
4	21.59	6	0.5	118	55.61	4.30	3.78
4	21.59	6	0.5	118	55.58	4.30	3.89
6	32.38	6	0.5	118	56.07	4.15	3.78
8	43.18	6	0.5	118	55.76	4.20	3.83
8	43.18	6	0.5	118	55.66	4.10	3.87
10	53.97	6	0.5	118	56.08	4.22	3.82
2	10.79	8	0.5	157	35.41	4.42	3.59
4	21.59	8	0.5	157	55.50	4.29	3.85
6	32.38	8	0.5	157	55.82	4.15	3.75
8	43.18	8	0.5	157	55.75	4.21	3.88
8	43.18	8	0.5	157	56.24	4.15	3.86
10	53.97	8	0.5	157	55.72	4.24	3.84
2	10.79	10	0.5	197	35.34	4.39	3.50
4	21.59	10	0.5	197	56.07	4.42	3.81
6	32.38	10	0.5	197	55.69	4.13	3.71
8	43.18	10	0.5	197	55.48	4.18	4.04
10	53.97	10	0.5	197	55.77	4.25	3.72

All temperatures were averaged over 1 min measurements at steady-state.

A-8 Nusselt numbers for heat transfer experiments

A-8.1 Steady flow in the plain and SPC meso-tube

meso-tube	Flow rate (ml min^{-1})	Re_n	f (Hz)	x_0 (m)	Re_o	LMTD	U_{21}	Nu_s	h_s	Nu_t	New correlation	M-S correlation
Plain	2	10.79	0	0	0	14.26	33.79	44.99	13042	0.28	0.42	0.14
		10.79	0	0	0	14.03	34.43	44.99	13042	0.29	0.42	0.14
	4	21.59	0	0	0	12.68	77.19	44.99	13042	0.67	0.94	0.33
		21.59	0	0	0	12.91	75.79	44.99	13042	0.66	0.94	0.33
	6	32.38	0	0	0	13.60	106.72	44.99	13042	0.95	1.51	0.56
		32.38	0	0	0	11.94	123.95	44.99	13042	1.12	1.51	0.56
	8	43.18	0	0	0	12.04	162.75	44.99	13042	1.53	2.11	0.82
		43.18	0	0	0	11.90	164.57	44.99	13042	1.55	2.11	0.82
	10	53.97	0	0	0	12.91	188.88	44.99	13042	1.82	2.73	1.09
		53.97	0	0	0	12.73	191.55	44.99	13042	1.86	2.73	1.09
SPC	2	10.79	0	0	0	11.83	30.80	44.99	13042	0.26	0.42	0.14
	4	21.59	0	0	0	11.93	107.25	44.99	13042	0.95	0.94	0.33
	6	32.38	0	0	0	11.96	162.56	44.99	13042	1.53	1.51	0.56
	8	43.18	0	0	0	11.22	229.50	44.99	13042	2.31	2.11	0.82
	10	53.97	0	0	0	12.77	251.49	44.99	13042	2.60	2.73	1.09

All Nu_t values were obtained from steady-state measurements.

A-8.2 Unsteady flow in the SPC meso-tube with varying amplitude

Flow rate (ml min^{-1})	Re_n	f (Hz)	x_0 (m)	Re_o	LMTD	U_{21}	Nu_s	h_s	Nu_t	New correlation	M-S correlation
8	43.18	2	0.5	39	11.05	231.85	44.99	13042	2.34	2.43	1.03
8	43.18	4	0.5	79	10.97	233.76	44.99	13042	2.37	2.44	1.80
8	43.18	6	0.5	118	10.80	236.47	44.99	13042	2.40	2.45	3.20
8	43.18	8	0.5	157	11.00	233.36	44.99	13042	2.36	2.46	5.31
8	43.18	10	0.5	197	11.31	228.85	44.99	13042	2.31	2.47	8.16
8	43.18	2	1	79	11.28	224.58	44.99	13042	2.25	2.28	1.80
8	43.18	4	1	157	10.72	238.79	44.99	13042	2.43	2.29	5.31
8	43.18	6	1	236	10.67	242.22	44.99	13042	2.48	2.29	11.78
8	43.18	8	1	315	10.59	240.49	44.99	13042	2.45	2.30	21.45
8	43.18	10	1	393	10.70	237.77	44.99	13042	2.42	2.30	34.53
8	43.18	2	1.5	118	11.82	214.26	44.99	13042	2.13	2.22	3.20
8	43.18	4	1.5	236	10.94	235.92	44.99	13042	2.40	2.23	11.78
8	43.18	6	1.5	354	10.78	238.50	44.99	13042	2.43	2.24	27.56
8	43.18	8	1.5	472	10.80	236.47	44.99	13042	2.40	2.24	51.17
8	43.18	10	1.5	590	11.22	227.44	44.99	13042	2.29	2.24	83.08
8	43.18	2	2	157	12.27	204.60	44.99	13042	2.01	2.20	5.31
8	43.18	4	2	315	11.24	228.07	44.99	13042	2.30	2.20	21.45
8	43.18	6	2	472	11.11	231.06	44.99	13042	2.33	2.21	51.17
8	43.18	8	2	629	11.28	227.79	44.99	13042	2.29	2.21	95.63
8	43.18	10	2	786	11.22	227.35	44.99	13042	2.29	2.21	155.72

All Nu_t values were obtained from steady-state measurements.

A-8.3 Unsteady flow in the SPC meso-tube with fixed amplitude

Flow rate (ml min^{-1})	Re_n	f (Hz)	x_0 (m)	Re_o	LMTD	U_{21}	Nu_s	h_s	Nu_t	New correlation	M-S correlation
2	10.79	2	0.5	39	10.56	35.73	44.99	13042	0.30	0.47	0.36
4	21.59	2	0.5	39	10.79	118.52	44.99	13042	1.07	1.06	0.55
6	32.38	2	0.5	39	10.46	185.33	44.99	13042	1.78	1.72	0.78
8	43.18	2	0.5	39	10.64	242.13	44.99	13042	2.48	2.42	1.03
10	53.97	2	0.5	39	11.93	270.70	44.99	13042	2.86	3.16	1.30
2	10.79	4	0.5	79	9.02	43.44	44.99	13042	0.36	0.47	1.16
4	21.59	4	0.5	79	10.65	120.74	44.99	13042	1.09	1.07	1.34
4	21.59	4	0.5	79	10.41	123.40	44.99	13042	1.12	1.07	1.34
6	32.38	4	0.5	79	10.32	189.32	44.99	13042	1.83	1.73	1.56
8	43.18	4	0.5	79	10.77	240.85	44.99	13042	2.46	2.44	1.80
8	43.18	4	0.5	79	9.56	271.85	44.99	13042	2.87	2.44	1.80
10	53.97	4	0.5	79	10.73	299.93	44.99	13042	3.27	3.19	2.06
2	10.79	6	0.5	118	8.39	46.67	44.99	13042	0.39	0.47	2.64
4	21.59	6	0.5	118	11.15	115.39	44.99	13042	1.04	1.07	2.80
4	21.59	6	0.5	118	10.58	121.59	44.99	13042	1.10	1.07	2.80
6	32.38	6	0.5	118	10.48	186.41	44.99	13042	1.80	1.74	2.99
8	43.18	6	0.5	118	10.45	247.58	44.99	13042	2.55	2.45	3.20
8	43.18	6	0.5	118	9.53	271.50	44.99	13042	2.87	2.45	3.20
10	53.97	6	0.5	118	10.68	304.51	44.99	13042	3.34	3.20	3.44
2	10.79	8	0.5	157	8.50	45.73	44.99	13042	0.38	0.47	4.85
4	21.59	8	0.5	157	10.75	119.48	44.99	13042	1.08	1.08	4.97
6	32.38	8	0.5	157	10.59	183.53	44.99	13042	1.76	1.74	5.13
8	43.18	8	0.5	157	10.21	253.13	44.99	13042	2.62	2.46	5.31
8	43.18	8	0.5	157	9.97	262.23	44.99	13042	2.74	2.46	5.31
10	53.97	8	0.5	157	10.59	304.93	44.99	13042	3.35	3.21	5.51
2	10.79	10	0.5	197	8.63	44.98	44.99	13042	0.38	0.47	7.84
4	21.59	10	0.5	197	11.60	111.69	44.99	13042	1.00	1.08	7.91
6	32.38	10	0.5	197	10.75	180.52	44.99	13042	1.73	1.75	8.02
8	43.18	10	0.5	197	8.76	293.70	44.99	13042	3.18	2.47	8.16
10	53.97	10	0.5	197	11.23	288	44.99	13042	3.10	3.22	8.31

All Nu_t values were obtained from steady-state measurements.

A-9 Sensitivity matrix for estimability analysis

		a	b	c	α	β	γ	θ
$\boldsymbol{Z} =$	$(S_n)_{u1f1}$	1.000	0.000	0.000	3.178	0.517	0.000	0.000
	$(S_n)_{u1f2}$	0.905	0.095	0.086	2.877	0.468	0.028	0.381
	$(S_n)_{u1f3}$	0.900	0.100	0.091	2.861	0.466	0.036	0.401
	$(S_n)_{u1f4}$	0.897	0.103	0.093	2.852	0.464	0.040	0.413
	$(S_n)_{u1f5}$	0.895	0.105	0.095	2.845	0.463	0.043	0.421
	$(S_n)_{u1f6}$	0.893	0.107	0.097	2.839	0.462	0.046	0.428
	$(S_n)_{u2f1}$	1.000	0.000	0.000	4.281	0.517	0.000	0.000
	$(S_n)_{u2f2}$	0.889	0.111	0.101	3.804	0.460	0.033	0.610
	$(S_n)_{u2f3}$	0.883	0.117	0.107	3.780	0.457	0.042	0.641
	$(S_n)_{u2f4}$	0.879	0.121	0.110	3.765	0.455	0.047	0.659
	$(S_n)_{u2f5}$	0.877	0.123	0.112	3.755	0.454	0.051	0.673
	$(S_n)_{u2f6}$	0.875	0.000	0.114	3.746	0.453	0.054	0.684
	$(S_n)_{u3f1}$	1.000	0.000	0.000	4.969	0.517	0.000	0.000
	$(S_n)_{u3f2}$	0.878	0.122	0.111	4.361	0.454	0.036	0.781
	$(S_n)_{u3f3}$	0.871	0.129	0.117	4.330	0.451	0.046	0.821
	$(S_n)_{u3f4}$	0.868	0.132	0.120	4.312	0.449	0.051	0.844
	$(S_n)_{u3f5}$	0.865	0.135	0.123	4.299	0.447	0.056	0.861
	$(S_n)_{u3f6}$	0.863	0.137	0.125	4.289	0.446	0.059	0.875
	$(S_n)_{u4f1}$	1.000	0.000	0.000	5.477	0.517	0.000	0.000
	$(S_n)_{u4f2}$	0.869	0.131	0.119	4.762	0.450	0.039	0.923
	$(S_n)_{u4f3}$	0.863	0.137	0.125	4.726	0.446	0.049	0.970
	$(S_n)_{u4f4}$	0.859	0.141	0.128	4.705	0.444	0.055	0.997
	$(S_n)_{u4f5}$	0.856	0.144	0.131	4.689	0.443	0.059	1.017
	$(S_n)_{u4f6}$	0.854	0.146	0.133	4.677	0.442	0.063	1.033
	$(S_n)_{u5f1}$	1.000	0.000	0.000	5.883	0.517	0.000	0.000
	$(S_n)_{u5f2}$	0.863	0.137	0.125	5.075	0.446	0.041	1.047
	$(S_n)_{u5f3}$	0.856	0.144	0.131	5.035	0.443	0.051	1.099
	$(S_n)_{u5f4}$	0.852	0.148	0.135	5.011	0.441	0.058	1.129
	$(S_n)_{u5f5}$	0.849	0.151	0.137	4.994	0.439	0.062	1.151
	$(S_n)_{u5f6}$	0.847	0.153	0.140	4.980	0.438	0.066	1.169
	$(S_n)_{f1u1}$	1.000	0.000	0.000	3.178	0.517	0.000	0.000
	$(S_n)_{f1u2}$	1.000	0.000	0.000	4.281	0.517	0.000	0.000
	$(S_n)_{f1u3}$	1.000	0.000	0.000	4.969	0.517	0.000	0.000
	$(S_n)_{f1u4}$	1.000	0.000	0.000	5.477	0.517	0.000	0.000
	$(S_n)_{f1u5}$	1.000	0.000	0.000	5.883	0.517	0.000	0.000
	$(S_n)_{f2u1}$	0.905	0.095	0.086	2.876	0.468	0.028	0.381
	$(S_n)_{f2u2}$	0.888	0.112	0.101	3.804	0.459	0.033	0.610
	$(S_n)_{f2u3}$	0.878	0.122	0.111	4.361	0.454	0.036	0.782
	$(S_n)_{f2u4}$	0.869	0.131	0.119	4.761	0.450	0.039	0.924
	$(S_n)_{f2u5}$	0.863	0.137	0.125	5.074	0.446	0.041	1.047
	$(S_n)_{f3u1}$	0.900	0.100	0.091	2.861	0.466	0.036	0.401
	$(S_n)_{f3u2}$	0.883	0.117	0.107	3.780	0.457	0.042	0.641
	$(S_n)_{f3u3}$	0.871	0.129	0.117	4.330	0.451	0.046	0.821

		a	b	c	α	β	γ	θ
$\boldsymbol{Z} =$	$(S_n)_{f3u4}$	0.863	0.137	0.125	4.726	0.446	0.049	0.970
	$(S_n)_{f3u5}$	0.856	0.144	0.131	5.035	0.443	0.051	1.099
	$(S_n)_{f4u1}$	0.897	0.103	0.093	2.852	0.464	0.040	0.413
	$(S_n)_{f4u2}$	0.879	0.121	0.110	3.765	0.455	0.047	0.659
	$(S_n)_{f4u3}$	0.868	0.132	0.120	4.312	0.449	0.051	0.844
	$(S_n)_{f4u4}$	0.859	0.141	0.128	4.705	0.444	0.055	0.997
	$(S_n)_{f4u5}$	0.852	0.148	0.135	5.011	0.441	0.058	1.129
	$(S_n)_{f5u1}$	0.895	0.105	0.095	2.845	0.463	0.043	0.421
	$(S_n)_{f5u2}$	0.877	0.123	0.112	3.755	0.454	0.051	0.673
	$(S_n)_{f5u3}$	0.865	0.135	0.123	4.299	0.447	0.056	0.861
	$(S_n)_{f5u4}$	0.856	0.144	0.131	4.689	0.443	0.059	1.017
	$(S_n)_{f5u5}$	0.849	0.151	0.137	4.994	0.439	0.062	1.151
	$(S_n)_{f6u1}$	0.893	0.107	0.097	2.839	0.462	0.046	0.428
	$(S_n)_{f6u2}$	0.875	0.125	0.114	3.746	0.453	0.054	0.922
	$(S_n)_{f6u3}$	0.863	0.137	0.125	4.289	0.446	0.059	0.875
	$(S_n)_{f6u4}$	0.854	0.146	0.133	4.677	0.442	0.063	1.033
	$(S_n)_{f6u5}$	0.847	0.153	0.140	4.980	0.438	0.066	1.169

where n is the parameter number, f and u are the frequency and velocity variables.

A-10Performance at just-suspended speed, N_{js}

Mixing duty	Vessel ID	100 ml jacketed vessel	100 ml jacketed vessel
	Liquid volume (l)	0.1	0.1
	Mass of solids (kg)	0.025	0.025
	Total volume of solids & liquid (l)	0.12	0.12
	Scale factor (-)	1	1
	Mass ratio of solid to liquid (%)	24.8	24.8
	Liquid fill level, H (mm)	39	39
	Total surface area (m^2)	0.01	0.01
Performance at N rpm	Agitator speed, N (rpm)	500	400
	Suspension condition	Probably suspended	Not suspended
	Total power input, P (W)	0.01	0.00
	Power input per unit mass (W kg^{-1})	0.058	0.030
	Vessel Reynolds number, Re (-)	7.50×10^3	6.00×10^3
	Vessel flow regime	Transitional	Transitional
	Tip speed, V_{tip} (m s^{-1})	0.79	0.63
	Bulk liquid velocity (m s^{-1})	0.07	0.05
	Vessel averaged turbulent shear rate (s^{-1})	241	173
	Impeller averaged turbulent shear rate (s^{-1})	574	411
	Impeller averaged laminar shear rate (s^{-1})	92	73
	Particle settling velocity (cm s^{-1})	0.54	0.54
Performance at N_{js}	Just suspended speed, N_{js} (rpm)	554	554
	Total power input, P_{js} (W)	0.01	0.01
	Power input per unit mass (W kg^{-1})	0.079	0.079
	Vessel Reynolds number, Re_{js} (-)	8.31×10^3	8.31×10^3
	Tip speed, $V_{tip,js}$(m s^{-1})	0.87	0.87
	Bulk liquid velocity (m s^{-1})	0.08	0.08

	Vessel ID	100 ml jacketed vessel	100 ml jacketed vessel
	Vessel averaged shear rate (s^{-1})	282	282
	Impeller averaged shear rate (s^{-1})	670	670
	Impeller averaged laminar shear rate (s^{-1})	102	102
Physical properties	Liquid density, ρ (kg m^{-3})	1000	1000
	Liquid dynamic viscosity, μ (cP)	1.00	1.00
	Particle density, ρ_p (kg m^{-3})	1610	1610
	Mean particle size, d_p (µm)	100	100
	Average density of slurry (kg m^{-3})	1081	1081
Vessel Geometry	Base shape	DIN Torispherical	DIN Torispherical
	Inner vessel diameter, T (mm)	60	60
	Total height to tan (mm)	55	55
	Maximum volume (l), from database	0.10	0.10
	Base height (mm)	11.6	11.6
	Base volume (l)	0.02	0.02
	Impeller type	Retreat curve impeller	Retreat curve impeller
	Tip diameter (mm)	30.0	30.0
	Clearance (mm)	10.0	10.0
	Projected blade width (mm)	6.0	6.0
	Impeller S number (-)	3.5	3.5

A-11 Estimated UA in 100 ml jacketed vessel

Vessel Geometry	Vessel ID	100 ml jacketed vessel
	Tank diameter, T (mm)	60
	Liquid volume (l)	0.10
	Maximum volume (l), from database	0.10
	Liquid mass (kg)	0.10
	Heat transfer area, A (m^2)	0.010
	Liquid height, H (mm)	39
Process side	Impeller type	Retreat curve impeller
	Impeller diameter (mm)	30
	Agitator speed (rpm)	500
	Solvent name	Water
	Temperature (°C)	60.0
	Fouling factor (W m^{-2} K^{-1})	5000.00
Wall and lining	Wall thickness (mm)	2.50
	Material of construction	Glass (borosilicate)
Service side	Jacket type	Annular unbaffled
	Heat transfer medium	SYLTHERM 8002
	Mass flow rate (kg s^{-1})	1.00
	Temperature (C)	20.0
	Fouling factor (W m^{-2} K^{-1})	1200
Results summary	Inside (process) heat transfer coefficient, h_i (W m^{-2} K^{-1})	3557
	Wall heat transfer coefficient, h_w (W m^{-2} K^{-1})	301
	Outside (service) heat transfer coefficient, h_o (W m^{-2} K^{-1})	1739
	U (W m^{-2} K^{-1})	239
	UA (W K^{-1})	2.39
	Duty (kW)	-0.095
	Heating or cooling rate?	Cooling rate
	Rate (C min^{-1})	-13.654
	T_{jout} (C)	20.06
	T_{wall} (C)	57.31
Process	Solvent	Water
	Density (kg m^{-3})	998
	Specific heat capacity (kJ kg^{-1} K^{-1})	4.200
	Thermal conductivity (W m^{-1} K^{-1})	0.594
	Viscosity (cP)	0.512
Vessel wall	Wall thermal conductivity (W m^{-1} K^{-1})	1.09
Service	Heat transfer medium	SYLTHERM 8002
	Density (kg m^{-3})	930.11
	Specific heat capacity (kJ kg^{-1} K^{-1})	1.608
	Thermal conductivity (W m^{-1} K^{-1})	0.135
	Viscosity (cP)	9.646

A-12 Continuous platforms

Figure A-1 SPC mesoscale crystalliser platform.

Figure A-2 MSMPR platform.

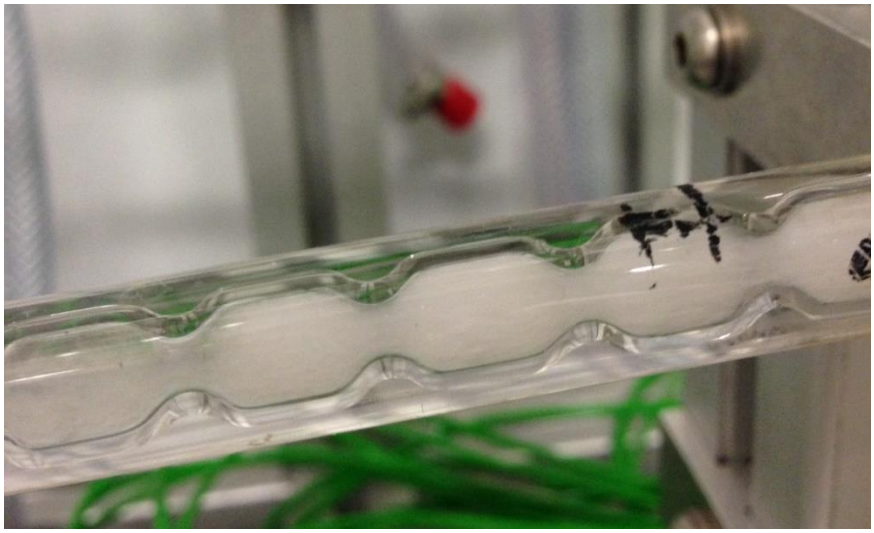

Figure A-3 Seeded crystallisation in the SPC meso-tube.

A-13 Equipment and accessories

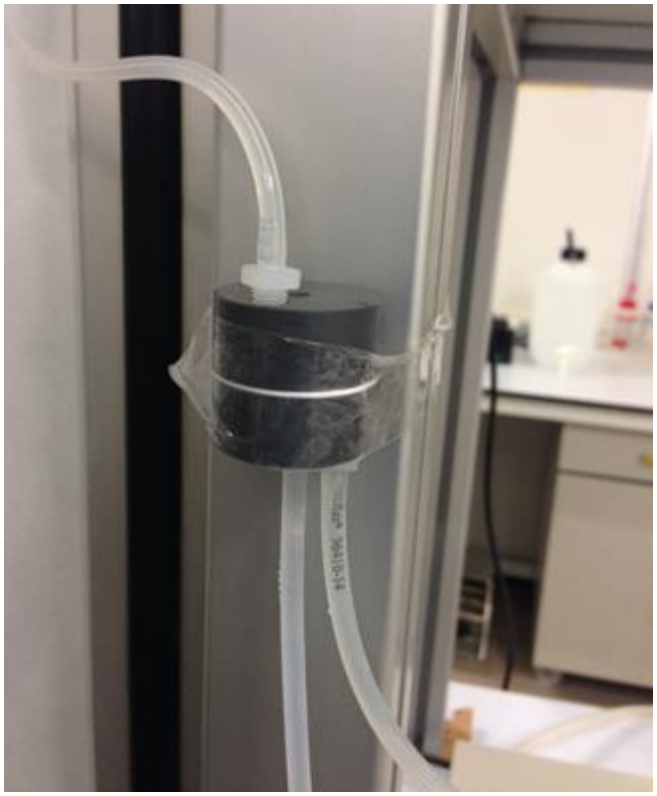

Figure A-4 In-line bubble trap for seed line.

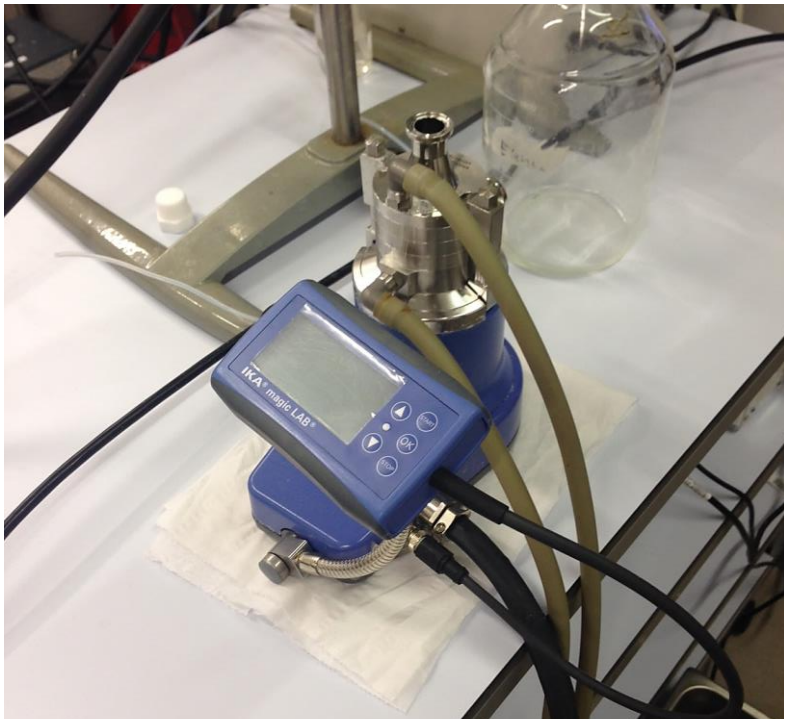

Figure A-5 IKA magic LAB® wet mill device.

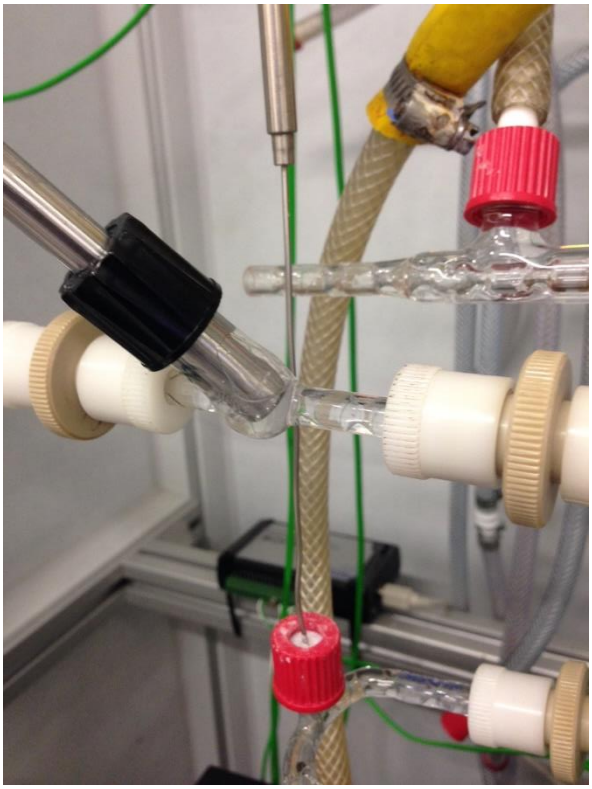

Figure A-6 FBRM probe housing with G400 probe inserted

A-14 Technical drawings

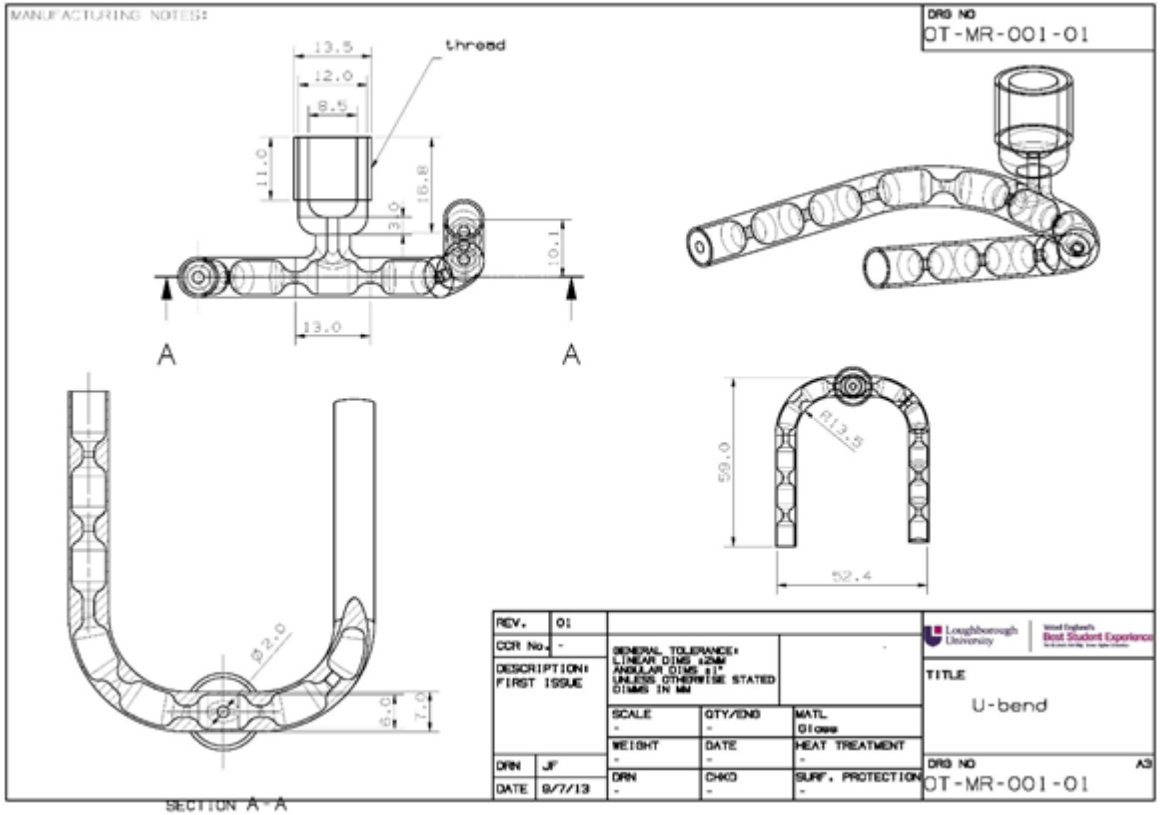

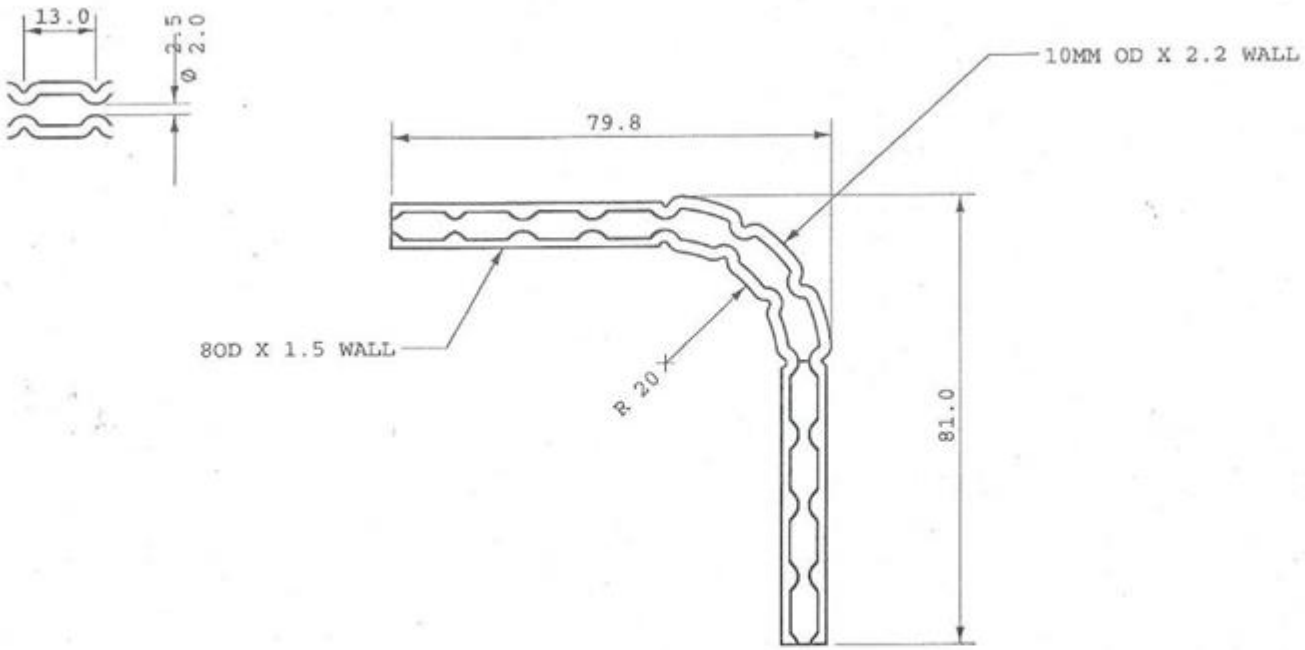

Cambridge Reactor Design Ltd.

Order Code	:	387
Drawing	:	Bend - 90 Deg.
Material	:	Pyrex 10 OD x 2.2 Wall
Finish	:	
Scale	:	1:1 (A4)
Tolerances	:	0 Decimal Place +/- 0.4
	:	1 Decimal Place +/- 0.1
	:	2 Decimal Places +/- 0.05
Drawn by	:	CHM
Version	:	2
Date	:	11-04-05

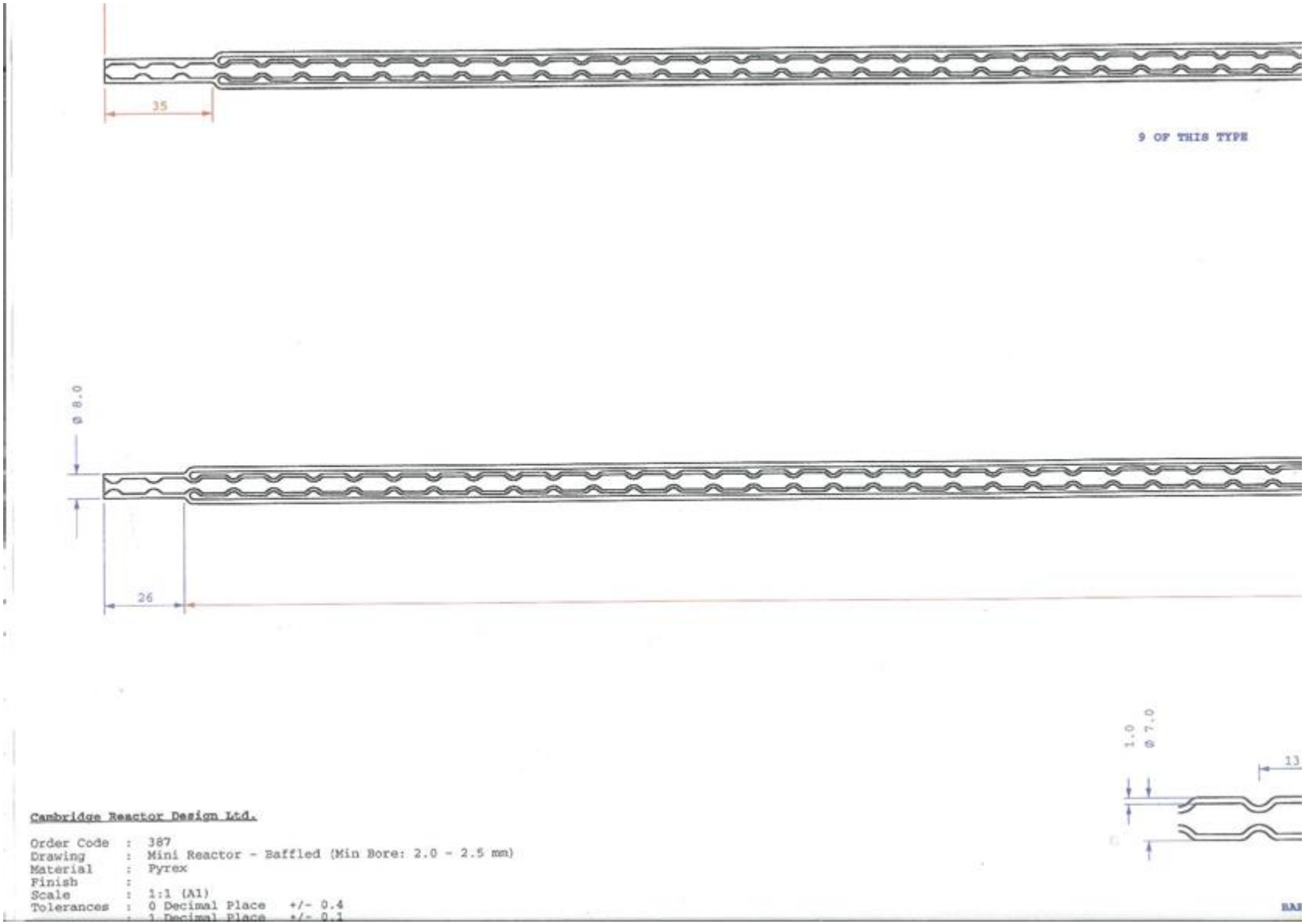
35
9 OF THIS TYPE
ø 8.0
26
1.0
ø 7.0
13
Cambridge Reactor Design Ltd.
Order Code : 387
Drawing : Mini Reactor - Baffled (Min Bore: 2.0 - 2.5 mm)
Material : Pyrex
Finish :
Scale : 1:1 (A1)
Tolerances : 0 Decimal Place +/- 0.4
1 Decimal Place +/- 0.1

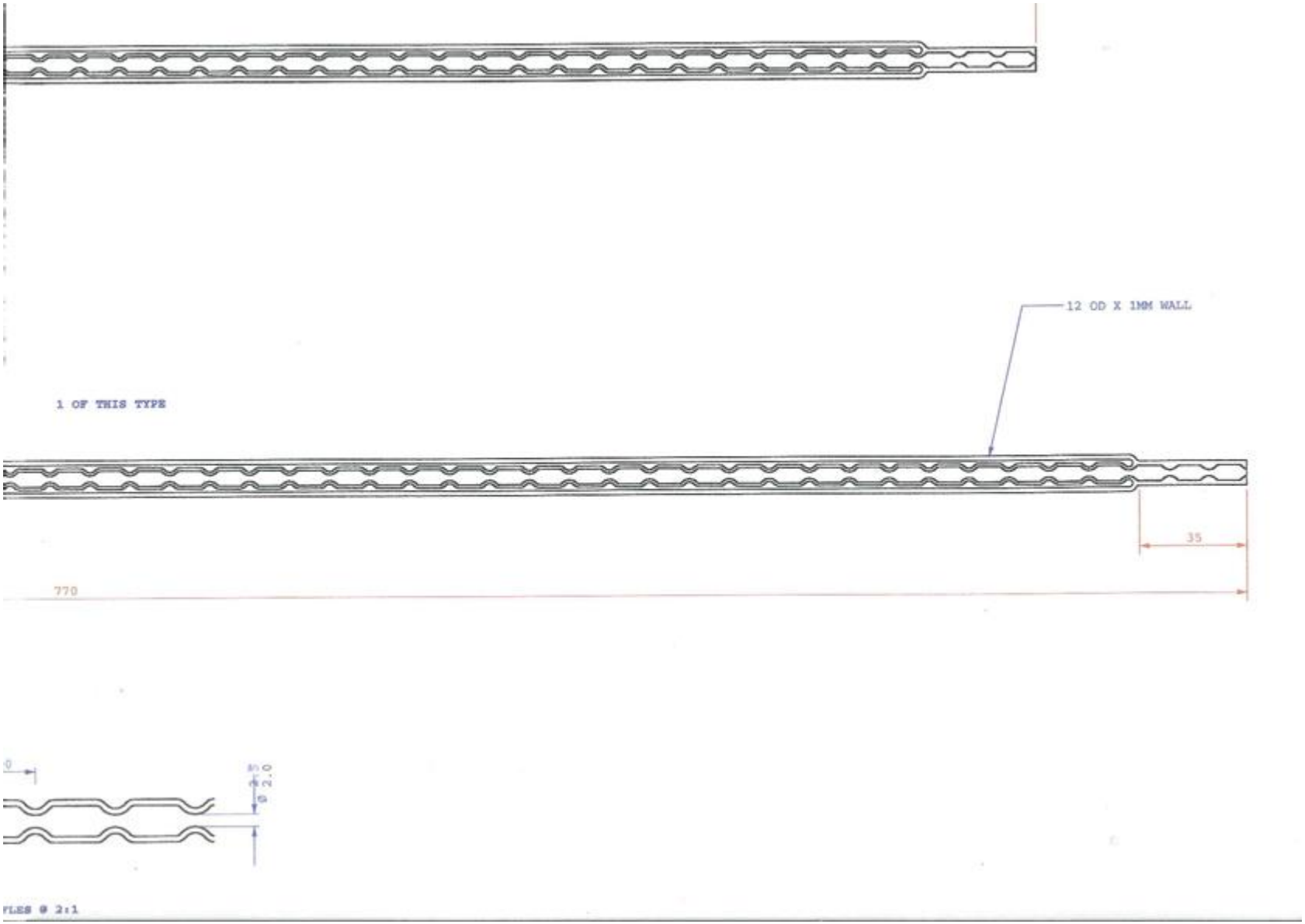
12 OD X 1MM WALL
1 OF THIS TYPE
35
770
2.0
FLES @ 2:1

Appendix B

B-1 List of publications, presentations, awards

B-1.1 Journal articles

Onyemelukwe, I.I., Benyahia, B., Reis, N.M., Nagy, Z.K., Rielly, C.D., 2018. The heat transfer characteristics of a mesoscale continuous oscillatory flow crystalliser with smooth periodic constrictions, Int. J. Heat Mass Transfer, 123, 1109 – 1119. https://doi.org/10.1016/j.ijheatmasstransfer.2018.03.015.

Onyemelukwe, I.I., Parsons, A.R., Wheatcroft, H.P, Robertson, A., Nagy, Z.K., Rielly, C.D., 2018. The role of residence time distribution in the continuous steady-state mixed suspension mixed product removal crystallisation of glycine, Cryst. Growth. Des., 19, 66 – 80. http://doi.org/10.1021/acs.cgd.8b00853.

B-1.2 Conference presentations

Onyemelukwe, I.I., Su, Q., Nagy, Z.K., Rielly, C.D., 2017. The effect of axial dispersion on crystal size distribution in a meso-scale continuous oscillatory baffled crystalliser, in AIChE Annual Meeting, Minneapolis, USA, October 29 – November 3.

Onyemelukwe, I.I., Nagy, Z.K., Rielly, C.D., 2015. Development of continuous crystallisation of glycine in the SPC mesoscale crystalliser, in CMAC Open Day, Glasgow, UK.

B-1.3 Poster presentations

Onyemelukwe, I.I., Nagy, Z.K., Rielly, C.D., 2017. Effects of residence time, oscillation conditions, cooling profile, seed size and loading on the seeded cooling crystallisation of glycine in the mesoscale oscillatory flow crystalliser. CMAC Open Day.

Onyemelukwe, I.I., Nagy, Z.K., Rielly, C.D., 2015. Development of continuous crystallisation of glycine in the SPC mesoscale crystalliser. CMAC Open Day.

Onyemelukwe, I.I., Nagy, Z.K., Rielly, C.D., 2014. An empirical correlation for the tube-side Nusselt number for oscillatory flow in a meso-tube with smooth periodic constrictions. CMAC Internal Research Day.

Onyemelukwe, I.I., Su, Q., Nagy, Z.K., Rielly, C.D., 2014. Axial dispersion of the liquid and solid phases for crystallisation in a mesoscale crystalliser. CMAC Internal Research Day.

B-1.4 Awards

Best Poster Prize for: Onyemelukwe, I.I., Su, Q., Nagy, Z.K., Rielly, C.D., 2014. Axial dispersion of the liquid and solid phases for crystallisation in a mesoscale crystalliser. CMAC Internal Research Day.